8-2018

Materials science of blood clot formation in insects: experimental methods for a multiscale in-situ investigation

Patel Aprelev
Clemson University, pavel.apr@gmail.com

MATERIALS SCIENCE OF BLOOD CLOT FORMATION IN INSECTS: EXPERIMENTAL METHODS FOR A MULTISCALE IN-SITU INVESTIGATION

A Dissertation
Presented to
the Graduate School of
Clemson University

In Partial Fulfillment
of the Requirements for the Degree
Doctor of Philosophy
Materials Science and Engineering

---

by
Pavel Aprelev
August 2018

Accepted by:
Dr. Konstantin Kornev, Committee Chair
Dr. Marek Urban
Dr. Igor Luzinov
Dr. Peter Adler

ABSTRACT

This dissertation is structured around the development of a micro and nano-rheological instrument capable of measuring mPa·s-level viscosity of nanoliter droplets and micron thick films in a 10-20 second timeframe and using it to study the kinetics of formation of a blood clot in insects. To understand the materials science behind this clot formation, we enrich the microrheological study with studies of extensional rheology of various maturity stages of clots as well as studies of the surface tension isotherms, dynamic surface tensions, and surface rheology. To study the rapidly changing structure of the clots, we employ high magnification microscopy and scanning electron microscopy. Overall, we perform a detailed study of physical materials properties and structure of the material, which helps us better understand its outstanding performance.

In Chapter 1, we introduce an engineering reader to the biological aspect of the problem and discuss the functionality of the material in an insect body. In Chapter 2, we discuss the importance of understanding multiscale rheology of the material and review the current methodologies available and their limitations with regards to the study of changing insect blood. In chapter 3, we discuss the principle of our methodology and the realization of the device with which we study the nanorheology with high precision and temporal resolution. In chapter 4, we present nanoscale viscosity measurements of blood of adult butterflies and moths: *Manduca sexta*, *Vanessa cardui*, and *Danaus plexippus* and discuss the significant deviations of the viscosities from the viscosity of water. In chapter 5, we present the nanorheological measurements of forming and maturing clots in

the blood of *M. sexta* caterpillars and present the discovery of characteristic times of formation of these clots. In chapter 6, we present and discuss the fibrous and cellular structures of the forming blood clots of *M. sexta* caterpillars. In chapter 7, we study extensional rheology of forming blood clots of *M. sexta* caterpillars. In chapter 8, we discuss the structure formed in the clots in response to our extensional experiments and relate that to the functions of the clot constituents. Finally, in chapter 9, we study the materials properties of the surface of hemolymph of adult *M. sexta*, *V. cardui*, *D. plexippus,* and caterpillar *M. sexta* and relate them to the nano and microrheological measurements we performed on the material. We thus characterize the time-dependent structure-properties-performance triangles of blood and the forming blood clots in the studied insects.

DEDICATION

This dissertation is dedicated to my wife Raisa and my parents for their support and encouragement throughout my PhD study.

ACKNOWLEDGMENTS

First of all, I would like to thank my advisor, Dr. Konstantin Kornev, for his guidance and support during my PhD study at Clemson University. I would also like to express my gratitude to my committee members, Dr. Igor Luzinov, Dr. Marek Urban and Dr. Peter Adler for their valuable comments and suggestions.

I would also like to thank all the past and current group members, in particular, Dr. Yu Gu, Dr. Maryana Nave, Dr. Artem Trofimov, Chengqi Zhang, Luke Sande, Vaibhav Palkar and Tatiana Stepanova, and Dr. Arthur Salamatin for their help and support during this journey as well as undergraduate research students, Chadwick Walls, Bonni McKinney, Bryan Wiggers, Jovan Corbitt, Ryan Arthur, Gilles Mohl, and Yanick Schlesinger.

I'm also thankful to Kimberly Ivey, Dr. Ruslan Burtovyy, Dr. James Townsend, Dr. Zhaoxi Chen, Dr. Nickolay Borodinov, Dr. Charles Beard, Dr. Terri Bruce, Rhonda Powell, Ben Fellows, Kathleen Davis, Dr. Thompson Mefford, Dr. Alexander Klepp, Dr. Stephen Foulger, Dmitriy Davydovich, Dr. Dmitrii Gill, Dr. Alexey Vertigel, Dr. Vladimir Reukov, Dr. Jeremiah Bowers, Dr. Nishanth Tharayil, Dr. Zeyu Zhao, Dr. Joshua Tong, Dr. Gary Lickfield, Dr. Deborah Lickfield, Robert Bowen and all staff of MS&E department for their continuous support.

Finally, I would like to acknowledge the following funding sources. NSF Projects: PoLS 1305338 and IOS-1354956. Air Force Office of Scientific Research (FA9550-12-1-0459). NASA South Carolina Space Consortium Graduate Research Fellowship.

TABLE OF CONTENTS

Page

Table of Contents (Continued) Page

Table of Contents (Continued) Page

Table of Contents (Continued) Page

LIST OF TABLES

List of Tables (Continued) Page

LIST OF FIGURES

Figure Page

LIST OF NOTATIONS

Symbol	Explanation
A	absorbance
A_m	molecular area
a_n, b_n, c_n	coil calibration coefficients
B	magnetic field
C	concentration
Ca	capillary number
D	density
De	Deborah number
D_i	diffusion coefficient
D_r	dilution ratio
e	elementary charge
G	elastic modulus
I	ionic strength of the solutions
k	second order viscosity coefficient
K	arbitrary constant
k_B	Boltzmann constant
L	length of particle
l	distance between two adjacent cells
m	mass
m	magnetic moment
M	molarity
M_w	molecular weight
n	number of samples studied
N_A	Avogadro's number
$O()$	order of
p	aspect ratio of particle
r	particle radius
R	Radius of a liquid bridge
R_0	initial radius of a liquid bridge
R_1 and R_2	principal radii of a curved surface
R_d	maximum radius of the droplet
Re	Reynolds number
R_f	radius of the fiber or filament
T	temperature

List of Notations (Continued)

t	time
T	temperature
t_i	incubation time
t_s	surface age
u	fluid viscosity
V	volume
v	number concentration
V_n	voltage across coil n
w	mass fraction
We	weber number
α	cell-cell-cell opening angle
β	cell-cell-plasma opening angle
γ	cell-cell-pseudopodia opening angle
Γ_b^σ	surface excess or adsorption
ΔP	pressure differential across the interface
ε	perturbation to the aspect ratio
ε_s	dielectric constant of the solvent
$\varepsilon 0$	permittivity of free space
[η]	intrinsic viscosity
η	viscosity of the solution
η_h	viscosity of hemolymph
η_s	viscosity of the pure solvent
ϑ_c	contact angle
ϑ_o	opening angle between two cells
κ^{-1}	Debye length
ξ	amplitude of oscillation
π	surface pressure
ρ	resistivity of liquid
σ	surface tension
τ	exponential time of exponential viscosity increase
τ_p	characteristic time of the flow process
τ_r	relaxation time
φ	angle that the rod makes with a stationary reference axis
φ_0	initial orientation of the rod
φ_m	maximum packing fraction
φ_p	volume fraction of a particle
ψ_s	surface potential

List of Notations (Continued)

ω_c	critical frequency of rotation
ω_r	elastic parameter

CHAPTER I

INTRODUCTION: BLOOD IN INSECTS (HEMOLYMPH)

In this chapter, we introduce an engineer reader to the physiological role of hemolymph –insect blood – in Lepidoptera – an order of butterflies and moths – at different developmental stages of the insect. We will cover the peculiarities of the circulation system, the primary function of hemolymph, and the role of hemocytes – blood cells.

1.1 RELEVANCE OF STUDY OF INSECTS TO HUMAN LIVES

There are more insects on our planet than any other macro-organisms. Over several hundred million years, evolution diversified this class of animals to become pollinators, soil fertilizers, and plant harvesters. The feeding habits of some insects made them rely on the blood of mammals, which enabled them to transmit diseases harmful to humans and domesticated animals. Blood-feeding insects that transmit parasites are responsible for more human deaths and sicknesses than any other group of macro-organisms and exert a significant socioeconomic burden. The alarming statistics of insect-borne diseases call for a paradigm shift in methodologies and approaches to significantly broaden and complement the research efforts currently dominated by a molecular-centric insect immunology.

Insects have an open circulatory system underneath a rigid exoskeleton, which means that the blood flow is not constricted by blood vessels. This, in addition to its small volume, means that when an insect gets damaged, it is at a great risk of desiccation

and infection. To combat this issue, insects developed rapid and localized activation mechanisms of hemolymph to halt blood loss and infection that involve coagulation and clot formation (1). An understanding of these mechanisms is vital for developing countermeasures to control insect-borne diseases and pest outbreaks. The response to injury varies across species and life stages and can involve cellular or humoral reactions mediated by macromolecules in plasma (2-5).

We will focus our study on Lepidoptera – an order of butterflies and moths – and will henceforth discuss this order exclusively. Wax moths (*Galleria mellonella*) and tobacco hawk moths (*Manduca sexta*) have been serving as model systems for biologists and biochemists (6, 7) in analyses of hemolymph coagulation (4, 8-13) and other important biomolecular studies. Since *M. sexta* is native to our region, we will focus our studies on this species and complement it with two other native species: Monarch butterflies (*Danaus plexippus*), and painted lady butterflies (*Vanessa cardui*).

1.2 FUNCTIONS OF LIPIDS AND LIPOPROTEINS

Generally, animals store energy in the form of lipids, and Lepidoptera is no different. During muscular activity, these lipids are released and delivered to the muscles. Flying muscular activity is highly demanding in terms of energy. Unlike mammals that can increase the blood flow to the muscles during activity, insects, which have an open circulatory system, have developed an alternative control method for fuel deli. In this section, we outline the role of hemolymph constituents in fuel transport from fat tissue to muscle tissue. (For more detailed reviews, see (14) (15)).

The path of energy particles from storage to utilization is illustrated in Figure 1 and is as follows. In insects, the lipids are stored in the form of triglycerides (TAG) (esters derived from glycerol and three fatty acids), transported in the form of diglycerides (DAG) (esters derived from glycerol with two fatty acids) and used in the form of free fatty acids (FFA). DAGs are never transported by themselves due to the fact that any contact of a free-flowing DAG with water immediately hydrolyzes it and creates FFAs, which are readily absorbed by the muscles. Instead, a particle – called lipophorin – acts as a reusable shuttle and transports the DAGs from the fat body to the muscle. This particle consists of two proteins (called apolipophorin-I and apolipophorin-II), and other building blocks (lipids, sterols, and hydrocarbons). This particle has a relatively high density and is conventionally called a High Density Lipophorin (HDLP). The HDLP serves as an initial binding site for DAGs. Because DAGs have hydrophobic fatty acid end groups, they attract a surfactant-like protein called apolipophorin-III, which is freely available in hemolymph. When apolipophorin-III is unbound, it is coiled into an prolate particle; when it is bound, it uncoils, exposing its hydrophobic groups (16). A bound apolipophorin-III can serve as a new landing site for another DAG, which in turn is covered by another apolipophorin-III. This new structure – the HDLP covered with DAGs and apolipophorin-III has a lower density and is consequently named Low Density Lipophorin (LDLP).

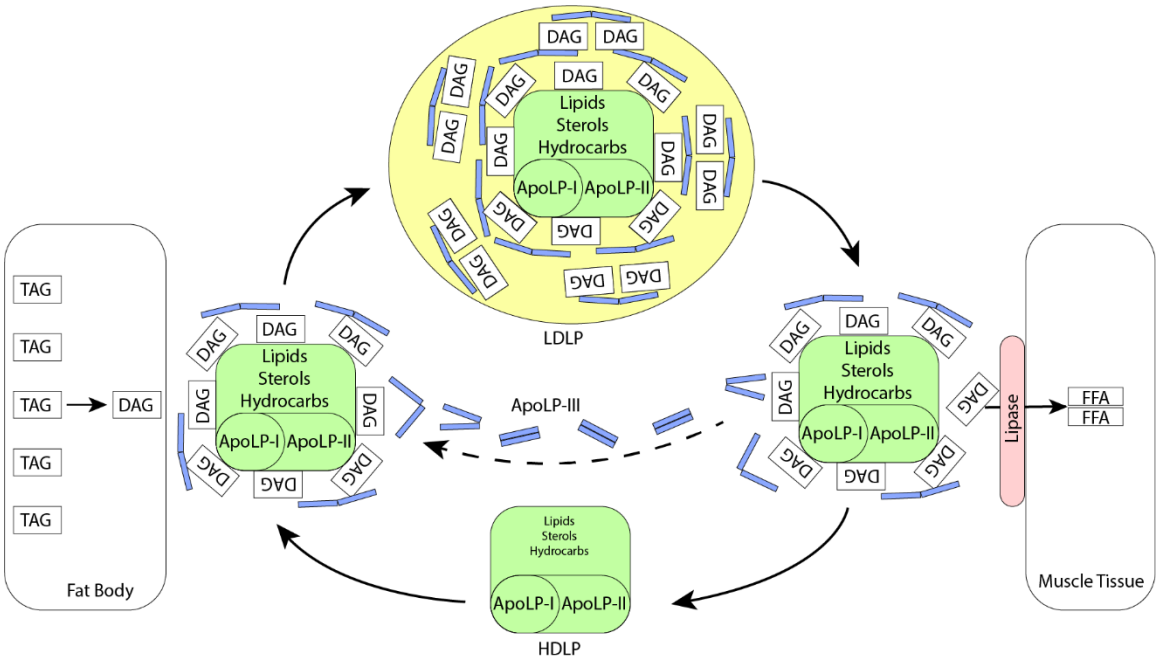

Figure 1. Diagram of energy transport mechanism in hemolymph of flying insects. Adapted from (14)and (15).

Particle	Molecular weight, M_w (kDa)	Density, ρ (g/ml)	Concentration in hemolymph of *M. sexta* adults, C (mg/ml)	Estimated volume fraction[1], φ	Structural properties
Apolipophorin-I	240 (17, 18)	N/A	N/A	N/A	Is associated with HDLP and LDLP
Apolipophorin-II	240 (17, 18)	N/A	N/A	N/A	Is associated with HDLP and LDLP

[1] Calculated as: $\varphi = C/\rho$

Apolipophorin-III	18.1 (19)	1.37[2] (19)	Total: 17±5 [3] Estimated as: Relaxed: 9 Flying: 0	Relaxed 0.0062 (lower-end estimate) Flying: 0	Surfactant-like When in bulk, folded on itself [η] = 6 (16)
HDLP	600(20)	1.15 (21)	Estimated as: Relaxed: 30 Flying: 0	Relaxed: 0.026 Flying: 0	Spherical particle(22)
LDLP	1560 (23)	1.03 (23)	Estimated as: Relaxed: 7.8 Flying: 92	Relaxed: 0.0078 Flying: 0.092	Spherical particle(22)
LTP	900 - 1400 (24)	1.23 (25)	Trace amounts (26)	~0	Spherical head with a long tail

Table 1. Physical properties of some hemolymph constituents in M. sexta.

Another particle, called Lipid Transfer Particle (LTP), is present in hemolymph and is thought to take part in the transfer of lipids from the fat body to the muscle tissue (reviewed in (14)). LTP has similar building blocks to the HDLP (source), but has a different structure. It has a large spherical head (~ 13 nm in diameter) and a long

[2] Lower-end estimate, calculated from amino acid composition

[3] About half of it is free and half of it is associated with lipophorins, when insect is relaxed

cylindrical tail (~ 6 nm in diameter and 38 nm in length) with a hinge in the middle (14). Its role in the context of DAG transfer has been investigated in specific scenarios. It facilitates the transfer of DAGs from the fat body to the LDLP and HDLP particles(20). At the same time, it does not facilitate the transfer of DAGs from LDLP to the fat (20). It has never been observed in transferring the DAGs from LDLP to the HDLP. LTP originating from caterpillars, however, has been observed to facilitate the transfer of DAGs from LDLP to a human LDL (27). As such, LTP from adults can receive DAGs from the fat body and donate DAGs to LDLP and HDLP. It is unclear, however, whether LTP from adults is able to redistribute the DAGs between LDLP and HDLP away from the fat body.

In principle, by having more apolipophorin-III, the system is able to transport more DAGs. There is a limit, however, to how many apolipophorin-III molecules can associate with an LDLP particle. In adult *M. sexta*, that number was determined to be 16 – two are a part of the HDLP particle, and 14 associate along with the DAGs to form the LDLP (23).

The LDLP travels through the body of the insect until it reaches an enzyme that can strip the DAGs from it. This enzyme, called lipase, is found on the walls of the muscular tissue. As such, the DAGs are stripped off of the LDLP near the muscle tissue, undergo hydrolysis, become FFA, and are absorbed into the muscle tissue.

Overall, flying insects have an energy deli system that can deliver high amounts of energy stored in DAG molecules by having a low amount of HDLP (foundation particles) and a high amount of apolipophorin-III (mortar material). Therefore, an insect

that has higher energy demand will have a higher concentration of HDLP and apolipophorin-III.

1.3 FUNCTION OF CELLS (HEMOCYTES) IN CLOTTING/ DEFENSE MECHANISM

In Lepidoptera, the hemocyte count differs dramatically across life stages – while caterpillars have these cells in abundanc, adults have almost none (4, 5, 7, 28, 29). In Lepidoptera, six kinds of hemocytes have been found: plasmatocytes, granulocytes, oenocytoids, spherulocytes, coagulocytes, and prohemocytes (see (30) and (31) for reviews). Oenocytoids contain chemicals that are required for production of melanin – a dark biopolymer that is found at wound sites. These chemicals are released into plasma when oenocytoids burst at the wound site relatively quickly. Granulocytes are adhesive cells and are the first cells that make contact with a foreign object. They are thought to aid plasmocytes in the formation of shells around foreign objects and melanized material. plasmatocytes form barriers by interlinking via desmosomes – cell-to-cell junctures that are randomly arranged on the membranes.(31-33) Due to a tubular structure of the cytoplasm of plasmatocytes, these formations effectively make a tubular barrier.(30) Spherule cells are slightly larger than granulocytes. Coagulocytes resemble granulocytes; they are fragile and lead to the release of cytoplasmic materials, which precipitates in

various morphologies. Finally, prohemocytes are small, round cells that are thought to be stem cells. (31)

1.4 CLOTTING

Different insects exhibit different clotting mechanisms of hemolymph. Some demonstrate no apparent coagulation, others demonstrate hemocyte aggregation, and some exhibit both hemocyte aggregation as well as plasma aggregation with formation of fibrin-like fibers! (34)

Clotting of hemolymph of Lepidoptera caterpillars consists of four steps (35-37). First, the hemocytes undergo degranulation and disintegration. At the same time, plasmatocytes and granulocytes extrude thread-like pseudopodias in response to foreign surfaces (38, 39). This leads to production of extracellular aggregates, which consist of hemocytes, cell debris, and an extracellular matrix. These aggregates form the primary soft clot, thus sealing the wound. Second, a cascade reaction is activated to cross-link the proteins in the soft clot, forming a hard clot. The hard clot is reinforced by a fibrous network, which first appears after 8 minutes and fully covers the wound and all involved cells after 20 minutes (40). This network consists of material different from the pseudopodia. Hemolymph extracted through a needle (thus bypassing the wound) does demonstrate pseudopodial extensions of hemocytes, but does not grow the fibrous network (39-41). This suggests that the triggers for the network formation are released into hemolymph from the hard tissue via the wound. Third, the plasmatocytes are

attracted to the hard clot. They spread across the clot and form a scab. Finally, the epidermis is regenerated, growing across the wound and replacing the scab.

The fibrous structure formation is particularly interesting as it is could be compared to fibrin formation in humans. Work by Minnick et al (1986) (39)describes the filament formations in the clotting hemolymph of early 5^{th} instar *M. sexta* caterpillars as extracted via a 2mm incision immediately anterior to the horn of the caterpillar (42). According to this study, fibrous strands only form in hemolymph in the presence of M13 protein – a glucose-specific lectin – and with glucose concentration below $5*10^{-4}$ M. Two relevant scenarios were discussed: 1. Hemolymph required an incubation time of 30 minutes before strands became observable; 2. Hemolymph with added M13 concentrate (obtained by fractionation of hemolymph from bacteria-treated caterpillars) started forming these strands within 10 seconds.

Geng et al (1988) (41) further explore this phenomenon. Hemolymph that was collected from an incision in the tip of an abdominal proleg on a glass coverslip formed fibrous structures in both untreated and bacteria-treated caterpillars. Hemolymph of untreated caterpillars that was collected via a hypodermic needle from pericardial space, however, did not produce these structures while observed for several hours. Furthermore, even when this hemolymph was exposed to a glass substrate, no fibers were observed. The hemocytes in this hemolymph did not aggregate in the bulk, but adhered to glass substrate when exposed to it. Geng also observed that hemolymph that was extracted via a hypodermic needle and never contacted the wound did not form these filaments in healthy caterpillars, but did form them in bacteria-treated caterpillars. When the fibrous

structure was fractioned using HPLC and incubated by itself, no filaments were reformed. When the fractions were incubated in hemolymph, however, fibrous structure quickly reformed. The fibrous structures also rapidly formed when isolated M13 protein was added to hemolymph collected with a needle. The structures also formed when M13 was added to cell-free hemolymph as well as to a mixture of salts, amino acids, sugars, and vitamins (GICCM). This suggests that cells do not contribute any building blocks for the fibrous structure and are only involved in the early stages of clot formation.

Due to the low volumes and fast kinetics of clotting, little attention has been given to the primary clot formation in Lepidoptera. Due to the heavy involvement of hemocytes in the early stages of clotting kinetics and drastically different hemocyte counts at different life stages in Lepidoptera, it is fair to expect the clotting kinetics in adults to be different from the clotting kinetics in caterpillars.

1.5 CONCLUSION AND HYPOTHESIS

Hemolymph is a complex liquid that acts across multiple scales to facilitate locomotion, nutrient transport, and wound healing in Lepidoptera. While its physiology has been investigated by both classical and micro-biologists, its physical properties – such as viscosity, elastic modulus, or surface tension – have not been investigated. Due to the varying components, these properties should differ across species and life stages. During clotting, these properties are also expected to drastically change.

1.6 REFERENCES

1. Chapman RF. The insects : structure and function. 4th ed. Cambridge, UK ; New York, NY: Cambridge University Press; 1998. xvii, 770 p. p,
2. Vilmos P, Kurucz E. Insect immunity: evolutionary roots of the mammalian innate immune system. Immunology Letters. 1998;62:59-66,
3. Lavine MD, Strand MR. Insect hemocytes and their role in immunity. Insect Biochemistry and Molecular Biology. 2002;32:1295-309.10.1016/B978-012373976-6.50004-5
4. Strand MR. The insect cellular immune response. Insect Science. 2008;15(1):1-14.10.1111/j.1744-7917.2008.00183.x
5. Ratcliffe NA, Rowley AF, Fitzgerald SW, Rhodes CP. Invertebrate immunity - basic concepts and recent advances. IntRevCytol. 1985;97:183-350.
6. Goldsmith MR, Wilkins AS. Molecular model systems in the Lepidoptera. Cambridge, UK: Cambridge University Press; 2006. 560 p,
7. Gupta AP. Insect hemocytes: development, forms, functions and techniques. Cambridge, UK: Cambridge University Press; 2009.
8. Gregoire C. Hemolymph coagulation. In: Rockstein M, editor. The Physiology of Insecta. 5. New York: Academic Press; 1974. p. 309-60,
9. Gregoire CH. Blood coagulation in arthropods. V. Studies on hemolymph coagulation in 420 species of insects. Arch Biol. 1955;66((1)):103-48.
10. Salt GW. The cellular defence reactions of insects. Cambridge: Cambroidge University Press; 1970.
11. Theopold U, Li D, Fabbri M, Scherfer C, Schmidt O. The coagulation of insect hemolymph. Cellular and Molecular Life Sciences. 2002;59:363-72.10.1007/s00018-002-8428-4
12. Dushay MS. Insect hemolymph clotting. Cellular and Molecular Life Sciences. 2009;66:2643-50.10.1007/s00018-009-0036-0
13. Jiang H, Vilcinskas A, Kanost MR. Immunity in Lepidopteran insects. In: Soderhall K, editor. Invertebrate Immunity. Advances in Experimental Medicine and Biology. 708. Berlin: Springer-Verlag Berlin; 2010. p. 181-204.
14. Ryan RO. Dynamics of insect lipophorin metabolism. J Lipid Res. 1990;31:1725-39,
15. Van der Horst DJ. Lipid transport function of lipoproteins in flying insects. Biochimica et Biophysica Acta (BBA) - Lipids and Lipid Metabolism. 1990;1047:195-211.10.1016/0005-2760(90)90518-3
16. Kawooya JK, Meredith SC, Wells MA, Kézdy FJ, Law JH. Physical and surface properties of insect apolipophorin III. The Journal of biological chemistry. 1986;261:13588-91,
17. Weers P, Marrewijk WV, Beenakkers A. Biosynthesis of locust lipophorin. Apolipophorins I and II originate from a common precursor. Journal of Biological. 1993,
18. Shapiro JP, Keim PS, Law JH. Structural studies on lipophorin, an insect lipoprotein. The Journal of biological chemistry. 1984;259:3680-5,

19. Kawooya JK, Keim PS, Ryan R, Shapiro, P J, Samaraweera P, Lawn JH. Insect Apolipophorin III: purification and properteis. The Journal of biological chemistry. 1984;259:10733-7,
20. Pattnaik NM, Mundall EC, Trambusti BG, Law JH, Kézdy FJ. Isolation and characterization of a larval lipoprotein from the hemolymph of *Manduca sexta*. Comparative Biochemistry and Physiology Part B: Comparative Biochemistry. 1979;63:469-76.10.1016/0305-0491(79)90048-8
21. Ryan R, Prasad SV, Henriksen EJ, Wells MA, Law JH. Lipoprotein Interconversions in an Insect , *Manduca sexta*. Journal of Biological Chemistry. 1986;261(2):563-8,
22. van der Horst DJ, van Hoof D, van Marrewijk WJA, Rodenburg KW. Alternative lipid mobilization: The insect shuttle system. Molecular and Cellular Biochemistry. 2002;239:113-9.10.1023/A:1020541010547
23. Wells M, Ryan R, Kawooya J, Law J. The role of apolipophorin III in in vivo lipoprotein interconversions in adult *Manduca sexta*. Journal of Biological Chemistry. 1987,
24. Ryan RO, Howe A, Scraba DG. Studies of the morphology and structure of the plasma lipid transfer particle from the tobacco hornworm, *Manduca sexta*. J Lipid Res. 1990;31:871-9,
25. Inouye LS, Lotufo GR. Comparison of macro-gravimetric and micro-colorimetric lipid determination methods. Talanta. 2006;70:584-7.10.1016/j.talanta.2006.01.024
26. Hirayama Y, Chino H. Lipid transfer particle in locust hemolymph: purification and characterization. J Lipid Res. 1990;31:793-9,
27. Blacklock BJ, Smillie M, Ryan RO. Insect lipid transfer particle can facilitate net vectorial lipid transfer via a carrier-mediated mechanism. Journal of Biological Chemistry. 1992;267:14033-7,
28. Beetz S, Holthusen TK, Koolman J, Trenczek T. Correlation of hemocyte counts with different developmental parameters during the last larval instar of the tobacco hornworm, *Manduca sexta*. Archives of Insect Biochemistry and Physiology. 2008;67(2):63-75.10.1002/arch.20221
29. Lackie AM. Haemocyte behaviour. Advances in Insect Physiology. 1988;21:85-178.10.1016/s0065-2806(08)60123-x
30. Ribeiro C, Brehelin M. Insect haemocytes: What type of cell is that? Journal of Insect Physiology. 2006;52(5):417-29.10.1016/j.jinsphys.2006.01.005
31. Lavine MD, Strand MR. Insect hemocytes and their role in immunity. Insect Biochemistry and Molecular Biology. 2002;32(10):1295-309. Doi 10.1016/S0965-1748(02)00092-9
32. Ratcliffe NA, Gagen SJ. Studies on Invivo Cellular Reactions of Insects - Ultrastructural Analysis of Nodule Formation in Galleria-Mellonella. Tissue Cell. 1977;9(1):73-85.Doi 10.1016/0040-8166(77)90050-7
33. Rowley AF, Ratcliffe NA. Granular Cells of Galleria-Mellonella during Clotting and Phagocytic Reactions Invitro. Tissue Cell. 1976;8(3):437-46.Doi 10.1016/0040-8166(76)90004-5

34. Wigglesworth VB. The Principles of Insect Physiology. 1982:1-7.10.1007/978-94-009-5973-6
35. Ratcliffe NA, Rowley AF. Comparative Synopsis of the Structure and Function of the Blood-Cells of Insects and Other Invertebrates. Developmental and Comparative Immunology. 1979;3(2):189-221.Doi 10.1016/S0145-305x(79)80020-8
36. Gupta AP. Insect hemocytes : development, forms, functions, and techniques. Cambridge Eng. ; New York: Cambridge University Press; 1979. 614 p,
37. Rowley AF, Ratcliffe NA. Histological Study of Wound-Healing and Hemocyte Function in Wax-Moth Galleria-Mellonella. Journal of Morphology. 1978;157(2):181-99.DOI 10.1002/jmor.1051570206
38. Gregoire C. Hemolymph coagulation. The Physiology of Insecta (Second Edition): Elsevier; 1974. p. 309-60,
39. Minnick MF, Rupp RA, Spence KD. A Bacterial-Induced Lectin Which Triggers Hemocyte Coagulation in Manduca-sexta. Biochem Biophys Res Commun. 1986;137(2):729-35.Doi 10.1016/0006-291x(86)91139-3
40. Geng C. Studies of hemolymph coagulation in *Manduca sexta*: Purdue University; 1990.
41. Geng CX, Dunn PE. Hemostasis in Larvae of Manduca-sexta - Formation of a Fibrous Coagulum by Hemolymph-Proteins. Biochem Biophys Res Commun. 1988;155(2):1060-5.Doi 10.1016/S0006-291x(88)80604-1
42. Hughes JA, Hurlbert RE, Rupp RA, Spence KD. Bacteria-induced haemolymph proteins of *Manduca sexta* pupae and larvae. Journal of Insect Physiology. 1983;29(8):625-32,

CHAPTER II

INTRODUCTION: MECHANICAL CHARACTERIZATION OF HEMOLYMPH

2.1 IMPORTANCE OF UNDERSTANDING OF PHYSICAL PROPERTIES OF HEMOLYMPH

As discussed in the previous chapter, Lepidoptera hemolymph is only available in minute amounts (5-20 μl from adults and 200-300 μl from *M. sexta* caterpillar) and rapidly changes its properties when extracted from the body under normal conditions. Characterization of such rapidly changing materials is particularly challenging. In this chapter, we introduce the concept of microrheology, explain its importance with regards to hemolymph, review the state-of-the-art methodologies, and describe our approach for this study.

2.1.1 Introduction to viscosity, elasticity, and nano-rheology

Rheology is the study of how matter responds to external mechanical perturbation. The response can dissipate the injected energy into heat via friction between molecules or store the energy by elastically deforming the molecules or molecule linkages. The primer is referred to as viscous response, conceptually represented by a dashpot, and the material property that characterizes it is called viscosity, η. The former is referred to as the elastic response, conceptually represented by a spring, and the material property that characterizes it is called the elastic modulus, E. Liquids that have elasticity are called viscoelastic liquids.

Viscosity is the ratio between the load and the deformation rate of the material. For instance, shear viscosity of the material, η_s, is defined as a ratio of the shear stress, σ, and the shear rate, $\dot{\gamma}$,

$$\eta_s = \sigma / \dot{\gamma} \tag{2.1}$$

Viscosity can be dependent or independent of the shear rate. In Newtonian liquids, viscosity is independent of the shear rate. In shear-thinning liquids, viscosity decreases with shear rate. In shear-thickening liquids, viscosity increases with shear rate.

Elastic modulus is the ratio between the load and the deformation and is difficult to define in liquids due to its flow. There are several models that aim to describe a viscoelastic material in terms of viscosity and elastic modulus. The Maxwell model describes the majority of polymer solutions that are not gels, is conceptually represented by a dashpot and a spring in series and has the following equation:

$$\dot{\gamma} = \frac{\sigma}{\eta} + \frac{\dot{\sigma}}{E} \tag{2.2}$$

The Kelvin-Voigt model describes a gel, is conceptually represented by a spring and a dashpot in parallel and has the following equation:

$$\sigma = E\gamma + \eta\dot{\gamma} \tag{2.3}$$

These two models can be generalized with the standard linear solid model to more accurately describe loading and unloading of the material as well as the generalized Maxwell model to include a distribution of response times of the material.

In liquids, viscosity is typically a function of the solvent-solvent molecule interactions and may be increased by adding solutes. Different models aim to predict the

viscosity increase as a function of volume fraction of solutes, φ, (1, 2) solute particle shape (3-7) or charge of solutes in an ionic solution (8). We will discuss these models in more detail in Chapter 4. Viscosity in a liquid can be independent of the shear rate, such as in Newtonian liquids Elasticity is typically observed in liquids with long chain molecules that stretch in response to deformation.

The response of the material is dependent on the scale at which it is being probed. For example, a suspension of cells in plasma might behave like a Newtonian suspension of solid microbeads on a macroscale. When the probe is comparable in size to a cell and the loads are small, however, the elastic properties of the individual cells become important and the material response might be that of a gel. For multiscale processes, such as wound healing, it is important to understand the rheological properties of the material on all scales. As such, it is important to study the nanorheology and microrheology of the material as it changes.

2.2 LITERATURE REVIEW OF NANORHEOLOGICAL METHODS

Small volumes of available material make its study on a small scale of its rapidly changing properties particularly challenging. To address the challenges of *in situ* characterization of rheological properties of materials, different experimental methods have been proposed and developed (see (9) for a review). In many cases, rheological characteristics of materials are inferred by comparing the translational and/or rotational motions of different tracers against available models of particle-medium interactions (10, 11).

The tracer - or probe - is considered passive when its motion is caused by the forces exerted by the surrounding medium. The probe is considered active when it actively deforms the medium and is used to transfer the load onto the medium(12-14). Small passive tracers are subject to thermal excitations and hence randomly move through the surrounding material. The mean squared displacement (MSD) of probes can be directly measured using the light-scattering techniques (15, 16). The rheological properties of the material are therefore extracted from the MSD by using a model of Brownian motion(17, 18). For example, applying the Stokes-Einstein relation for a spherical tracer moving in a Newtonian fluid, one can infer fluid viscosity. Advanced passive microrheological techniques have been used in studies of complex fluids (see (11) for review) and various biological media (see (19) for review) by applying models of particle motion in viscous or viscoelastic media. The method, however, assumes a purely diffusive motion of the probes and the analysis of experimental data is significantly complicated by the presence of flow, heterogeneity of the sample, or proximity to the substrate (20).

Active microrheological techniques have an advantage of controlling the load on the probes, allowing for the stress-controlled studies. The methods of force application range from atomic force microscopy tips for surface probing (21, 22), to optical tweezers on highly refractive probes in highly transparent materials (23-26), to magnetic actuation or rotation of magnetic probes (27-37). The latter two methods are able to apply the load remotely and without any mechanical contact with the probe. Optical tweezers, however, rely on high-intensity light to apply the force, which can significantly increase the local temperature near the probe and alter the sampled medium. Magnetic actuation,

meanwhile, is able to apply a load directly on the magnetic probes without any disturbance of the medium, making this technique non-destructive and thus highly attractive.

Many materials can be made magnetic by dispersing magnetic micro and nanoparicles in them. These micro and nanoparticles are available on market or can be produced in the laboratory (see, for review, Refs. (38)). Magnetic particles can be considered active probes because they can be put in motion by applying an external magnetic field. The idea of using magnetic tracers to probe rheological properties of materials was originated from the pioneering work of Crick and Hughes(37, 39-46). Crick and Hughes used magnetic particles to probe viscosity and elastic reaction of cytoplasm. An applied rotating magnetic field exerts a torque on a magnetic particle, which is balanced by the viscous and elastic torques acting from the medium. Crick and Hughes studied the reaction of the medium on a step-like pulse of the external magnetic field. They monitored the particle relaxation to its equilibrium position. Following their ideas, magnetic tracers, mostly spherical micro- and nano-particles, have been used in different applications (47-49).

Magnetic tracers are typically tracked by either directly filming the tracer movement or using some indirect methods of the particle detection. Examples of indirect methods include measurements of AC susceptibility (50), coercivity (39, 51, 52) or remanence (10, 31, 37, 40, 41, 43, 45, 46, 53-58). The rheological properties of materials are obtained by comparing experimental data with predictions of appropriate models of particle/medium interactions (31, 53, 55-66). Anisotropic particles such as wires, rods,

and chains have attracted attention of nanorheologists only recently (67). Magnetic nanorods have several advantages over spherical nanoparticles: due to their anisotropic shape, rotational motions of nanorods can be easily tracked and analyzed from the microscope images. Moreover, magnetization of a rod-like particle is often codirected with the rod axis(55, 68, 69). This fact significantly simplifies the models of nanorod rotation making rheological measurements reliable. (For a review of various nanowires, see (70))

Magnetic rotational spectroscopy (MRS) takes advantage of a distinguishable behavior of rotating tracers as the frequency of applied rotating field changes. Unlike many methods based on the analysis of small amplitude oscillations, MRS with magnetic nanorods enjoys analysis of the full revolutions of magnetic tracers, which are much easier to track using inexpensive microscopes. Nanorods can be kept strictly in the focal plane of the microscope by controlling the applied magnetic field. Moreover, nanorods as thin as hundreds of nanometers in diameter can be seen with dark field imaging. Therefore, the MRS with magnetic nanorods provides accurate data on submicron rheology of materials(71).

As first shown by Frenkel (7, 72), rotation of a rod-like particle in a Newtonian fluid changes from synchronous, when the rod continuously follows the rotating field, to asynchronous, when the rod periodically swings back and forth. This transition occurs at a certain frequency of the rotating magnetic field. Frenkel's effect was actively employed in the last century to study rod-like polymers and liquid crystals(68). Direct observations of the critical behavior of rod-like particles, however, were lacking, and all measurements

were conducted indirectly. The critical transition from synchronous to asynchronous rotation was first visualized only in 2005 when carbon nanotubes filled with magnetic nanoparticles were used for these purposes(68). Transition from synchronous to asynchronous rotation of magnetic nanotubes was used to estimate the magnetic properties of the composite nanotubes (31, 42, 43, 55, 61, 69, 73-76). (For a detailed review of MRS, see (34, 77).)

With the recent progress in nanotechnology and microfluidics, MRS has experienced a growing interest in the community of researchers dealing with the analysis of small samples (29-32, 61, 78-87). Recent studies show that accurate tracking of a single probe can yield accurate rheological measurements (27-34). While such measurements are successfully used to study highly viscous liquids, they are difficult to perform with low viscous liquids, such as dilute aqueous solutions of biopolymers, surfactants, and salts. For such liquids, the torque applied on the probes must be low – e.g, for a nickel nanorod of 200 nm in diameter and 10 μm in length in water of 1 mPa·s viscosity, the torque needs to be roughly 10^{-17} N·m. To apply such a torque on such a rod, the applied magnetic field must be on the order of 100 μT. When magnetic fields are microTesla weak, control over the movement of magnetic probe is hindered by the presence of Earth's magnetic field, which ranges from 50 μT to 100 μT. The applied magnetic field is disturbed by this bias thus significantly affecting the readings of magnetic sensors that pick up the responses of magnetic probes. Therefore, for accurate measurements, the magnetic field needs to be accurately controlled and Earth's magnetic field needs to be actively cancelled.

Moreover, to collect the spectral data at different frequencies of rotation, a lot of time is needed. This does not allow the study of a rapidly changing material as the time required to gather statistics on a measurement is on the order of minutes – by the time a measurement is performed, a clot may already have been formed. We modify this technique to significantly reduce the temporal resolution to below 10 seconds, making it appropriate for this study. We discuss these modifications further in the next chapter.

2.3 LITERATURE REVIEW OF EXTENSIONAL MICRORHEOLOGY

The methodologies for microscale rheological characterization range from microfluidic methods in the low viscosity limit to liquid filament (88-93) stretching and capillary breakup rheometers at medium and high viscosities (94) (95-97) (see (98) for review). We will focus on the latter due to the possibility of quick sample deli for measurement.

The kinetics of liquid column disappearance have been studied in liquids of different rheological properties. (94, 98-115). Main applications of this research are inkjet printing (116), liquid faucets and dispensers (116-118), and rheological characterization of liquids available in small quantities (98, 99, 112). The latter application is of particular interest to us, since we are interested in rheological characterization of hemolymph.

A simple and attractive method of studying rheology of a liquid in response to extension was developed by Entov, Bazilevskii and Rozhkov later adopted by other groups. (94, 99-104). The method is based on creating a liquid column between two surfaces and tracking the decrease of the diameter of its neck as a function of time. The

methodology has been used to study low viscosity liquids(98, 105, 107), high viscosity liquids(94, 106, 107), viscoelastic liquids (98, 105, 107-109), suspensions (107, 110, 119, 120), liquid crystals(111), as well as various biological fluids (112) and has been thoroughly reviewed (110, 113-115). The decay kinetics of the liquid bridges with different rheological properties exhibit distinguishing characteristic features. For instance, Newtonian liquids demonstrate a linear decay of the thinnest part of the liquid bridge. A Maxwell viscoelastic liquid develops a uniform liquid filament with an exponential time decay of its radius. A high molecular weight polymer, meanwhile, might develop droplets on the surface of the liquid filament. We use this method to study hemolymph of caterpillars, which is available in amounts sufficient for this method.

2.4 CONCLUSION

To understand the behavior of hemolymph during wound clotting, it is important to study its rheology at multiple scaled. We have introduced the methodologies for nano- and micro-rheological characterization of liquids. The nanorheological method of MRS in the state at which it is described in the literature cannot perform measurements quickly enough to track the rapidly changing properties of hemolymph. We have thus modified and improved the method to allow for measurements at high temporal resolution of less than 10 seconds.

2.5 REFERENCES

1. Einstein A. A new determination of the molecular dimensions. Ann Phys-Berlin. 1906;19(2):289-306.

2. Batchelor GK. Effect of Brownian-Motion on Bulk Stress in a Suspension of Spherical-Particles. J Fluid Mech. 1977;83(Nov):97-117.Doi 10.1017/S0022112077001062
3. Brenner H, Condiff D. Transport mechanics in systems of orientable particles. IV. convective transport. J Colloid Interf Sci. 1974;47:199-264.10.1016/0021-9797(74)90093-9
4. Bird RB, Warner HR, Evans DC. Kinetic theory and rheology of dumbbell suspensions with Brownian motion. Fortschritte der Hochpolymeren-Forschung. Berlin, Heidelberg: Springer Berlin Heidelberg; 1971. p. 1-90.10.1007/3-540-05483-9_9
5. Hinch EJ, Leal LG. Effect of Brownian Motion on Rheological Properties of a Suspension of Non-Spherical Particles. J Fluid Mech. 1972;52(Apr25):683-&.Doi 10.1017/S002211207200271x
6. Batchelor GK. An introduction to fluid dynamics. New York: Cambridge University Press; 2000.
7. Doi M, Edwards SF. The theory of polymer dynamics. Oxford: Clarendon Press; 1988. xiii, 391 p. p,
8. Russel WB, Saville DA, Schowalter WR. Colloidal dispersions. Cambridge ; New York: Cambridge University Press; 1989. xvii, 525 p., 1 leaf of plates p,
9. Castro DJ, Song J-O, Lade RK, Francis LF. Magnetic Microrheology for Characterization of Viscosity in Coatings. Protective Coatings: Springer; 2017. p. 115-36,
10. Wilson LG, Harrison AW, Schofield AB, Arlt J, Poon WCK. Passive and Active Microrheology of Hard-sphere Colloids. Journal of Physical Chemistry B. 2009;113(12):3806-12.Doi 10.1021/Jp8079028
11. Squires TM, Mason TG. Fluid Mechanics of Microrheology. Annu Rev Fluid Mech. 2010;42:413-38.10.1146/annurev-fluid-121108-145608
12. Mason TG, Gang H, Weitz DA. Rheology of complex fluids measured by dynamic light scattering. J Mol Struct. 1996;383(1-3):81-90.Doi 10.1016/S0022-2860(96)09272-1
13. Mason TG, Gang H, Weitz DA. Diffusing-wave-spectroscopy measurements of viscoelasticity of complex fluids. J Opt Soc Am A. 1997;14(1):139-49.Doi 10.1364/Josaa.14.000139
14. Scheffold F, Romer S, Cardinaux F, Bissig H, Stradner A, Rojas-Ochoa LF, Trappe V, Urban C, Skipetrov SE, Cipelletti L, Schurtenberger P. New trends in optical microrheology of complex fluids and gels. Prog Coll Pol Sci S. 2004;123:141-6.Doi 10.1007/B11748
15. Banchio AJ, Nagele G, Bergenholtz J. Viscoelasticity and generalized Stokes-Einstein relations of colloidal dispersions. Journal of Chemical Physics. 1999;111(18):8721-40.Doi 10.1063/1.480212
16. Mason TG, Weitz DA. Optical measurements of frequency dependent linear viscoelastic moduli of complex fluids. Physical Review Letters. 1995;74(7):1250-3.10.1103/PhysRevLett.74.1250
17. Graham DL, Ferreira HA, Freitas PP. Magnetoresistive-based biosensors and biochips. Trends in Biotechnology. 2004;22(9):455-62.

18. Krishnan KM. Biomedical Nanomagnetics: A Spin Through Possibilities in Imaging, Diagnostics, and Therapy. Ieee Transactions on Magnetics. 2010;46(7):2523-58.10.1109/tmag.2010.2046907
19. Weihs D, Mason TG, Teitell MA. Bio-microrheology: A frontier in microrheology. Biophys J. 2006;91(11):4296-305.10.1529/biophysj.106.081109
20. Puertas AM, Voigtmann T. Microrheology of colloidal systems. J Phys-Condens Mat. 2014;26(24).
21. Connizzo BK, Grodzinsky AJ. Tendon exhibits complex poroelastic behavior at the nanoscale as revealed by high-frequency AFM-based rheology. Journal of Biomechanics. 2017;54:11-8,
22. Devailly C, Laurent J, Steinberger A, Bellon L, Ciliberto S. Microrheology measurements with a hanging-fiber AFM probe. arXiv preprint arXiv:13112217. 2013,
23. Yao A, Tassieri M, Padgett M, Cooper J. Microrheology with optical tweezers. Lab on a Chip. 2009;9(17):2568-75,
24. Furst EM. Applications of laser tweezers in complex fluid rheology. Curr Opin Colloid In. 2005;10(1-2):79-86.
25. Meyer A, Marshall A, Bush BG, Furst EM. Laser tweezer microrheology of a colloidal suspension. Journal of rheology. 2006;50(1):77-92,
26. Wilson LG, Poon WC. Small-world rheology: an introduction to probe-based active microrheology. Phys Chem Chem Phys. 2011;13(22):10617-30,
27. Aprelev P, Gu Y, Burtovyy R, Luzinov I, Kornev KG. Synthesis and characterization of nanorods for magnetic rotational spectroscopy. Journal of Applied Physics. 2015;118:074901.10.1063/1.4928401
28. Gu Y, Chen Z, Borodinov N, Luzinov I, Peng F, Kornev KG. Kinetics of evaporation and gel formation in thin films of ceramic precursors. Langmuir. 2014:DOI: 10.1021/la5037986,
29. Berret JF. Local viscoelasticity of living cells measured by rotational magnetic spectroscopy. Nature Communications. 2016;7.10.1038/ncomms10134
30. Brasovs A, Cīmurs J, Ērglis K, Zeltins A, Berret J-F, Cēbers A. Magnetic microrods as a tool for microrheology. Soft Matter. 2015;11.10.1039/C4SM02454K
31. Chevry L, Sampathkumar NK, Cebers A, Berret JF. Magnetic wire-based sensors for the microrheology of complex fluids. Physical Review E. 2013;88(6).062306

10.1103/PhysRevE.88.062306
32. Loosli F, Najm M, Berret JF. Viscoelasticity of model surfactant solutions, determined by magnetic rotation spectroscopy. Colloids and Surfaces a-Physicochemical and Engineering Aspects. 2016;510:143-9.10.1016/j.colsurfa.2016.06.019
33. Tokarev A, Aprelev A, Zakharov MN, Korneva G, Gogotsi Y, Kornev KG. Multifunctional magnetic rotator for micro and nanorheological studies. Review of Scientific Instruments. 2012;83(6):065110, http://dx.doi.org/10.1063/1.4729795
34. Gu Y, Kornev KG. Ferromagnetic Nanorods in Applications to Control of the In-Plane Anisotropy of Composite Films and for In Situ Characterization of the Film Rheology. Advanced Functional Materials. 2016;26(22):3796-808.10.1002/adfm.201504205

35. Rich JP, Lammerding J, McKinley GH, Doyle PS. Nonlinear microrheology of an aging, yield stress fluid using magnetic tweezers. Soft Matter. 2011;7(21):9933-43,
36. Habdas P, Schaar D, Levitt AC, Weeks ER. Forced motion of a probe particle near the colloidal glass transition. EPL (Europhysics Letters). 2004;67(3):477,
37. Amblard F, Maggs AC, Yurke B, Pargellis AN, Leibler S. Subdiffusion and anomalous local viscoelasticity in actin networks. Physical Review Letters. 1996;77(21):4470-3.
38. Crick FHC, Hughes AFW. The physical properties of cytoplasm: A study by means of the magnetic particle method Part I. Experimental. Experimental Cell Research. 1950;1(1):37-80.10.1016/0014-4827(50)90048-6
39. Valberg PA, Feldman HA. Magnetic Particle Motions within Living Cells - Measurement of Cytoplasmic Viscosity and Motile Activity. Biophysical Journal. 1987;52(4):551-61.
40. Schmidt FG, Ziemann F, Sackmann E. Shear field mapping in actin networks by using magnetic tweezers. European Biophysics Journal with Biophysics Letters. 1996;24(5):348-53.
41. Li Y, Burke D, Kopelman R, Burns M. Asynchronous Magnetic Bead Rotation (AMBR) Microviscometer for Label-Free DNA Analysis. Biosensors. 2014;4(1):76-89,
42. McNaughton BH, Kinnunen P, Smith RG, Pei SN, Torres-Isea R, Kopelman R, Clarke R. Compact sensor for measuring nonlinear rotational dynamics of driven magnetic microspheres with biomedical applications. Journal of Magnetism and Magnetic Materials. 2009;321(10):1648-52.10.1016/j.jmmm.2009.02.106
43. McNaughton BH, Kehbein KA, Anker JN, Kopelman R. Sudden breakdown in linear response of a rotationally driven magnetic microparticle and application to physical and chemical microsensing. Journal of Physical Chemistry B. 2006;110(38):18958-64.10.1021/jp060139h
44. Amblard F, Yurke B, Pargellis A, Leibler S. A magnetic manipulator for studying local rheology and micromechanical properties of biological systems. Review of Scientific Instruments. 1996;67(3):818-27.Doi 10.1063/1.1146816
45. Ziemann F, Radler J, Sackmann E. Local Measurements of Viscoelastic Moduli of Entangled Actin Networks Using an Oscillating Magnetic Bead Micro-Rheometer. Biophysical Journal. 1994;66(6):2210-6.
46. Bausch AR, Moller W, Sackmann E. Measurement of local viscoelasticity and forces in living cells by magnetic tweezers. Biophysical Journal. 1999;76(1):573-9.
47. Barrera C, Florian-Algarin V, Acevedo A, Rinaldi C. Monitoring gelation using magnetic nanoparticles. Soft Matter. 2010;6(15):3662-8.Doi 10.1039/C003284k
48. Calero-DdelC VL, Santiago-Quinonez DI, Rinaldi C. Quantitative nanoscale viscosity measurements using magnetic nanoparticles and SQUID AC susceptibility measurements. Soft Matter. 2011;7(9):4497-503.Doi 10.1039/C0sm00902d
49. Roeben E, Roeder L, Teusch S, Effertz M, Deiters UK, Schmidt AM. Magnetic particle nanorheology. Colloid and Polymer Science. 2014;292(8):2013-23.DOI 10.1007/s00396-014-3289-6
50. Roeder L, Bender P, Tschope A, Birringer R, Schmidt AM. Shear modulus determination in model hydrogels by means of elongated magnetic nanoprobes. Journal

of Polymer Science Part B-Polymer Physics. 2012;50(24):1772-81.Doi 10.1002/Polb.23202
51. Zaner KS, Valberg PA. Viscoelasticity of F-Actin Measured with Magnetic Microparticles. Journal of Cell Biology. 1989;109(5):2233-43.DOI 10.1083/jcb.109.5.2233
52. Valberg PA, Albertini DF. Cytoplasmic Motions, Rheology, and Structure Probed by a Novel Magnetic Particle Method. Journal of Cell Biology. 1985;101(1):130-40.DOI 10.1083/jcb.101.1.130
53. Celedon A, Hale CM, Wirtz D. Magnetic Manipulation of Nanorods in the Nucleus of Living Cells. Biophysical Journal. 2011;101(8):1880-6.DOI 10.1016/j.bpj.2011.09.008
54. Kinnunen P, Sinn I, McNaughton BH, Newton DW, Burns MA, Kopelman R. Monitoring the growth and drug susceptibility of individual bacteria using asynchronous magnetic bead rotation sensors. Biosensors & bioelectronics. 2011;26(5):2751-5.DOI 10.1016/j.bios.2010.10.010
55. Tokarev A, Luzinov I, Owens JR, Kornev KG. Magnetic Rotational Spectroscopy with Nanorods to Probe Time-Dependent Rheology of Microdroplets. Langmuir. 2012;28(26):10064-71.10.1021/la3019474
56. Tokarev A, Kaufman B, Gu Y, Andrukh T, Adler PH, Kornev KG. Probing viscosity of nanoliter droplets of butterfly saliva by magnetic rotational spectroscopy. Applied Physics Letters. 2013;102(3).10.1063/1.4788927
57. Wilhelm C, Browaeys J, Ponton A, Bacri JC. Rotational magnetic particles microrheology: The Maxwellian case. Physical Review E. 2003;67(1).Doi 10.1103/Physreve.67.011504

58. Cappallo N, Lapointe C, Reich DH, Leheny RL. Nonlinear microrheology of wormlike micelle solutions using ferromagnetic nanowire probes. Physical Review E. 2007;76(3).Doi 10.1103/Physreve.76.031505

59. Dhar P, Cao YY, Fischer TM, Zasadzinski JA. Active Interfacial Shear Microrheology of Aging Protein Films. Physical Review Letters. 2010;104(1).Doi 10.1103/Physrevlett.104.016001

60. Keshoju K, Xing H, Sun L. Magnetic field driven nanowire rotation in suspension. Applied Physics Letters. 2007;91(12).Doi 10.1063/1.2789184

61. Frka-Petesic B, Erglis K, Berret JF, Cebers A, Dupuis V, Fresnais J, Sandre O, Perzynski R. Dynamics of paramagnetic nanostructured rods under rotating field. Journal of Magnetism and Magnetic Materials. 2011;323(10):1309-13.10.1016/j.jmmm.2010.11.036
62. Wilhelm C, Gazeau F, Bacri JC. Rotational magnetic endosome microrheology: Viscoelastic architecture inside living cells. Physical Review E. 2003;67(6).Doi 10.1103/Physreve.67.061908

63. Erglis K, Ose V, Zeltins A, Cebers A. Viscoelasticity of the bacteriophage Pf1 network measured by magnetic microrheology. Magnetohydrodynamics. 2010;46(1):23-9.
64. Allione M, Torre B, Casu A, Falqui A, Piacenza P, Di Corato R, Pellegrino T, Diaspro A. Rod-shaped nanostructures based on superparamagnetic nanocrystals as viscosity sensors in liquid. Journal of Applied Physics. 2011;110(6). Doi 10.1063/1.3638695

65. Anguelouch A, Leheny RL, Reich DH. Application of ferromagnetic nanowires to interfacial microrheology. Applied Physics Letters. 2006;89(11). Doi 10.1063/1.2349841

66. Chippada U, Yurke B, Georges PC, Langrana NA. A Nonintrusive Method of Measuring the Local Mechanical Properties of Soft Hydrogels Using Magnetic Microneedles. Journal of Biomechanical Engineering-Transactions of the Asme. 2009;131(2). Doi 10.1115/1.3005166

67. Chikazumi So, Graham CD. Physics of ferromagnetism. 2nd ed. Oxford ; New York: Oxford University Press; 2009. xii, 655.
68. Korneva G, Ye H, Gogotsi Y, Halverson D, Friedman G, Bradley J-C, Kornev KG. Carbon Nanotubes Loaded with Magnetic Particles. Nano Letters. 2005;5(5):879-84.10.1021/nl0502928
69. Tokarev A, Rubin B, Bedford M, Kornev KG. Magnetic Nanorods for Optofluidic Applications. AIP Conference proceedings. 2010;1311: 204-209.
70. Dresselhaus MS, Black MR, Meunier V, Rabin O. Nanowires. Springer Handbook of Nanotechnology: Springer; 2017. p. 249-301,
71. Frenkel J. Kinetic theory of liquids. New York: Dover; 1955.
72. Larson RG. The structure and rheology of complex fluids. Gubbins KE, editor. New York: Oxford University Press; 1999. 663 p,
73. Tokarev A, Kaufman B, Gu Y, Andrukh T, Adler PH, Kornev KG. Probing viscosity of nanoliter droplets of butterfly saliva by magnetic rotational spectroscopy. Applied Physics Letters. 2013;102(3):33701.

74. Wilson LG, Poon WCK. Small-world rheology: an introduction to probe-based active microrheology. Physical Chemistry Chemical Physics. 2011;13(22):10617-30.10.1039/c0cp01564d
75. Ghosh A, Mandal P, Karmakar S, Ghosh A. Analytical theory and stability analysis of an elongated nanoscale object under external torque. Phys Chem Chem Phys. 2013;15(26):10817-23.10.1039/c3cp50701g
76. Keshoju K, Xing H, Sun L. Magnetic field driven nanowire rotation in suspension. Applied Physics Letters. 2007;91(12):123114, http://dx.doi.org/10.1063/1.2789184

77. Kornev KG, Gu Y, Aprelev P, Tokarev A. Magnetic rotational spectroscopy for probing rheology of nanoliter droplets and thin films. Magnetic Characterization Techniques for Nanomaterials: Springer; 2017. p. 51-83,

78. Kim K, Guo JH, Xu XB, Fan DL. Recent Progress on Man-Made Inorganic Nanomachines. Small. 2015;11(33):4037-57.10.1002/smll.201500407
79. Li LG, Abedini-Nassab R, Yellen BB. Monolithically integrated Helmholtz coils by 3-dimensional printing. Applied Physics Letters. 2014;104(25).10.1063/1.4885441
80. Shields CW, Livingston CE, Yellen BB, Lopez GP, Murdoch DM. Magnetographic array for the capture and enumeration of single cells and cell pairs. Biomicrofluidics. 2014;8(4).10.1063/1.4885840
81. Ewoldt RH, Johnston MT, Caretta LM. Experimental Challenges of Shear Rheology: How to Avoid Bad Data. In: Spagnolie SE, editor. Complex Fluids in Biological Systems: Experiment, Theory, and Computation. Biological and Medical Physics Biomedical Engineering. New York: Springer; 2015. p. 207-41.10.1007/978-1-4939-2065-5_6
82. Tschope A, Kramer F, Birster K, Gratz M, Birringer R. Quantification of magneto-optically active nanorods and inactive aggregates in nickel nanorod colloids. Colloid and Interface Science Communications. 2016;10:11-4.10.1016/j.colcom.2016.03.001
83. Klein T, Laptev A, Gunther A, Bender P, Tschope A, Birringer R. Magnetic-field-dependent optical transmission of nickel nanorod colloidal dispersions. Journal of Applied Physics. 2009;106(11):114301-6, http://link.aip.org/link/?JAP/106/114301/1
84. McNaughton BH, Agayan RR, Wang JX, Kopelman R. Physiochemical microparticle sensors based on nonlinear magnetic oscillations. Sensors and Actuators B-Chemical. 2007;121(1):330-40,
85. Nguyen KVT, Anker JN. Detecting de-gelation through tissue using magnetically modulated optical nanoprobes (MagMOONs). Sensors and Actuators B-Chemical. 2014;205:313-21.10.1016/j.snb.2014.08.073
86. Mattia D, Gogotsi Y. Review: static and dynamic behavior of liquids inside carbon nanotubes. Microfluidics and Nanofluidics. 2008;5(3):289-305.10.1007/s10404-008-0293-5
87. Freedman JR, Mattia D, Korneva G, Gogotsi Y, Friedman G, Fontecchio AK. Magnetically assembled carbon nanotube tipped pipettes. Applied Physics Letters. 2007;90(10),
88. Squires TM, Quake SR. Microfluidics: Fluid physics at the nanoliter scale. Rev Mod Phys. 2005;77(3):977-1026.DOI 10.1103/RevModPhys.77.977
89. Soulages J, Oliveira MSN, Sousa PC, Alves MA, McKinley GH. Investigating the stability of viscoelastic stagnation flows in T-shaped microchannels. Journal of Non-Newtonian Fluid Mechanics. 2009;163(1-3):9-24.10.1016/j.jnnfm.2009.06.002
90. Nordstrom KN, Verneuil E, Arratia P, Basu A, Zhang Z, Yodh AG, Gollub JP, Durian DJ. Microfluidic rheology of soft colloids above and below jamming. Physical review letters. 2010;105(17):175701,
91. Pipe CJ, McKinley GH. Microfluidic rheometry. Mechanics Research Communications. 2009;36(1):110-20,
92. Wehrman M, Milstrey M, Lindberg S, Schultz K. Combining Microfluidics and Microrheology to Determine Rheological Properties of Soft Matter during Repeated Phase Transitions. Journal of visualized experiments: JoVE. 2018(134),

93. Kim Y, Kim J, Scheideler O, Cimenelli E, Sohn LL. Microfluidic Rheology to Study Effects of Cell Cycle to Viscoelastic Properties of Epithelial Cells. Biophys J. 2018;114(3):541a,
94. McKinley GH, Sridhar T. Filament-stretching rheometry of complex fluids. Annu Rev Fluid Mech. 2002;34:375-415.10.1146/annurev.fluid.34.083001.125207
95. Munstedt H. New Universal Extensional Rheometer for Polymer Melts - Measurements on a Polystyrene Sample. Journal of Rheology. 1979;23(4):421-36.Doi 10.1122/1.549544
96. Meissner J. Experimental Aspects in Polymer Melt Elongational Rheometry. Chem Eng Commun. 1985;33(1-4):159-80.
97. Franck A, Germany TI. The ARES-EVF: Option for measuring extensional viscosity of polymer melts. TA Instruments Germany–Internal Report–PN002. 2007,
98. Galindo-Rosales FJ, Alves MA, Oliveira MSN. Microdevices for extensional rheometry of low viscosity elastic liquids: a review. Microfluidics and Nanofluidics. 2013;14(1-2):1-19.10.1007/s10404-012-1028-1
99. Bazilevsky AV, Entov VM, Rozhkov AN, editors. Liquid filament microrheometer and some of its applications. The Golden Jubilee Meeting of the British Society of Rheology and Third European Rheology Conference; 1990; Edinburgh, UK.
100. Marshall KA, Liedtke AM, Todt AH, Walker TW. Extensional rheometry with a handheld mobile device. Exp Fluids. 2017;58(6).10.1007/s00348-017-2351-9

101. Anna SL, Rogers C, McKinley GH. On controlling the kinematics of a filament stretching rheometer using a real-time active control mechanism. Journal of Non-Newtonian Fluid Mechanics. 1999;87(2-3):307-35.Doi 10.1016/S0377-0257(99)00072-5
102. Campo-Deano L, Clasen C. The slow retraction method (SRM) for the determination of ultra-short relaxation times in capillary breakup extensional rheometry experiments. Journal of Non-Newtonian Fluid Mechanics. 2010;165(23-24):1688-99.10.1016/j.jnnfm.2010.09.007
103. Niedzwiedz K, Buggisch H, Willenbacher N. Extensional rheology of concentrated emulsions as probed by capillary breakup elongational rheometry (CaBER). Rheol Acta. 2010;49(11-12):1103-16.10.1007/s00397-010-0477-2
104. Roche M, Kellay H, Stone HA. Heterogeneity and the Role of Normal Stresses during the Extensional Thinning of Non-Brownian Shear-Thickening Fluids. Physical Review Letters. 2011;107(13). 10.1103/PhysRevLett.107.134503

105. Dinic J, Zhang YR, Jimenez LN, Sharma V. Extensional Relaxation Times of Dilute, Aqueous Polymer Solutions. Acs Macro Letters. 2015;4(7):804-8.10.1021/acsmacrolett.5b00393
106. McKinley GH, Tripathi A. How to extract the Newtonian viscosity from capillary breakup measurements in a filament rheometer. Journal of Rheology. 2000;44(3):653-70.Doi 10.1122/1.551105
107. Mackley MR, Butler SA, Huxley S, Reis NM, Barbosa AI, Tembely M. The observation and evaluation of extensional filament deformation and breakup profiles for Non Newtonian fluids using a high strain rate double piston apparatus. Journal of Non-Newtonian Fluid Mechanics. 2017;239:13-27.10.1016/j.jnnfm.2016.11.009

108. Bazilevskii AV, Rozhkov AN. Dynamics of capillary breakup of elastic jets. Fluid Dynamics. 2014;49(6):827-43.10.1134/s0015462814060143
109. Bazilevskii AV. Dynamics of horizontal viscoelastic fluid filaments. Fluid Dynamics. 2013;48(1):97-108.10.1134/s0015462813010110
110. Hubbe MA, Tayeb P, Joyce M, Tyagi P, Kehoe M, Dimic-Misic K, Pal L. Rheology of Nanocellulose-rich Aqueous Suspensions: A Review. Bioresources. 2017;12(4):9556-661.
111. Godinho MH, Pieranski P, Sotta P. Hygroscopic study of hydroxypropylcellulose Structure and strain-induced birefringence of capillary bridges. European Physical Journal E. 2016;39(9).10.1140/epje/i2016-16089-2
112. Bazilevsky AV, Entov VM, Rozhkov AN. Breakup of a liquid bridge as a method of rheological testing of biological fluids. Fluid Dynamics. 2011;46(4):613-22.10.1134/S0015462811040119
113. Haward SJ. Microfluidic extensional rheometry using stagnation point flow. Biomicrofluidics. 2016;10(4).10.1063/1.4945604
114. Petrie CJS. One hundred years of extensional flow. Journal of Non-Newtonian Fluid Mechanics. 2006;137(1-3):1-14.10.1016/j.jnnfm.2006.01.010
115. Hou YY, Kassim HO. Instrument techniques for rheometry. Review of Scientific Instruments. 2005;76(10).10.1063/1.2085048
116. Basaran OA, Gao HJ, Bhat PP. Nonstandard Inkjets. In: Davis SH, Moin P, editors. Annual Review of Fluid Mechanics, Vol 45. Annual Review of Fluid Mechanics. 452013. p. 85-113.10.1146/annurev-fluid-120710-101148
117. Tuladhar TR, Mackley MR. Filament stretching rheometry and break-up behaviour of low viscosity polymer solutions and inkjet fluids. Journal of Non-Newtonian Fluid Mechanics. 2008;148(1-3):97-108.10.1016/j.jnnfm.2007.04.015
118. Hoath S, Martin G, Tuladhar T, Mackley M, Hutchings I. Links between fluid rheology and drop-on-demand jetting and printability. Nip24/Digital Fabrication 2008: 24th International Conference on Digital Printing Technologies, Technical Program and Proceedings. 2008:130.
119. Mathues W, McIlroy C, Harlen OG, Clasen C. Capillary breakup of suspensions near pinch-off. Phys Fluids. 2015;27(9). 10.1063/1.4930011

120. Alexandrou AN, Bazilevskii AV, Entov VM, Rozhkov AN, Sharaf A. Breakup of a Capillary Bridge of Suspensions. Fluid Dynamics. 2010;45(6):952-64.10.1134/S001546281006013x

CHAPTER III

MODIFICATION OF MAGNETIC ROTATIONAL SPECTROSCOPY AND DEVELOPMENT OF MAGNETIC STAGE FOR HIGH-SPEED NANO- AND MICRORHEOLOGY

3.1 INTRODUCTION

In the previous chapter, we introduced the current challenges of nanorheological characterization of rapidly changing samples available in minute amounts. In this chapter, we address all these challenges by offering a new design of a magnetic microTesla stage for optical microscopy of droplets and films within a controlled environment. The earlier publication by our group dealt with a rotation stage providing some milliTesla magnetic fields (1). Here we discuss a new design, integrating magnetic coils with a 3D magnetic sensor with the feedback control, which allows us to significantly decrease the field. At the same time, the stage offers the user flexibility to control the 3D field configuration and is able to create a locally uniform field within the focal plane of the microscope objective. The optical cell equipped with the environment control circuit is fit under the Olympus BX51 upright microscope. We illustrate robustness of this stage by studying viscous properties of liquids with a high-speed rheological technique based on Magnetic Rotational Spectroscopy (2-5), using magnetic nano- and microrods as the probes.

3.2 DESIGN OF THE MAGNETIC STAGE

3.2.1 Design overview

The following challenges need to be addressed, when designing a stage for manipulation of magnetic probes with a microTesla rotating magnetic field in the focal plane of the microscope stage.

1) The magnetic field of Earth is three-dimensional (3D). It has to be cancelled in the focal plane of the microscope with an equal and opposite field. The cancelling 3D field has to be controlled on demand to guarantee that at different geographic locations with different Earth's magnetic field the stage will work correctly.

2) The magnetic field in the region of interest must be uniform and the magnetic gradient, which may cause a translational motion of magnetic probe, must be minimized.

3) The composition and humidity of the gas around the sample must be maintained to be the same during measurements or changed on demand in a controlled fashion using an environmental chamber.

The design that addresses all three challenges is schematically presented in Figure 1. Five independently driven magnetic coils surround the magnetic sensor, which measures the three orthogonal components of magnetic field. It thus becomes convenient to work in a Cartesian coordinate system with the origin located at the sensor center and axes aligned with the axes of the sensor. The xy plane thus becomes parallel to the ground. Coils 1 and 3 are placed in tandem and equidistant from the sensor, such that their axes are parallel to the x-axis. Similarly, the axes of coils 2 and 4 are parallel to the y-axis. Due to the spatial constraints associated with the need to accommodate an objective of a microscope and an

environmental chamber, coil 5 is positioned directly underneath the sensor with its axis parallel to z-axis. The produced 3D magnetic field satisfies all three criteria.

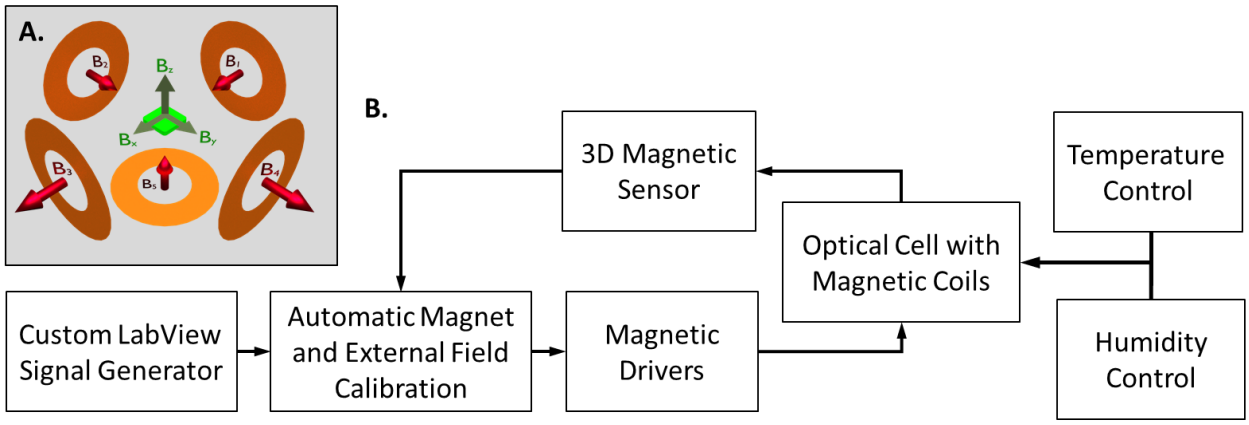

Figure 2. (A) A schematic of 5 independent magnetic coils each producing its own magnetic field (B_1-B_5). The sensor (green square) measures and records the resultant three vector components of the magnetic field (B_x, B_y, B_z). Coils 1 and 3 are aligned relative to the x-axis, coils 2 and 4 are aligned relative to the y-axes, and coil 5 is aligned relative to the z-axis (B) Basic elements of the magnetic stage with the environmental control.

The design of the stage was implemented in an instrument presented schematically in Figure 2. Five coils with a magnetic sensor create the required magnetic field at the location of the sample (Figure 2 A, B). The coils are driven by a signal generator software written in LabView for a NI-DAQ voltage generator coupled with a power amplifier. The produced magnetic field is measured by the magnetic sensor and fed to the software in a feedback loop; the software calculates what signal to send to each magnet. This way, any constant magnetic field can be created to counter any ambient field. This constant component is superimposed with a rotating magnetic field of a desired amplitude and frequency to rotate magnetic probes. By observing the motion of the probes with a camera coupled with a microscope, the magnetic field can be adjusted in real time to induce the

desired mode of rotation. For further analysis of the probe rotations, LabView VISION package algorithms are used.

The humidity and temperature of the sample on the magnetic stage are stabilized with an environment control system that pumps a gas of desired composition and humidity over the surface of the sample at a low flow rate. During the experiment, a droplet of the sample is placed in the chamber allowing evaporation to occur. The vapor mixes with supplied humidified nitrogen and exits the chamber. The sample thus evaporates until its equilibrium vapor pressure becomes equal to the vapor pressure of the supplied nitrogen-vapor mixture.

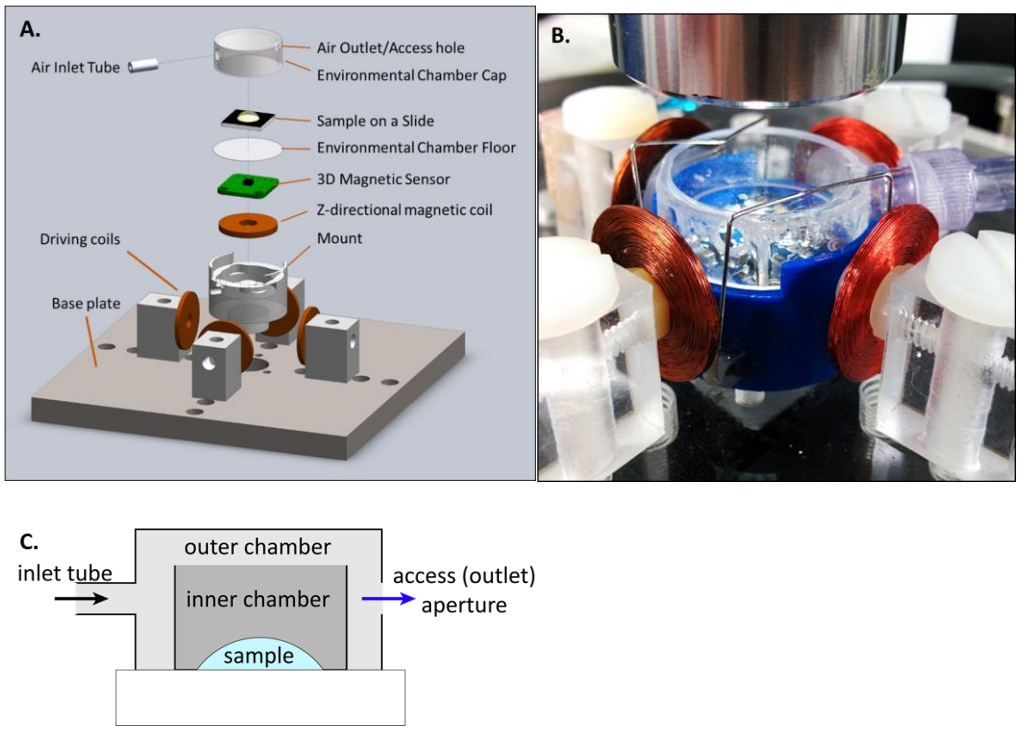

Figure 3. Schematics (A, C) and a photograph (B) of the magnetic stage with environmental control. (A) Basic elements of the magnetic stage with the environmental control. (B) A photograph of the optical cell with environmental control surrounded by five magnetic coils mounted under a microscope. (C) A cross-section schematic of the supply system of nitrogen of controlled humidity to the optical cell (not to scale). The inner chamber consists of an open-ended cylinder; the wall of this cylinder is schematically; the height of the inner chamber is slightly smaller than that of the outer

chamber, leaving a small gap for the gas to flow through. As the gas moves over the inner cylinder, it gets mixed with the water vapor form the sample.

3.2.2 Details of the engineering implementation

The above design is implemented in the following way (Figure 2.A). A microscope-compatible acrylic base plate holds the four driving coils (HobbyEngineering) firmly attached, each facing the center of the stage. Resting in the center of the stage is a 3D printed mount that holds the fifth out-of-plane coil directly underneath the magnetic sensor (HMC5883L, Adafruit), which measures the three components of the magnetic field. The sensor is covered by a thin cover glass, serving as a floor of the measuring chamber. A slide with magnetic probes suspended in the studied sample is placed directly on the chamber floor, thus ensuring the distance between the sample and the sensor is under 1 mm. Thus, the field measured by the sensor has the same magnitude and direction as the field that propagates through the sample and acts on the probes. The chamber is covered by a transparent cap with the inlet and outlet ports for the circulating gas. This cap seals the environmental chamber and allows one to observe the motion of magnetic probes with a microscope.

The dimensions of the system were designed with the following spatial constraints. To produce the smallest gradient with a tandem two-coil configuration, the distance between the coils must be minimized. At the same time, however, the magnetic sensor (19x20 mm) and a microscope objective of diameter ($d_{objective}$ = 32mm) must be able to fit between the coils. For that reason, the driving coils of diameter (d_{coils} = 25 mm) were mounted 33 mm apart. The mount, which has to hold the out-of-plane coil and the sensor, had the diameter of 29 mm. The diameter and the height of the environmental chamber

were limited by the diameter of the mount and the working distance of the objective, respectively. To fit the mount, the diameter of the chamber was chosen to be 25 mm. The working distance of a 50x Olympus lens is 10mm; thus the height of the chamber was made to be 9 mm; the height of the inner chamber cylinder was 8.5 mm.

To verify whether the coil separation distance yields an acceptable field with minimal gradient, finite element analysis was performed with COMSOL software. Two coils of radius R_{coils}, identical in geometry to the coils used in the setup, were placed uniaxially with a separation distance d_{coils}. The magnetic field and its gradient generated by the coils were calculated for different d_{coils}/R_{coils} ratios. For the ratio used in the instrument (d_{coils}/R_{coils}=2.6), both variables were plotted on a 2D slice through the central axis (Figure 4A). For other values of d_{coils}/R_{coils}, the magnetic field and the magnetic gradient along the center axis were plotted in Figure 4 B and C, respectively. It is clear that the coil configuration used in the instrument yields zero gradient at the center between the two coils and a uniform magnetic field for several millimeters around the center point.

A similar analysis was performed to verify that a single z-coil produces an acceptable region of uniform field at the sample (Figure 4D). The analysis demonstrates that at a distance of $0.08 \cdot R_{coils}$ away from the coil, which is the distance between the coil and the sample in the instrument, the field is uniform over roughly $0.2 \cdot R_{coils}$. In the instrument, this corresponds to a region of 5mm in diameter, which is larger than the size of a typical sample droplet. This analysis demonstrates that the magnetic field produced by the magnetic stage is uniform and gradient-free in in all three directions at the sample location.

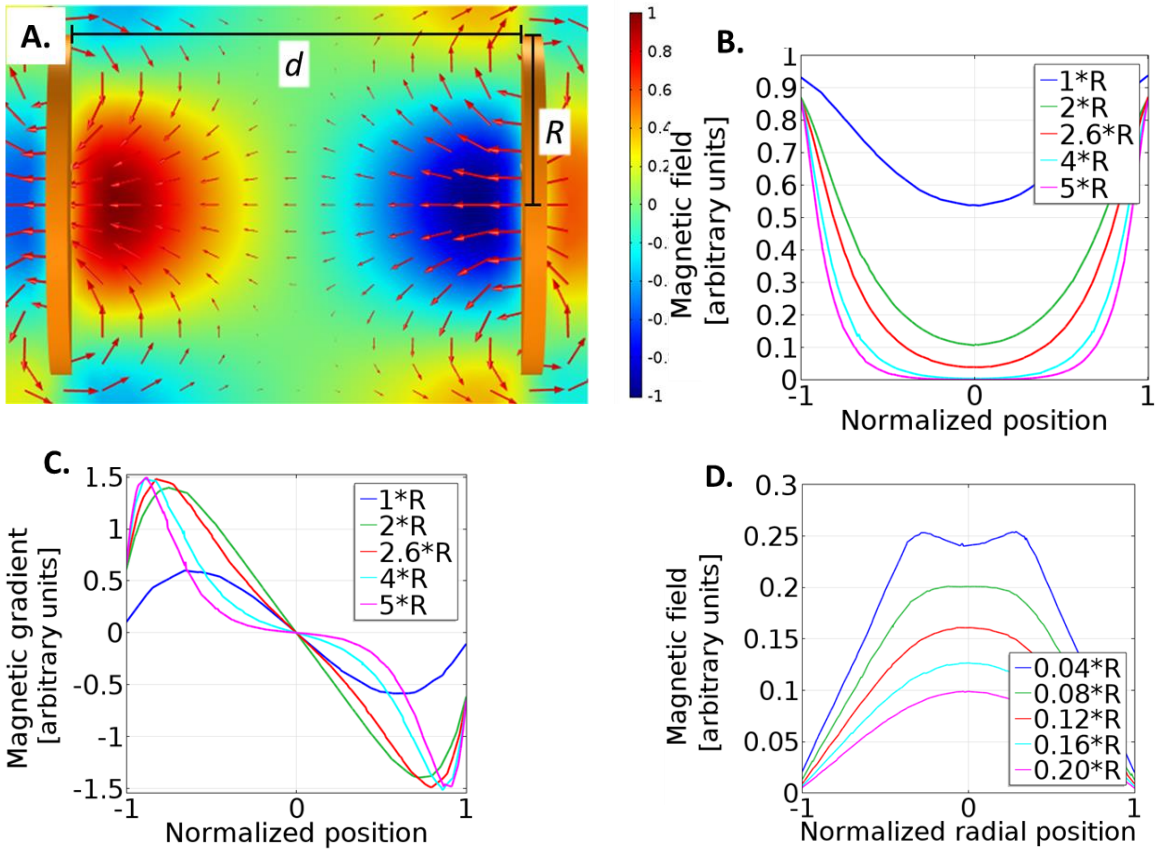

Figure 4. Results of a finite element analysis of magnetic field generated by (A-C) a pair of coils and (D) a single coil. (A) An arrow plot of the magnetic field superimposed with a heatmap plot of the magnetic gradient generated by a pair of coils of radius R_{coils} separated by a distance $d_{coils}=2.6 \cdot R_{coils}$. The geometry is similar to the coil configuration of the instrument. The arrows in the arrow plot are scaled logarithmically with a range quotient of 100. (B) Plots of the magnetic field in the axial direction along the axis of the coils for several separation distances. The position is normalized by $d_{coils}/2$ and the zero coordinate is the midpoint between the coils. (C) Plots of the magnetic gradient in the axial direction along the axis of the coils for several separation distances. The position is normalized by d/2 and the zero coordinate is the midpoint between the coils. (D) Plots of a magnetic field created by a single coil in the axial direction along a radial coordinate. The radial coordinate is normalized by the coil radius. This analysis demonstrates that at a distance of $0.08 \cdot R_{coils}$ away from the coil, the field is uniform over roughly $0.2 \cdot R_{coils}$. For a coil of 25mm in diameter, this corresponds to a 5x5 mm area 2 mm away from the coil.

To control the environment around the studied sample, an environmental control module was implemented. The environmental control of the sample is performed by flowing a gas of controlled composition and humidity through the environmental chamber

(Figure 2C). After passing through the chamber, the gas is released directly into the atmosphere through an aperture of diameter ($d_{apperture}$ = 2mm) that simultaneously serves as an access point for the user to the sample. The smallest allowable flow rate of the gas through the environmental chamber is thus controlled by the diffusive flux of air from the atmosphere back into the chamber. The evaluation of Peclet number and an experimental verification (details in Supplementary Information 1) place the low-end constraint of the flow rate at 1 Standard Cubic Foot per Hour (1 SCFH = $7.8 \cdot 10^{-6}\ m^3/s$). The upper constraint of the flow rate is due to the induced flow in the sample at the liquid-gas interface. To lower the effect of the induced flow, we separated the environmental chamber into two – inner and outer in Figure 2.C - with a cylindrical wall. The wall lowers the flow of gas directly over the surface of the sample, yet still allows the sample vapors to mix with the supplied gas. With this wall, the maximum flow rate was experimentally determined to be 2 SCFH or $15 \cdot 10^{-6}\ m^3/s$. The workable range of the flow rates of supplied gas was thus determined to be between 1 and 2 SCFH ($7.8 \cdot 10^{-6}\ m^3/s$ and $15 \cdot 10^{-6}\ m^3/s$, respectively).

In the current study, the environmental chamber was supplied with a nitrogen gas – water vapor mixture. For this purpose, the design of Ref.(6) was adapted and fitted with a humidity sensor (HIH-3040, Sparkfun) at the input to the environmental chamber. The details of the supply system are discussed in Supplementary Information 1.

By introducing a heating element into the environmental chamber, we are also able to set the temperature of the sample. A polyimide film-based flexible heating element (KA-808, Omegalux) was placed underneath the sample. A DC regulated power supply

(CSI12001X, Circuit Specialists) was connected to the heating element and controlled with a LabView program to maintain the temperature on the glass slide. The temperature on the slide was measured with a thermocouple connected to a temperature controller (TC-3300, CAL Controls LTD) and used for feedback control of the temperature. The details on this system can be found in Refs. (1, 7). During heating, the magnetic field generated by the current in the heating element was negligible and was not detected by the magnetic sensor.

3.2.3 Communication with a computer

A LabVIEW program produces the signal for the magnetic coils via an analog PCI board (NI-PCI 6722). The signal then gets amplified by five magnetic drivers. Our setup uses custom-made magnetic drivers that are based on the power operational amplifiers (PA02, Apex); alternatively, commercially available magnetic drivers can be used.

The magnetic sensor communicates with the LabView program via the I2C protocol and is able to record up to 75 measurements per second. The humidity sensor communicates with the programs via analogue voltage and is able to produce a measurement e two seconds.

3.2.4 Magnetic Signal Generator Software

To create a desired magnetic field, the magnetic controller program calculates the voltage to apply over each magnetic coil. Five coils create a magnetic field; the 3D magnetic sensor measures its three orthogonal components in the X, Y, and Z directions at the location right under the sample. (Figure 1A).

The naïve approach for setting the magnetic field is to assume identical coils andperfect alignment along their respective axes, and ignore the ambient field. We

demonstrate in Figure 6A that this approach yields unacceptably inaccurate results at low fields.

The coils cannot be perfectly aligned relative to their axes and are not perfectly identical. Therefore, one cannot *a priori* assume field uniformity; each coil contributes differently to all three components of the field. Due to the Biot–Savart law, these contributions are linear with respect to the voltage over the coil. Assuming that any ambient magnetic field is constant and does not depend on the voltages over the coils, each component of the magnetic field is expressed as the sum of the ambient field and a linearly scaled voltage over the coil:

$$\begin{aligned} B_X &= B_{X0} + a_1V_1 + a_2V_2 + a_3V_3 + a_4V_4 + a_5V_5 \\ B_Y &= B_{Y0} + b_1V_1 + b_2V_2 + b_3V_3 + b_4V_4 + b_5V_5 \\ B_Z &= B_{Z0} + c_1V_1 + c_2V_2 + c_3V_3 + c_4V_4 + c_5V_5 \end{aligned} \quad (4)$$

where B_x, B_y, and B_z are the components of the total magnetic field measured by the sensor, B_{x0}, B_{y0}, and B_{z0} are the components of the constant ambient magnetic field, $V_n, n = 1,2,3,4,5$ are the voltages supplied to the magnetic drivers, and a_n, b_n and c_n are the calibration coefficients for the five coils.

To find the coefficients a_n, b_n and c_n, the program communicates with the 3D magnetic sensor and performs the following series of steps:

1. Sends a zero voltage over each coil and collects a magnetic field measurement. We thus obtain the value of ambient magnetic field (B_{X0}, B_{Y0}, and B_{Z0}).
2. Incrementally increases voltage over each coil, while keeping all other voltages zeroed (e.g , V_1= 0.1V, 0.2V, 0.3V… 1V, while $V_2 = V_3 = V_4 = V_5$ =0V). At each

step, the program collects a magnetic field measurement. It thus obtains a linear plot of each component of the magnetic field versus voltage applied over each coil.

3. Linearly fits each plot, thus finding each of the coefficients (a_n b_n and c_n) in equation (1) (Figure 4).

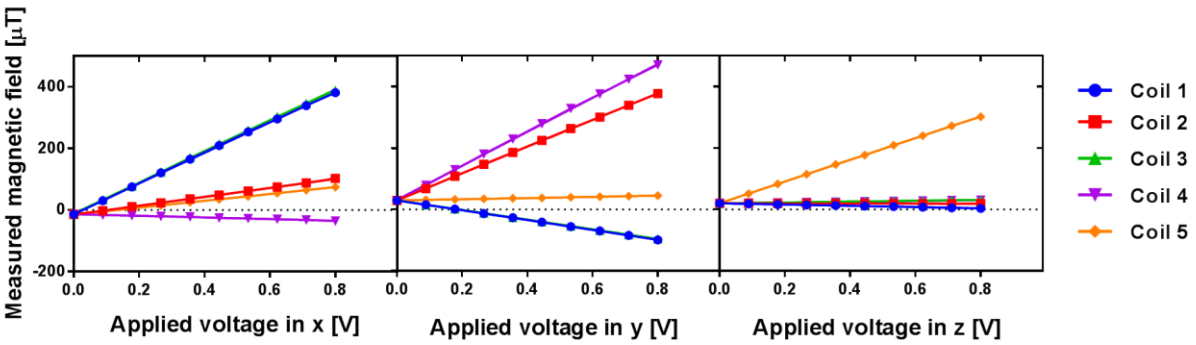

	B_0	m_1	m_2	m_3	m_4	m_5
X-direction	-14	495	143	508	-27	111
Y-direction	29	-160	435	-157	553	19
Z-direction	19	-20	-1	14	13	354

Figure 5. (Top) A typical example of calibration plots of each component of the magnetic field versus voltage applied over each coil obtained as a result of the calibration algorithm. (Bottom) The table of the results of linear regressions of each plot. B_0 is the average y-intercept and is interpreted as the ambient magnetic field in a given direction. m_n is the slope of the field produced vs. voltage supplied to coil n in a given direction. m_n in x-, y-, and z- directions correspond to a_n, b_n, and c_n coefficients in equation 1.

Once the coefficients are obtained, equations (4) must be solved for V_1, V_2, V_3, V_4, and V_5 at given values of B_x, B_y, and B_z. This provides a challenge, however, since there are three equations and five unknowns. The number of unknowns is reduced to three by taking into account that for the magnetic gradient to be minimal, the voltage over the coils must be applied so that both coils contribute equal components of the magnetic field in the direction

of their alignment axis (*i.e.* the axis specified by the magnetic sensor). Mathematically, this statement is expressed as

$$a_1 V_1 = a_3 V_3 \quad b_2 V_2 = b_4 V_4 \quad \Rightarrow \quad V_3 = \frac{a_1 V_1}{a_3} \quad V_4 = \frac{b_2 V_2}{b_4} \tag{5}$$

Substituting equation (5) into equation(4) , and solving the resulting system of equations, the supplied voltages in terms of components of the desired magnetic field are obtained as

$$\begin{bmatrix} V_1 \\ V_2 \\ V_5 \end{bmatrix} = \begin{bmatrix} 2a_1 & a_2 + a_4 \frac{b_2}{b_4} & a_5 \\ \frac{a_3}{a_1} b_1 + b_3 & 2b_4 & b_5 \\ \frac{a_3}{a_1} c_1 + c_3 & \frac{b_4}{b_2} c_2 + c_4 & c_5 \end{bmatrix}^{-1} \begin{bmatrix} B_X - B_{0X} \\ B_Y - B_{0Y} \\ B_Z - B_{0Z} \end{bmatrix} \tag{6}$$

The user is then free to specify any magnetic field. The software then calculates the voltages to send to each coil to create this field. The profile of the time-dependent components of the desired magnetic field is created using a built-in LabVIEW algorithm called “Basic Function Generator.” The user has a choice of a sine, square, sawtooth, or a triangle wave with adjustable parameters, such as the amplitude, frequency, and bias. This feature allows the user to quickly and accurately define the desired spatial and time profile of the magnetic field. Furthermore, the program can merge a series of waveforms with different parameters together – *e.g.* a sine wave with an increasing frequency.

In many applications, a 2D rotating field is required to manipulate magnetic particles (3, 5, 8-10). We thus demonstrate the applicability of the calibration algorithm by cancelling out the ambient magnetic field of 38μT (Earth's magnetic field in Clemson, SC) and imposing a rotating field of 100μT in the XY plane (Figure 5 B). With the applied calibration, the system is able to set a precisely defined magnetic field, accounting for Earth's magnetic field and the slight misalignment of magnetic coils.

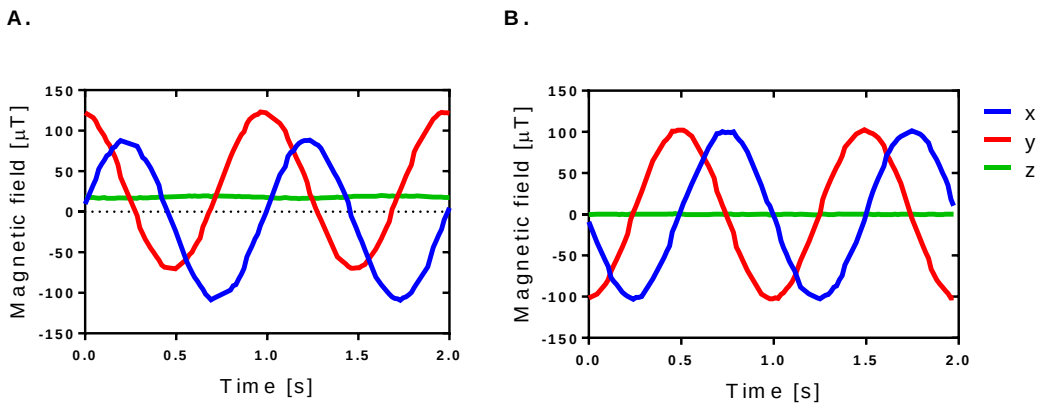

Figure 6. Demonstration of effectiveness of elimination of the ambient magnetic field. *(A) A measured profile of a generated magnetic field with a1=a3=b2=b4*, all others = 0. *The offsets are caused by Earth's magnetic field and unwanted oscillations in the z-component are caused by an imperfect alignment of magnets. (B) A measured profile of the generated 100μT rotating magnetic field in the xy-plane after calibration. The offsets and unwanted oscillations are removed.*

3.3 MATERIALS AND METHODS: PROBING FLUID VISCOSITY WITH MAGNETIC RODS

We demonstrate the robustness and variability of the instrument by performing microrheological measurements of the viscosity standards under different conditions. To demonstrate the effectiveness of the temperature control, we vary the temperature of the sample, while controlling sample evaporation. To demonstrate the effectiveness of

humidity control, we vary the environmental humidity, while maintaining a constant temperature.

To determine the viscosity of the sample, we modify the method of magnetic rotational spectroscopy (MRS) with ferromagnetic rod-like probes. The method allows to accurately detect viscosity changes of the liquid medium by tracking the changes of frequency of rotation of magnetic probes. The experiment consists of measuring the probe rotation frequency at the known viscosity and environmental conditions, then changing the environmental conditions, and tracking the changes in rotation behavior of the probe. We thus obtain the plots of viscosity as a function of temperature and humidity (Section 3.3.6).

3.3.1 Measuring viscosity

A magnetic field ***B*** acting on a ferromagnetic rod with a magnetic moment, ***m***, exerts a mechanical torque $\boldsymbol{\tau}_m = \mathbf{m} \times \mathbf{B}$ (11, 12). If the rod is suspended in a viscous medium of viscosity η, the medium responds to the rod rotation with a torque $\boldsymbol{\tau}_\mathrm{v} = \eta\gamma\dot{\varphi}\hat{\mathbf{e}}$ opposing its rotation, where $\dot{\varphi}$ is the angular velocity of the rod, φ is the angle that the magnetic moment ***m*** makes with a fixed axis x, $\hat{\mathbf{e}}$ is the unit vector pointing perpendicularly to the plane of rotation, and γ is the drag coefficient, which is defined for a rod of length l and diameter d, $l/d >> 1$, as(13, 14) : $\gamma = 2\pi l^3 \left(6\ln\left(2\,l/d\right) - 3\right)^{-1}$. After writing the balance of magnetic and viscous torques as $\mathbf{m} \times \mathbf{B} = \eta\gamma\dot{\varphi}\hat{\mathbf{e}}$ and solving this equation, one obtains trajectories of the rod endpoints during rotation. These trajectories depend on the viscosity of the medium. Knowing the rod parameters m and γ and knowing the angular frequency of the applied field ω and B, one can identify the viscosity of the liquid (3). This model and

experiments reveal a complex behavior of a magnetic rod in the 2D rotating magnetic field(3). For the in-plane rotation, the torque balance is reduced to the following equation(15-18):

$$\dot{\varphi} = -\omega_c \sin(\varphi - \omega t) \tag{7}$$

where $\omega_c = mB/(\eta\gamma)$ is the critical frequency of the rod rotation(3). When the frequency of the rotating magnetic field is below this critical frequency, the probe is synchronously rotating with the field at frequency ω, and magnetic moment makes a constant angle with the field, $\theta = \varphi - \omega t$. The angle θ is obtained by solving transcendental equation $\omega = \omega_c \sin\theta$. When the frequency of the rotating magnetic field is set above the critical frequency, $\omega/\omega_c > 1$ the transcendental equation does not make any sense, i.e. the solution $\theta = const$ does not satisfy equation (4), suggesting that the probe cannot rotate synchronously with the field. The rod keeps rotating in the same plane, but the trajectory of the rod end acquires an oscillatory time periodic component. In this *asynchronous* rotation, the rod keeps revolving periodically with the period of the rod oscillation ω_r depending on the frequency of applied field, $\omega_r = \omega_r(\omega)$. Recently, equation (4) was generalized on viscoelastic fluids and gels assuming the same form of the drag coefficient (4, 19-21).

Traditionally, the Magnetic Rotational Spectroscopy relies on the analysis of spectrum $\omega_r = \omega_r(\omega)$ (3, 20) when one needs to change the frequency of a rotating field in a broad range of frequencies from below to above the critical frequency covering all the features of rod rotation (16, 17, 19, 20, 22). The major shortcoming of this methodology is

the inability to probe rheology of materials with the properties rapidly changing with time. If the critical frequency of the system is 1Hz, which is typical for many liquids-probe systems (3, 20), and each data point is collected during at least 10 revolutions of the rod, a single measurement would take at least 10 seconds. To study the spectrum $\omega_r = \omega_r(\omega)$, one needs at least 10 measurements at 10 different frequencies; this requires, $10 \times 10 = 100$ seconds. To collect statistics, *i.e.* repeating the experiment 10 more times, one needs ~ 17 minutes. This is a lower-end estimate, which assumes that no time is required to switch between frequencies; a realistic experiment will take longer. Thus, while the methodology is viable for probing liquids with non-changing properties, it does not work for liquids that change their properties at this time scale. There are many examples where such viscosity characterization is challenging, including evaporating solutions and samples undergoing chemical reactions[55,](23, 24).

One can significantly speed up the measurements by developing a particle tracking algorithm and fitting the experimental trajectories of magnetic rods with the theoretical ones predicted by equation (4). A single fitting parameter in this model, $\omega_c = mB/(\eta\gamma)$, allows one to make this analysis straightforward. For a system with a critical frequency of 1Hz, a single measurement would take only 10-20 seconds. Using few visible rods rotating simultaneously in the focal plane of observation, one can gather statistics in one video. This allows for tracking the viscosity of a rapidly changing liquid – something impossible to do with MRS. We have used this idea and a first generation of the 5-coil setup to study the magnetic properties of ferromagnetic probes (15). This idea was further developed and is now illustrated here using the magnetic stage with environmental control. We

demonstrate the effectiveness of a single frequency measurement in both stable liquids and in liquids with rapidly changing properties. The probes of different length can be effectively used with this stage; we studied probes with the length ranging from several micrometers to millimeters. Nanorods were prepared from nickel using electro-chemical template synthesis in accordance with the protocol outlined in Ref. (15). As an example of nanoprobes, the 340nm diameter and 15-20μm length nanorods are used in this paper. As an example of microprobes, the 50μm diameter and 1-2mm length rods are used; a stainless steel SUS304 wire (Tokusen) was cut in pieces to make these microprobes.

3.3.2 Video analysis

An optical microscope equipped with a camera allows one to track the 100 nm thick and a few microns long nanorods(3). The imaging is often complicated by non-uniform backgrounds and foreign objects, which are abundant in microrheologically complex samples such as biofluids. Moreover, in samples with an open liquid-air interface, one often encounters fluid flows drifting the probes through the sample. Thus, one has to follow not only the probe rotation, but also its translation movement. All these challenges are resolved with a custom code based on LabVIEW Vision Development Module. This is a convenient solution, since the user can adjust video analysis parameters on the fly to obtain best results.

The nanorod image extraction algorithm is as follows. First, the user specifies the region of interest where the software should find the nanorod; all objects outside of this region are disregarded. A binarized image is then created using either constant threshold values or background correction via IMAQ Local Threshold algorithm. Binarization of the image sometimes causes artificial holes to appear in objects; these holes are automatically

filled in using IMAQ FillHole algorithm to insure correct further analysis. Any analysis of objects that are not fully imaged (i.e. located at the edge of the frame) would result in faulty results; such objects are deleted using IMAQ RejectBorder algorithm. Foreign objects, such as cells or dust, or noise in the image may result in faulty analysis; these imperfections are typically either smaller or larger than the nanorod and are thus filtered out by size using IMAQ RemoveParticle algorithms. As a result of these steps, a new image is created where only the nanorods of interest remain. For these nanorods, the orientation angle, the position, and the length are extracted using IMAQ Particle Analysis Report and IMAQ Clamp Max algorithms, respectively. To prepare for the analysis of the next frame, the region of interest is programmatically shifted to the coordinates of the nanorod and rotated to align with the orientation of the nanorod.

This process is applied to e frame in the specified segment of the video. The algorithm tracks the nanorod in each frame of the video and rejects any undesirable objects. The measurements of apparent length of the nanorod image in each frame provide a metric for analysis of the angle of declination of the nanorod axis from its original plane of rotation. The effectiveness of the algorithm is illustrated in Figure 7. In this example, the angle of rotation φ increases and periodically oscillates with time. The apparent length of the nanorod remains constant suggesting that the nanorod rotates in the focal plane. The program struggled with one frame (number 134) and produced a shorter length than expected. The algorithm, however, was able to successfully analyze all the consequent frames providing all necessary data for further analysis.

Once the data is extracted, the angular trajectory of the rod $\varphi(t)$ is fitted with equation (7) using the Levenberg–Marquardt function in LabView with ω_c as an adjustable parameter. The volume and the γ parameter of the probe are calculated using the average nanorod length l extracted from the video and diameter d. The magnetic moment m of the probe is then calculated from the calculated volume and the saturation magnetization M_s of the material as $m = 4\pi d^2 l M_s$. The viscosity is then calculated as $\eta = mB/(\omega_c \gamma)$. For this particular example in Figure 7, the viscosity was measured to be 2.8 mPa·s.

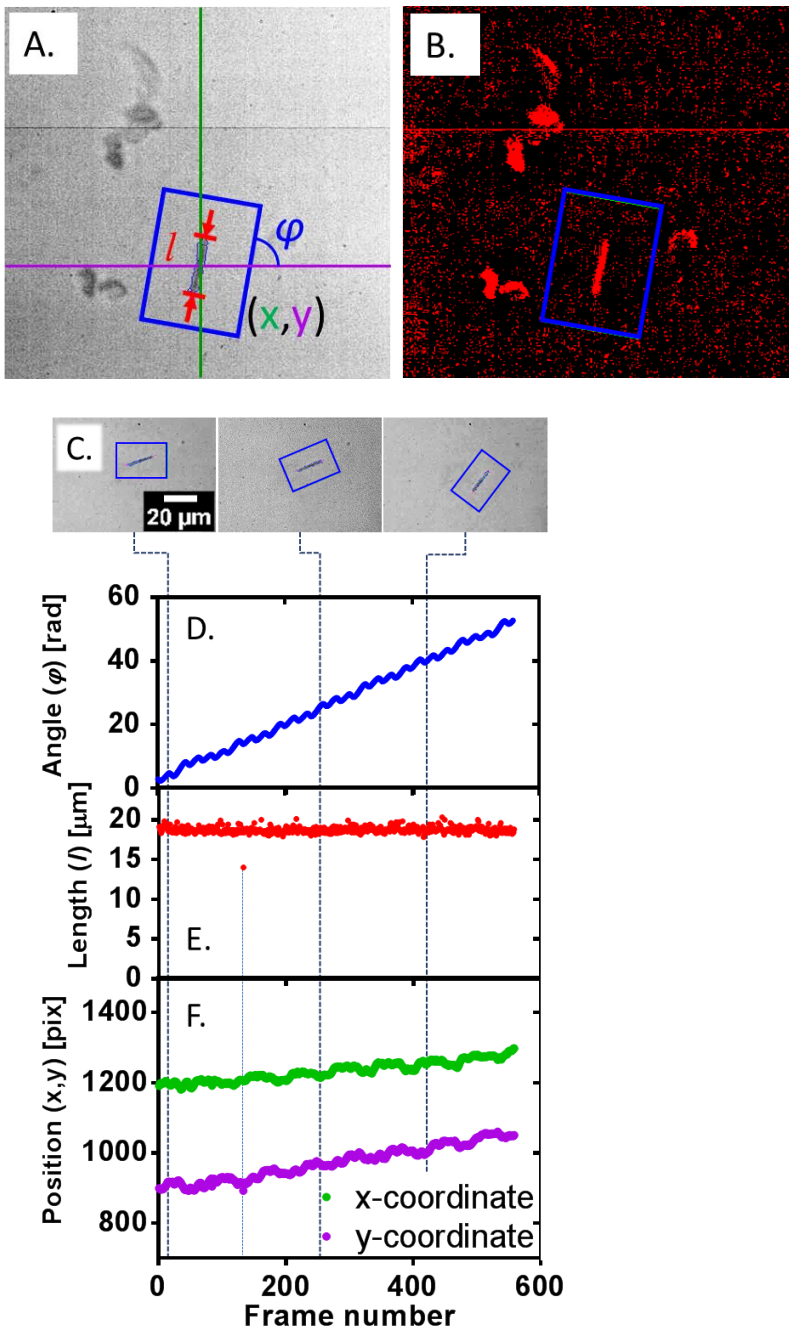

Figure 7. (A) An example image of the nanorod superimposed with the measured results for that particular frame. (B) A binary image of the frame with imperfections due to noise, uneven background, and present particles; the imperfections are removed by the developed software. (C) A gallery of frames showing a drifting nanorod with several foreign objects; (D) The extracted angle φ, (E) apparent length l, and (F) the in-plane coordinates (x,y) (in pixels) of the rod center mass for each frame.

3.3.3 Control of the out-of-plane rotation

During experimental observations of asynchronous rotation of ferromagnetic probes, we have detected that sometimes the apparent length of the observed nanorod changes. This implies that the nanorod declines out of the plane of rotation of the magnetic field (Figure 8). This behavior was most often observed when the coil calibration became inaccurate, as a result of either a change in the ambient magnetic field – due to accidental rotation of the set-up or movement of a magnetic object in the lab – or heating of the coils due to an overly high current. This, in turn, led to an inaccurate cancelation of the ambient magnetic field and resulted in a slight bias of the rotating field. The problem was easily resolved by recalibrating the system and did not significantly hamper the rheological measurements. It did, however, allow us to document an interesting regime of nanorod rotation that was theoretically predicted for soft magnetic nanorods (25), but never experimentally observed.

The explanation of this phenomenon is as follows. The net magnetic torque on the nanorod is always directed along the shortest path between the nanorod and the magnetic field. When the vectors of magnetic moment and external rotating field form an angle θ that is much smaller than 180 degrees, the net torque $\mathbf{m}\times\mathbf{B}\propto\sin\vartheta$ drives the nanorod to rotate in the focal plane as shown in Figure 8 A and B. When the magnetic moment is antiparallel to the applied field, the magnetic torque is $\mathbf{m}\times\mathbf{B}\propto\sin\vartheta\approx 0$, and any out-of-plane bias field changes the torque direction causing the nanorod to decline from the focal plane as shown in Figures 7 C, D, and E. When a nanorod rotates near its critical frequency, it spends a relatively long time in the direction antiparallel to the magnetic field. At this position, the nanorod is sensitive to any small out-of-plane perturbations of magnetic field.

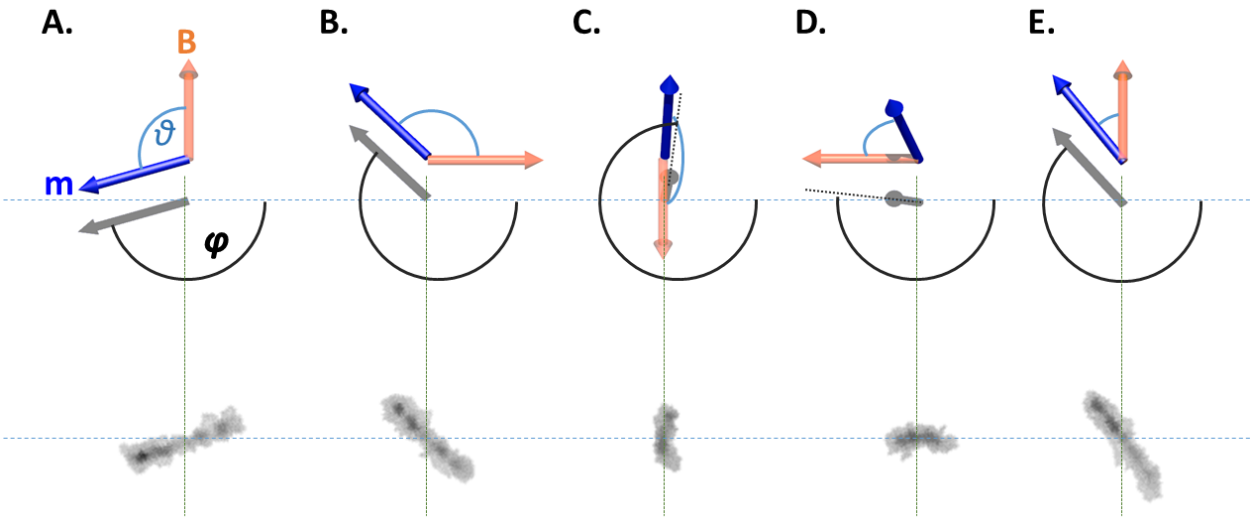

Figure 8. (Bottom) A gallery of snapshots of a ferromagnetic nanorod rotating at the onset of the out-of-plane rotation regime. (Top) A series of schematics to explain the behavior of the rod by illustrating the 3D orientations of the magnetic field **B** (orange), the orientation of the magnetic moment of the nanorod **m** (blue), the angle θ along the shortest path between **m** and **B**, the projection of **m** on a plane parallel to the rotation of the field (grey), and the angle φ that the projection makes with a stationary axis. The magnetic field rotates in the focal plane, while the nanorod and associated magnetic moment vector comes out of plane. The more the nanorod comes out of plane, the shorter its projection on the focal plane becomes. (A, B) the angle θ is relatively small and lies in the focal plane, so the nanorod rotates in the same plane. (C) As the angle θ approaches 180°, a small out-of-plane bias magnetic field makes the angle θ come out of the plane, causing the nanorod to stick out of the plane. (D) Once the nanorod gets out of the focal plane, it follows the shortest path to the magnetic field. (E) The nanorod orientation approaches the focal plane, but never makes it exactly in-plane again.

An extracted trajectory φ(t) and associated apparent length $l(t)$ of the nanorod are shown in Figure 9. In contrast to Figure 7 where the apparent length does not change during the observation time, in Figure 9, the apparent length of the nanorod changes with time. Quantitatively, one can characterize the level of nanorod deviation from the plane of field rotation by introducing the declination angle $\beta = \arccos(l_{apparent}/l)$, where $l_{apparent}$ is the length of visible projection of the nanorod on the focal plane, i.e. the plane of field

rotation and l is the actual length of the nanorod. The shorter the apparent length, the greater the inclination angle of the nanorod axis with respect to the plane of field rotation; the angle β approaches $\pi/2$ as the apparent length $l_{apparent}$ goes to zero and approaches zero as the apparent length approaches the actual length, $l_{apparent} \approx l$ implying that the rod is closer to the plane of rotating field. The graphs in Figure 9 confirm that the nanorod is subject to the out-of-plane precession. The plots reveal that until frame 400, the nanorod asynchronously rotates in plane of the field rotation. At frame 400, out-of-plane oscillations (oscillation in angle β) appear and increase until frame 650, when the nanorod apparently switches to the out-of-plane synchronous rotation: the trajectory φ(t) looks linear as it should be for a synchronous rotation of the nanorod with a rotating field. After frame 650, however, the apparent length of the nanorod oscillates around a declination angle of 50 degrees. Thus, after frame 650, the nanorod rotation has a precession component as well as an oscillatory component around the precession cone.

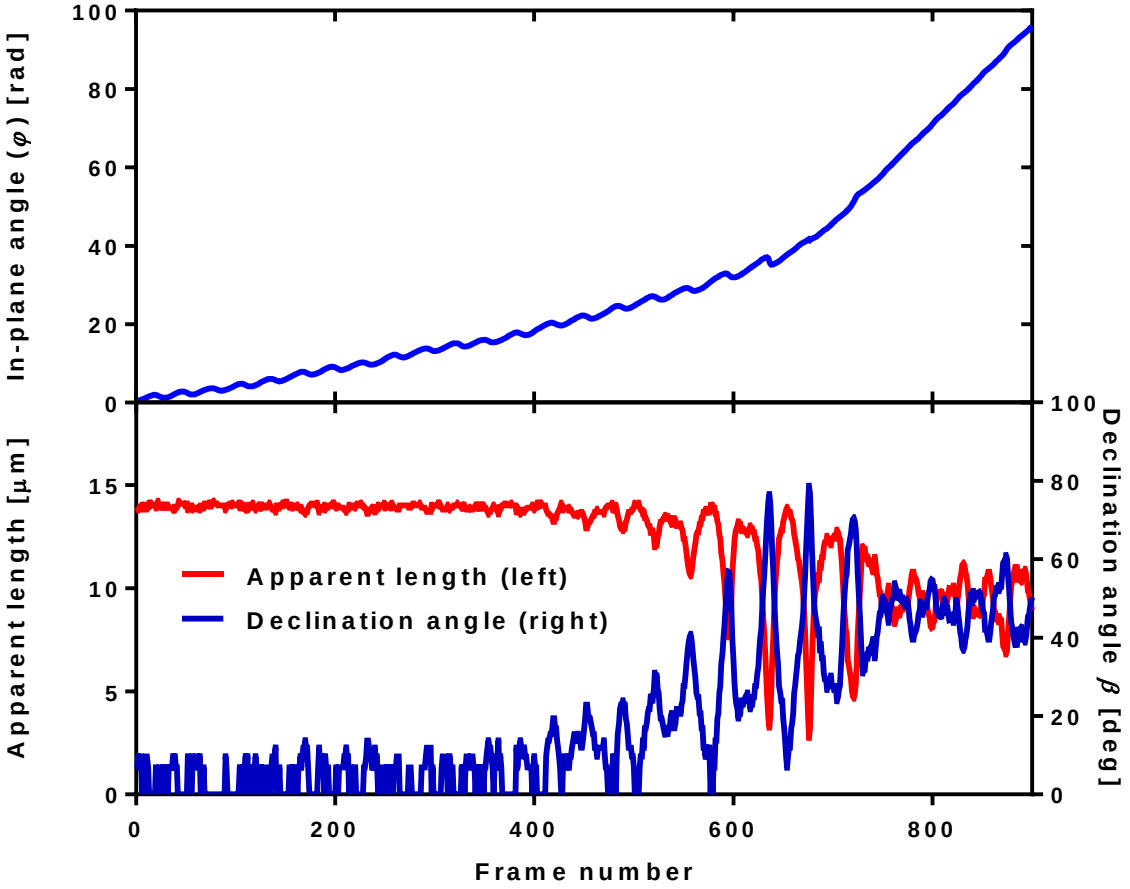

Figure 9. (Top) in-plane angle of the rotating nanorod. (Bottom) apparent length of the nanorod along with extracted out-of-plane declination angle.

A qualitatively similar out-of-plane rotation of a nanorod driven by a planar rotating magnetic field was predicted for a magnetically soft nanorod (25). As shown in Ref. (25), the nanorod magnetic moment does not have to align with the nanorod long axis and is able to decline under the influence of an external 2D magnetic field, i.e. a planar rotation of the nanorod is inherently unstable and no bias field is needed to push the nanorod out of plane. The tendency of the magnetic moment to align with the long axis of the rod is quantified by the materials parameter, the energy of magnetic anisotropy, *K*(26). When the material

is magnetically soft, *K* is small, the direction of the magnetic moment relative to the long axis of the rod can be easily changed; when the material is magnetically hard, K is large, and the direction of the magnetic moment can only be changed with a strong applied magnetic field. The nanorods used in this study were shown to be magnetically hard with the energy of magnetic anisotropy $K=22*10^3$ J/m^3 (15).

Cimurs and Cebers showed that the out of plane rotation of a magnetically soft nanorod describes a cone of the angle γ with the normal vector to the focal plane (25). This angle is related to the *K* parameter as (25):

$$1-\cos^2\gamma=\left(\frac{\omega_c}{\omega_H}\right)^2\left(1-\left(\frac{B}{B_a}\right)^2\right) \tag{8}$$

where ω_H is the frequency of rotating magnetic field, *B* is the magnitude of the applied magnetic field, $B_a=K/M_r$, , and M_r is the remanent magnetization of the nanorod material. Using the experimental values of the presented case – $\omega_c = 1.14\ Hz, \omega_H = 2\ Hz$, B = 100 μT, M_r = 140*10^3 A/m , and K=22*10^3 J/m^3 – we solve equation (5) to obtain the cone angle $\gamma = 34°$. This theoretical angle differs from the experimentally observed cone angle, $= 90° - \beta = 40°$. Moreover, if we attempt to solve equation (5) for $(B/B_a)^2$, using $\gamma = 40°$, and the same experimental parameters, we obtain $(B/B_a)^2 < 0$, which is physically impossible.

This discrepancy between theory and experiment comes from the assumption that the field is rotating in plane without any bias and the nanorod is magnetically soft. Thus, the Cimurs - Cebers theory is not sufficient to explain these experiments: there is a slight bias in the field and the nanorod material is magnetically hard. To understand the

contributions of both magnetic anisotropy and an out-of-plane magnetic field, a thorough study needs to be conducted to analyze the nanorod behavior as a function of these parameters.

3.3.4 Supply system for nitrogen gas - water vapor mixture

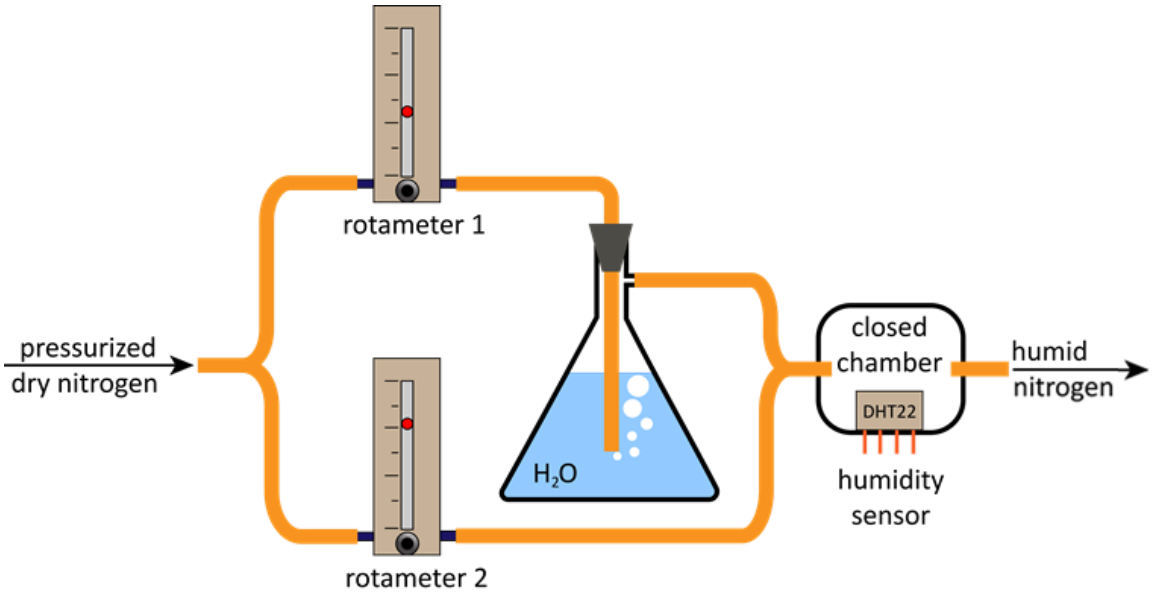

Figure 10. A schematic of the supply system of nitrogen of controlled humidity with a humidity sensor.

To supply the nitrogen/water vapor mixture of controlled humidity to the environmental chamber, the design of Ref.(6) was adapted to our case (Figure 10). Initially, a pressurized dry nitrogen gas is split between two rotameters that allow for manual control of the flow through them. The gas that is fed through one rotameter is fed into a sealed flask and is bubbled through a deionized water reservoir to reach a saturation humidity. It is then mixed with dry gas fed through the second rotameter and led into a sealed chamber, where a humidity sensor (HIH-3040, Sparkfun) measures its humidity. The HIH-3040

humidity sensor was calibrated on the aqueous glycerol solutions of known concentrations according to the tabulated values of humidity.(27) By changing the relative flow through the two rotameters and reading the measured humidity from the sensor, one gains a complete control of the humidity of the fed nitrogen gas. Finally, the nitrogen gas of known humidity is fed to the environmental chamber with the sample. Due to the low heat capacity of the air, the gas temperature in the chamber is equal to the temperature in the room, which is measured with a thermometer (Traceable, Fisher Scientific).

3.3.5 Determination of the lower bound of the flow rate in the environmental chamber.

The supplied nitrogen leaves the environmental chamber (Figure 2.C.) through the outlet port directly into the atmosphere. Therefore, the possibility of counter diffusion of air from the atmosphere back into the environmental chamber was a concern. To diminish this counter diffusion, one has to ensure that the flow of gas leaving the chamber through the outlet port via advection is significantly greater than its flow due to molecular diffusion. The outlet diameter d_{out} sets a characteristic scale for this transport problem: one can estimate whether advection prevails over molecular diffusion in an imaginary hemisphere of diameter d_{out} adjacent to the outlet by calculating the Peclet number $Pe = U \cdot d_{out}/D$, where *U* is the mean flow velocity of nitrogen and *D* is the diffusion coefficient of the air or water molecules in nitrogen. The diffusion coefficients of the most important air components in nitrogen at 25°C are known (28): the water vapor - $D=0.21*10^{-4}$ m^2/s ; carbon dioxide (CO_2) – $D=0.14*10^{-4}$ m^2/s , nitrogen oxide (NO) $D=0.18*10^{-4}$ m^2/s. Thus, these individual gas components of air have roughly the same diffusion coefficient in

nitrogen. We take D=0.2*10^{-4} m^2/s for the estimates of Peclet number. The mean velocity is calculated through the given flowrate Q as $U = 4Q/(\pi d_{out}^2)$. With the flowrate Q = 1 Standard Cubic Foot per Hour (1 SCFH = $7.8 \cdot 10^{-6}\ m^3/s$), the Peclet number is roughly $Pe\ = 2.5 \cdot 10^2$, suggesting that convective diffusion of the water vapor prevails over its molecular diffusion in the chamber. Therefore, at the nitrogen flow rates above 1 SCFH, the air outside the chamber should not drastically change the partial vapor pressure in the chamber; one expects that the humidity measured in the supply system is about the same as that measured in the chamber.

To verify this statement, a secondary humidity sensor (HIH-4030, Sparkfun) was temporarily placed directly inside the outer environmental chamber (Figure 3.C), nitrogen of various humidities and flow rates was passed through the system, and the readings from both sensors were compared (Figure 11). In the first experiment, a range of humidities was supplied at two flow rates 1 SCFH and 0.5 SCFH ($7.8 \cdot 10^{-6}\frac{m^3}{s}$ and $3.9 \cdot 10^{-6}\ m^3/s$, respectively). The humidity measured by the sensor embedded in the system was plotted against the humidity measured directly in the chamber for both cases (Figure 11.A) The black line represents a perfect correlation in humidities between the two locations. The blue and red points show the actual measurements and demonstrate the discrepancy in the humidities between the two locations. At the higher flow rate, the discrepancy is contained under 5% in the low humidity limit, while at low flow rate, the discrepancy reaches up to 15%. Thus, for the uncertainty of the humidity measurement to be contained within 5%, the flow rate of at least 1 SCFH ($7.8 \cdot 10^{-6}\frac{m^3}{s}$) must be used.

In the second experiment, nitrogen of 0% humidity was supplied to the system at different flow rates. The measured values from both sensors are plotted against the flow rate in Figure 11.B. In an ideal situation, both sensors should measure 0%. Due to counter diffusion, however, the discrepancy between the sensors increases as flow rate is decreased. The discrepancy at 1 SCFH ($7.8 \cdot 10^{-6} \frac{m^3}{s}$) flow rate is roughly 5%, which is consistent with the estimations and the first experiment. We thus confirm the lower bound for the supplied gas flow rate to be 1 SCFH($7.8 \cdot 10^{-6} \frac{m^3}{s}$).

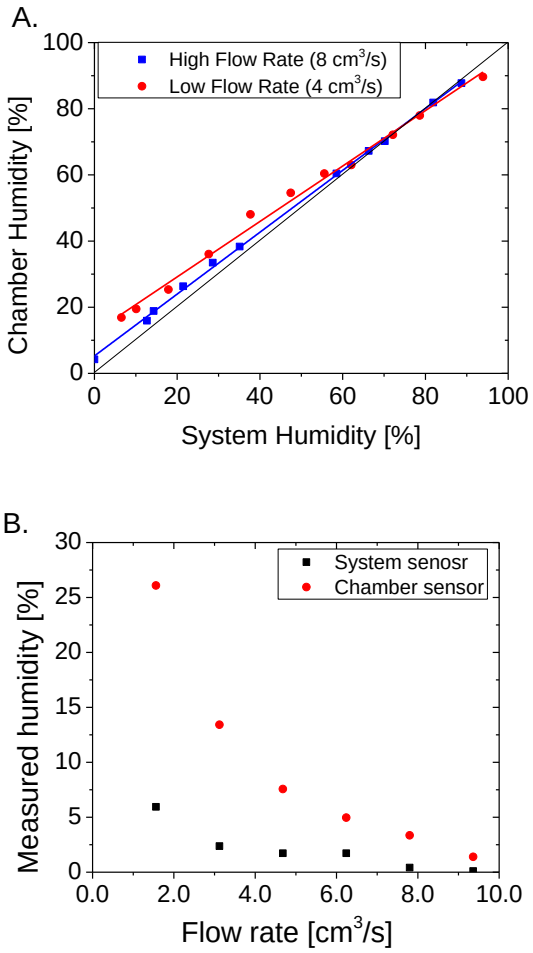

Figure 11. A. Calibration of the humidity in the environmental chamber with the system humidity. The high flow rate data correspond to the Peclet number of about 250, and the low flow rate data correspond to the Peclet number of about 125. B. Dependence of the water vapor content in the supplied system and in the chamber on the flow rate. The measurements were taken after the system had reached equilibrium and the values no longer changed.

3.3.6 Micro and nanorheology

The developed magnetic stage is able to work with different magnetic particles ranging from hundreds of nanometers to millimeters. Stainless steel microrods (50 μm in diameter) were used to replicate the tabulated viscosity of aqueous ethylene glycol

solutions of varying concentrations providing viscosities ranging from 1 mPa·s to 10 mPa·s. The probes were placed in deionized water and the critical frequency ω_{cr} was measured. Since the viscosity of water is known, $\eta = 1$ mPa·s, and applied magnetic field is known as well, this measurement has served as a reference specifying the m/γ ratio. Then, the same probes were used to measure the critical frequency of solutions with different concentrations of ethylene glycol. Each solution gives its own critical frequency $\omega_{cr}^{solution}$ from which the solution viscosity was calculated. The results of these experiments are summarized in Figure 12 A, where the tabulated viscosity is shown as a solid line. The experimental points fall on this line confirming the validity of the developed protocol.

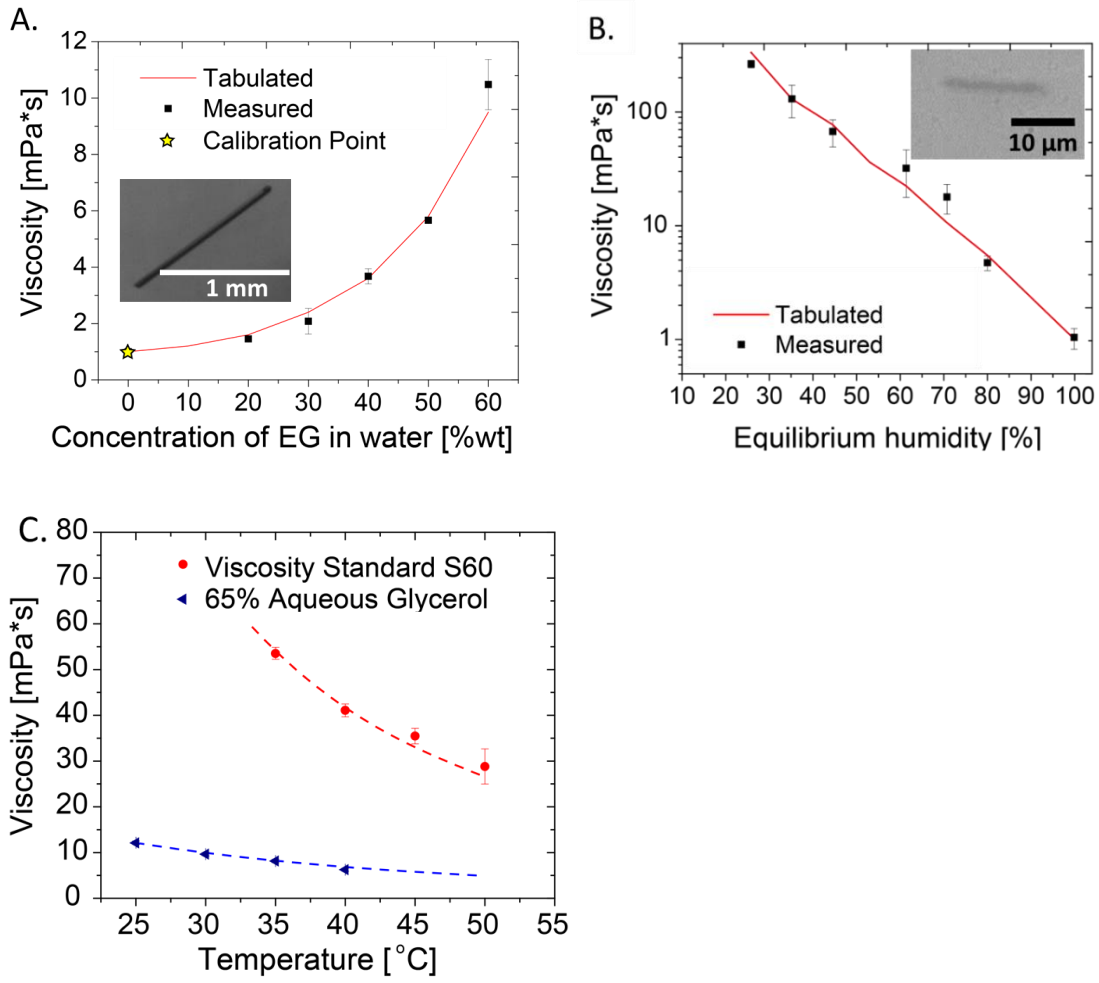

Figure 12. A) Profile of the measured viscosity of prepared aqueous ethylene glycol (EG) solutions using stainless steel SUS304 microrods. Tabulated values are taken from(29) and interpolated for the room temperature. The error bars indicate the standard deviation calculated from several measurements. (insert in A) A micrograph of a stainless steel SUS304 microrod in the studied solution. (B) The measured viscosity of aqueous glycerol solutions measured with nickel nanorods versus equilibrium humidity. The tabulated values are taken from Refs. (27) and(30) and interpolated for the room temperature during the experiment. Three probes were used to measure each point. (insert in B) A micrograph of a nickel nanorod in the studied solution. (C) The temperature dependence of viscosities of the Viscosity Standard S60 and 65% aqueous glycerol solutions. The dotted lines represent the tabulated values of viscosities. The solid symbols represent the data measured with nickel nanorods. Three probes were used for a Viscosity Standard S60 measurement and a single probe was used to probe viscosity of glycerol solution.

To illustrate the capabilities of the humidity control system, the aqueous glycerol solutions of various concentrations were studied by pumping the nitrogen-water vapor mixture through the chamber while keeping the temperature constant. The humidity of nitrogen gas was varied and, simultaneously, the solution viscosity was measured with nickel nanorods. Since the solvent (water) was free to condense or evaporate from the solution, the concentration of water changed in the sample until it reached equilibrium with the humid gas around it. Thus, by controlling the humidity around the sample, one controls the water concertation in the sample. Using rotating probes, one can directly relate the equilibrium humidity to viscosity. This is an important advancement for characterization of aqueous droplets and thin films, as it eliminates an unnecessary step of relating both of those parameters to concentration – a significant challenge for small samples. The interpolated tabulated values of equilibrium humidity as a function of concentration(27, 31) and viscosity as a function of concentration(30) were used as the references.

The experimental protocol was as follows: nickel nanorods were prepared using electro-chemical template synthesis and characterized in accordance with the protocol outlined in Ref. (15): the diameter and the magnetization were measured to be 340 ± 30 nm and 160 ± 40 kA/m, accordingly; the length which changes after sonication of the prepared suspension, was extracted from the video analysis. An aqueous solution of glycerol of 50% by weight (79% equilibrium humidity at 22°C) was prepared, in which nickel nanorods were suspended. The humidity in the chamber was then altered to a desired value, thus initiating evaporation of water from the droplet. The critical frequency $\omega_{cr}^{solution}$ was measured as a function of time, until the droplet reached equilibrium. The

viscosity of solution at equilibrium was then calculated from the critical frequency and recorded for a given humidity and the process was repeated for a different humidity. The measured values of equilibrium viscosity as a function of humidity of the supplied gas are presented in Figure 12 B. Value for the viscosity for 100% humidity was measured by suspending nanorods in deionized water. Again, the experimental points fall on the tabulated curve, confirming the validity of the developed protocol.

To demonstrate the effectiveness of the temperature control, we performed experiments with nickel nanorods in two temperature-dependent viscosity standards – Viscosity Standard S60 (Cannon Instrument Company) and 65% aqueous glycerol solution. To prevent liquid evaporation, all experiments were conducted in a closed container – a glass slide with a cover slip.

The experimental protocol was as follows: the nickel nanorods were suspended in a sample, which was heated to a desired temperature at which the critical frequency $\omega_{cr}^{solution}$ was measured, from which the viscosity was calculated and then correlated with the tabulated value. The sample was then heated to a new temperature, and a new critical frequency was measured and viscosity was calculated. In Figure 12 C, the measured viscosities vs temperature of the S60 viscosity standard and the glycerin solution are presented along with the tabulated values of the viscosity standards.

The developed magnetic stage with environmental control system is a convenient tool to study complex solutions undergoing different phase transportations upon solvent evaporation. As an illustration, we show a complex behavior of the viscosity of a surfactant-cosurfactant solution - cetylpyridinium chloride-sodium salicylate-brine (CPCl-

NaSal). A phase diagram for this ternary system in the 2D cetylpyridinium chloride-sodium salicylate plane has been characterized structurally as well as rheologically in Refs.(32-37). These papers dealt with the liquid phases only. The drying kinetics of this system and phase behavior, however, have not been investigated due to the difficulty of tracking of the rheological properties of a drying sample under varying conditions. Here, we present a comparison of the time-dependent microscopic viscosity as well as final morphology of two drop-casted samples of 2% CPCl-NaSal in 0.5% NaCl brine as they dry up in nitrogen of 0% and 57% humidity.

The sample viscosity can depend on the probe location. The viscosity is measured at the location of the probe starting from deposition of the sample until complete encapsulation of the probe by a crystal dendrite. The period of probe rotation (τ = 5s) was chosen to be much greater than the relaxation time of the solution (τ = 0.14 ± 0.01s)(5); thus, the Newtonian model of liquid, eq. (4), accurately predicts the nanorod behavior (Figure 10, B) and no elastic contribution is detected. The time dependence of viscosity (Figure 10, A) of the two drying samples demonstrates some differences in the drying kinetics.

When the film evaporates, the viscosity of both samples increases until it hits a plateau at relative viscosity of 2. The viscosity of both solutions remains almost constant for some time. This suggests that as both samples evaporate, they reach a phase in which either evaporation significantly slows down or the viscosity stops being dependent on the concentration of water. The local viscosity of a sample that was dried at 0% humidity, however, gets to the plateau more quickly and increases more sharply several seconds

before the crystal consumes the nanorod. The nanorod does not drift during the dendrite approach until the crystal embraces the nanorod completely.

In contrast to this behavior, the local viscosity of the sample dried at 57% humidity leaves the plateau phase more slowly and takes several minutes to gradually increase its value. During the crystal growth, two nanorods were captured on the video. The nanorod that is positioned closer to the dendrite moves towards it significantly quicker than the one located farther away. This suggests that some flow has been developed in the crystal vicinity. The final microstructure of the sample (Figure 10, D, left) appears drastically different from that formed at 0% humidity (Figure 10, C, left).

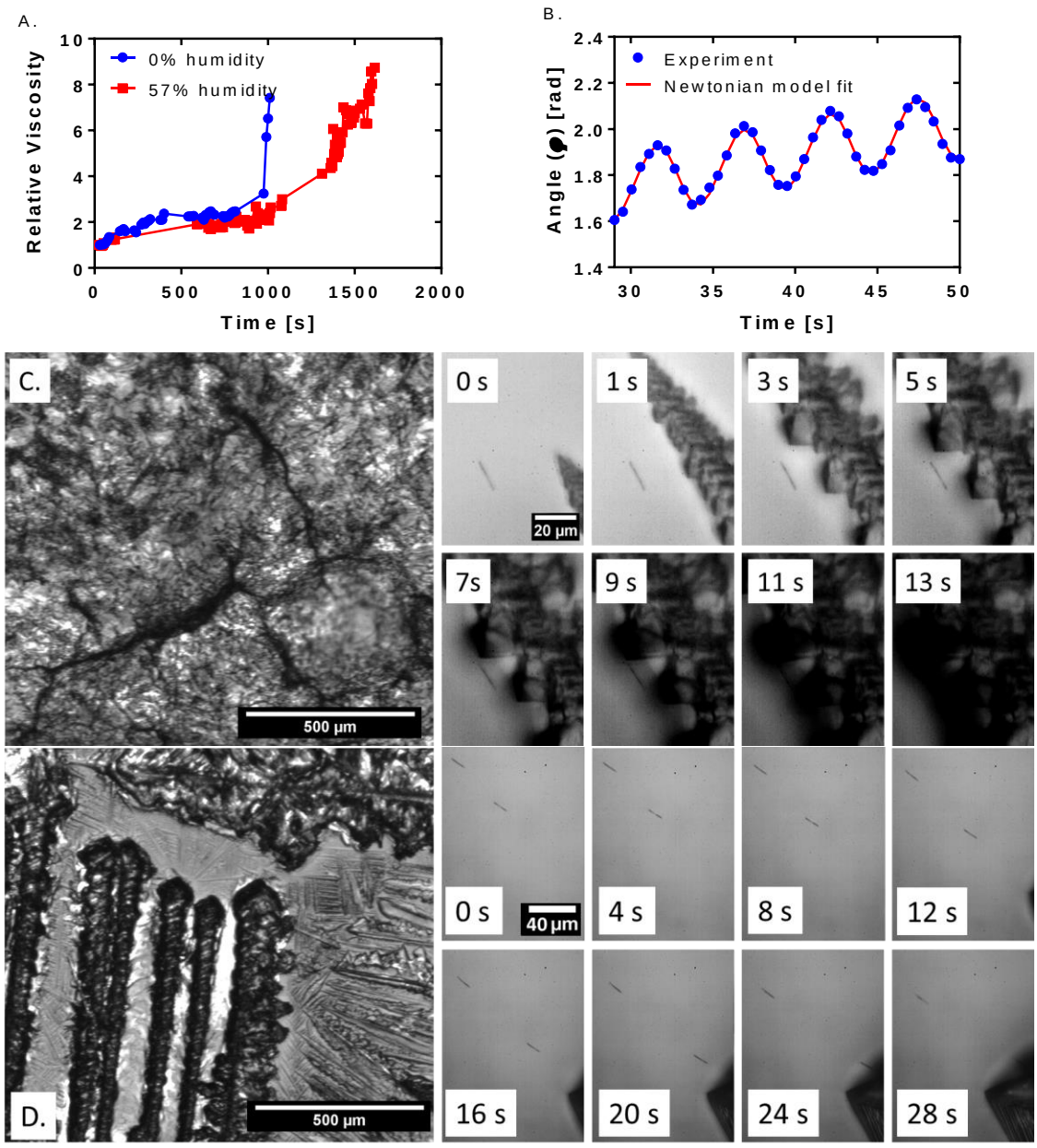

Figure 10. (A) The time dependence of viscosity in a thin film of CPCl-NaSal drying in pure nitrogen (0% humidity) and in nitrogen of 57% humidity. The viscosity is measured at the location of the probe starting from the moment of film deposition until complete encapsulation of the probe by a crystal dendrite. (B) An extracted trajectory along with its fit by eq. (4) for the nanorod in the film held at 57% humidity. To avoid any elastic contribution to the probe rotation, the period of rotation was chosen to be much lower than the relaxation time of the solution. [55] (C left) A polarized micrograph of a sample dried at 0% humidity. A multidomain structure with cracks or grain boundaries is observed. (C right) A gallery of snapshots showing a nanorod in the vicinity of a growing

dendrite. The dendrite grows relatively fast and the nanorod does not drift in the sample. (D left) A polarized micrograph of a sample dried at 57% humidity. Multiple dendrites are ordered in arrays. (D right) A gallery of snapshots showing a nanorod near a growing dendrite. As the crystal grows near the nanorod, the nanorod gets pulled towards the crystal, indicating that the growing crystal generates a flow.

3.4 CONCLUSION

A multifunctional magnetic stage for optical microscopy with temperature and humidity control was developed. It addresses the challenges associated with magnetic probing of materials at the hundreds of microTesla magnetic fields. By applying a special procedure to zero out a bias ambient magnetic field and apply a uniform rotating field to rotate magnetic probes, the stage was used for analysis of rheological properties of fluids of viscosities ranging from mPa·s to Pa·s with measurements carried out in as little as 10 seconds. To demonstrate the reliability and robustness of the instrument, the rotation of magnetic probes of various sizes has been tracked to study a wide range of solutions with different viscosities in different environmental conditions. By performing viscosity measurements on samples of aqueous glycerol solutions with a free surface in a controlled humidity, it has been demonstrated for the first time that viscosity as a function of humidity can be directly measured without explicitly linking viscosity through concentration of a volatile component. The technique also allows one to study kinetics of evaporation and solidification of a model for different complex fluids. A surfactant-cosurfactant system (CPCl-NaSal) was used as an illustration of its complex phase behavior at different humidities.

We envision that this multifunctional magnetic stage will be useful not only for the environmentally controlled nano- and microrheological studies, but also for various

applications where optical tracking of response of material or probes to low magnetic fields is critical.

3.5 REFERENCES

1. Tokarev A, Aprelev A, Zakharov MN, Korneva G, Gogotsi Y, Kornev KG. Multifunctional magnetic rotator for micro and nanorheological studies. Review of Scientific Instruments. 2012;83(6):065110, http://dx.doi.org/10.1063/1.4729795
2. Kornev KG, Gu Y, Aprelev P, Tokarev A. Magnetic Rotational Spectroscopy for Probing Rheology of Nanoliter Droplets and Thin Films. In: Kumar C, editor. Magnetic Characterization Techniques for Nanomaterials. Berlin, Heidelberg: Springer Berlin Heidelberg; 2017. p. 51-83.10.1007/978-3-662-52780-1_2
3. Gu Y, Kornev KG. Ferromagnetic Nanorods in Applications to Control of the In-Plane Anisotropy of Composite Films and for In Situ Characterization of the Film Rheology. Advanced Functional Materials. 2016;26(22):3796-808.10.1002/adfm.201504205
4. Berret JF. Local viscoelasticity of living cells measured by rotational magnetic spectroscopy. Nature Communications. 2016;7.10.1038/ncomms10134
5. Loosli F, Najm M, Chan R, Oikonomou E, Grados A, Receveur M, Berret J-F. Wire-Active Microrheology to Differentiate Viscoelastic Liquids from Soft Solids. ChemPhysChem. 2016;17(24):4134-43,
6. Kiefersauer R, Than ME, Dobbek H, Gremer L, Melero M, Strobl S, Dias JM, Soulimane T, Huber R. A novel free-mounting system for protein crystals: Transformation and improvement of diffraction power by accurately controlled humidity changes. Journal of Applied Crystallography. 2000;33:1223-30.10.1107/S0021889800008049
7. Burtovyy R, Rubin B, Kesimci MO, Luzinov I, Owens J, Kornev KG. Surface Differential Scanning Calorimeter for Evaluation of Evaporative Cooling Efficiency. Journal of Engineered Fibers and Fabrics. 2012;7:58-62.
8. Erb RM, Martin JJ, Soheilian R, Pan CZ, Barber JR. Actuating Soft Matter with Magnetic Torque. Advanced Functional Materials. 2016;26(22):3859-80.10.1002/adfm.201504699
9. Tokarev A, Yatvin J, Trotsenko O, Locklin J, Minko S. Nanostructured Soft Matter with Magnetic Nanoparticles. Advanced Functional Materials. 2016;26(22):3761-82.10.1002/adfm.201504443
10. Tierno P. Recent advances in anisotropic magnetic colloids: realization, assembly and applications. Physical Chemistry Chemical Physics. 2014;16(43):23515-28.10.1039/c4cp03099k
11. Rosensweig RE. Ferrohydrodynamics. Cambrige: Cambrige University Press; 1985.

12. Blums E, Cebers A, Maiorov MM. Magnetic fluids. New York: Walter de Gruyter; 1997. p. 11-66,
13. Doi M, Edwards SF. The theory of polymer dynamics. Oxford: Clarendon Press; 1988. xiii, 391 p. p,
14. Dusenbery DB. Living at micro scale : the unexpected physics of being small. Cambridge, Mass.: Harvard University Press; 2009. xxx, 416 p. p,
15. Aprelev P, Gu Y, Burtovyy R, Luzinov I, Kornev KG. Synthesis and characterization of nanorods for magnetic rotational spectroscopy. Journal of Applied Physics. 2015;118:074901.10.1063/1.4928401
16. Brasovs A, Cīmurs J, Ērglis K, Zeltins A, Berret J-F, Cēbers A. Magnetic microrods as a tool for microrheology. Soft Matter. 2015;11.10.1039/C4SM02454K
17. Tokarev A, Kaufman B, Gu Y, Andrukh T, Adler PH, Kornev KG. Probing viscosity of nanoliter droplets of butterfly saliva by magnetic rotational spectroscopy. Applied Physics Letters. 2013;102(3):33701.

18. Gu Y, Chen Z, Borodinov N, Luzinov I, Peng F, Kornev KG. Kinetics of evaporation and gel formation in thin films of ceramic precursors. Langmuir. 2014:DOI: 10.1021/la5037986,
19. Chevry L, Sampathkumar NK, Cebers A, Berret J-F-F. Magnetic wire-based sensors for the microrheology of complex fluids. Physical Review E. 2013;88:62306.10.1103/PhysRevE.88.062306
20. Berret JF. Microrheology of viscoelastic solutions studied by magnetic rotational spectroscopy. International Journal of Nanotechnology. 2016;13(8-9):597-603.10.1504/ijnt.2016.079661
21. Chevry L, Sampathkumar NK, Cebers A, Berret JF. Magnetic wire-based sensors for the microrheology of complex fluids. Physical Review E. 2013;88(6).10.1103/PhysRevE.88.062306
22. Loosli F, Najm M, Chan R, Oikonomou E, Grados A, Receveur M, Berret J-F. Wire-Active Microrheology to Differentiate Viscoelastic Liquids from Soft Solids. Chemphyschem : a European journal of chemical physics and physical chemistry. 2016;17(24):4134-43.10.1002/cphc.201601037
23. Grayson JW, Zhang Y, Mutzel A, Renbaum-Wolff L, Boge O, Kamal S, Herrmann H, Martin ST, Bertram AK. Effect of varying experimental conditions on the viscosity of alpha-pinene derived secondary organic material. Atmospheric Chemistry and Physics. 2016;16(10):6027-40.10.5194/acp-16-6027-2016
24. Renbaum-Wolff L, Grayson JW, Bertram AK. Technical Note: New methodology for measuring viscosities in small volumes characteristic of environmental chamber particle samples. Atmospheric Chemistry and Physics. 2013;13(2):791-802.10.5194/acp-13-791-2013
25. Cimurs J, Cebers A. Three-dimensional dynamics of a particle with a finite energy of magnetic anisotropy in a rotating magnetic field. Physical Review E. 2013;88(6).
26. Chikazumi SO, Graham CD. Physics of ferromagnetism. 2nd ed. Oxford ; New York: Oxford University Press; 2009. xii, 655 p. p,

27. BRAUN JV, BRAUN JD. A Simplified Method of Preparing Solutions Of Glycerol and Water for Humidity Control—A Technical Note. CORROSION. 1958;14:17-8.10.5006/0010-9312-14.3.17
28. Massman WJ. A review of the molecular diffusivities of H2O, CO2, CH4, CO, O-3, SO2, NH3, N2O, NO, AND NO2 in air, O-2 AND N-2 near STP. Atmos Environ. 1998;32(6):1111-27.10.1016/s1352-2310(97)00391-9
29. MEGlobal. Ethylene Glycol Product Guide. MEGlobal. 2008:1-33,
30. Jerome FS, Tseng JT, Fan LT. Viscosities of aqueous glycol solutions. Journal of Chemical & Engineering Data. 1968;13:496-.10.1021/je60039a010
31. Wheeler MJ, Russi S, Bowler MG, Bowler MW. Measurement of the equilibrium relative humidity for common precipitant concentrations: Facilitating controlled dehydration experiments. Acta Crystallographica Section F: Structural Biology and Crystallization Communications. 2012;68:111-4.10.1107/S1744309111054029
32. Berret J-F. Rheology of Wormlike Micelles : Equilibrium Properties and Shear Banding Transition. Molecular Gels. 2005:235-75.10.1007/1-4020-3689-2_20
33. Berret J-F, Roux D, Gregoire P. Isotropic-to-nematic transition in wormlike micelles under shear To cite this version : Isotropic-to-nematic. Journal de Physique II,. 1994;4 (8):1261-79.10.1051/jp2:1994198
34. Lerouge S, Berret J-F. Shear-induced transitions and instabilities in surfactant wormlike micelles.
35. Berret JF, Porte G. Metastable versus unstable transients at the onset of a shear-induced phase transition. Physical Review E. 1999;60(4):4268-71.
36. Rehage H, Hoffmann H. Rheological Properties of Viscoelastic Surfactant Systems. J Phys Chem. 1988;92(16):4712-9.
37. Rehage H, Hoffmann H. Viscoelastic Surfactant Solutions - Model Systems for Rheological Research. Mol Phys. 1991;74(5):933-73.

CHAPTER IV

VISCOSITY OF HEMOLYMPH OF ADULT BUTTERFLIES AND MOTHS

4.1 INTRODUCTION

As reviewed in chapter 1, one of the primary roles of hemolymph in adult Lepidoptera is the transport of nutrients from the fat body to the muscles. This process is aided by special multifunctional polymer particles working as the shuttles first taking the fuel in from the fat body and then carrying it to the muscles through the circulating hemolymph. These nanoparticles are identified as the high-density lipophorins (HDLP), low-density lipophorins (LDLP), apolypophorin-III (apoL-III), and lipid transfer particles (LTP) (1, 2). Typically, lipoproteins are charged (3). It has been hypothesized that apoL-III uses its charges to stabilize its coiled configuration in polar hemolymph (1, 2).

The three-dimensional atomic structure of apoL-III found in *L. migratoria* was determined using X-ray scattering (4). This analysis reveals that the apoL-III nanoparticle in the globular state is an elongated ellipsoid with an aspect ratio of about 3. HDLP and LDLP are spherical particles (5). From the data on their molecular weight, M_w, and density, D, we can estimate their volume, V, as: $V = Mw/D$ and diameter, *d*, as $d = \left(\frac{6V}{\pi}\right)^{1/3}$. For HDLP, using Mw_{HDLP} = 600 kDa (6) and D_{HDLP} = 1.15 g/ml (7), we estimate the diameter $d_{HDLP} \approx 12$ nm. This is smaller than what was reported by Ryan as measured from SEM images, $d_{HDLP} \approx 17$ nm (8). For LDLP, using Mw_{LDLP} = 1560 kDa (7, 9) and D_{LDLP} = 1.03 g/ml (7, 9), we estimate the diameter $d_{LDLP} \approx 16$ nm, which is

considerably smaller than that has been measured in *Locusts migratora*, $d_{LDLP} \approx 30$ nm (10).

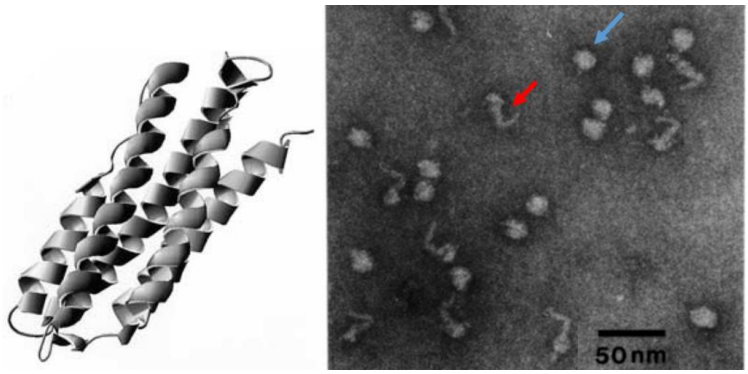

Figure 13. (left) Three-dimensional structure of apoL-III as reproduced from X-ray scattering analysis with 2.4 angstrom resolution (4). (Image reproduced from (11)) (right) SEM image of Lipid transfer particles (labeled with a red arrow) and HDLP, spherical particles of diameter d ≈ 17 nm (labeled with a blue arrow) (Image reproduces from (8)).

Concentrations of most of these constituents in hemolymph are largely documented for *M. sexta*. The mass concentration of apoL-III in adults, is $C_{A,a3}$ = 17±5 mg/ml (12). Roughly half of apoL-III, $C_{A,a3,free} = C_{A,a3,as}$ ~ 8.7 mg/ml are freely dispersed in hemolymph, and half of it is associated with LDLP. For comparison, the concentration of apoL-III in caterpillars is $C_{C,a3}$ = 0.46 mg/ml and none of it is associated with lipophorins (12). Stoichiometrically in adults of *M. sexta*, 2 apoL-III particles are associated with HDLP and 16 apoL-III are associated with LDLP, so the molarity M of these particles can be expressed as $M_{A,a3,as} = 16M_{LDLP} + 2M_{HDLP}$. Concentrations of HDLP and LDLP in hemolymph vary and depend on the particular activity of an insect. To the best of my knowledge, their total concentration has not been yet reported. When

the insect is at rest, however, a molar ratio of 10 HDLP : 1 LDLP particles is maintained, $M_{HDLP} = 10M_{LDLP}$ (13).

The concentration of LTP is be low in *Locusta migratoria*; only 160 μg was found in 400 mg of extracted protein (14). This suggests that it only serves as a catalyst and has no rheological consequences.

Summarizing available data from the literature on resting *M. sexta*, the following estimates are calculated.

From the concentration $C_{A,a3}$ and molecular weight $M_{w,a3}$ of apoL-III in adults, we calculate its molarity as: $M_{a3} = \frac{C_{A,a3}}{Mw_{a3}} = \frac{17\left[\frac{g}{L}\right]}{18100\left[\frac{g}{mol}\right]} = 0.94\left[\frac{mmol}{L}\right]$. Since half of it is associated, $M_{A,a3,as} \approx 0.5\left[\frac{mmol}{L}\right]$.

Since $M_{A,a3,as} = 16M_{LDLP} + 2M_{HDLP}$ and $M_{HDLP} = 10M_{LDLP}$,

$M_{A,a3,as} = 16M_{LDLP} + 20M_{LDLP} = 36M_{LDLP}$ and thus, $M_{LDLP} \approx 0.015\left[\frac{mmol}{L}\right]$ and $M_{HDLP} \approx 0.15\left[\frac{mmol}{L}\right]$.

We can then estimate the mass concentration of each particle as

$$C = M \cdot Mw \tag{4.1}$$

and the estimated mass concentrations of HDLP, and LDLP are $C_{HDLP} \approx 90$ mg/ml, and $C_{LDLP} \approx 23$ mg/ml.

We can then estimate the volume fraction of each particle as

$$\varphi_p = C/D \tag{4.2}$$

And the estimated volume fractions of apoL-III, HDLP, and LDLP are $\varphi_{a3,\,free} \approx 0.01$, $\varphi_{HDLP} \approx 0.08$, and $\varphi_{LDLP} \approx 0.02$.

Table 2. Literature values and our estimations of the molecular weight, density, concentration, volume fraction and particle diameter of constituents of hemolymph.

Particle	Molecular weight, Mw [kDa]	Density, D [g/ml]	Concentration in hemolymph of *M. sexta* adults, *C* [mg/ml]	Estimated volume fraction, φ_p	Estimated particle diameter, *d* [nm]
Apolipophorin-I	240 (15, 16)	N/A	N/A	N/A	N/A
Apolipophorin-II	240 (15, 16)	N/A	N/A	N/A	N/A
Apolipophorin-III	18.1 (17)	1.37[4] (17)	Total: 17±5 (12) Free: ~ 9 Associated: ~ 9	Free, estimated as: 0.01	1.8 Aspect ratio: 3 (Breiter, Kanost et al. 1991)
HDLP	600(6)	1.15 (7)	Estimated as: 90	Estimated as: 0.08	Estimated: 12 Measured: 17 (8)
LDLP	1560 (9)	1.03 (9)	Estimated as: 23	Estimated as: 0.02	Estimated: 17 Measured in *L. migratora:* 30 (10)
LTP	900 - 1400 (18)	1.23 (19)	Trace amounts (14)	~ 0	6.4-7.5

Similarly to the vertebrates, different salts are dissolved in the blood of insects. Estimated from the *Bombyx mori* data, total concentration of salts is 2.9 g/l (20).

[4] Lower-end estimate, calculated from amino acid composition

Hemolymph contains many other biopolymers carrying different functions; however, concentration of these biopolymers is much smaller and hence their contribution to viscosity is presumably insignificant. Dissociated salt ions and proteins affect the conductivity of hemolymph and significantly influence the rheological behavior of hemolymph through long range electrostatic interactions sometimes leading to the protein folding/unfolding and self-assembly into macromolecular networks.

In this chapter, we use the microrheological methodology developed in the previous chapter to probe viscous and surface properties of minute volumes of hemolymph and use them to study three species: Monarch butterfly (*Danaus plexippus*), Painted Lady butterfly (*Vanessa cardui*), and Hawkmoth (*Manduca sexta*). We hypothesize that the viscosity of hemolymph across species will increase with the volume fractions of solid particulates as well as with the amount of charged hemolymph constituents.

To evaluate this effect, we estimate the Debye length by measuring the resistivity of the liquid and apply theory described in Chapter 14 of (21). To evaluate the contribution of the other proteins in *M. sexta*, meanwhile, we assume that they constitute all currently unaccounted components with the average density of $D_{proteins} = 1.37$ g/cm^3 (22). Using the results from Table 4, this means that the concentration of these proteins is $C_{protein,other}$ = 0.04 g/ml, and the contributing volume fraction is $\varphi_{proteins,other}$ = 0.03.

4.2 THEORETICAL VISCOSITY OF A SUSPENSION

For a more comprehensive review of this topic, see (23)

Addition of particles to a liquid carrier typically increases the macroscopic viscosity of the suspension. Einstein was the first to quantitatively describe this effect considering a dilute suspension of spherical particles; then great progress has been done generalizing this theory to more concentrated dispersions (24, 25) . Elongated (26) and dumbbell-shaped (26, 27) particles significantly increase the drag force and torque, disturbing larger liquid volume during the motion. Therefore, even if present in a minute amount, elongated particles may significantly alter viscosity.

Insects, including butterflies and moths, generate minute shear stresses during locomotion and flight. Consequently, reviewing the existing theories of suspension viscosities, the zero-shear rate limit is of the main importance for us. Moreover, the volume fraction of biopolymer particles in hemolymph of adult Lepidoptera is of the order of 0.1 (Table 1). Therefore, only the limit of small concentration of spherical and elongated particles is of interest.

If a liquid carrier without particles has viscosity η_s, after addition of particles of the volume fraction φ_p, the viscosity of suspension, η, increases as

$$\eta = \eta_s \left(1 + [\eta]\varphi_p\right) \tag{4.3}$$

where $[\eta]$ is called the intrinsic viscosity *(23).* The intrinsic viscosity contribution arises from the viscous dissipation produced by the flow around a single particle. As the concentration of particles increases, the particles start to interact with each other and hence viscosity increases, which can be described by the following equation *(23)*

$$\eta = \eta_s \left(1 + [\eta]\varphi_p + k\varphi_p{}^2\right) \tag{4.4}$$

where coefficient k depends only on the particle geometry.

Hemolymph contains both spherical particles, such as LDLP and HDLP, as well as elongated particles, such as Apol-III and LTP. To specify the constants $[\eta]$ and k in eqs. (4.3) and (4.4). We therefore review the existing viscosity theories for dispersions with spherical and elongated particles

4.2.1.1 Spherical particles

For spherical particles, the intrinsic viscosity was calculated by Einstein in 1906 (24) to be $[\eta]_{sphere} = 5/2$. The second order coefficient for a scenario where convective flow was more important than Brownian motion was calculated by Batchelor in 1977 (25) as k = 6.2, making the resultant expressions for viscosity,

$$\frac{\eta}{\eta_s} = 1 + 5/2\,\varphi_p + 6.2\varphi_p^{\,2} \tag{4.5}$$

This equation well describes the data obtained for sterically stabilized polystyrene spheres of diameter d=430 nm and 870 nm up to $\varphi_p < 0.1$. In 1989, de Kruif (28) showed that a semi-empirical equation

$$\frac{\eta}{\eta_s} = \left(1 - \varphi_p / \varphi_m\right)^{-2} \tag{4.6}$$

explains viscosity of colloidal dispersions with the volume fraction of particles less than 0.6, $\varphi_p < 0.6$, irrespective of the particle size; here φ_m is the maximum packing fraction. For the low shear rate limit of interest, $\varphi_m = 0.63$ ($\varphi_m = 0.71$ for the high shear rate limit). Taylor expanding the de Kruif equation up to the 4th order

$$\frac{\eta}{\eta_s} = 1 + \frac{2}{\varphi_m}\varphi_p + \frac{3}{\varphi_m^{\,2}}\varphi_p^{\,2} + \frac{4}{\varphi_m^{\,3}}\varphi_p^{\,3} + \frac{5}{\varphi_m^{\,4}}\varphi_p^{\,4} \tag{4.7}$$

and comparing it with equation (4.6), we confirm that equation (4.7) satisfactorily describes all models for the volume fraction of particles less than $\varphi_p < 0.25$ (Figure 14).

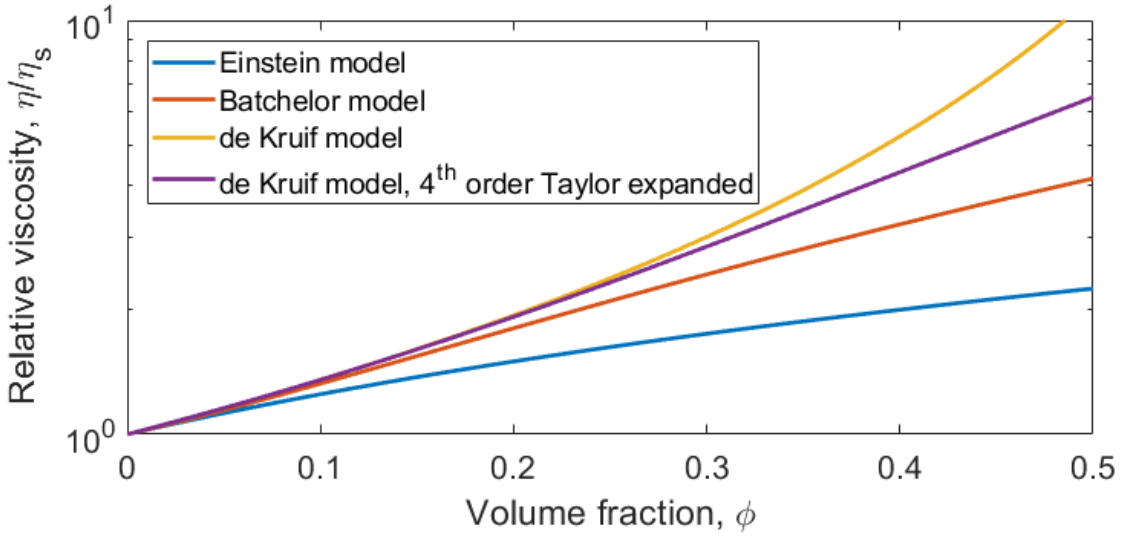

Figure 14. Dependence of relative viscosity on the volume fractions of spherical particles according to three models: Einstein, Batchelor, and de Kruif, as well as the de Kruif equation which has been Taylor expanded to the 4th order with respect to φ_p. The y-axis (η/η_s) is logarithmic.

4.2.1.2 Elongated particles

Consider an elliptical spheroid with an aspect ratio $p = l/d$, where d is the diameter of the particle and l is its length. Hinch and Leal (29) calculated the intrinsic viscosity to be $[\eta] = \frac{5}{2} + 0.777\varepsilon$ for a spheroid of a small aspect ratio, p=1+ε, where $\varepsilon < 1$ and $[\eta] = \frac{4p^2}{15\ln(p)}$ for $p \to \infty$. Following Doi and Edwards (30) we can find the intrinsic viscosity for cylindrical particles to be

$$[\eta] = \frac{8}{45} p^2 \left(1 - \frac{1}{p^4}\right)\left(\frac{2p^2 - 1}{2p(p^2-1)^{1/2}} \ln \frac{p + (p^2-1)^{1/2}}{p - (p^2-1)^{1/2}} - 1\right)^{-1} \quad (4.8)$$

For elongated particles, the particle-particles interactions are expected to play a role when the particles can no longer rotate freely, or when the number concentration of rods *v* reaches a value proportional to L^3, where L is the length of the particle. It has been experimentally shown (31) that the proportionality constant is roughly 30, meaning that the transition occurs when $\varphi_p \approx 30\pi d^2 / 4L^2 = 24\left(d / L\right)^2$. The concentration of known elongated particles present in hemolymph (apoL-III) is lower than the expected transition concentration; thus no particle-particle interactions will be considered.

The intrinsic viscosity of isolated *M. sexta* apoL-III particles in a sodium phosphate buffer of pH 7.0 has been previously measured to be $\left[\eta_{apoLIII}\right]$ = 5.98± 0.09 (32). This value corresponds to a cylinder with the aspect ratio of 4.1 using the Doi Edwards model (4.8). The discrepancy between the direct measurement and the inferred measurement via intrinsic viscosity could be due to the effect of surface charge of the particle, which would increase the apparent size and volume fraction of the particle. We discuss this phenomenon in the next section.

4.2.1.3 Effect of charge of spherical particles on viscosity

Any surface charge present on the suspended particles changes the viscosity of the liquid. This happens because the charge changes the effective size of the particles suspended in the liquid, which, in turn, changes the effective maximum packing factor. Following the logic of Ref. (21), we arrive at the conclusion that the maximum packing factor and the effective volume fraction of charged particles at low shear rates scale as

$$\varphi_m = 0.63\left(2r/b\right)^3$$
$$\varphi_{eff} = \left(2r/b\right)^{-3}\varphi_p \tag{4.9}$$

respectively, where r is the particle radius, and

$$b = \kappa^{-1}\ln\left(\alpha/\ln\left[\alpha/\ln\left\{\alpha/...\right\}\right]\right)$$
$$\alpha = 4\pi\varepsilon_0\varepsilon_s{\psi_s}^2 r^2\kappa\exp\left(2r\kappa\right)/k_B T \tag{4.10}$$

where $\kappa^{-1} = \sqrt{\frac{\varepsilon_0\varepsilon_s kT}{2N_A e^2 I}}$ is the Debye length, ε_0 is the permittivity of free space, ε_s is the dielectric constant of the solvent, ψ_s is the surface potential, k_B is the Boltzmann constant, and T is the temperature, N_A is the Avogadro's number, e is the elementary charge, and I is the ionic strength of the liquid. For aqueous solutions at room temperature, $\kappa^{-1} = \frac{0.304}{\sqrt{I}}$ and the ionic strength is expressed in mol/L. In an unknown solution, the Debye length can be calculated from the measured resistivity, ρ, as (33):

$$\kappa^{-1} = \sqrt{\varepsilon_0 D_i \rho} \tag{4.11}$$

where D_i is the diffusion coefficient of the ions, which in aqueous solutions ranges between $0.6*10^{-9}$ to $2*10^{-9}$ m^2/s (34).

At $\varphi_p < \varphi_m$ the system follows equation (4.6) with a corrected effective packing fraction fairly well (21) :

$$\frac{\eta_{charged}}{\eta_s} = 1 + \frac{2}{\varphi_m\left(2r/d\right)^3}\varphi_p + \frac{3}{{\varphi_m}^2\left(2r/d\right)^6}{\varphi_p}^2 + O\left({\varphi_p}^3\right) \tag{4.12}$$

We can numerically analyze the dependence of the relative viscosity on the volume fraction at different resisivities of the solution (Figure 15, left) and on the surface charge of the particles at different volume fraction of charged particles (Figure 15, right).

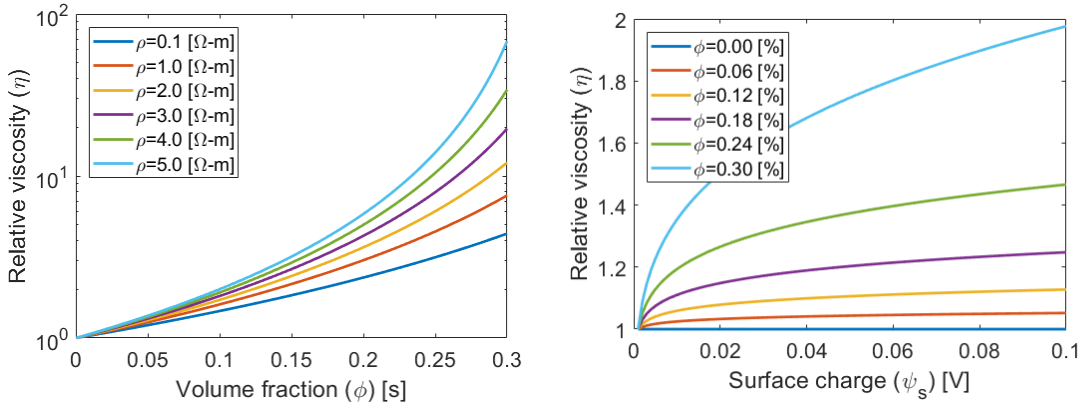

Figure 15. (Left) A plot of relative viscosity as a function of volume fraction of charged particles at different resisitivities of the liquid and surface potential ψ_s = 50 mV. (Right) A plot of relative viscosity as a function of surface charge on the particles at different volume fractions of the charged particles and resistivity ρ= 2 (Ω-m). All calculations performed for the particles of radius r =10 nm,

At the volume fractions above the threshold packing fraction, $\varphi_p > \varphi_m$, a phase transition occurs, and the dispersion behaves like a viscoelastic solid with the shear modulus dependent on the volume fraction, particle size, and ionic strength. (21) This behavior lies outside the scope of this work and will not be described further.

4.2.2 Expected viscosity of hemolymph

As discussed, hemolymph is a mixture of different particles that differ in size, aspect ratio, and surface charge. When spherical and elongated charged particles, are mixed together in a suspension, each particle interacts with the liquid and sometimes with other particles. The interaction between the particle and the liquid depends on the shape and the surface charge of the particle as well as the Debye length of the liquid.

According to (25), these particle-particle interactions cause second – or higher – order dependencies of φ_p. The coefficient of interaction between spherical particles is irrespective of the size (25). Determination of the interaction coefficient between

elongated and spherical particles requires analysis of interparticle polarization and collisions, which is out of the scope of this work. Instead, we assume that the coefficient of particle-particle interaction is the same across all particles. We apply this logic to the Taylor expanded de Kruif model, and assume that any interactions of $O(\varphi_p^2)$ or higher follow the rules of spherical particle interactions. Thus, the expression for the estimated viscosity of hemolymph, η_h, thus becomes

$$\frac{\eta_h}{\eta_w} = 1 + \sum_i [\eta_i]\varphi_i + f(\varphi_{tot})$$
$$f(\varphi_{tot}) = \frac{3}{\varphi_m{}^2}\varphi_{tot}{}^2 + \frac{4}{\varphi_m{}^3}\varphi_{tot}{}^3 + \frac{5}{\varphi_m{}^4}\varphi_{tot}{}^4 \quad (4.13)$$

where φ_{tot} is the total volume fraction of particles. Since hemolymph has multiple components of different mass fractions and densities, the challenge now becomes finding the values of all φ_i and φ_{tot}. Since a lot of data is available for the composition of the lipid transfer system in *M. sexta*, we are able to specify the contribution of HDLP, LDLP, and apoLIII explicitly. For the estimation purposes, we can treat the rest of the constituents as black-box 'protein'. The prediction for viscosity of hemolymph of *M. sexta* disregarding all charge effects thus becomes:

$$\frac{\eta_h}{\eta_w} = 1 + [\eta_{sphere}](\varphi_{HDLP} + \varphi_{LDLP} + \varphi_{protein}) + [\eta_{apoLIII}]\varphi_{apoLIII} + f(\varphi_{tot}) \quad (4.14)$$

where $[\eta_{sphere}] = 2/\varphi_m = 3.17$ and $[\eta_{apoLIII}] = 5.98 \pm 0.09$ (32).

Some proteins in hemolymph are charged and are believed to use their charge to stabilize themselves (15, 35, 36). Since the surface charge of spherical particles changes

the effective particle size (21), the same argument can be made for elongated particles with a small aspect ratio, such as apoliopophorin-III. The surface charges of individual particles have not been determined. Instead, we will assume that all particles have some average surface charge. Thus, for the particles in hemolymph, the effective volume fraction of each type of particle will be adjusted as $\varphi_{i,eff} = \varphi_i \left(2r_i / b_i\right)^{-3}$.

Thus, the expression for the viscosity of hemolymph in terms of its known constituents is:

$$\frac{\eta_h}{\eta_w} = 1 + \left[\eta_{sphere}\right]\left(\frac{\varphi_{HDLP}}{\left(2r_{HDLP}/b_{HDLP}\right)^3} + \frac{\varphi_{LDLP}}{\left(2r_{LDLP}/b_{LDLP}\right)^3} + \frac{\varphi_{protein}}{\left(2r_{protein}/b_{protein}\right)^3}\right) + \left[\eta_{apoLIII}\right]\frac{\varphi_{apoLIII}}{\left(2r_{apoLIII}/b_{apoLIII}\right)^3} + f\left(\frac{\varphi_{tot}}{\left(2r_{average}/b_{average}\right)^3}\right) \quad (4.15)$$

where $r_{average}$ is the average radius of particles in the sample and $b_{average}$ is a function of $r_{average}$.

4.3 EXPERIMENTAL RESULTS

Viscosity of hemolymph droplets of two butterflies (*D. plexippus* and *V. cardui)* and one moth (*M. sexta*) were measured. The droplets were placed on the MRS stage and covered with a cap; a nitrogen gas of 100% water vapor humidity was continuously flashed through the chamber as discussed in Chapter 3. To verify the hemolymph stability against coagulation or droplet evaporation, the viscosity was measured as a function of time for 35 minutes. The stability experiment (Figure 16, insert) revealed that the viscosity remains stable for about 17 minutes before it started rapidly increasing. The

viscosity that was measured during this stable time period was considered as the viscosity of the unchanged hemolymph and was compared across the species; the data that were obtained after the stable period were disregarded. The number of measurements that were performed is presented in Table 3.

Table 3. The number of adult specimens studied, number of probes used, and the number of measurements performed during the whole study as well as during the time, in which the sample was stable.

		D. plexippus (Monarch)	*V. Cardui* (Painted Lady)	*M. sexta* (Hawkmoth)
Collected within the stable time segment	# of insects	5	8	10
	# of nanorods	9	11	16
	# of hemolymph droplets	90	22	94
Total samples collected within the stable and the unstable segments	# of insects	6	8	10
	# of nanorods	12	12	16
	# of hemolymph droplets	134	45	120

The hemolymph viscosity during the stable regime of *D. plexippus* and *V. cardui*, and *M. sexta* was η = 1.4± 0.5 mPa*s, 1.6± 0.5 mPa*s, and 2.4± 1 mPa*s respectively. The results are demonstrated in Figure 1.b. The error bars represent the standard deviation of the measurements, calculated from the statistical distribution of the results. The statistical significance of the results against the viscosity of DI water (results obtained in chapter 3) was determined using the 1-way t-test and the results are presented above the bar graphs in Figure 16.

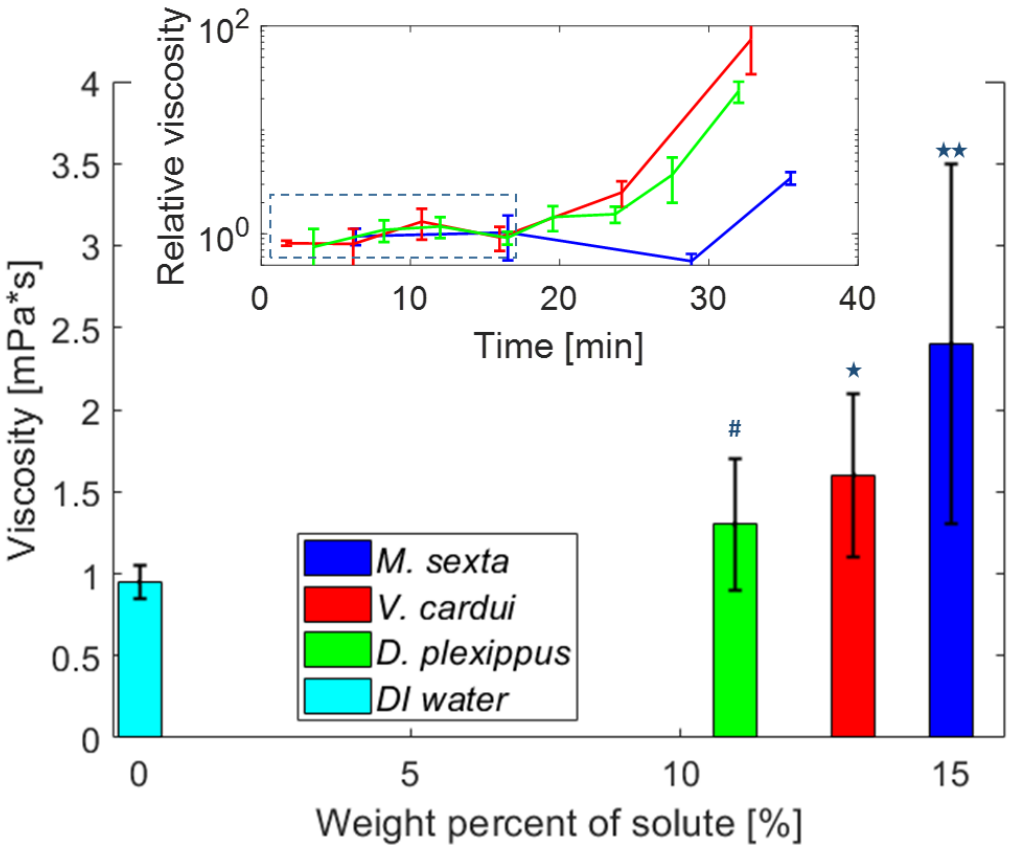

Figure 16. Comparison of the measured hemolymph viscosity values for adult *M. sexta*, *V. cardui*, and *D. plexippus*. All measurements were made during the stable viscosity window of time. (insert) The relative viscosity vs time of hemolymph of the three species. The viscosity remains stable during the first 17 minutes of testing. Statistical significance was analyzed with a 1-way t-test against DI water measured with the same method at the same conditions. # - no statistical difference ($p' > 0.05$). * - statistical difference with $p' < 0.05$. ** - statistical difference with $p' < 0.01$.

To determine the causes of increased viscosity of hemolymph in different species, we analyzed the solute mass fraction w, the resistivity ρ, the concentration of proteins C_p, and the particle size distribution. The results are presented in Table 4.

Table 4. The solute mass fraction obtained from drying of hemolymph samples, the concentration of proteins obtained from a UV-vis spectrum, average particle radius obtained from dynamic light scattering, and the resistivity of hemolymph of adults of three species of Lepidoptera: *M. sexta*, *V. cardui*, and *D. plexippus*. The total number of samples produced from the number of specimen studied is indicated under the results.

	D. plexippus (Monarch)	*V. cardui* (Painted Lady)	*M. sexta* (Hawkmoth)
Solute mass fraction, *w* (wt%)	0.108±0.009	0.127±0.013	0.150±0.015
N (insects : droplets)	(3:9)	(3:9)	(3:10)
Concentration of proteins, C_p (UV-Vis) [mg/ml]	90±40	Not studied	130±10
N (insects : droplets)	(1:1)	(0:0)	(1:1)
Average particle diameter, d (DLS) [nm]	6.1±0.3	7±0.5	8.2±0.6
N (insects : droplets)	(2:8)	(2:8)	(3:28)
Resistivity, ρ [ohm-m]	Not studied	1.3	1.6±0.1
N (insects : droplets)	(4:6)	(1:1)	(0:0)

Due to the adherent nature of some hemocytes, they sometimes attached themselves to the probes. When that happened, the hemocyte began rotating with the probe. Figure 17 A, illustrates an example of such a behavior in the hemolymph of painted ladies where six hemocytes adhered to two probes. One batch of the studied *D. plexippus* had an increased cell count, which was most likely caused by a disease. In those samples, the cells have been adhering to the probes and to each other, forming large networks; an example of this in presented in Figure 17 B. This phenomenon is predominant in clotting of hemolymph of caterpillars, where the hemocyte count is much higher than that in adults. We study this in detail in the next chapter.

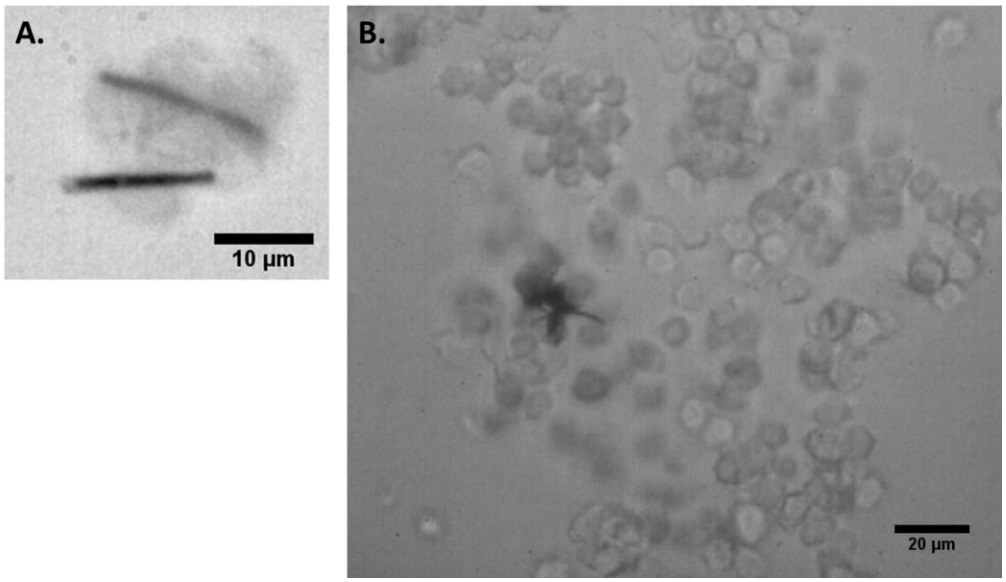

Figure 17. Hemocytes adhering to the nanoprobes in samples of hemolymph of (A) adult *V. cardui*, (B) presumably diseased adult *D. plexippus*, exhibiting an abundancy of hemocytes.

4.4 DISCUSSION

Having measured the viscosity and resistivity of hemolymph, the average size of particles and the concentration of proteins for three species of Lepidoptera, we can evaluate the significance of several physical parameters on the overall viscosity. Namely, we calculate the expected viscosity for the three species using Batchelor's and de Kruif's approximations (equations (4.5) and (4.6)), which assume that all particles are spherical. To allow for comparison across species, we assume that the density of all the solutes is the same, $D_{solutes} = D_{proteins} = 1.37$ mg/ml, as suggested by (22). The models describe the measured viscosities in *D. plexippus* and *V. cardui* well, but fall short in describing the viscosity of *M. sexta* (Table 5).

Table 5. Estimated viscosity of the three species, according to the Batchelor and the De Kruif models. The mass fractions were converted to volume fractions by assuming that all constituents are proteins with a density of 1.37 mg/ml (22). The units of calculated viscosity are mPa-s.

	D. plexippus (Monarch)	*V. cardui* (Painted Lady)	*M. sexta* (Hawkmoth)
Batchelor, equation (4.5)	1.4	1.5	1.6
de Kruif, equation (4.7)	1.4	1.6	1.7

Better knowledge of the constituents of hemolymph in *M. sexta* that are responsible for energy transfer allows us to better estimate the viscosity of hemolymph of that species and look closely at the contributions of each constituent to the total viscosity. We first use equation (4.14) along with the densities and the estimated volume fractions from Table 2 and the intrinsic viscosity of apoL-III obtained by Kawooya *et al*. to be $\left[\eta_{apoLIII}\right]$ = 5.98 ± 0.09 (32). Overall, the model does not predict the viscosity of *M. sexta* any better than the simplified Batchelor or De Kruif models.

Using the same parameters, but taking into account the conductivity of the liquid and the surface charge of the particles with equation (4.15) yield much more promising results. Due to the lack of information on the surface charges of the constituent particles in hemolymph, we cannot directly use the charged particle model to predict the viscosity. Instead, we use the measured viscosity and conductivity of hemolymph of *M. sexta* and assume that an average particle surface potential is in the millivolt range (Figure 18). We then find the surface potential that results in the average measured value of viscosity to

be 7 mV, which is similar to the surface charge of serum lipoproteins (3). The contributions of the known constituent particles are presented in Table 6. According to this model, the interactions between the energy carriers and the liquid constitute roughly 80% of the viscosity increase.

Table 6. Estimated viscosity from equations (4.14) and (4.15). The units of calculated viscosity are mPa-s

	apoL-III ($\eta_{apoLIII}$)	HDLP (η_{HDLP})	LDLP (η_{LDLP})	remaining protein ($\eta_{protein}$)	particle-particle f(φ_{tot})	total ($\eta_{hemolymph}$)
Non-charged, eq (4.14)	0.03	0.25	0.07	0.09	0.19	1.6
Charged, eq (4.15)	0.10	0.42	0.10	0.14	0.64	2.4

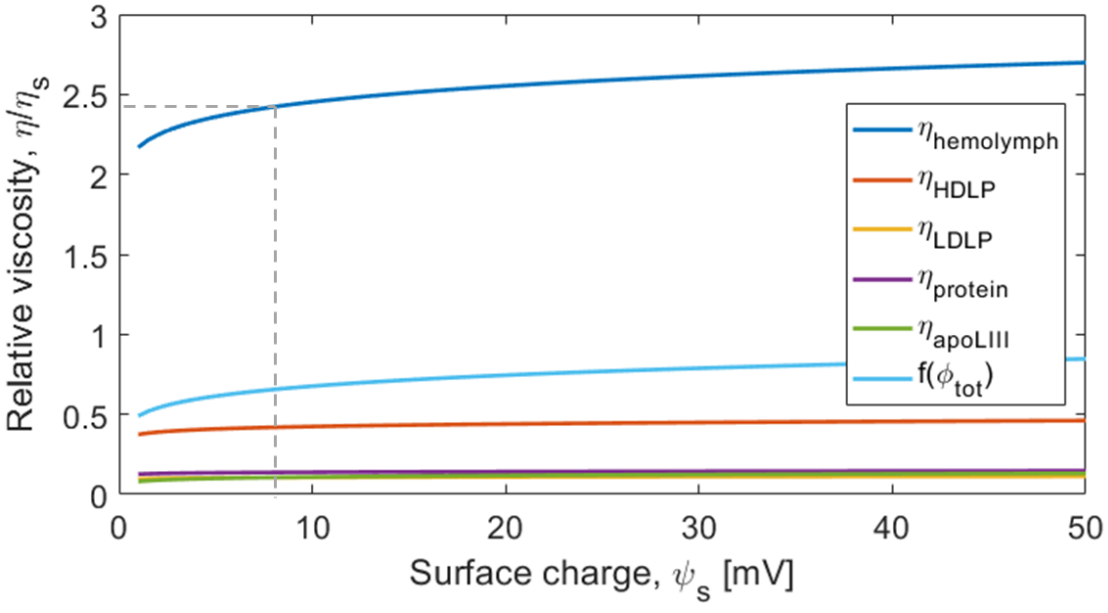

Figure 18. Dependency on the predicted viscosity of hemolymph of *M. sexta* – as well as partial viscosity contributions of the hemolymph constituent particles – on the average

surface charge of the particles. The measured value of viscosity (2.4) corresponds to 7 mV average charge.

The fact that the viscosity of the two butterflies, *V. cardui*, and *D. plexippus*, can be described by a model that ignores charged particles leads one to believe that the average charge of the particles is low. This could either be due to the charged particles themselves having a structure that leads to a lower surface charge than that in *M. sexta* or that the charged particles having the same structure, but with the concentration of the charged particles much lower. The second scenario is more likely and could be explained by a supposition that the lipid carrying particles are the main source of surface charge. Then, since the heavier *M. sexta* moth requires more energy to fly than the lighter butterflies, the concentration of charged lipoproteins is higher. We check this hypothesis in chapter 10 by studying the surface properties of hemolymph: since lipoproteins are surface active, their higher amount should more greatly affect the surface tension of the liquid.

4.5 CONCLUSION

We have measured the micro-scale viscosity of hemolymph of three species of Lepidoptera, *M. sexta*, *V. cardui*, and *D. plexippus*, using modified MRS. We have used several rheological models to describe the measured viscosity in the context of what is known about hemolymph constituents. To aid these theoretical descriptions, we have also measured the mass fraction of solutes in hemolymph by evaporating water from hemolymph, the concentration of proteins from UV-Vis spectral analysis, and the Debye length of the liquid from resistivity measurements. We have found out that the viscosity

of hemolymph of lighter butterflies, *V. cardui*, and *D. plexippus*, can be described using models of solid particle suspensions, while the viscosity of hemolymph of heavier *M. sexta* moths can only be explained by taking the charge of these particles and the Debye length of the liquid into account. This leads to a supposition that the concentration of charged particles in the hemolymph of the moth is much higher that of lighter butterflies, presumably due to higher energy requirements for flight.

4.6 MATERIALS AND METHODS

4.6.1 Viscosity measurement of hemolymph

The measurement of viscosity of hemolymph was performed with the modified MRS method (discussed in detail in chapter 3), which is capable of measuring a mPa·s level viscosity of nanoliter droplets and micron thick films in a 10-20 second timeframe. The method is based on tracking and analyzing the rotation of nickel nanoprobes suspended in the liquid sample and rotated with a rotating magnetic field.

4.6.2 Sample preparation for MRS

To prepare a sample of hemolymph for MRS, a slide with a well was cleaned and placed in the magnetic stage. A 20 μL of methanol with suspended nanorods was sonicated and placed on the side. The methanol was allowed to evaporate, leaving the nanorods on the slide. The environmental chamber was then fastened to the stage and one hundred percent humid nitrogen was passed through it. After allowing the chamber to come to equilibrium, hemolymph was pipetted from a capillary tube onto the glass slide with the nanorods. Special care was taken to ensure that no air bubbles were created in

the sample during this deposition. The hemolymph was agitated to evenly disperse the rods using a clean glass rod.

4.6.2.1 Extraction of hemolymph

Traditionally, extraction of hemolymph for biochemical analysis was done by first decapitating the insect, placing the insect into the desired solution, and centrifuging the insect. For the study of physical properties, it was necessary to extract undiluted hemolymph and either work with it as such, or dilute it at known dilutions. Furthermore, it was important to minimize the contamination of the sample with scales. Thus, new extraction procedures were developed for each species.

Insects were restrained at the wings with a clothes pin to prevent excessive movement and scale contamination. An incision was made and the hemolymph was collected using capillary action of a 5 μl or 20 μl capillary tube (Durmmond, 1-000-0050 or 3-000-210, respectively) immediately upon exiting the body. The details of extraction protocol for both butterflies and moths are presented in Figure 1.

Typically, in both species of butterflies studied, hemolymph began exiting the body immediately after the incision and forms a small droplet at the wound. The flow rate of hemolymph and the volume of the droplet, however, varies between specimens. This produces a challenge during collection. When the volume of the droplet is not sufficient to form a meniscus on the internal wall of the capillary tube, capillary action does not occur and no hemolymph can be collected. In that case, a capillary tube with a smaller inner diameter needs to be used. Once the meniscus forms and capillary action occurs, however, 0.5-3 microliters of hemolymph can be collected. This process can take

between 5 seconds to several minutes, depending on the flow rate of hemolymph as it exits the body. Once inside the capillary tube, the collected hemolymph is not exposed to the atmosphere and does not change its color or properties for tens of minutes, suggesting that it undergoes no evaporation or oxidation.

The measurements for *M. sexta* moths were particularly challenging due the moth's inability to re-hydrate in lab conditions. This led to a quick dehydration of the specimen and, consequently, a low success rate of its hemolymph extraction; it was only possible to extract hemolymph from roughly 30% of specimens within 2-3 days from emergence. Extractable volumes of hemolymph ranged from 0.5μl to 30 μl for this specie.

Color of hemolymph varied across insects. In Painted ladies, the color varied between dark green and light yellow; in monarch, the color varied between light blue and green; in *M. sexta*, the color was light green.

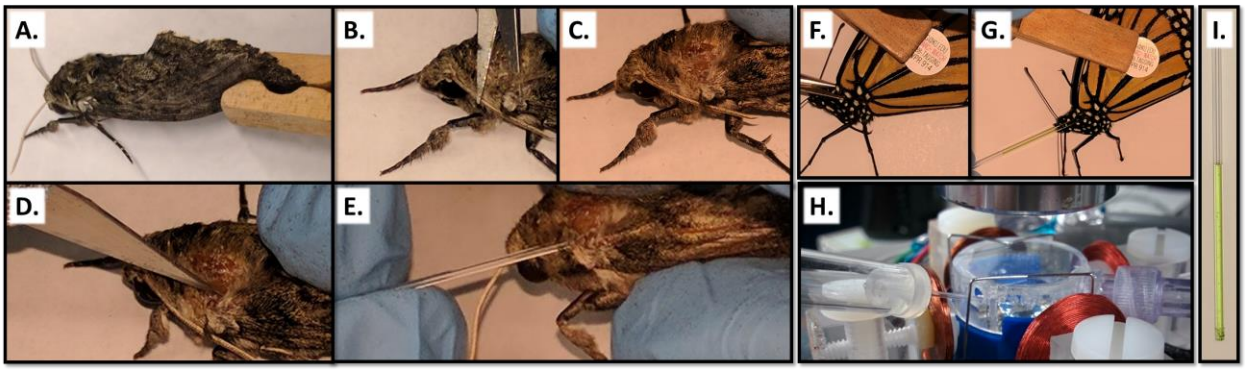

Figure 19. (A-E) Extraction protocol for hemolymph from *M. sexta* moths. (A) The moths were restrained with their wings down, exposing the dorsal thorax. (B) The tegulum was removed with surgical scissors, thus removing scales and exposing (C) the sclerotized thorax. (D) An incision was made between the sclerotized thorax and the wing at the wing articulation membrane using a razor blade. (E) Hemolymph was collected by placing the tip of the capillary tube underneath the articulation membrane through the insision. (F-G) Extraction protocol for hemolymph from painted lady and monarch

butterflies. (F) The butterflies were restrained with their wings pointing up exposing the base of the wing. The incision was then performed at the base of the wing with surgical scissors. (G) Hemolymph was collected using a capillary tube from the beading hemolymph at the wound cite. (H) Hemolymph was delivered from the capillary tube to the experimental setup using a capillary micropipette (Drummond, 1-000-0050). (I) A photograph of *M. sexta* hemolymph in a 5µl capillary tube.

4.6.2.2 Dispersion of probes in the sample

To perform a measurement, magnetic nanorods needed to be dispersed in hemolymph in the following manner. The nanorods were first dispersed in methanol by sonication. A droplet of nanorod-methanol suspension was placed on a glass slide and allowed to dry at room conditions. The nanorods remained, weakly attached to the glass slide with Van der Waals forces. Hemolymph was then deposited on the glass slide from the capillary tube and stirred with a glass rod, dispersing the nanorods. A rotating magnetic field of 300 μT in amplitude and 9-15 Hz in frequency was applied to rotate the probes in their asynchronous regime. The rotation was recorded and analyzed to extract the critical frequency ω_c, from which the viscosity was calculated using (equation).

4.6.2.3 Stabilization of the sample during viscosity measurement

To control for oxidation and evaporation of the sample during measurement, two methods were used. The first method consisted of placing the sample between a glass slide with a 40 um well and a cover slip. This method relied on the fact that surface interaction only happened at the edges of the sample; far away from the edge of the sample, however, the sample demonstrated no color, texture, or viscosity change for almost two hours. This method was used only for preliminary studies as it yielded low success rates of the measurement.

The second method consisted of placing the sample in a custom-made environmental chamber designed to fit together with the magnetic stage (see chapter 2 for details). The chamber had an inlet port for a supplied gas of controlled composition to enter and an outlet port for the gas to exit. The outlet port also acted as an access aperture, allowing one to have access to the sample during the operation of the chamber. During the operation, a flow of pure nitrogen gas was bubbled through DI water to saturate it with water vapor and passed through the environmental chamber and over the surface of the sample. As a result of this, no oxidation occurred, which was verified by the absence of color change in the sample during experiment. Due to the water vapor in the nitrogen, evaporation was also significantly slowed down. This was verified by relative viscosity vs. time plot (Figure 16), which indicates no viscosity change over a 20-minute period.

Even though the second method provided a shorter time frame of sample stability, it was the method of choice, because it resulted in a sample of larger thickness. This allowed the nanorods to rotate farther away from the substrate, preventing their undesired adhesion to it. In cases when nanorods did adhere to the substrate, the open surface of the sample and the access aperture allowed for additional stirring of the sample to re-disperse the nanorods. Thus, the second method of sample control yielded more successful measurements. All *M. sexta*, *D. plexupus*, and *V. cardui* and monarch as well as most painted lady samples were measured with this method. Two samples of painted lady were measured using the first method during the preliminary study; since the age of those specimen was not tracked, however, the measurements of those two specimen are of

limited use to the biological community. Nevertheless, the viscosity of the painted lady hemolymph was the same across both methods.

4.6.3 Solute mass concentration and volume fraction measurement

To evaluate whether the viscosity could be simply explained by the Batchelor or the de Kruif relations, the mass fraction of the solute in hemolymph was measured and the volume fraction was estimated. For these models, these estimations were used instead of more accurate data presented in Table 5; the more accurate data are not available for *V. cardui* and *D. plexippus*. This approximation thus allows us to compare all three species.

The mass fraction is calculated by first measuring the mass of a sample of extracted hemolymph, m_h, dehydrating the sample, and measuring the mass of the solid remains, m_s. The mass of the water is then equal to $m_w = m_h - m_s$ and the mass fraction of the solute is then calculated as $\omega_s = \frac{m_s}{m_h}$.

The volume fraction was estimated from the assumption that polymers constitute most of the solute mass in hemolymph and have the average density of $D_{proteins} = 1.37$ g/cm^3 (22). With this assumption, the volume fraction was calculated from the mass of water and the mass of the solute as $\varphi_p = \frac{m_p / D_{proteins}}{m_p / D_{proteins} + m_H / D_H}$ where m_p and m_H are the masses of protein and water in a given sample of hemolymph, respectively; $D_{proteins}$ and D_H are the densities of protein and water, respectively.

4.6.3.1 Evaporation under vacuum

To determine the masses of water and solute in samples of hemolymph across species, the following procedure was used. First, hemolymph was extracted using a capillary tube. A metal TGA pan was weighted on a microbalance (Sartorius, MP210S). A droplet of hemolymph was placed on the pan and weighted within 10 seconds of deposition, providing the initial wet mass of the sample, m_h. The sample was placed in vacuum overnight and weighted again, providing the mass of the solid material, m_s.

At least nine samples from three specimens of each species were measured in this manner.

4.6.3.2 Dry sample thermal gravimetric analysis (TGA)

Thermal gravimetric analysis is a thermal analytic technique that tracks the mass of the sample in response to a changing ambient temperature. The thermally calibrated microbalance is located in a temperature-controlled environmental chamber actively flushed with dry nitrogen. As the temperature in the chamber is increased, the sample vaporizes and changes in mass. The temperature and the mass of the sample are tracked as a function of time. In our case, TGA was performed on the samples that underwent evaporation under vacuum overnight. This measurement was used to quantify how much water remained trapped in the sample after evaporation in vacuum. AutoTGA 295 was used to perform this analysis.

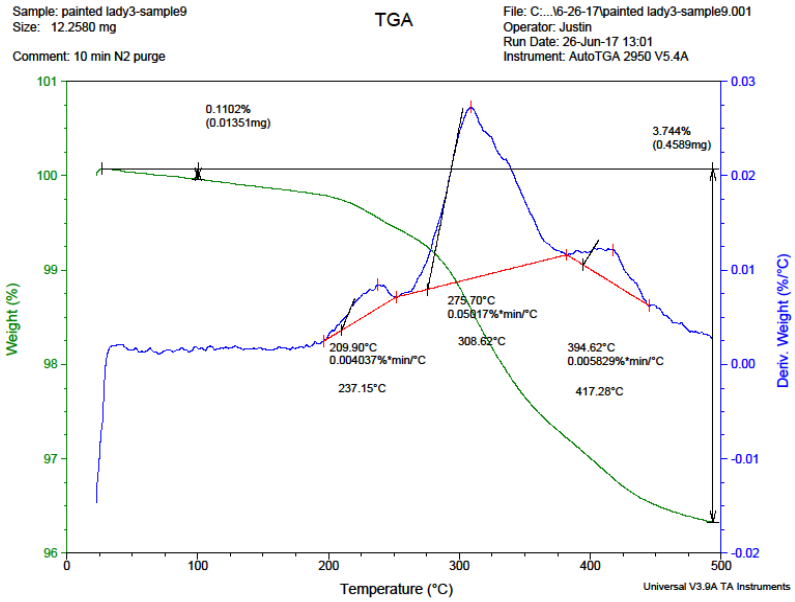
Sample: painted lady3-sample9
Size: 12.2580 mg
Comment: 10 min N2 purge
TGA
File: C:...\6-26-17\painted lady3-sample9.001
Operator: Justin
Run Date: 26-Jun-17 13:01
Instrument: AutoTGA 2950 V5.4A
0.1102%
(0.01351mg)
3.744%
(0.4589mg)
275.70°C
0.05817%*min/°C
308.62°C
209.90°C
0.004037%*min/°C
237.15°C
394.62°C
0.005829%*min/°C
417.28°C
Weight (%)
Deriv. Weight (%/°C)
Temperature (°C)
Universal V3.9A TA Instruments

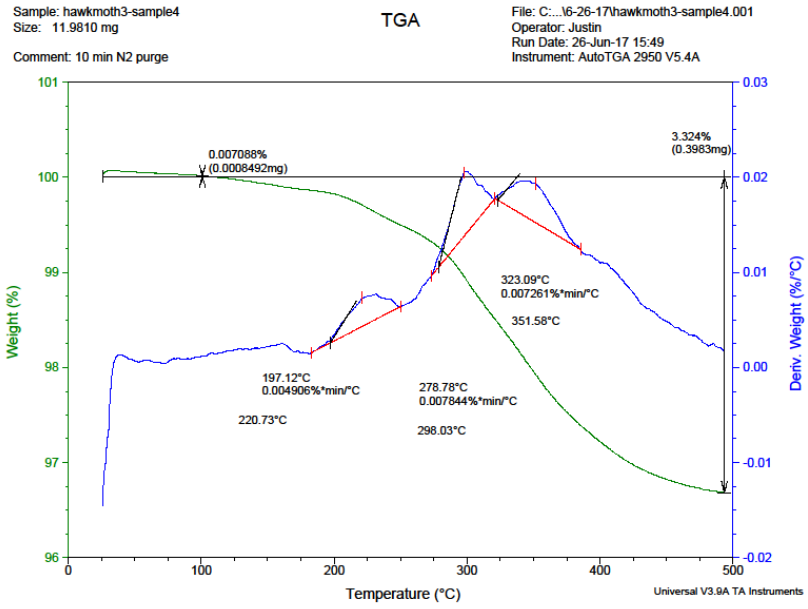
Sample: hawkmoth3-sample4
Size: 11.9810 mg
Comment: 10 min N2 purge
TGA
File: C:...\6-26-17\hawkmoth3-sample4.001
Operator: Justin
Run Date: 26-Jun-17 15:49
Instrument: AutoTGA 2950 V5.4A
0.007088%
(0.0008492mg)
3.324%
(0.3983mg)
323.09°C
0.007261%*min/°C
351.58°C
197.12°C
0.004906%*min/°C
220.73°C
278.78°C
0.007844%*min/°C
298.03°C
Weight (%)
Deriv. Weight (%/°C)
Temperature (°C)
Universal V3.9A TA Instruments

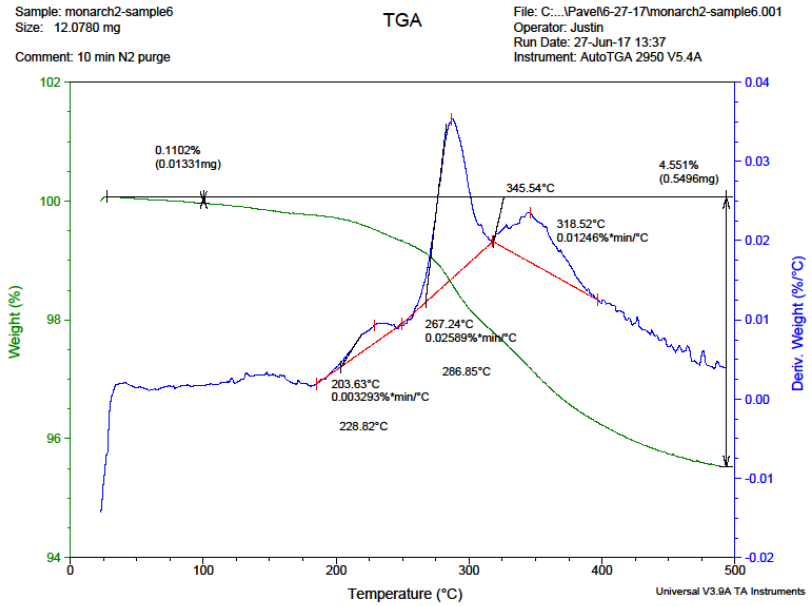

Figure 20. Illustrative TGA profiles of hemolymph of each of the studied species.

4.6.4 Conductivity measurement

The sample resistivity was measured in the AC regime using a high-performance potentiostat (Gamry Instruments, Reference 3000) in the following way. Hemolymph from *M. sexta* moths was collected into capillary tubes (Drummond, 3-000-210-G) using the method described in Section 4.6.2.1. Copper wires (360 um in diameter) were inserted into the capillary tube from each end, such that one of their stripped ends rested in the liquid and acted as electrodes. The other ends of the wires were attached to the potentiostat in an open circuit configuration. Care was taken to make sure that no air bubbles were formed between the two copper wire electrodes. During the measurement, the resistivity was measured as the function of frequency of the applied potential across the electrodes.

The response was measured as a complex value of impedance, where the reactive impedance is the imaginary component and the resistive impedance is the real

component. The measured signal was a sum of the impedances of both the electrode and the liquid. At higher frequencies, the response of the electrodes contributed both imaginary and real components of impedance. As the frequency was lowered, the response of the electrode decreased until 0. Since the liquid does not have any reactive impedance, when the measured reactive impedance was 0, the signal was known to only be a representation of the liquid response. The resistance was measured at that frequency. The sample conductivity was then calculated as $\sigma = \rho A/l$, where ρ is resistivity of the sample, A is the cross-sectional area of the sample and l is the distance between the two copper wire electrodes.

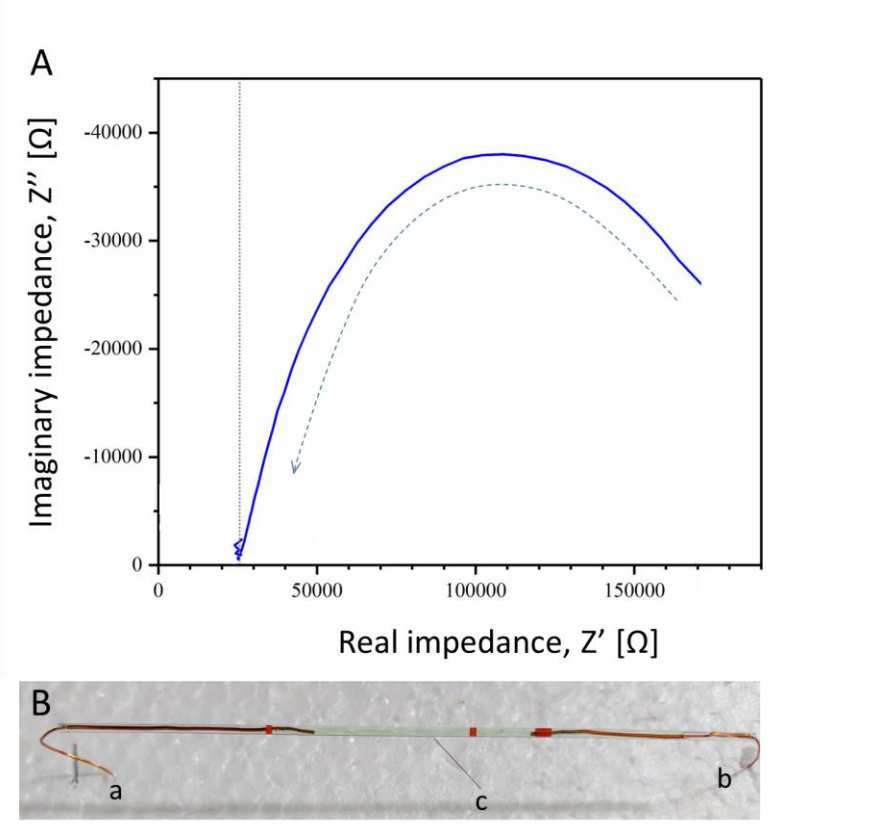

Figure 21. (A) A sample measurement of resistivity of the hemolymph of adult *M. sexta*. The vertical grey dashed line indicated the resistance of the liquid, while the curve to the

right of the dashed line indicates the complex response of the probe-liquid system. The dashed arrow shows the direction of the measurement during the frequency decrease. (B) A photograph of the experimental set-up. (a) and (b) mark the two copper wire electrodes, whose ends are submerged in (c) hemolymph inside the capillary tube. The distance between the ends of the electrodes is determined using image analysis in ImageJ.

4.6.5 Dynamic Light Scattering to determine the size of particulates

4.6.5.1 Methodology

Dynamic light scattering was performed to measure the size and verify the concentration of protein coils in hemolymph. DLS was performed on *M. sexta* hemolymph samples using Malvern Zetasizer Nano ZS. Hemolymph was extracted and diluted in water and 7.2pH phosphate buffer solution (PBS). When diluted with water, the proteins precipitated and made the measurement impossible. When diluted with PBS, no precipitation occurred and the coil radius was successfully measured. A total of 5 samples were measured from 3 specimens of *M. sexta* moths, 3 samples were measured from 3 specimens of *V. cardui* butterflies, and 3 samples were measured from 3 specimens of *D. plexippus* butterflies.

4.6.5.2 Sample preparation

For each sample, 10-15 microliters of hemolymph were diluted in 2 ml of PBS, thus yielding the dilution ratio, D_r, ranging from 130 to 200. Since the DLS experiment yields a measure of the volume fraction of proteins of a given size in the diluted sample, φ_d, the volume fraction of these proteins in the undiluted hemolymph, φ_p, can be calculated as $\varphi_p = \varphi_d D_r$.

4.6.6 UV-VIS Spectroscopy to determine the relative concentration of proteins

4.6.6.1 Methodology

UV-visible absorption spectrum was measured for diluted hemolymph of each species to determine the concentration of protein in the sample, following the methodology described in (37). The method is based on the tendency of proteins to absorb light at 205 and 280 nm. At ranges of absorbance below 2, the concentration of polymer scales linearly with the absorbance, *A*, following the following relations:

$$C_{protein} \approx A_{280\,nm} \tag{4.16}$$

$$C_{protein} \approx A_{205} / 31 \tag{4.17}$$

Where $C_{protein}$ is the concentration of protein in mg/ml and A is the absorbance of the sample at that wavelength.

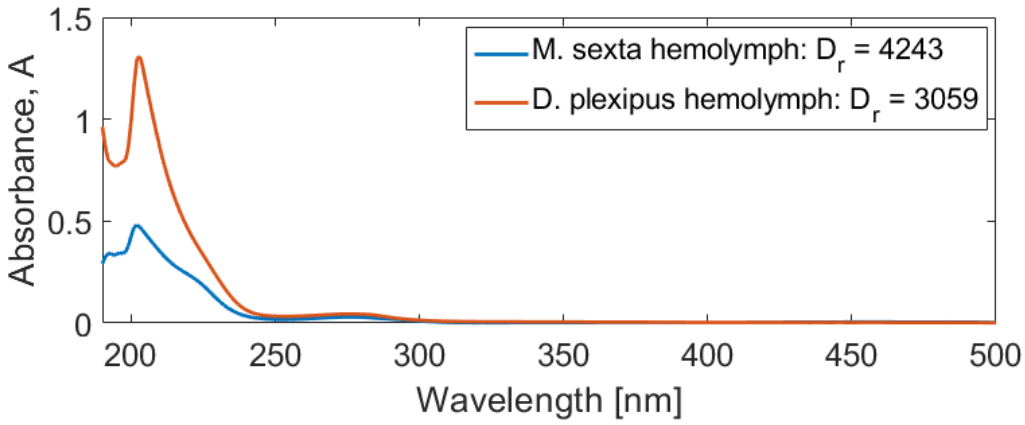

Figure 22. Absorbance spectra of diluted samples of *M. sexta* and *D. plexippus* hemolymph. D_r is the dilution ratio of the measured sample

Note: There appears to be a misprint in the book (37), where it reads $C_{protein} \approx 31 A_{205}$, which is not logical, since the peak at 205 is roughly 30 times larger than the peak at 280.

The reference (38) cited in the book also leads one to believe that the equation in (37) is a misprint.

4.6.6.2 Sample preparation

Hemolymph was extracted from the insect as described in section 4.6.2.1 and diluted in 3 ml of PBS and placed in quartz cuvettes. An absorption spectrum was taken with pure PBS as reference at wavelengths between 800 and 190 nm. If any peaks registered as having absorption of above 2, two milliliters of sample were removed from the cuvette and two milliliters of pure PBS were added. A new dilution ratio was calculated and a new spectrum was measured.

4.7 REFERENCES

1. Ryan R, Oikawa K, Kay C. Conformational, thermodynamic, and stability properties of *Manduca sexta* apolipophorin III. Journal of Biological Chemistry. 1993,
2. Narayanaswami V, Ryan RO. Molecular basis of exchangeable apolipoprotein function. BBA-Mol Cell Biol Lipids. 2000;1483(1):15-36.Doi 10.1016/S1388-1981(99)00176-6
3. Sparks DL, Phillips MC. Quantitative Measurement of Lipoprotein Surface-Charge by Agarose-Gel Electrophoresis. J Lipid Res. 1992;33(1):123-30.
4. Breiter DR, Kanost MR, Benning MM, Wesenberg G, Law JH, Wells MA, Rayment I, Holden HM. Molecular-Structure of an Apolipoprotein Determined at 2.5-a Resolution. Biochemistry-Us. 1991;30(3):603-8.DOI 10.1021/bi00217a002
5. van der Horst DJ, van Hoof D, van Marrewijk WJA, Rodenburg KW. Alternative lipid mobilization: The insect shuttle system. Molecular and Cellular Biochemistry. 2002;239:113-9.10.1023/A:1020541010547
6. Pattnaik NM, Mundall EC, Trambusti BG, Law JH, Kézdy FJ. Isolation and characterization of a larval lipoprotein from the hemolymph of *Manduca sexta*. Comparative Biochemistry and Physiology Part B: Comparative Biochemistry. 1979;63:469-76.10.1016/0305-0491(79)90048-8
7. Ryan R, Prasad SV, Henriksen EJ, Wells MA, Law JH. Lipoprotein Interconversions in an Insect , *Manduca sexta*. Journal of Biological Chemistry. 1986;261(2):563-8,
8. Ryan RO, Howe A, Scraba DG. Studies of the Morphology and Structure of the Plasma-Lipid Transfer Particle from the Tobacco Hornworm, Manduca-sexta. J Lipid Res. 1990;31(5):871-9.
9. Wells M, Ryan R, Kawooya J, Law J. The role of apolipophorin III in in vivo lipoprotein interconversions in adult *Manduca sexta*. Journal of Biological Chemistry. 1987,
10. Van Antwerpen R, Linnemans W, Van der Horst D, Beenakkers AT. Immunocytochemical localization of lipophorins in the flight muscles of the migratory locust (Locusts migratoria) at rest and during flight. Cell and tissue research. 1988;252(3):661-8,
11. van der Horst DJ, van Hoof D, van Marrewijk WJA, Rodenburg KW. Alternative lipid mobilization: The insect shuttle system. Mol Cell Biochem. 2002;239(1-2):113-9.10.1023/a:1020541010547
12. Kawooya JK, Keim PS, Ryan RO, Shapiro JP, Samaraweera P, Law JH. Insect Apolipophorin-Iii - Purification and Properties. Journal of Biological Chemistry. 1984;259(17):733-7.
13. Ryan RO, Horst DJvd. Lipid Transport Biochemistry and Its Role in Energy Production. Annual Review of Entomology. 2000;45:233-60.10.1146/annurev.ento.45.1.233
14. Hirayama Y, Chino H. Lipid transfer particle in locust hemolymph: purification and characterization. J Lipid Res. 1990;31:793-9,

15. Weers P, Marrewijk WV, Beenakkers A. Biosynthesis of locust lipophorin. Apolipophorins I and II originate from a common precursor. Journal of Biological. 1993,
16. Shapiro JP, Keim PS, Law JH. Structural studies on lipophorin, an insect lipoprotein. The Journal of biological chemistry. 1984;259:3680-5,
17. Kawooya JK, Keim PS, Ryan R, Shapiro, P J, Samaraweera P, Lawn JH. Insect Apolipophorin III: purification and properteis. The Journal of biological chemistry. 1984;259:10733-7,
18. Ryan RO, Howe A, Scraba DG. Studies of the morphology and structure of the plasma lipid transfer particle from the tobacco hornworm, *Manduca sexta*. J Lipid Res. 1990;31:871-9,
19. Inouye LS, Lotufo GR. Comparison of macro-gravimetric and micro-colorimetric lipid determination methods. Talanta. 2006;70:584-7.10.1016/j.talanta.2006.01.024
20. Naoumoff M, Jeuniaux C. [Changes in the inorganic cation component of hemolymph during development and metamorphosis of some Lepidopterans]. Archives internationales de physiologie et de biochimie. 1970;78:357-65,
21. Russel WB, Saville DA, Schowalter WR. Colloidal dispersions. Cambridge ; New York: Cambridge University Press; 1989. xvii, 525 p., 1 leaf of plates p,
22. Erickson HP. Size and shape of protein molecules at the nanometer level determined by sedimentation, gel filtration, and electron microscopy. Biological Procedures Online. 2009;11:32-51.10.1007/s12575-009-9008-x
23. Larson RG. Particulate Suspensions. In: Gubbins K, editor. The structure and Rheology of Complex Fluids. New York: Oxford University Press; 1999. p. 263-318,
24. Einstein A. A new determination of the molecular dimensions. Ann Phys-Berlin. 1906;19(2):289-306.
25. Batchelor GK. Effect of Brownian-Motion on Bulk Stress in a Suspension of Spherical-Particles. J Fluid Mech. 1977;83(Nov):97-117.Doi 10.1017/S0022112077001062
26. Brenner H, Condiff D. Transport mechanics in systems of orientable particles. IV. convective transport. J Colloid Interf Sci. 1974;47:199-264.10.1016/0021-9797(74)90093-9
27. Bird RB, Warner HR, Evans DC. Kinetic theory and rheology of dumbbell suspensions with Brownian motion. Fortschritte der Hochpolymeren-Forschung. Berlin, Heidelberg: Springer Berlin Heidelberg; 1971. p. 1-90.10.1007/3-540-05483-9_9
28. van der Werff JC, de Kruif CG. Hard-sphere Colloidal Dispersions: The Scaling of Rheological Properties with Particle Size, Volume Fraction, and Shear Rate. Journal of Rheology. 1989;33(3):421-54.10.1122/1.550062
29. Hinch EJ, Leal LG. Effect of Brownian Motion on Rheological Properties of a Suspension of Non-Spherical Particles. J Fluid Mech. 1972;52(Apr25):683-&.Doi 10.1017/S002211207200271x
30. Doi M, Edwards SF. The theory of polymer dynamics. Oxford: Clarendon Press; 1988. xiii, 391 p. p,
31. Mori Y, Ookubo N, Hayakawa R. Low-Frequency and High-Frequency Relaxations in Dynamic Electric Birefringence of Poly(Gamma-Benzyl-L-Glutamate) in Meta-Cresol. J Polym Sci Pol Phys. 1982;20(11):2111-24.

32. Kawooya JK, Meredith SC, Wells MA, Kézdy FJ, Law JH. Physical and surface properties of insect apolipophorin III. The Journal of biological chemistry. 1986;261:13588-91,
33. Standardization IOf. Colloidal systems -- Methods for zeta-potential determination. Part 1: Electroacoustic and electrokinetic phenomena2012. p. 27,
34. Cussler EL. Diffusion, mass transfer in fluid systems. Cambridge Cambridgeshire ; New York: Cambridge University Press; 1984. xii, 525.
35. Ryan RO, Oikawa K, Kay CM. Conformational, Thermodynamic, and Stability Properties of Manduca-sexta Apolipophorin-Iii. Journal of Biological Chemistry. 1993;268(3):1525-30.
36. Weers PMM, Ryan RO. Apolipophorin III: Role model apolipoprotein. Insect Biochemistry and Molecular Biology. 2006;36(4):231-40.10.1016/j.ibmb.2006.01.001
37. Stoscheck CM. Quantitation of Proteins. In: Deutscher MP, editor. Methods in Enzymology. San Diego, California: Academic Press; 1990. p. 50-60,
38. Scopes RH. Measurement of protein by spectrophotometry at 205 nm. Analytical Biochemistry. 1974;59:277-82.10.1016/0003-2697(74)90034-7

CHAPTER V

NANORHEOLOGY OF HEMOLYMPH OF CATERPILLARS

5.1 INTRODUCTION

As discussed in Chapter 1, hemolymph plays an important role in insects' lives, serving as a medium for energy transfer, as a medium for insect locomotion hydraulics, as a first line of defense against invading microorganisms, and as a healing agent after wounding. While its physiological roles have been studied in the past, its physical properties, such as rheology and surface tension have never been studied. In the previous chapter, we discussed the rheology of hemolymph of adults of several species of Lepidoptera. In this chapter, we will focus on rheology of hemolymph of larva (caterpillars) of *M. sexta*.

Larval hemolymph has a different composition from adult hemolymph with the most notable difference being an abundance of free cells called hemocytes (1-3). Estimated from the cell count, assuming an average diameter of a single cell to be 5 μm, the hemocytes constitute roughly 0.1-03 vol% (3, 4). Some of these hemocytes are inert, while others are adhesive and rapidly attach to foreign surfaces and invaders (5-13). Recent efforts of measuring viscosity of larval hemolymph with cone-and-plate rheometers proved difficult presumably due to structures that these hemocytes form after extraction from the body (14).

5.1.1 Methodology and hypothesis.

In this study, we use the modified MRS technique with nickel nanorods to study the shear rheology of hemolymph of *M. sexta* caterpillars during clotting after extracting it from a wound. The goal is to perform these experiments with minimal interaction with the sample to not disrupt the clotting process. We hypothesize that the nanorods will be able to probe the rheology of the material. Since larval hemolymph is abundant with hemocytes, we expect it to have different properties from the adult hemocyte-free hemolymph discussed in the previous chapter.

5.2 RESULTS AND DISCUSSION

To gain insight into the behavior of hemolymph in response to shear perturbations, we suspended magnetic probes in incubating droplets of hemolymph, rotated them with a magnetic field, and tracked the response of the material. Hemocytes quickly adhered to the probes and drastically changed the local properties.

5.2.1 Nanoscale rheology and rigidification of cellular aggregates

The nanoscopic rheological behavior of cell-rich hemolymph is different from the behavior of hemolymph of adults. Whereas in adult hemolymph the nanorods were able to rotate freely, the nanorods in caterpillar hemolymph were almost immediately occluded by the cells, changing their mode of rotation. This behavior is presented in Figure 23. An aggregate of nickel nanorods was rotated in a 1.5 mT magnetic field with a 1 Hz frequency. Initially, the probes either fully rotated or rotated with some oscillations around the mean direction of rotation, similarly to how they behaved in the hemolymph of adults. This happened for several seconds after initial dispersion of the probes in the

sample. Next, hemocytes began adhering to each other and to the probes. As this happened, the probes changed their rotation mode. The probes continued to oscillate with a high amplitude, but the mean orientation no longer changed. As time went on, the amplitude of these oscillations decreased non-linearly with time, approaching zero.

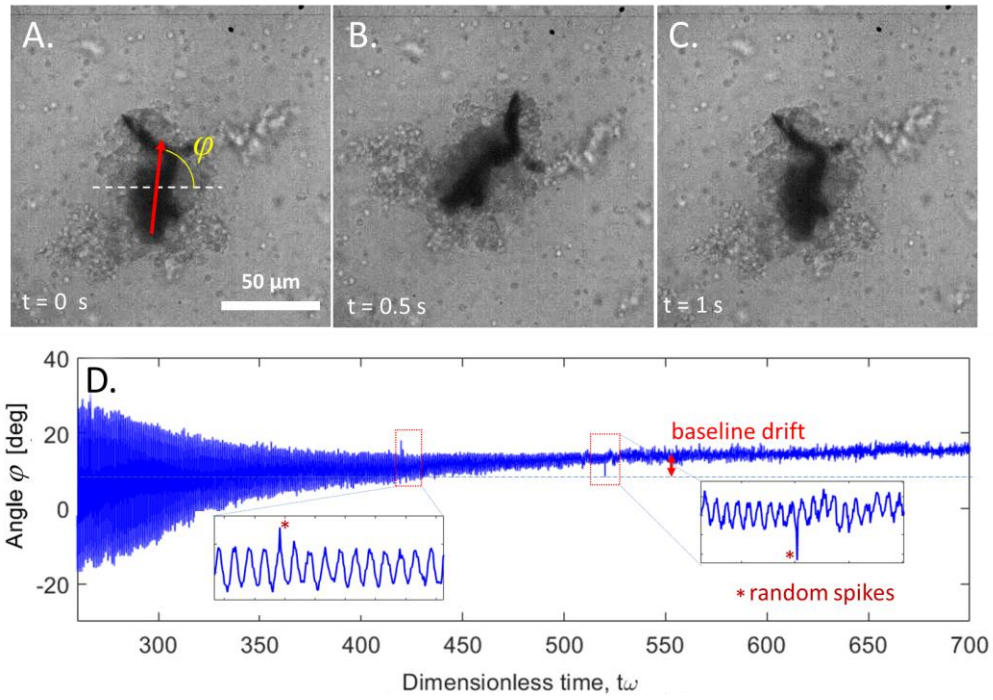

Figure 23. Rotation of an agglomerate of magnetic nanoprobes adhered to by hemocytes. (A-F) A gallery of snapshots during various stages of cross-linking of the clot. (A-C) 5 minutes after the wound is made. The cells form a large clump that is relatively soft. The black probe oscillates with a large amplitude. (D) A full profile and (inserts) zoomed in segments of orientation of a single probe agglomerate as a function of time. The amplitude of the periodic motion decreases with time, which signifies an increased rigidity of the material.

As discussed in the previous chapter, the cellular aggregates grow during the first two minutes of the clot formation. With time, the aggregates stop growing and begin shrinking in size. During this stage, the cells appear to pack more closely and the aggregates darken. This behavior is accompanied by a decrease in amplitude of periodic

motion of the nanoprobe aggregate. This is indicative of a viscoelastic material with changing rheological properties (15, 16).

We propose two scenarios describing exponentially fading oscillations of a magnetic probe. In the first scenario, the probe might be hinged to the cell aggregate, remaining partially exposed to the fluid, as the two-dimensional image of the cell aggregate cannot guarantee that the probe is not sticking out of the aggregate in the z-direction. Thus, when the probe is forced to rotate in response to the magnetic torque, it experiences an elastic reaction from the aggregate and a viscous drag from the fluid (Figure 24, A). This scenario can be modeled with the Maxwell model, where the spring models the elastic reaction of the aggregate matrix and the dashpot models the viscous friction of the fluid (17, 18).

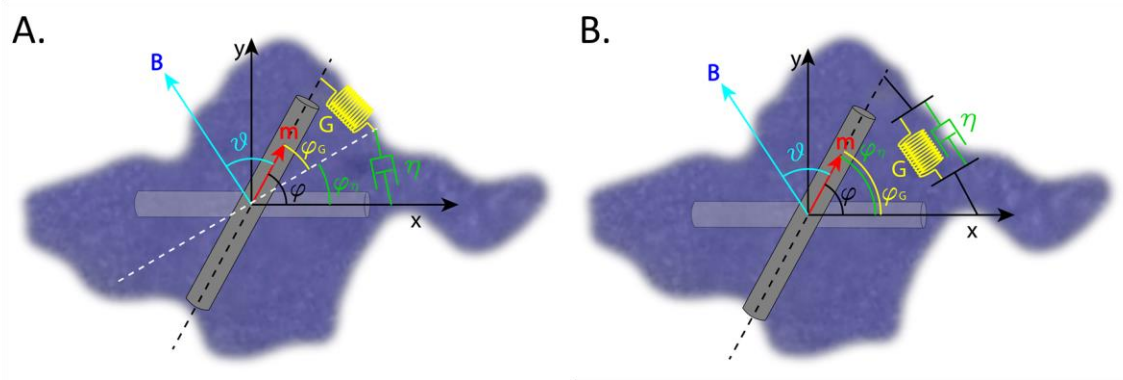

Figure 24. Schematics of the two scenarios of material response to the probe oscillation. The original orientation of the rod is in translucent black and the current position of the probe is in black. The probe is surrounded by the cells and proteins. (A) The probe is exposed to the elastic aggregate and the viscous plasma, which respond as an elastic and a viscous torques in series. (B) the probe is completely embedded in the gel-like aggregate, which responds as an elastic and a viscous torques in parallel.

In the second scenario, the probe might be completely embedded in a gel-like material formed by the cells and the connecting medium (Figure 24, B). The gel-like

material responds elastically to the applied oscillating magnetic torque. Upon deformation of the matrix, a gel-like aggregate squeezes out plasma from its pores. This plasma flow contributes to a viscous drag on the magnetic probe, which is modeled as a dashpot (Figure 24, B)

Thus, in the second scenario, a dashpot modeling viscous friction and an elastic spring modeling elastic response of the gel, both set in parallel, oppose the magnetic torque. This second scenario corresponds to the Kelvin-Voigt model of viscoelasticity (16, 19).

In the Maxwell model, the viscous, τ_η , elastic, τ_G , and magnetic, τ_m , torques are equal to each other $\tau_\eta = \tau_G = \tau_\mathrm{m}$. Introducing the drag coefficient γ, which is proportional to viscosity, η , and an effective shear modulus of the aggregate, *G*, the viscous and elastic torques are written as $\tau_\eta = \gamma \mathrm{d}\varphi_\eta/\mathrm{d}t$, $\tau_G = \gamma G\, \varphi_G/\eta$, where φ_η and φ_G are the rotation angles associated with the spring and dashpot displacements, respectively, and *t* is time. The angular displacement of the probe satisfies the relation $\varphi_\eta + \varphi_G = \varphi$. Thus, the torque balance provides the equation governing probe rotation (17):

$$\frac{\mathrm{d}\varphi}{\mathrm{d}t} - \frac{\eta}{\gamma G}\frac{\mathrm{d}\tau_\mathrm{m}}{\mathrm{d}t} = \frac{\tau_\mathrm{m}}{\gamma} \tag{5.1}$$

In the Kelvin-Voigt model, when the dashpot and the spring are in parallel, the torques satisfy the relation $\tau_\mathrm{m}=\tau_\eta+\tau_G$, and the angular displacements are the same for the spring and dashpot, $\varphi_\eta=\varphi_G=\varphi$. The torque balance for the Kelvin-Voigt model is thus:

$$\frac{\mathrm{d}\varphi}{\mathrm{d}t} + \frac{G}{\eta}\varphi = \frac{\tau_\mathrm{m}}{\gamma} \tag{5.2}$$

When the second term in equations (5.1) and (5.2) is absent, these two models become identical and describe the probe behavior in a Newtonian liquid, which does not sustain any shear stress and hence does not show any elastic response.

5.2.2 Numeric analysis of rigidifying medium of Newtonian, Maxwell and Kelvin-Voigt models

According to the three introduced rheological models, the rotation of the probe, is described by the following equations

Newtonian medium

$$\begin{aligned} \frac{d\varphi}{dt} &= \omega_c \sin\left(\omega t - \varphi\right) \\ \frac{d\varphi}{d\tilde{t}} &= \tilde{\omega}_c \sin\left(\tilde{t} - \varphi\right) \end{aligned} \tag{5.3}$$

Maxwell medium

$$\begin{aligned} \frac{d\varphi}{dt} &= \frac{\omega_c \sin\left(\omega t - \varphi\right) + \omega \dfrac{\omega_c}{\omega_r} \cos\left(\omega t - \varphi\right)}{1 + \dfrac{\omega_c}{\omega_r} \cos\left(\omega t - \varphi\right)} \\ \frac{d\varphi}{d\tilde{t}} &= \frac{\tilde{\omega}_c \sin\left(\tilde{t} - \varphi\right) + \dfrac{\tilde{\omega}_c}{\tilde{\omega}_r} \cos\left(\tilde{t} - \varphi\right)}{1 + \dfrac{\tilde{\omega}_c}{\tilde{\omega}_r} \cos\left(\tilde{t} - \varphi\right)} \end{aligned} \tag{5.4}$$

Kelvin-Voigt medium

$$\begin{aligned} \frac{d\varphi}{dt} &= \omega_c \sin\left(\omega t - \varphi\right) - \omega_r \varphi \\ \frac{d\varphi}{d\tilde{t}} &= \tilde{\omega}_c \sin\left(\tilde{t} - \varphi\right) - \tilde{\omega}_r \varphi \end{aligned} \tag{5.5}$$

where φ is the angle that the rod makes with a stationary reference axis, t is time, $\omega_c \propto \eta^{-1}$, η is viscosity, $\omega_r = \dfrac{G}{\eta}$, G is the elastic modulus and the normalized values are as follows.

$$\begin{aligned}\tilde{\omega}_c &= \omega_c / \omega \\ \tilde{\omega}_r &= \omega_r / \omega \\ \tilde{\tau} &= \omega\tau \\ \tilde{t} &= \omega t\end{aligned} \tag{5.6}$$

In our experiments, we observe that the cell aggregates mature with time and their properties change sufficiently fast. We will thus consider the probe behavior as the viscosity and/or the elastic modulus of the media increase exponentially fast. In particular, we will consider two cases which can be written in normalized form as:

$$\tilde{\omega}_c\left(\tilde{t}\right) = \tilde{\omega}_{c0}\exp\left(-\tilde{t}/\tilde{\tau}\right);\ \tilde{\omega}_c/\tilde{\omega}_r \propto G \approx const \tag{5.7}$$

$$\tilde{\omega}_c\left(\tilde{t}\right) = \tilde{\omega}_{c0}\exp\left(-\tilde{t}/\tilde{\tau}\right);\ \tilde{\omega}_r = const\text{ , }i.e.\ G \propto \exp\left(\tilde{t}/\tilde{\tau}\right) \tag{5.8}$$

In the case of equation (5.7), the critical frequency ω_c exponentially decreases, which corresponds to the viscosity η exponentially increasing, and ω_c/ω_r remains constant, which corresponds to the elastic modulus G remaining constant. In the case of equation (5.8), ω_c again exponentially decreases, which corresponds to the viscosity exponentially increasing, and ω_r remains constant, which corresponds to the elastic modulus G exponentially increasing as well. In both cases, we set the numerical parameters such that the characteristic time of the oscillation of the probe is much lower than the characteristic time of the materials parameters change.

The first case implies that the viscosity of the liquid increases exponentially and the elastic modulus remains constant. The probe behavior for each of the three models is

presented in Figure 25. The oscillations around the mean exhibit a decreasing amplitude in Newtonian and Kelvin-Voigt models and do not change in the Maxwell model. The slope of the mean in Newtonian and Maxwell models decreases and approaches 0. The mean for the Kelvin-Voigt model does not change and remains at 0.

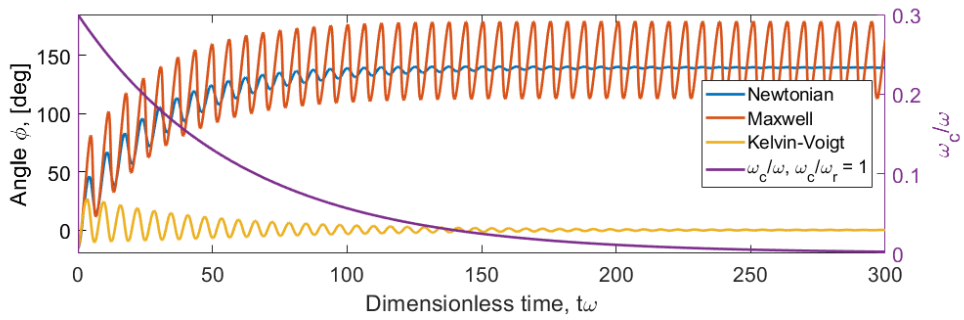

Figure 25. Illustration of the behavior of a ferromagnetic probe rotated with a magnetic field with ω=1 in (blue) Newtonian, (orange) Maxwell, and (yellow) Kelvin-Voigt media with a constant $\omega_c/\omega_r = 0.5$ and (purple, right axis) exponentially decreasing ω_c. The oscillations around the mean exhibit a decreasing amplitude in Newtonian and Kelvin-Voigt models and do not change in the Maxwell model. The mean angle in Newtonian and Maxwell models approaches a constant. The mean angle for the Kelvin-Voigt model does not change and remains at 0.

The second case implies that the viscosity and the elastic modulus of the liquid increase exponentially fast, but at the same rate. The probe behavior for the three models is presented in Figure 26. The behavior of the probe for the Newtonian model is identical to the first case, since ω_r for it is not defined. The probe in Maxwell fluid, however, experiences a decreasing amplitude of oscillation around the mean and the slope of the mean decreases and approaches 0. The behavior of the Kelvin-Voigt probe, while not quantitively identical to the first case, does not seem to have any qualitatively distinguishing features from it. In the second case at low values of ω_c (to the right of the blue dashed line in Figure 26), both Maxwell and Kelvin-Voigt models show decreasing

oscillations with a non-changing mean angle. In this scenario, both models represent similar materials that are elastic and do not flow and it is difficult to qualitatively distinguish between the two models.

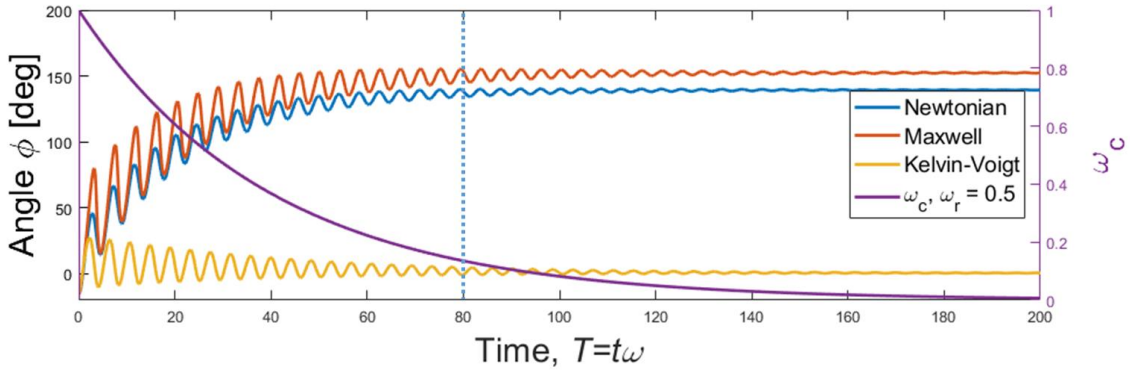

Figure 26. Illustration of the behavior of a ferromagnetic probe rotated with a magnetic field with ω=1 in (blue) Newtonian, (orange) Maxwell, and (yellow) Kelvin-Voigt media with a constant $\omega_r = 0.5$ and (purple, right axis) exponentially decreasing ω_c. The oscillations around the mean exhibit a decreasing amplitude in all three models. The slope of the mean in Newtonian and Maxwell models decreases and approaches 0. The mean for the Kelvin-Voigt model does not change and remains at 0.

Thus, it seems from this preliminary analysis that three scenarios are relevant to the experiment at hand: the Kelvin-Voigt model where the viscosity of the material increases exponentially and the elastic modulus remains constant, the Kelvin-Voigt model where the viscosity and the elastic modulus of the material increase exponentially, and the Maxwell model where the viscosity is high initially and both viscosity and the elastic modulus of the material increase exponentially. It remains unknown, however, whether the two seemingly different equations describe a non-flowing, rigidifying material similarly. To answer this question, we first linearize the equations to find the dependency of the amplitude of the angular oscillations on the changing ω_c and ω_r.

5.2.3 Linearization of the Maxwell model at high viscosity.

Beginning with normalized equation (5.4), and seeing from experiment that as time increases indefinitely, $\tilde{t} \to \infty$ angle φ of the probe approaches a constant value, $\varphi \to \varphi_0$. Thus, at large times, we can write $\varphi = \varphi_0 - \xi$, where $|\xi| << 1$is the amplitude of an oscillation. From experiment, we can set the value of $\varphi_0 = 0$. The trigonometric functions components from these equations can thus be rewritten as:

$$\sin(\tilde{t} - \varphi) = \sin(\tilde{t} + \xi) \tag{5.9}$$

$$\cos(\tilde{t} - \varphi) = \cos(\tilde{t} + \xi) \tag{5.10}$$

Applying a trigonometric identity and Taylor expansion over ξ equation (5.9) takes the form of

$$\sin(\tilde{t} - \varphi) \approx \sin(\tilde{t}) + \xi \cos(\tilde{t}) \tag{5.11}$$

Similarly, equation (5.10) takes the form of

$$\cos(\tilde{t} - \varphi) \approx \cos(\tilde{t}) + \xi \sin(\tilde{t}) + O(\xi^2) \tag{5.12}$$

Substituting equations (5.11) and (5.12) into Maxwell equation (5.4) and factoring out ξ, we obtain

$$\begin{aligned} -\frac{d\xi}{d\tilde{t}} = \xi\left[\frac{\tilde{\omega}_c(\tilde{t})}{\tilde{\omega}_r(\tilde{t})}\sin(\tilde{t}) - \tilde{\omega}_c(\tilde{t})\cos(\tilde{t})\right] - \\ -\tilde{\omega}_c(\tilde{t})\sin(\tilde{t}) - \frac{\tilde{\omega}_c(\tilde{t})}{\tilde{\omega}_r(\tilde{t})}\cos(\tilde{t}) \end{aligned} \tag{5.13}$$

Since at large time $\tilde{t}$, the amplitude ξ is small and the viscosity is high (ω_c is low), both terms inside the brackets are small, leaving the declination from the mean dependence as

$$\frac{d\xi}{d\tilde{t}} = \tilde{\omega}_c(\tilde{t})\sin(\tilde{t}) + \frac{\tilde{\omega}_c(\tilde{t})}{\tilde{\omega}_r(\tilde{t})}\cos(\tilde{t}) \tag{5.14}$$

Now, considering only the case of exponentially increasing viscosity and constant elastic modulus (equation (5.7)), the behavior of the oscillations takes the form of

$$\frac{d\xi}{d\tilde{t}} = \tilde{\omega}_{c0}\exp\left(-\tilde{t}/\tilde{\tau}\right)\sin(\tilde{t}) + K\cos(\tilde{t}) \tag{5.15}$$

where K is a constant. This relation can now be integrated to find the dependency of the angle of the probe as a function of time for this scenario.

$$\xi = \frac{-\tilde{\omega}_{c0}\tilde{\tau}\exp\left(-\tilde{t}/\tilde{\tau}\right)}{1+\tilde{\tau}^2}\left(\tilde{\tau}\cos(T) + \sin(T)\right) + K\sin(T) \tag{5.16}$$

Since during experiment, we track the amplitude of these oscillation ξ_A, we are interested in the prefactors of the periodic function and not the phase. Thus, we aim to obtain he form of the expression, where the amplitude is easily observable. Since

$$A\sin(x) + B\cos(x) = \sqrt{A^2 + B^2}\,\sin(x+\alpha) \tag{5.17}$$

where $\alpha = \arctan(B/A)$, equation (5.16) can be rewritten as

$$\xi = \frac{-\tilde{\omega}_{c0}\tilde{\tau}\exp\left(-\tilde{t}/\tilde{\tau}\right)}{\sqrt{\tilde{\tau}^2+1}}\sin\left(\tilde{t} + \tan^{-1}(\tilde{\tau})\right) + K\sin(\tilde{t}) \tag{5.18}$$

Furthermore, the amplitude of the sum of amplitudes of two sine functions with an arbitrary phase shift, $A\sin(x+\alpha) + B\sin(x)$, can be shown to equal $\sqrt{A^2 + B^2 + 2AB\cos(a)}$. Thus, the amplitude of the oscillations for the current case is expressed as

$$\xi_A = \sqrt{\left(\frac{\tilde{\omega}_{c0}\tilde{\tau}\exp\left(-\tilde{t}/\tilde{\tau}\right)}{\sqrt{\tilde{\tau}^2+1}}\right)^2 + K^2 - \frac{2K\tilde{\omega}_{c0}\tilde{\tau}\exp\left(-\tilde{t}/\tilde{\tau}\right)}{\tilde{\tau}^2+1}} \tag{5.19}$$

Since in experiment, $\tilde{\tau} >> 1$, the expression can be Taylor expanded\ to

$$\xi_A = \sqrt{\tilde{\omega}_{c0}{}^2\exp\left(-2\tilde{t}/\tilde{\tau}\right) + K^2 - \frac{2K\tilde{\omega}_{c0}}{\tilde{\tau}}\exp\left(-\tilde{t}/\tilde{\omega}\right) + O\left(\frac{1}{\tilde{\tau}^2}\right)} \tag{5.20}$$

The kinetics of the amplitude of oscillation of a probe rotating in a Maxwell liquid with properties changing according to (5.7), thus develop as follows. Initially, when $\tilde{t}$ is small, depending on the elastic modulus and thus K, $\tilde{\omega}_{c0}$ contributes a significant portion to the amplitude. As time goes on, the contribution of $\tilde{\omega}_{c0}$ becomes less and less significant and the amplitude approaches K. This is consistent with the behavior of the Maxwell model presented in Figure 25 and does not represent the experimental data. Thus, this case will no longer be considered.

Let us now consider the behavior of amplitude in the case of exponentially increasing viscosity and exponentially increasing elastic modulus (equation (5.8). Starting with equation (5.14), we substitute the explicit relations of $\tilde{\omega}_c$ and $\tilde{\omega}_r$ in time,

$$\frac{d\xi}{d\tilde{t}} = \tilde{\omega}_{c0}\exp\left(-\tilde{t}/\tilde{\tau}\right)\sin\left(\tilde{t}\right) + \frac{\tilde{\omega}_{c0}}{\tilde{\omega}_r}\exp\left(-\tilde{t}/\tilde{\tau}\right)\cos\left(\tilde{t}\right) \tag{5.21}$$

Again, we integrate to find the dependency of the angle of the probe as a function of time for this scenario.

$$\xi = -\frac{\tilde{\omega}_{c0}\tilde{\tau}\exp\left(-\tilde{t}/\tilde{\tau}\right)}{1+\tilde{\tau}^2}\left(\tilde{\tau}\cos\left(\tilde{t}\right)+\sin\left(\tilde{t}\right)\right)+ \frac{\tilde{\omega}_{c0}\tilde{\tau}\exp\left(-\tilde{t}/\tilde{\tau}\right)}{\tilde{\omega}_r\left(1+\tilde{\tau}^2\right)}\left(-\cos\left(\tilde{t}\right)+\tilde{\tau}\sin\left(\tilde{t}\right)\right) \tag{5.22}$$

Applying equation (5.17),

$$\xi = \frac{-\tilde{\omega}_{c0}\tilde{\tau}\exp\left(-\tilde{t}/\tilde{\tau}\right)}{\sqrt{\tilde{\tau}^2+1}}\sin\left(\tilde{t}+\tan^{-1}\left(\tilde{\tau}\right)\right)+ \frac{\tilde{\omega}_{c0}\tilde{\tau}\exp\left(-\tilde{t}/\tilde{\tau}\right)}{\tilde{\omega}_r\sqrt{\tilde{\tau}^2+1}}\left(\sin\left(\tilde{t}+\tan^{-1}\left(-1/\tilde{\tau}\right)\right)\right) \tag{5.23}$$

Writing the dependence of the amplitude as a function of time, we get

$$\xi_A = \sqrt{f_1+f_2}$$
$$f_1 = \left(\frac{-\tilde{\omega}_{c0}\tilde{\tau}\exp\left(-\tilde{t}/\tilde{\tau}\right)}{\tilde{\tau}^2+1}+\frac{\tilde{\omega}_{c0}\tilde{\tau}\exp\left(-\tilde{t}/\tilde{\tau}\right)}{\tilde{\omega}_r\sqrt{\tilde{\tau}^2+1}\sqrt{\tilde{\tau}^{-2}+1}}\right)^2 \tag{5.24}$$
$$f_2 = \left(\frac{-\tilde{\omega}_{c0}\tilde{\tau}^2\exp\left(-\tilde{t}/\tilde{\tau}\right)}{\tilde{\tau}^2+1}-\frac{\tilde{\omega}_{c0}\tilde{\tau}\exp\left(-\tilde{t}/\tilde{\tau}\right)}{\tilde{\tau}\tilde{\omega}_r\sqrt{\tilde{\tau}^2+1}\sqrt{\tilde{\tau}^{-2}+1}}\right)^2$$

Since in experiment $\tilde{\tau} >> 1$, the expression can be simplified to

$$f_1 = \left(\frac{-\tilde{\omega}_{c0}\exp\left(-\tilde{t}/\tilde{\tau}\right)}{\tilde{\tau}}+\frac{\tilde{\omega}_{c0}\exp\left(-\tilde{t}/\tilde{\tau}\right)}{\tilde{\tau}\tilde{\omega}_r}+O\left(\frac{1}{\tilde{\tau}^2}\right)\right)^2 \tag{5.25}$$
$$f_2 = \left(-\tilde{\omega}_{c0}\exp\left(-\tilde{t}/\tilde{\tau}\right)-\frac{\tilde{\omega}_{c0}\exp\left(-\tilde{t}/\tilde{\tau}\right)}{\tilde{\tau}\tilde{\omega}_r}+O\left(\frac{1}{\tilde{\tau}^2}\right)\right)^2$$

And algebraically expanded to

$$f_1 = \frac{\tilde{\omega}_{c0}{}^2 \exp\left(-2\tilde{t}/\tilde{\tau}\right)}{\tilde{\tau}^2} + \frac{\tilde{\omega}_{c0}{}^2 \exp\left(-2\tilde{t}/\tilde{\tau}\right)}{\tilde{\tau}^2 \tilde{\omega}_r{}^2} - 2\frac{\tilde{\omega}_{c0}{}^2 \exp\left(-2\tilde{t}/\tilde{\tau}\right)}{\tau^2 \omega^3 \omega_r}$$
$$f_2 = \frac{\omega_{c0}{}^2 \exp\left(-2\tilde{t}/\omega\tau\right)}{\omega^2} + \frac{\omega_{c0}{}^2 \exp\left(-2\tilde{t}/\omega\tau\right)}{\tau^2 \omega^2 \omega_r{}^2} + 2 \tag{5.26}$$

The exponent and $\tilde{\omega}_{c0}{}^2$ terms can be factored out to

$$\xi_A = \tilde{\omega}_{c0} \exp\left(-\tilde{t}/\tilde{\tau}\right)\sqrt{1 + \frac{2}{\tilde{\tau}\tilde{\omega}_r} + \frac{1}{\tilde{\tau}^2} + \frac{2}{\tilde{\tau}^2 \tilde{\omega}_r{}^2} - \frac{2}{\tilde{\tau}^2 \tilde{\omega}_r}} \tag{5.27}$$

5.2.4 Linearization of the Kelvin-Voigt model

Similar steps as above will be performed for the Kelvin-Voigt model for material changing according to equations (5.7) and (5.8). Beginning with normalized equation (5.5), we write the expression for deviations of the angle φ from the mean ξ at large $\tilde{t}$ as

$$\frac{d\xi}{d\tilde{t}} = -\xi\left[\tilde{\omega}_{\mathrm{r}}\left(\tilde{t}\right) + \tilde{\omega}_c\left(\tilde{t}\right)\cos\left(\tilde{t}\right)\right] - \tilde{\omega}_c\left(\tilde{t}\right)\sin\left(\tilde{t}\right) \tag{5.28}$$

Since at large time $\tilde{t}$, amplitude ξ is small and the viscosity is high ($\tilde{\omega}_c$ is low), the second bracketed term can be neglected. Thus,

$$\frac{d\xi}{d\tilde{t}} = -\xi\tilde{\omega}_{\mathrm{r}}\left(\tilde{t}\right) - \tilde{\omega}_c\left(\tilde{t}\right)\sin\left(\tilde{t}\right) \tag{5.29}$$

Now, let us consider only the case of exponentially increasing viscosity and constant elastic modulus (equation (5.7)). At large time $\tilde{t}$, the amplitude ξ and $\tilde{\omega}_r$ are small. The first term can thus be ignored as well. Plugging in the relation from equation (5.7), the profile of the oscillations takes the form of

$$\frac{d\xi}{d\tilde{t}} = -\tilde{\omega}_{c0} \exp\left(-\tilde{t}/\tilde{\tau}\right)\sin\left(\tilde{t}\right) \tag{5.30}$$

This relation can now be integrated to find the dependency of the angle of the probe in a Kelvin-Voigt medium as a function of time for this scenario.

$$\xi = \frac{-\tilde{\omega}_{c0}\tilde{\tau}\exp\left(-\tilde{t}/\tilde{\tau}\right)}{1+\tilde{\tau}^2}\left(\tilde{\tau}\cos\left(\tilde{t}\right)+\sin\left(\tilde{t}\right)\right) \tag{5.31}$$

Using equation (5.17), we can write the behavior of the amplitude as

$$\xi_A = \frac{\tilde{\omega}_{c0}\tilde{\tau}\exp\left(-\tilde{t}/\tilde{\tau}\right)}{\sqrt{\tilde{\tau}^2+1}} \tag{5.32}$$

Since in experiment $\tilde{\tau} >> 1$, the expression can be simplified to

$$\xi_A = \tilde{\omega}_{c0}\exp\left(-\tilde{t}/\tilde{\tau}\right)+O\left(\frac{1}{\tilde{\tau}}\right) \tag{5.33}$$

Performing similar analysis for the second case, where viscosity and the elastic modulus increase exponentially, and starting with equation (5.29) and plugging equations (5.8) for $\tilde{\omega}_c$ and $\tilde{\omega}_r$,

$$\frac{d\xi}{d\tilde{t}} = -\xi\tilde{\omega}_{\mathrm{r}} - \tilde{\omega}_{c0}\exp\left(-\tilde{t}/\tilde{\tau}\right)\sin\left(\tilde{t}\right) \tag{5.34}$$

Integrating, we get

$$\xi = \tilde{\omega}_{c0}\exp\left(-\tilde{t}/\tilde{\tau}\right)\cos\left(\tilde{t}\right) - \exp\left(-\tilde{t}\,\tilde{\omega}_r\right) \tag{5.35}$$

Again, keeping only the amplitude of the oscillating component, we have

$$\xi_A = \tilde{\omega}_{c0}\exp\left(-\tilde{t}/\tilde{\tau}\right) - \exp\left(-\tilde{t}\,\tilde{\omega}_r\right) \tag{5.36}$$

When $\tilde{\omega}_r > 1/\tilde{\tau}$, the positive left term decreases more slowly than the negative left term.

Equations (5.27), (5.33), and (5.36) that describe the amplitude of the oscillations of the probe in the Maxwell and Kelvin-Voigt liquids with exponentially increasing viscosity and elastic modulus, as well as the Kelvin Voigt liquid exponentially increasing viscosity and non-changing elastic modulus exhibit some similarities. Namely, all contain the exponentially decaying term $\tilde{\omega}_{c0}\exp\left(-\tilde{t}/\tilde{\tau}\right)$. Equation (5.27) contains terms where $1/\tilde{\tau}$ competes with $1/\tilde{\omega}_r$. Since from experiment we see that the time it takes the amplitudes to decay is large, $\tilde{\tau} >> 1$ and $1/\tilde{\tau} << 1$. In order for the $1/\tilde{\tau}\tilde{\omega}_r$ terms to be significant, $\tilde{\omega}_r$ needs to be small, which would constitute a soft material – a property we do not expect from a blood clot. Similarly, equation (5.36) contains a positive exponential with the decay rate $1/\tilde{\tau}$ and a negative exponential with a decay rate $\tilde{\omega}_r$. When $\tilde{\omega}_r > 1/\tilde{\tau}$, the positive left term decreases more slowly than the negative left term and dictates the kinetics of the equation. We would expect this from a relatively elastic material, which a clot likely is. Thus, the driving term in all three cases is $\tilde{\omega}_{c0}\exp\left(-\tilde{t}/\tilde{\tau}\right)$ and the amplitude in all three cases is described by

$$\xi_A = \tilde{\omega}_{c0}\exp\left(-\tilde{t}/\tilde{\tau}\right) \tag{5.37}$$

In the context of this experiment, the three cases are thus indistinguishable from each other and are equivalent in their description of the physical phenomenon studied.

5.2.5 Analysis of probe motion

The analysis of the probe motion in hemocyte-rich hemolymph has experimental challenges that prevent us from analyzing the rotating trajectories directly with MRS theory as we did in the study of adult hemolymph. In adult samples, for instance, the probe aggregates can be broken manually with a large glass rod shortly after their dispersion in the sample. In cell-rich hemolymph, the cells begin adhering to the surfaces and forming the structures almost immediately, rendering any manual manipulation of the sample destructive. The probes thus have a complex geometric shape as they consist of nanorod agglomerates. We are thus unable to determine the magnetic torque applied on the probes and as a result calculate the absolute viscosity and elastic modulus of the material. Thus, only the relative properties of the cell aggregate can be determined versus time.

Another experimental challenge is that the probes are obstructed by hemocyte aggregates. This makes the algorithm for extraction of the orientation of the probe less precise and prevents us from looking at the fine features of probe behavior. We thus resolve to tracking only the amplitude ξ_A of these oscillations to infer the changing material properties. ξ_A is extracted from the raw data in two steps. First, the data is filtered with a frequency filter. And second, the envelope of the oscillating function is numerically extracted.

The frequency filter is first applied to remove slow drift in the average orientation of the aggregate and sharp noise spikes that occur during image analysis. The apparent drift in the mean orientation, which can be seen from panel G in Figure 1, is caused by

the structural change of the aggregate, which does not reflect the response of the material to our manipulation. The random spikes in the extracted data, which can be seen in the inserts of panel G, are created during the video analysis and also do not represent the response of the material to external perturbation. Both types of signal defects can be corrected for by applying a frequency filter on the data.

A frequency filter is a method of data manipulation that removes undesired frequencies form the signal. In our case, the oscillations of the probe due to the magnetic field have the frequency of 1 Hz. Relative to these oscillations, the drift in the baseline is a low frequency process and the noise is a high-frequency defect. Thus, by applying a band-pass filter, we can eliminate all undesired effects. The filter was created using the MATLAB filter designer to create a narrow band filter that removes any oscillating components of the signal that are not within the 0.5 – 1.5 Hz region. The specific parameters of the filter are presented in the methods section. Once the data is passed through the filter, only the relevant data of the motion due to the magnetic perturbation remains (Figure 27, green) and ξ_A can be extracted.

The amplitude of the oscillations ξ_A as a function of time was obtained by extracting the envelope of the filtered data (Figure 27, blue). An envelope of an oscillating function is a curve tracing its maxima. The envelope was obtained using the MATLAB *envelope()* function, which calculates the upper and lower envelopes using a discrete Fourier transform of the data. The function creates a smooth curve, connecting the maxima. The insert in Figure 27 shows a close-up of the resultant envelope.

The extracted envelope of the data was then fitted with an exponential function $\xi_A = \xi_{A0} \exp\left(-\tilde{t} / \tilde{\tau}\right)$. An example of the fit of a dataset from a single sample with the decay time of $\tilde{\tau}$ = 77.1s is presented in Figure 27. Time-evolution of three samples from three caterpillars was successfully analyzed in this fashion to obtain the value of $\tilde{\tau}$ = 86 ±17. Since $\tilde{\tau} = \omega\tau$ and in the experiment $\omega = 1\,\text{Hz}$, the characteristic time of the soft clot exponential rigidification is τ = 86 ± 17s.

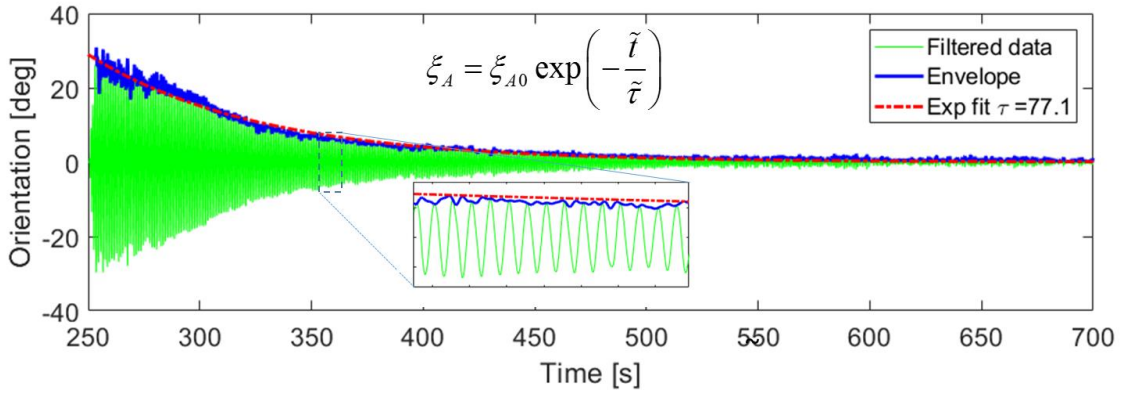

Figure 27. The (green) filtered oscillation of the magnetic probe embedded in an aggregate of hemocytes during clotting in response to the applied rotating magnetic field. The data has been (blue) enveloped, and (red dashed) fitted with an exponential function.

5.3 CONCLUSION

We have performed modified MRS experiments of hemocyte-rich hemolymph of *M. sexta* larvae using nanoprobes. Upon suspension on the probes in hemolymph, the hemocytes readily adhered to each other and the probes. This allowed us to probe the rheology of cellular aggregates as a function of time. We found that the probes oscillate with an exponentially decreasing amplitude. This behavior can be explained with a Kelvin-Voigt model of a material with an exponentially increasing viscosity and either a constant or an exponentially increasing elastic modulus as well as a Maxwell model of a

material with an exponentially increasing viscosity and elastic modulus. Due to the complex shape of the probes, it is impossible to measure the exact magnetic and response torques on the probe and thus calculate the exact rheological properties. Instead, we determine the characteristic time of exponential rigidification of the cellular aggregates in the clotting hemolymph as $\tau = 86 \pm 17$s.

5.4 MATERIALS AND METHODS

5.4.1 Dispersion of nanorods in the sample

Nickel nanorods, 200 nm in diameter and roughly 10 μm in length, were deposited in the caterpillar hemolymph samples in a similar fashion to the adult hemolymph samples with a few major distinctions. First, the nanorods suspended in methanol were deposited onto a glass slide. The methanol was allowed to evaporate, leaving the nanorods on the slide. An incision was then made on the 3rd proleg of the caterpillar and several droplets of hemolymph was dripped onto the slide. No additional interaction with the sample was performed to preserve any structure present in hemolymph. The sample was then transferred to an environmental chamber (described in Chapter 3) under nitrogen of 100% humidity inside the magnetic rotator, the rotating magnetic field was turned on and the sample was imaged under bright-field microscopy.

5.4.2 Filtering of data

The filter was implemented using the MATLAB *filter()* function, for which a custom filter was created using the MATLAB Filter Designer. The designed filter was a narrow band band-pass filter that removes any undesired oscillations not within 0.5 – 1.5 Hz region. We chose a Butterworth filter as it has a maximally flat frequency response

and does not disrupt the useful signal. The parameters specified for the function are presented in Table 7 and the frequency response of the filter is presented in Figure 28. The band width of the filter was chosen to minimize the irrelevant data, while minimizing the frequency-response delay of the filter. Typically, a small band gap introduces a phase shift of the filtered signal and makes the filtration process difficult at the edges of the dataset. (For further information about time-domain filters, see (20)). We demonstrate this in Figure 29 on a generated sine curve. The filtered sine wave exhibits a phase-shift relative to the original signal. The first four periods of the filtered signal (to the left of the red dotted line) do not have the same amplitude as the original sine wave. The same behavior can be observed with the actual dataset in Figure 30. For the analysis of the amplitude as a function of time, we are not concerned with the phase of the data. To reconcile the misrepresented amplitude, however, we discard the initial 4 oscillations of the filtered data prior to further analysis.

Table 7. Parameters of the used filter and their description.

Parameter	**Value**	**Description**
First Stopband Frequency	0.5 Hz	Frequencies below this are filtered out
First Passband Frequency	0.8 Hz	Frequencies between these two values are kept.
Second Passband Frequency	1.2 Hz	
Second Stopband Frequency	2.0 Hz	Frequencies above this are filtered out
First Stopband Attenuation	60 dB (*default*)	Minimum factor to divide the signal by at the first stopband frequency

Passband Ripple	1 dB (*default*)	factor to multiply the signal by between the passband frequencies
Second Stopband Attenuation	60 dB (*default*)	Minimum factor to divide the signal by at the second stopband frequency
Sampling Frequency	10 Hz	Sampling rate of the data. Equals to the framerate of the video

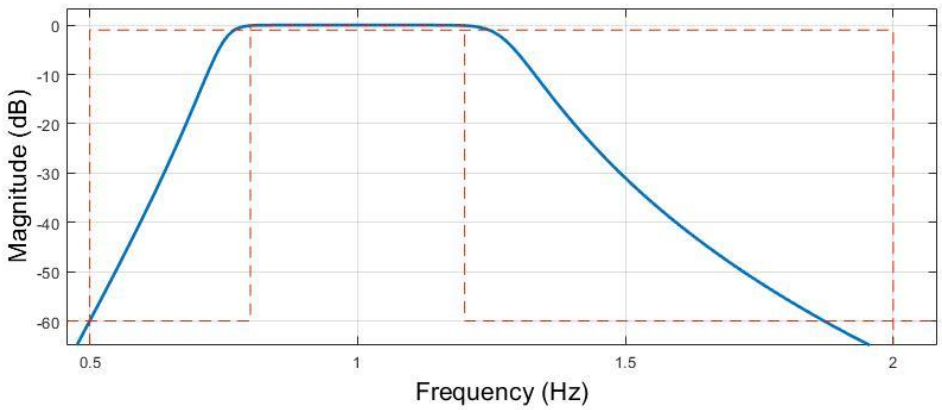

Figure 28. Frequency response of the band-pass filter used to process the oscillatory data of probe oscillation. The inner vertical dashed lines represent the passband frequencies, indicating the stable region of the response. The outer dashed lines represent the stopband frequencies; all signal outside this region gets filtered out.

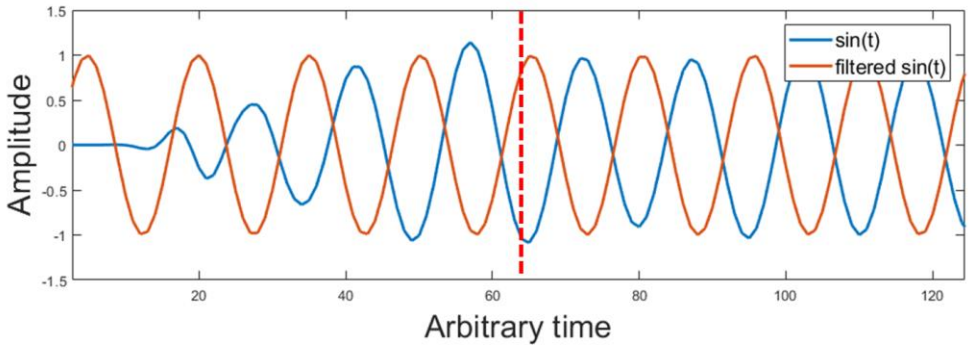

Figure 29. Demonstration of the artifact caused by the filter at the edge of the dataset. (Orange) a generated sine wave and (blue) a filtered sine wave plotted next to each other. The filtered sine wave exhibits a phase-shift relative to the original signal. The first four periods of the filtered signal (to the left of the red dotted line) do not have the same amplitude as the original sine wave.

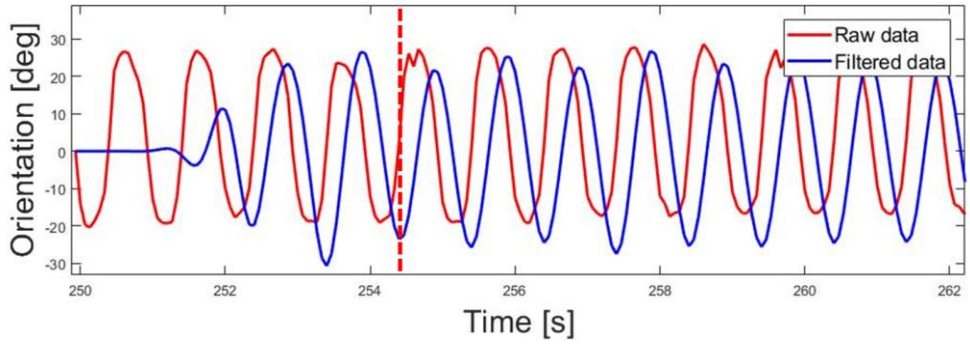

Figure 30. The initial several oscillations of the probe. The filtered data superimposed with the raw data. Due to the frequency response of the filter, a small phase-shift is present and the first several oscillations are not adequately represented. We thus remove the first four oscillations from the dataset.

The envelope was extracted from the filtered data using the MATLAB *envelope()* function. The function returns the upper and lower envelopes of the input data as the magnitude of its analytic signal. The analytic signal is calculated using the discrete Fourier transform of the data. For more information on the *envelope()* function, refer to MATLAB documentation.

5.5 REFERENCES

1. Wyatt GR. The Biochemistry of Insect Hemolymph. Annual Review of Entomology. 1961;6:75-102.10.1146/annurev.en.06.010161.000451
2. Mullins DE. Chemistry and Physiology of the Hemolymph, in "Integument, Respiration and Circulation". In: Kerkut GA, editor.: Elsevier Science; 2013. p. 356-92,
3. Wigglesworth VB. The Principles of Insect Physiology. 1982:1-7.10.1007/978-94-009-5973-6
4. Horohov DW, Dunn PE. Changes in the circulating hemocyte population of *Manduca sexta* larvae following injection of bacteria. J Invertebr Pathol. 1982;40:327-39.10.1016/0022-2011(82)90171-9
5. Gregoire CH. Blood coagulation in arthropods. V. Studies on hemolymph coagulation in 420 species of insects. Arch Biol. 1955;66((1)):103-48.
6. Ribeiro C, Brehélin M. Insect haemocytes: What type of cell is that? Journal of Insect Physiology. 2006;52:417-29.10.1016/j.jinsphys.2006.01.005
7. Rowley AF, Ratcliffe NA. The granular cells of Galleria mellonella during clotting and phagocytic reactions in vitro. Tissue and Cell. 1976;8:437-46.10.1016/0040-8166(76)90004-5
8. Arnold JW. The hemocytes of insects. In: Rockstein M, editor. The physiology of insecta. 5. 2nd ed. New York: Academic Press; 1974. p. 201-54
9. Gillespie JP, Kanost MR, Trenczek T. Biological mediators of insect immunity. Annual Review of Entomology. 1997;42:611-43.10.1146/annurev.ento.42.1.611
10. Lavine MD, Strand MR. Insect hemocytes and their role in immunity. Insect Biochemistry and Molecular Biology. 2002;32:1295-309.10.1016/B978-012373976-6.50004-5
11. Salt GW. The cellular defence reactions of insects. Cambridge: Cambroidge University Press; 1970.
12. Pech LL, Strand MR. Granular cells are required for encapsulation of foreign targets by insect haemocytes. J Cell Sci. 1996;109:2053-60.
13. Pech LL, Strand MR. Plasmatocytes from the moth Pseudoplusia includens induce apoptosis of granular cells. Journal of Insect Physiology. 2000;46(12):1565-73.10.1016/s0022-1910(00)00083-4
14. Kenny M, Giarra M, Rogers P, Barnes A, Socha J, editors. How temperature influences the viscosity of hornworm hemolymph. Society for Integrative and Comparative Biology; 2017 12-06-2017; New Orleans, LA.
15. Gu Y, Chen Z, Borodinov N, Luzinov I, Peng F, Kornev KG. Kinetics of evaporation and gel formation in thin films of ceramic precursors. Langmuir. 2014:14638–47,
16. Kornev KG, Gu Y, Aprelev P, Tokarev A. Magnetic rotational spectroscopy for probing rheology of nanoliter droplets and thin films". In: Kumar C, editor. SPRINGER book series on Characterization Tools for Nanoscience & Nanotechnology. 6. New York: SPRINGER; 2016,

17. Chevry L, Sampathkumar NK, Cebers A, Berret JF. Magnetic wire-based sensors for the microrheology of complex fluids. Physical Review E. 2013;88(6).10.1103/PhysRevE.88.062306
18. Berret JF. Local viscoelasticity of living cells measured by rotational magnetic spectroscopy. Nature Communications. 2016;7.10.1038/ncomms10134
19. Gu Y, Kornev KG. Ferromagnetic Nanorods in Applications to Control of the In-Plane Anisotropy of Composite Films and for In Situ Characterization of the Film Rheology. Advanced Functional Materials. 2016;26(22):3796-808.10.1002/adfm.201504205
20. Oppenheim A, Willsky A. Time- and Frequency Characterization of Signals and Systems. Signals & Ssystems. 2 ed: Pearson; 1996,

CHAPTER VI

STRUCTURAL IMAGING OF HEMOLYMPH OF CATERPILLARS

6.1 INTRODUCTION

6.1.1 Adhesive and non-adhesive cells

Hemocyte-rich hemolymph of caterpillars exhibits a distinguishable microrheological behavior compared to hemocyte-poor hemolymph of adults.

The composition of plasma in lepidopteran larvae (caterpillars) is complex. Sodium, potassium, calcium, magnesium, chloride, phosphate, amino acids, and various biopolymers and other organic and inorganic compounds make up 8 to 16 gm total per 100 ml of water (1, 2). Estimated from the cell count, assuming the average diameter of a single cell to be 5 μm, the cells constitute roughly 0.1-0.3 vol% of hemolymph (3, 4). These cells, called hemocytes, vary in size, shape and function (5-7). Six types of hemocytes have been identified (6, 8, 9). They can be broken into two groups: adhesive and non-adhesive (6, 9, 10). The adhesive hemocytes are more abundant. These hemocytes – called granular cells and plasmatocytes – are involved in wound healing and phagocytosis, engulfing a foreign particle by forming a vesicle around it (5, 6, 9-15). As first observed by Wigglesworth, during wound healing, these hemocytes accumulate at the wound cite and aid the regrowth of the epidermal (skin) cells (16). Non-adherent hemocytes include oenocytoids, which synthesize prophenoloxidase (proPO) – precursors for clots, and other types of cells (5, 6, 9, 11). The importance of different adhesive behavior of cells in the context of clot formation was predicted a long time ago by Steinberg (17-19) based on preliminary experimental work of Holtfreter (20-25).

6.1.2 Steinberg's differential adhesion hypothesis for cell aggregates

Steinberg's differential adhesion hypothesis (DAH) draws a parallel between cellular adhesion and the attraction of liquid molecules. A liquid on a macroscopic scale is a continuous medium with macroscopic mechanical properties, such as viscosity and surface tension. These macroscopic properties arise as a direct result of particle-to-particle interactions on the molecular scale. In multicomponent liquid mixtures, properties such as miscibility arise due to strong or weak interactions between molecules. Consider, for instance, a perfectly mixed mixture of hexane in water. The polar water molecules – while are not repelled form the non-polar hexane molecules – prefer to be surrounded by other polar water molecules and *vice versa*. As a result, distinct water and hexane droplets form in the mixture. As time goes on, like droplets combine to form two pure phases of water and hexane.

Tissues and cellular structures can also be treated as continuous media consisting of much smaller components – adhesive cells. The idea to treat cellular structures in such a way was inspired by cell sorting experiments performed by Holftreter, where he observed a tendency of alike cells to sort out and associate with each other (21, 23, 25). Steinberg hypothesized that this universal sorting is due to adhesive cells behaving in a similar fashion to liquid molecules - individual cells of the same type are more adhesive to each other than to other types of cells (17). Similar to the hexane/water example above, a uniformly mixed aggregate of two types of cells self-segregates into two distinct groups. The equilibrium configuration depends on the surface and interfacial tensions of the cell populations (26). These surface tensions have been experimentally demonstrated to be dependent on the adhesive properties of the cells (27, 28). Steinberg's DAH has

gathered extensive experimental and theoretical support for both vertebrates (19, 29-31) and invertebrates (32-35) and is currently widely accepted (36) . For a more detailed discussion of the DAH as well as other models of tissue growth, see (29).

In this chapter, we will attempt to provide a qualitative analysis of Steinberg's DAH in application to the clot formation in wounded caterpillars. If the DAH is indeed the driving mechanism behind the self-assembly of cells during the formation of the soft clot, we should expect adhesive cells to form drop-like aggregates in the plasma. It has been hypothesized that the hemocytes become adhesive after they are exposed to precursors in the epidermis (skin layer) of the caterpillars (8, 37). This means that hemocyte aggregates should only appear in the hemolymph extracted through a wound and not form in hemolymph extracted without contact with the wound.

6.1.3 Extracellular gelation

Hemocyte aggregation is not the only manifestation of hemolymph coagulation. Humoral reactions caused by the self-assembly of lipids and proteins, such as gelation and fibrin-like formations have been observed (37, 38). Gelation of extracellular material occurs during the soft clot formation, when the proteins become glycosylated and form fibrous strings (8, 39-41). In *Drosophila*, the soft clots were shown to be removable from the bulk of hemolymph by the 'pullout method' (39). The method consisted of suspending paramagnetic beads in the forming clot. These beads were coated with chemical anchors, allowing the clot to adhere to the beads. When the paramagnetic particles attach to the clot, the latter can be pulled out using a magnet. The formation of the clot was accompanied by thickening of the liquid and formation of fibers, which are

invisible with light microscopy but can be targeted with fluorescent labels (39). The magnetic pullout method is a great simple method for isolating the clot material, as it allows one to wash and purify the fibrous structure after extraction. It is a destructive method, as it requires extensive swirling to mix the soft clot with the magnetic beads. The soft clot is adherent and readily attaches itself to metal surfaces. As was shown in (42), this allows a soft clot filament to be drawn out from a droplet of hemolymph by dipping a needle in it. This indicates that this soft clot is a separate phase of hemolymph that forms inside the liquid. This behavior is consistent with the DAH, as adherent hemocytes and proteins self-assemble and sort themselves out into a gel-like material. The material organization in the clot has never been discussed in the literature and thus needs to be explored.

6.1.4 Formation of extracellular fibers

Extracellular fibrin-like filaments have also been observed in hemolymph of larval *M. sexta* and were able to be artificially produced in cell-free hemolymph (37, 38). Work by Minnick et al (43) describes the filament formations in the clotting hemolymph of early 5^{th} instar *M. sexta* as extracted via a 2mm incision immediately anterior to the horn of the caterpillar (44). According to this study, fibrous strands only form in hemolymph in the presence of M13 protein – a glucose-specific lectin – and with glucose concentration below $5*10^{-4}$ M. Two relevant scenarios were discussed: 1. As-is hemolymph required an incubation time of 30 minutes before strands became observable; 2. Hemolymph with the added M13 concentrate (obtained by fractionation of hemolymph from bacteria-treated caterpillars) started forming these strands within 10 seconds. Work

of Geng et al (37) further explored this phenomenon. Hemolymph that was collected from an incision in the tip of an abdominal proleg on a glass coverslip formed fibrous structures in both untreated and bacteria-treated caterpillars. Hemolymph of untreated caterpillars that was collected via a hypodermic needle from pericardial space, however, did not produce these structures while observed for several hours. Furthermore, even when this hemolymph was exposed to a glass substrate, no fibers were observed. The hemocytes in this hemolymph did not aggregate in the bulk, but adhered to glass substrate when exposed to it.

The fibrous structures rapidly formed when the isolated M13 protein was added to hemolymph. The structures also formed when M13 was added to the cell-free hemolymph as well as to a mixture of salts, amino acids, sugars, and vitamins ((45) for mixture composition). This suggests that cells do not contribute any building blocks for the fibrous structure. The contribution of these fibers to the clot formation is not clear and will be explored further in this chapter.

6.1.5 Challenges in studying of soft clots

Studies of the structure of the soft clot are challenging for several reasons. First, the clot begins to form within a minute after extraction of hemolymph from the body. The experimental protocols thus must be rapid. Second, the clot is highly adhesive to foreign surfaces, so the interaction with the material must be minimal. Third, the hemolymph must not be contaminated from internal (e.g. gut) or external sources. The extraction procedure thus must be rapid. Finally, the amount of analyzable materials is small – a single caterpillar can only provide several hundreds of microliters. This amount is higher

than what we have obtained from adults, but this material cannot be handled with capillary tubes, due to the aforementioned adhesiveness to foreign surfaces, which makes handing it challenging. The analytical methods thus must be adjusted accordingly.

6.1.6 Goals of the study

In this chapter, we aim to describe the structure of the self-assembled cellular and humoral clot material in incubated hemolymph. Wigglesworth's clotting scenario(16) coupled with Steinberg's differential adhesion hypothesis imply that highly anisotropic fibrous structures could form during early stages of wound healing. Thus, we follow Wigglesworth's scenario and Steinberg's DAH to explain the formation of these structures. We will also consider changes in clot materials as a function of incubation time.

We analyze the structure of the hemolymph using phase-enhanced microscopy, dye-labeled florescent microscopy, scanning electron microscopy, and microCT. We perform these studies for hemolymph after incubation at high humidity and *in-vitro* during incubation. The three-dimensional structures of the clots required all optical microscopy to be conducted with no cover slip to preserve the structures. Due to the instability of hemolymph after extraction, and the precision required to obtain clean samples, special procedures were developed to undertake this study. To better visualize certain aspects of the clot, the material was manipulated with and without probes and stretched into liquid filaments similar to those described in section 6.1.3 for *Drosophila*.

To capture the time evolution of the sample with SEM, the material was rapidly frozen in liquid nitrogen after certain incubation time and freeze-dried prior to imaging.

6.2 RESULTS

6.2.1 Hemocyte aggregation and densification

Optical observation under a bright field microscope (Olympus, BX-51) of in-vitro incubating hemolymph reveals that hemocytes self-assemble into large aggregates at the glass substrate. Figure 31 captures an example of such behavior. In panels A-E, the cells (visible as bright and dark circles) can be observed freely floating in the plasma (the grey background) as well as consisting as a part of the aggregate, which is labeled with purple on the images for illustration (Photoshop); t_i is the incubation time of the sample. The area of the purple-labeled aggregate was analyzed for several points and plotted versus incubation time in panel F. At t_i = 2 minutes, the area of the aggregate appears smaller than that at t_i = 2.9 minutes. This is most likely due to the fact that during that time, new cells adhere to the aggregate, increasing its size. After the 2.9-minute mark, the area can be seen to decrease at an initially high, but decreasing rate. After 10 minutes, the area seems to stop decreasing. Another observable dynamic is that initially, the aggregate appears to have a loosely packed structure and a branchy shape. As time goes on, however, the aggregate becomes less branchy and denser. This dynamic is consistent with the DAH hypothesis as it can be explained with an apparent surface tension of the aggregate. The apparent surface tension of the aggregate occurs since the aggregate effectively forms a separate phase from the plasma. This surface tension tends to squeeze the aggregate into a sphere, pushing out all of plasma from the inside. This is similar to the water-hexane example described above.

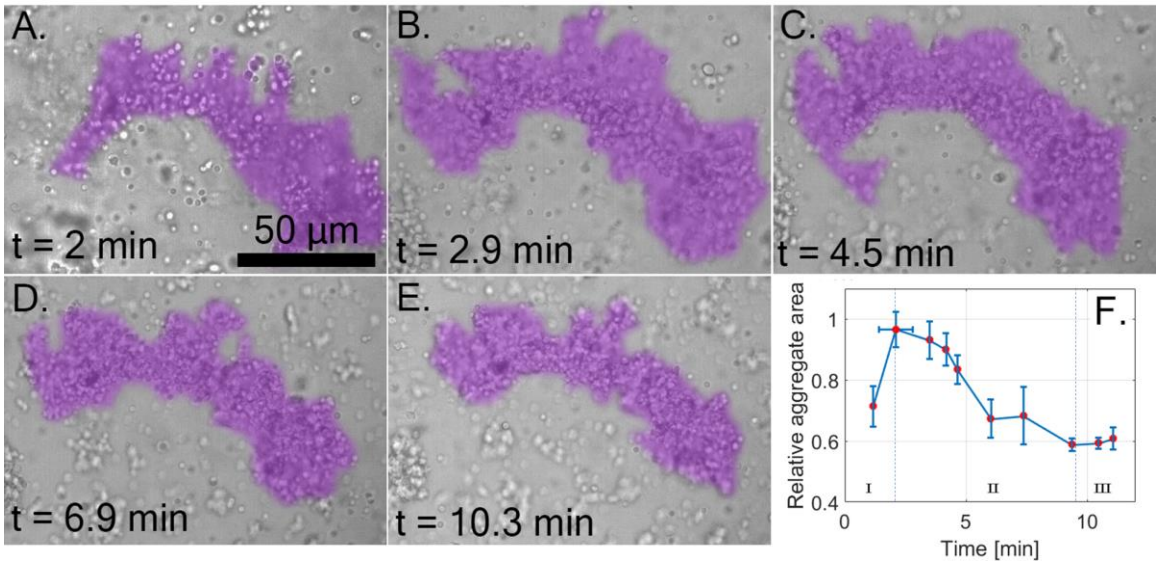

Figure 31. (A-E) A gallery of bright field micrographs of an in-vitro incubating droplet of M. sexta larva hemolymph during. The hemocytes can be seen as bright and dark circles both as freely floating in the plasma (grey background) and as a part of the aggregate (labeled with purple). t is the incubation time of the sample. Initially, the aggregate is loosely packed and has branchy structure. With time, the aggregate appears to become less branchy and denser. (F) The area of the purple aggregate is plotted versus incubation time, t, for three aggregates from different caterpillars. Initially, the area increases, likely due to the fact that new hemocytes adhere to the clot. At certain point, the area begins quickly decreasing. The decrease rate seems to approach 0 at around 10 minutes of incubation.

6.2.2 Time-lapse study of cellular dynamics using phase-enhanced microscopy

To obtain a clear understanding of the mechanisms behind the hemocyte migration, a time-lapse under high magnification in an inverted transmitted-light phase-enhanced microscope (Nikon Eclipse Ti) was recorded. Two snapshots are presented in Figure 32. Snapshots A and B are of the same location in the sample with timestamps of 10 and 60 minutes of incubation time, respectively. It appears that the hemocytes in A are loosely packed with amorphous material filling up space in the aggregates between the cells. This amorphous material is presumably pseudopodia – thread-like protrusions of the cell membrane of certain hemocytes. As time goes on and the clot matures, the

hemocytes appear to pack more closely with the amorphous material becoming significantly darker and denser. The average distance between the centers of any two adhered cells, l, decreases; at t_i = 2 minutes is l = 8.9±1.5 μm (N = 27) and at t_i = 7 minutes is l = 7.6 ± 1.1 μm (N = 37). The entirety of the movie is presented in supplementary material.

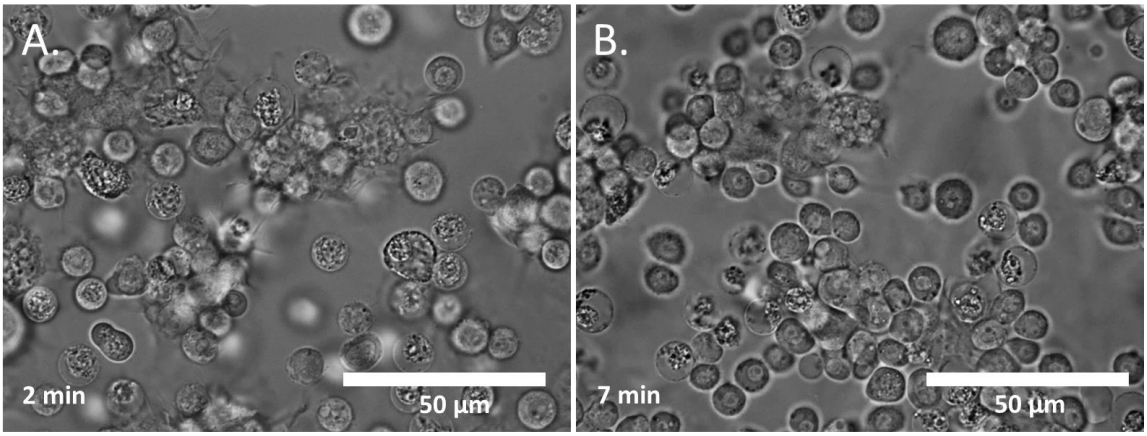

Figure 32. Two snapshots of a time-lapse (t_i = 2 and 7 minutes after extraction) under high magnification in an inverted transmitted light phased enhanced microscope. Aggregation of hemocytes, where hemocytes are connected with amorphous dark grey material, is visible. As incubation time increases, the hemocyte aggregates become closer packed and the connective grey material darkens. The average distance l between two adjacent hemocytes at t_i = 2 minutes is l = 8.9±1.5 μm (N = 27) and at t_i = 7 minutes is l = 7.6 ± 1.1 µm (N = 37).

6.2.2.1 Role of pseudopodia in hemocyte aggregation

Careful analysis of the time-lapse allows for the kinetics of the behavior of the pseudopodia to be studied. Figure 33 demonstrates the kinetics of growth of a single pseudopodium thread. The thread can be seen to extend from the mother cell and bend. This likely occurs to help the thread find a different cell surface to adhere to. Figure 34 presents a time-lapse gallery of the effect of pseudopodia on the development of a hemocyte aggregate. The pseudopodia (outlined in blue) can be seen to originate from

only a few cells and drastically change its shape with time. This is presumably to adhere to remote hemocytes and pull them closer to the mother cell of the pseudopodia. This way, the aggregates are able to grow larger, merge with nearby aggregates, and change their shape.

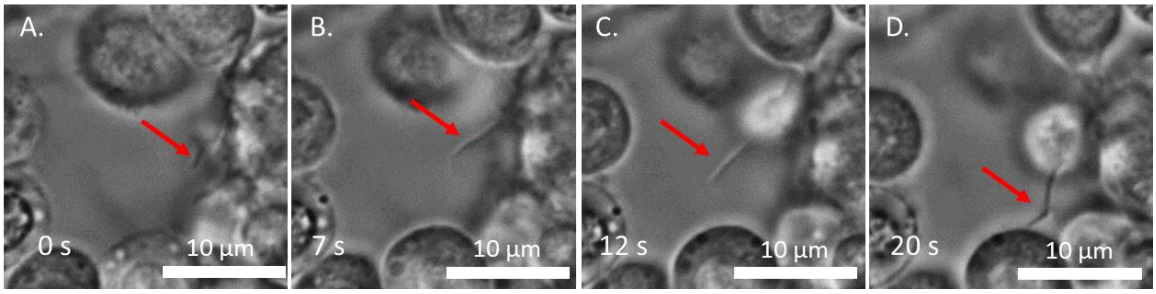

Figure 33. Growth of a single pseudopodium thread labeled with a red arrow. It can be seen that the thread bends as it extends. This possibly helps the thread find a different cell surface to adhere to.

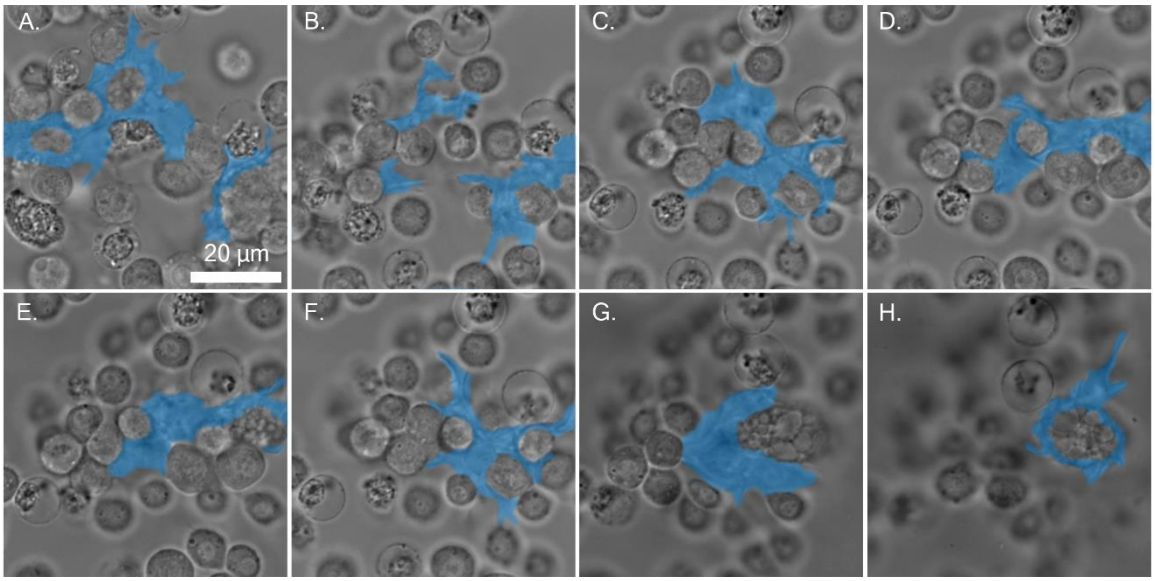

Figure 34. A time-lapse of the development of the pseudopodal extensions (outlined in blue). It can be seen that the extensions originate from only a few hemocytes and can extend for tens of microns.

6.2.2.2 Surface interaction between hemocytes

The surface behavior of hemocytes is an important parameter in the process of aggregation. When two hemocytes are in contact with each other, their surfaces interact. This surface interaction is dependent on the surface energies of the hemocytes and the medium around them. The opening angle that the cell membranes form when two cells are attached to each other (angle θ_o on Figure 35, D) is an important indicator of the surface energies of these interactions. This opening angle can be related to a conventionally defined contact angle (angle θc on Figure 35, D) as $\theta_c = 180 - \theta_o/2$, but in this context, it is more convenient to work with the concept of the opening angle. If the opening angle is small, the two cells prefer to maximize the cell-cell interfacial area and minimize the cell-medium area; this means that the cells are phobic towards the medium. Conversely, if the opening angle is large, the cells prefer to maximize the cell-medium area; this means that the cells are philic towards the medium. We consider three opening angle cases: angle α when three cells are touching (depicted in Figure 35, top-left); angle β when two cells are touching surrounded with plasma (depicted in Figure 35, middle-left); and angle γ when two cells are touching surrounded with pseudopodia (depicted in Figure 35, bottom-left). The number of measurements for each scenario is n_α=12, n_β = 14, and n_γ = 7 and the values were determined to be α = 120 ± 5°, β = 70 ± 11°, γ = 113 ± 6°, as is depicted in the bar graph in Figure 35. The angle α is as expected and serves as a reference. Angle β indicates that the hemocytes are phobic towards plasma and tend to minimize the cell/plasma interfacial area. Angle γ is greater than α, which indicates that

cell/pseudopodium interface is preferred to the cell/plasma interface, but smaller than β, which indicates that the cell/cell contact is preferential to the cell/pseudopodium contact.

From the measured opening angles, it is possible to extract the interfacial tensions of cell-plasma and cell-pesudopodia relative to the cell-cell interfacial tension. Consider a free-body-diagram in Figure 35.D Figure 35. The interfacial tension force between two identical cells sharing a flat interface, $\vec{\sigma}_{cell-cell}$, is balanced by two interfacial tension forces between the cell and the medium, $\vec{\sigma}_{cell-medium}$, as:

$$\vec{\sigma}_{cell-medium} + \vec{\sigma}_{cell-medium} + \vec{\sigma}_{cell-cell} = 0 \tag{1.38}$$

Writing the x-components of the force balance, we obtain

$$\sigma_{cell-medium}\cos(\frac{\theta_o}{2}) + \sigma_{cell-medium}\cos(\frac{\theta_o}{2}) = \sigma_{cell-cell} \tag{1.39}$$

where θ is the opening angle between the two cells measured from image analysis.

Introducing a parameter $\sigma^*_{medium} = \sigma_{cell-medium} \big/ \sigma_{cell-cell}$, we rewrite the equation as:

$$\sigma^*_{medium} = \frac{1}{2\cos(\frac{\theta_o}{2})} \tag{1.40}$$

Thus, the relative interfacial tensions between a cell and either another cell (σ^*_{cell}), pseudopodia ($\sigma^*_{pseudopodia}$), and plasma (σ^*_{plasma}) were calculated and are presented in the table in Figure 35.

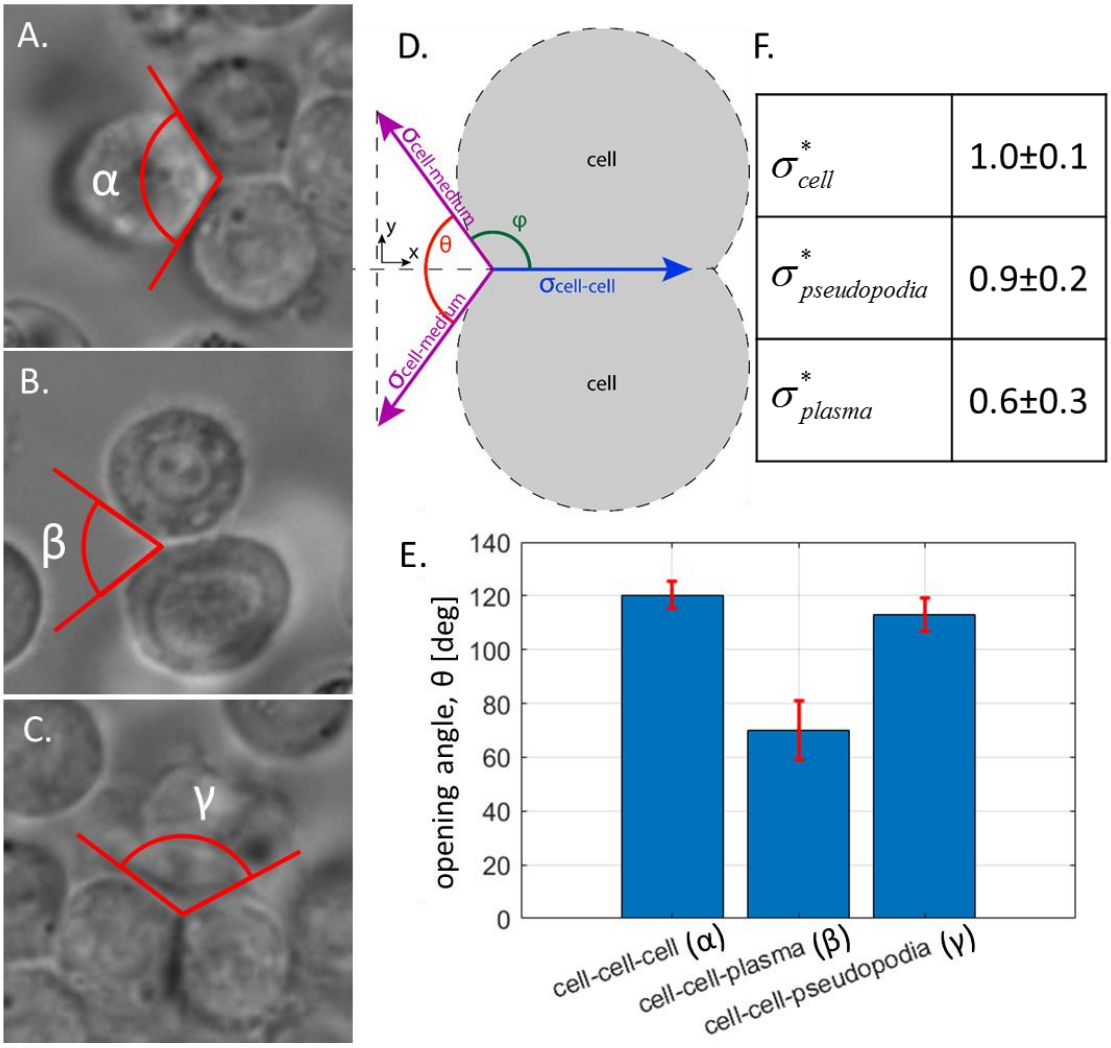

Figure 35. (A-C) The opening angle between two cells in three scenarios: (A) when three cells are in contact, two cells make a contact angle α; (B) when two cells are in contact with plasma, they make a contact angle β; (C) when two cells are in contact with pseudopodia, they make contact angle γ. (D) The free body diagram, in which we define the interfacial tensions σ, the opening angle θ, and the contact angle φ between two cells with a flat interface suspended in a medium. (E) A bar graph of measured opening angles. The number of measurements for each scenario is n_α=12, n_β = 14, and n_γ = 7. The error bars are the standard deviation of the measurement. (F) the table of calculated surface tension ratios according to equation (5.3)

The implication of the relative contact angles is that it is energetically preferential for the hemocyte to be surrounded by other hemocytes, it is slightly less preferential to be

surrounded with pseudopodia, and it is the least preferential to be surrounded by plasma. Consider a free-flowing hemocyte. As soon as a pseudopodium of another cell makes contact with this hemocyte, the pseudopodium wants to spread along its surface. This creates a pulling force between the two cells. As the hemocyte is pulled towards the mother cell of the pseudopodium, it may encounter another hemocyte attached to the same pseudopodium. As soon as the two hemocytes touch, they form an interface, which spreads since it is energetically preferable to the cell-plasma interface. The process may repeat for many hemocytes, leading to large aggregates.

A similar scenario to the one described above is observed in Figure 36, which presents a gallery of time-lapse frames, depicting a 4-cell cluster of an aggregate of hemocytes. The cells are colored in red, yellow, purple and pink and the involved pseudopodia are colored in blue. Initially (panel A), the red and yellow cells are lightly touching, and the pink cell is free-flowing near an extending pseudopodium. With time (panels B, C) the interface between red and yellow increases, while the pseudopodium attaches to the pink cell and drags it to the right. In panel D, the purple cell, which is attached to both red and pink cells, comes into focus, while the pseudopodium continues to drag the pink cell to the right. In panel E, the red/purple and the pink/purple interfaces grow and the pink cell, which is half-engulfed in pseudopodia, first touches the red cell. As the cell-cell interaction is energetically preferred to the cell-pseudopodia interaction, the pink cell disconnects from the pseudopodia and attaches to the red and yellow cells (panel F). In panel G, the red and pink cells disconnect and the cells temporarily form a diamond configuration. It appears that this happens due to the fact that the red cell

adheres to an aggregate on the top out of the frame and the pink cell adheres to an aggregate on the bottom. The two aggregates thus stretch the 4-cell aggregate vertically. In panel H the purple and yellow cells form an interface and the four cells remain in this configuration until the end of the observation.

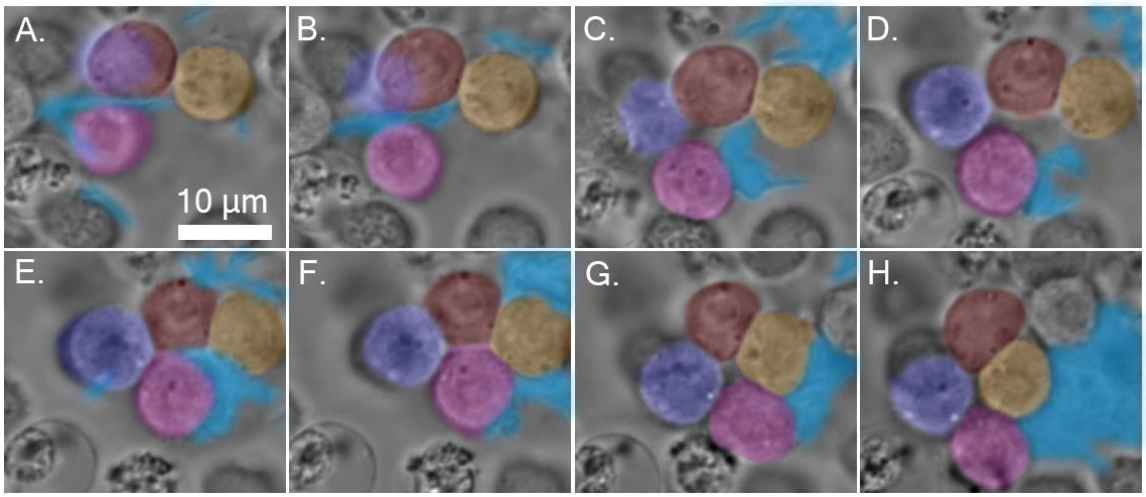

Figure 36. A close observation of a 4-cell segment of an aggregate developing. The cells are labeled with red, yellow, purple and pink and the involved pseudopodia are labeled with blue. See discussion in text.

The observations thus far are consistent with a long-standing hypothesis that plasmatocytes and granulocytes extrude pseudopodia in response to foreign surfaces and the other hemocytes adhere to the formed network (8, 10). The nature of the adhesion between the hemocytes, however, remains unclear. Are the cell membranes inherently adhesive or is there an adhesive agent in the plasma? Moreover, why do the cells often adhere and detach from each other during the early stages of the soft clot formation and remain adhered during the late stage? One explanation is that the initial adhesion between the cells is weak, but with time is facilitated by a protein from the plasma. We explore this hypothesis in the next section with targeted florescent staining.

6.2.3 Targeted staining and florescent imaging of glycosylated proteins

To gain insight into the nature of the material connecting the hemocytes in the aggregates, a florescent staining study was performed. Rhodamine-labeled peanut agglutinin (PNA) was chosen for this study, which was shown to efficiently label the clots of *Drosophila* (39, 41, 42) and *Galleria* (46) by binding to the clotting proteins, which are known to be highly glycosylated in many species (40). To verify the feasibility of this approach and to determine the optimal amount of dye to use, 0, 5, 10, and 15 μl of 50 μg/ml rhodamine-PNA dye solution were added to a 80-100 μl sample of hemolymph and imaged with a Nikon Ti-Eclipse fluorescent microscope (20X MImm with water, NA= 0.75, TRITC filter). The results (Figure 37) indicate that the PNA dye successfully labels the material between the cells in the aggregates and that optimal concentration of dye is between 5 and 10 μl of 50 μg/ml rhodamine-PNA solution per 100 μl of hemolymph. On the image, the brighter red region indicates a larger dye amount and therefore presence of the glycosylated proteins. A histogram stretch was performed for best visualization. The red background does not necessarily represent presence of extra dye. Instead, the highest brightness difference between the background and the object of interest is desired.

The uncertainty of the hemolymph volume in each sample comes from the necessity to minimize the interaction between hemolymph and foreign surfaces due to extreme adhesiveness of the hemocytes. Thus, hemolymph was bled directly from the caterpillar into the incubation wells and its volume could only be approximated by the number of drops that fell from the wound into each well. The volume of each drop was measured to be roughly 20 μl and each incubation well received 4-5 droplets.

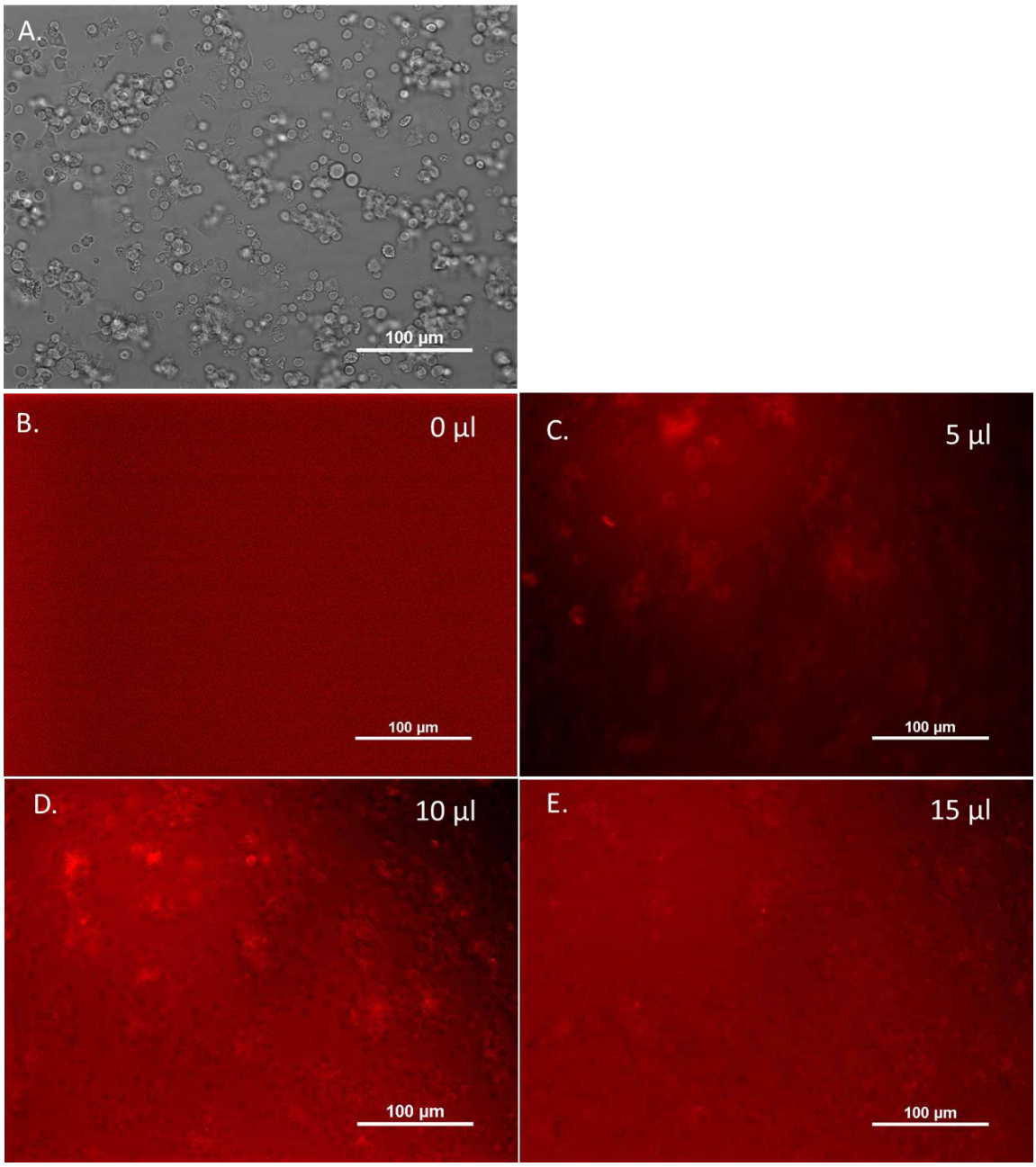

Figure 37. Hemolymph of *M. sexta* larvae stained and incubated for 10 minutes with the PNA dye. A.The phase-enhanced and B-C the fluorescent images of the cells and structures adhered to the substrate dyed with 0, 5, 10, and 15 µl of PNA, respectively. The brighter red region indicates a larger dye amount and therefore presence of the glycosylated proteins. The brightness and contrast of the images were adjusted for the best visibility, so the red background does not necessarily represent the presence of dye. Instead, the highest brightness difference between the background and the object of

interest is desired. The optimal dye volume per 100 μl of hemolymph is between 5 and 10 μl.

6.2.4 Florescent imaging of filamentous structure in incubated hemolymph – swirling and pullout

Following the successful labeling of the soft clot proteins, we checked the applicability of the soft clot pullout experiments in *Drosophila* (42) for the *M. sexta* larvae. The hemolymph was incubated with the dye and stirred with a needle. During stirring, the soft clot material adhered to the needle and was pulled out from the bulk of the sample along with the needle. The needle was then placed under a fluorescent microscope and the material that adhered to it was imaged using phase-enhanced and fluorescent microscopy. These images were compared with the images of the bulk hemolymph that remained after the stirring.

The images of the soft clot are presented in Figure 38. Panels A, C, and E depict the material unperturbed by the stirrer and panels B, D, and F depict the material adhered to the stirrer and pulled out from the hemolymph. Panel A is a composite image of a phase-enhanced (greyscale) and a fluorescence (red) micrographs. The phase-enhanced portion of the image reveals hemocyte aggregates and the fluorescent portion of the image reveals glycosylated proteins inside the aggregates. The glycosylated proteins do not appear outside of the aggregates. From panel C, which presents only the fluorescent micrograph from panel A, it appears that the proteins line the outer walls of the hemocytes inside the aggregates. Presumably, these proteins act as an adhesive for the hemocytes.

Similarly, panel B is a composite image of a phase-enhanced (greyscale) and a fluorescence (red) micrographs of the stirred and pulled-out soft clot. The phase-

enhanced portion of the image reveals a large structure of hemocytes in the lower and the right parts of the image and a lack of such structure on the top-left part of the image. The fluorescent portion of the image indicates that the hemocyte structure contains a large amount of the glycosylated proteins, which are absent outside of the structure on the top-left part of the image. The structure of the glycosylated proteins is better visualized on a fluorescent micrograph without the phase-enhanced portion (Figure 38 C). Due to a non-uniform background of the florescent image caused by the three-dimensionality of the large clot, it may be challenging to see the fibrous structure by eye. To guide the reader, the following analysis was performed.

The original image was broken into columns of pixels in a direction perpendicular to the fibers (vertically). The intensity profiles were extracted for each pixel column, and local maxima for each intensity profile were found. Each intensity profile was plotted with an offset corresponding to the pixel column location; the colors were varied for easier visualization. The locations of the profile intensity maxima were superimposed on the plot in blue (Figure 38 F). The intensity maxima form chains, corresponding to the fibers in the image. It can thus be clearly seen that the proteins form long fibrous structures inside the hemocyte clot similar to the one found in *Drosophila* and described as a soft clot (41). These fibrous structures are likely a result of stretching of the soft clot material during swirling and pulling out, as no well-developed fibrous structure can be seen on the unperturbed sample (Figure 38 E). We hypothesize that the protein material that forms the fibrous structure during stirring/pulling-out is initially stored between the hemocyte walls in the hemocyte aggregates. During stirring, the hemocyte aggregates

break up and the stresses induced by the stirrer stretch the proteins into long fibers. We address this further in chapter 9, where we discuss the structures formed in the liquid bridges during the pulling out of the soft clot from hemolymph.

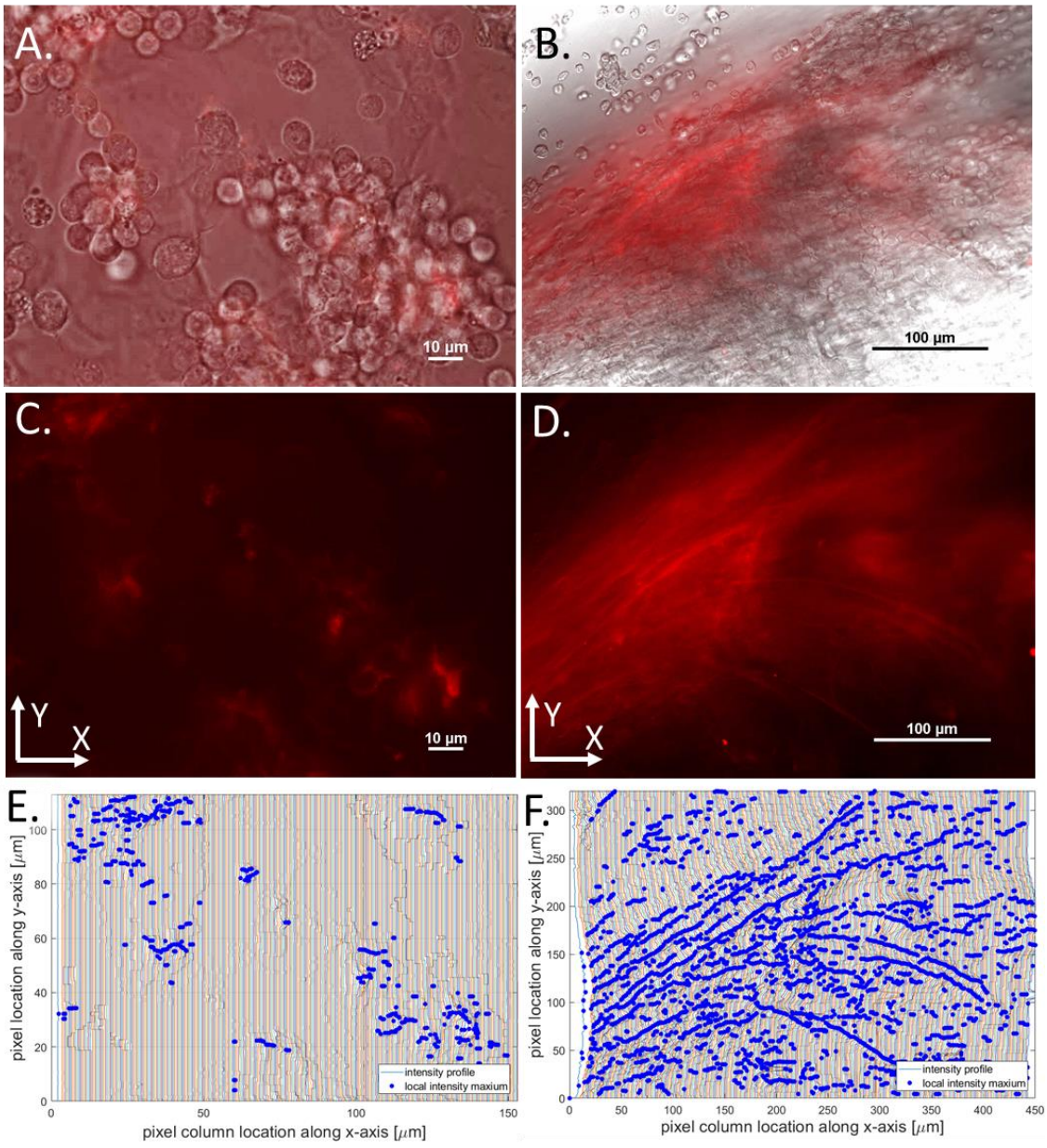

Figure 38. Hemolymph from *M. sexta* larvae stained with Rhodamine-labeled PNA and incubated for 8-15 minutes. (A, C, E) depict material unperturbed by the stirrer and (B,D,F) depict the material adhered to the stirrer(A and B) Composite imaged of phase-enhanced (greyscale) and fluorescence (red) micrographs of the unperturbed hemocyte aggregated and a 'pulled out' soft clot, respectively. The phase-enhanced portion of the image reveals hemocyte aggregates and the fluorescent portion of the image reveals glycosylated proteins inside the aggregates. The glycosylated proteins do not appear

outside of the aggregates. (C and D) The fluorescent micrographs of the unstirred material, and the 'pulled-out' clot, respectively. The labeled proteins line the outer walls of the hemocytes inside the unperturbed aggregates. The labeled proteins stretch into long fibers in the 'pulled-out' soft clot. (E) Extracted intensity profiles for the pixel columns of the florescent image with labeled local maxima of the profiles to represent fibers. No fibrous structure is visible in the unperturbed material and long fibers are apparent in the 'pulled-out' material.

As a control, hemolymph obtained from the pericardial puncture method was used. Since only several microliters of hemolymph could be obtained from this method, the amount of dye was also lowered by diluting the solution to 0.5 μg/ml and adding 10 μl of it to the sample. The rest of the procedure was the same. The results indicated no fibrous structure in the bulk. Furthermore, no clot adhered to the stirrer and thus it could not be imaged.

6.2.5 Rapidly frozen incubated hemolymph

There are two limitations to the optical microcopy techniques used thus far. First, the magnification is limited to the optical range, with the feature size larger than 400 nm. Second, the working distance at higher magnification is short (*e.g.* a 60x water-immersion objective used in this study had a working distance less than a millimeter) and only allows imaging next to the substrate. The study of structure far away from the substrate or interface thus calls for a different approach.

Scanning electron microscopy (SEM) offers a much improved resolution with a higher working distance. A downside of most SEM systems is the necessity for vacuum around the sample and relatively large signal accumulation time, which makes liquid state imaging of dynamic systems difficult. A countermeasure to this challenge is to rapidly freeze the sample, thus arresting all reactions, and to consequently freeze-dry the

sample by slowly sublimating the ice away, thus preserving the structure of the solutes during freezing. The freeze-dried sample can be easily observed under SEM. This technique has been used by biologists for decades (47). Additionally, the freeze-dried samples can be observed under x-ray microCT – a technique for imaging three-dimensional structure inside a solid sample.

6.2.5.1 SEM imaging of freeze-dried hemolymph

SEM images of freeze-dried hemolymph revealed a porous polymeric structure with bridges between the pores. In samples of hemolymph dripped via the wound for incubation times smaller than 10 minutes, the pores typically originate at the substrate and propagate upwards (Figure 39 A, C, D, E). This type of directional porosity is characteristic of directionally frozen polymeric solutions of high molecular weight, such as aqueous poly(vinyl alcohol) M_w = 10,000 g/mol , and ~10%wt concentration (48). For incubation times of 20 minutes or higher, the structure changes to lamellar (Figure 40 A, B, C, D and Figure 41 C, D). The structure in samples extracted with a pericardial method is also porous, but exhibits no directionality (Figure 43 and Figure 44). The pericardial sample with a smaller incubation time demonstrated a lower density uniform structure throughout the droplet (Figure 43), while the sample with higher incubation times demonstrate a higher density patchy structure (Figure 44).

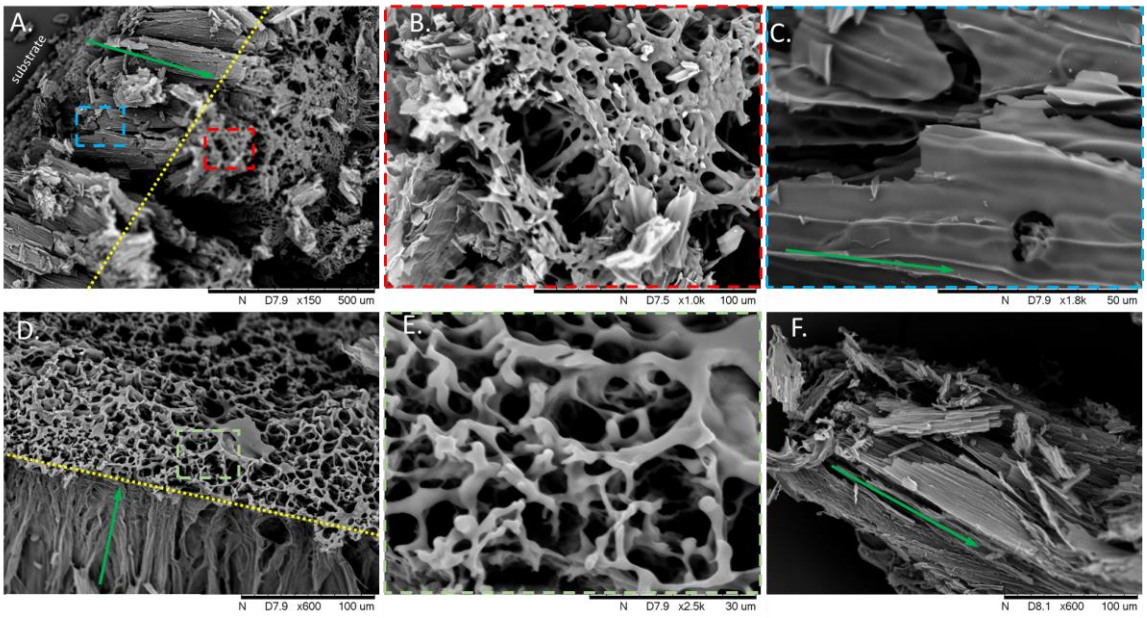

Figure 39. SEM image of a freeze-dried hemolymph from *M. sexta* larvae droplet. The sample was bled directly on a cold substrate. Extraction method: wound; incubation time: none. A piece of the sample was broken off to image the internal structure. The substrate is labeled with white text. The pore direction is labeled with a green arrow. The edge of the sample along the break separating the internal pore structure from the surface structure is labeled with a yellow dashed line. (A, D) The pores propagating from the substrate to the surface are apparent. (B) Zoomed-in micrograph of the surface segment from A. (C) Zoomed-in micrograph of the pores segment from A. (E) Zoomed-in micrograph of the surface segment from D. (F) A broken-off piece of sample from the main droplet demonstrating its structure.

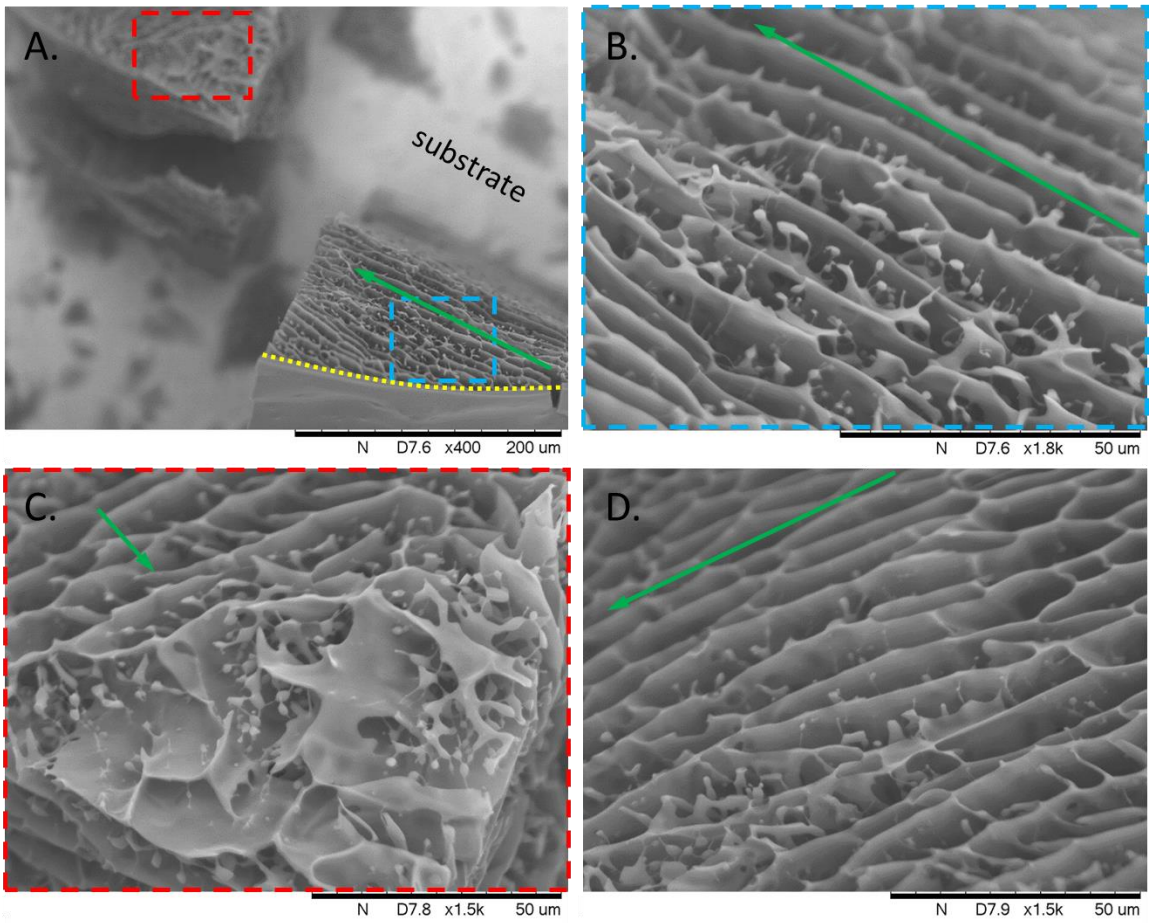

Figure 40. SEM image of the residue that remined on the substrate after the sample broke off during freeze-drying. Extraction method: wound; incubation time: 60 minutes. The substrate is labeled with black text. The pore direction is labeled with a green arrow. The edge of the sample along the break separating the internal pore structure from the surface structure is labeled with a yellow dashed line. (A) The substrate, the lamellar pores, and the smooth surface are visible. The pores do not seem to propagate from the substrate to the surface. The smooth surface is possibly an artifact of the sample preparation. (B-D) Zoomed-in images of the pores. Many small fibers propagating along the lamellae are visible.

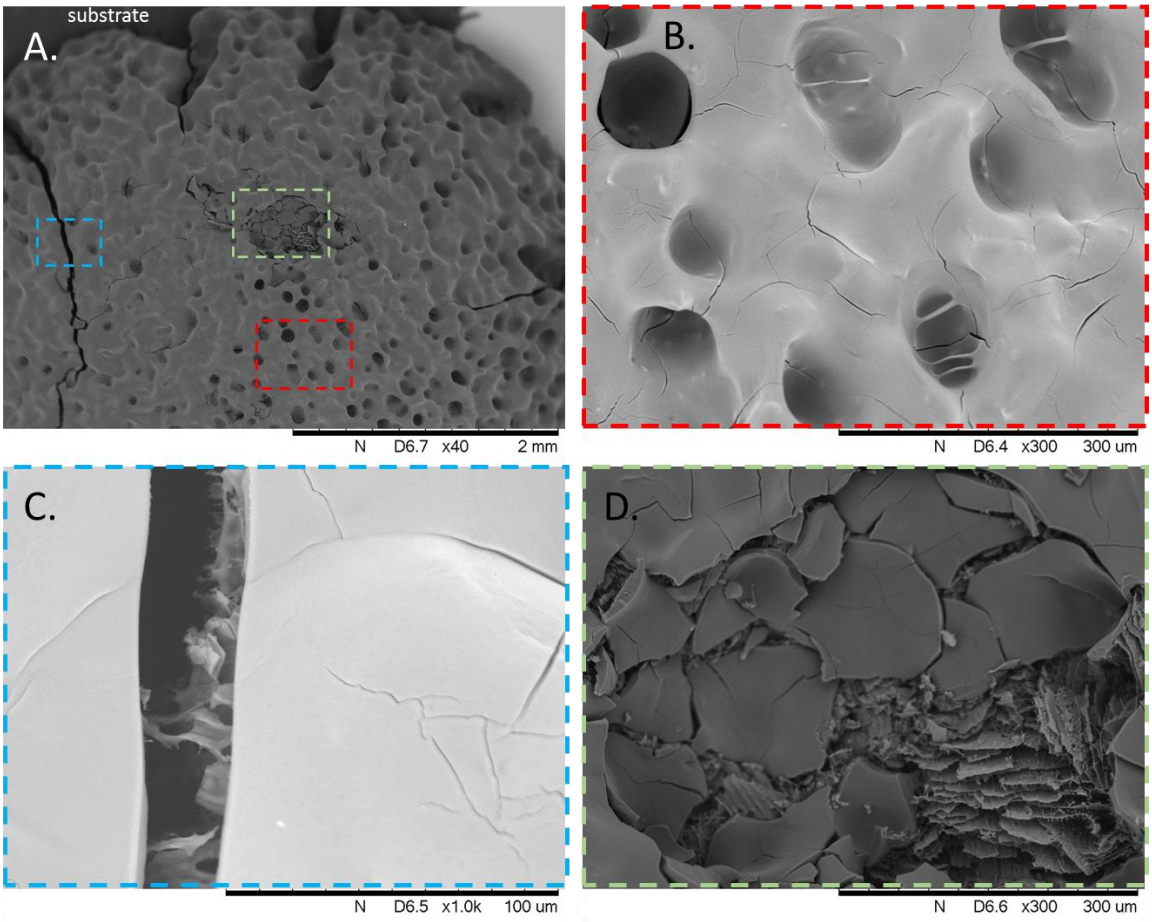

Figure 41. SEM image of a freeze-dried hemolymph droplet. Extraction method: wound; incubation time: 20 minutes. The substrate is labeled with white text. (A) The cracked droplet with a smooth porous surface. The pores are difficult to see. The smooth surface is possibly an artifact of the sample preparation. (B) A zoomed-in image of the surface. (C) A zoomed-in image of the crack. (D) A zoomed-in image of a broken segment of the sample. The lamellar structure underneath the surface is evident. The pores seem to propagate towards the surface of the sample. Fibers oriented perpendicularly to the lamellas appear.

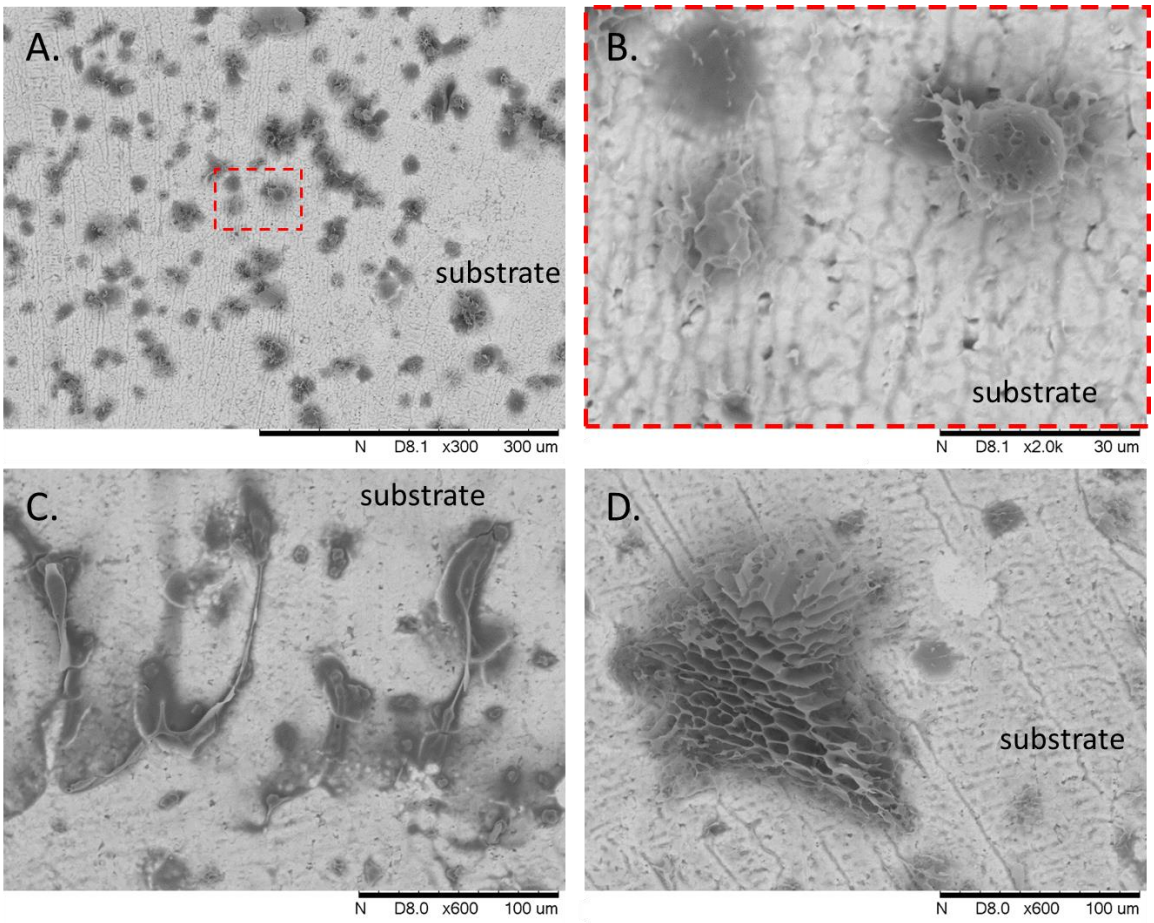

Figure 42. SEM image of the residue on the substrate after the sample broke off during freeze-drying. Extraction method: wound; incubation time: 20 minutes. The substrate is labeled with black text. (A) Small patches of the material were left behind after the sample droplet (imaged in Figure 41) broke off during freeze-drying. (B) A spherical object with a diameter of 15 µm, presumably a hemocyte. (B) Residue left on the substrate after the sample broke off. (C) Porous structure left on the substrate after the hemolymph droplet broke off. The pores propagate perpendicularly to the substrate.

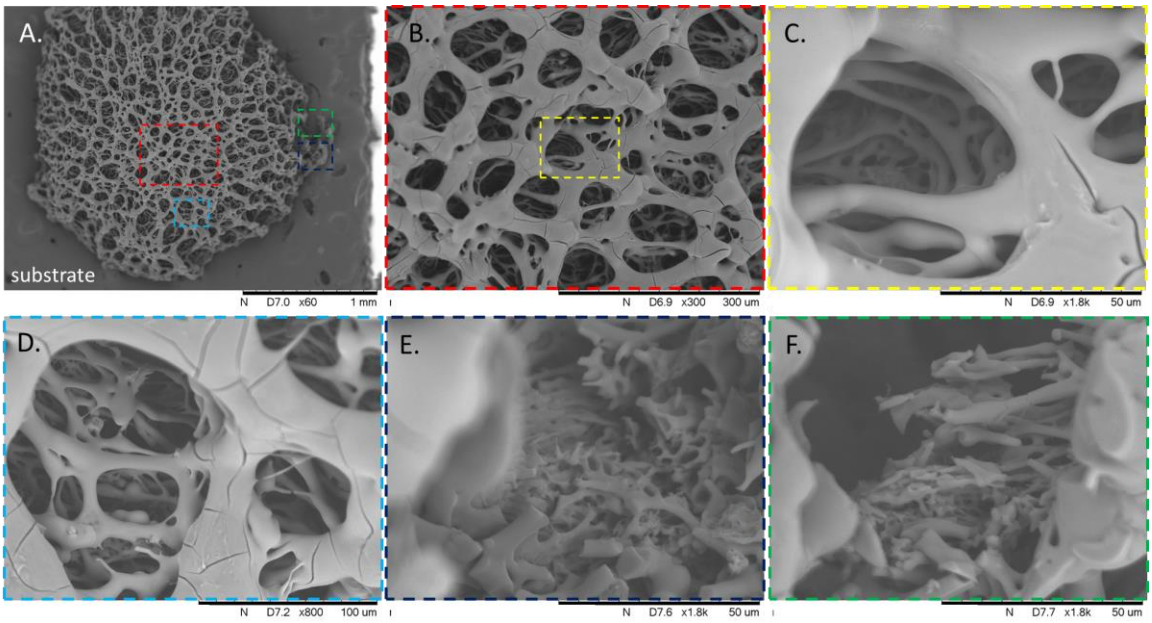

Figure 43. SEM image of a freeze-dried hemolymph droplet. Extraction method: pericardial space needle; incubation time: 40 seconds. The sample dripped with a pericardial method and frozen after 40 seconds after extraction. The substrate is labeled with white text. (A) The overview of the entire droplet against the substrate. The solid material is porous with no preferential direction to the pores. (B, C, D) Zoomed-in images of the pores. (E, F) Zoomed-in images of broken pores, demonstrating that the material inside pore walls is not hollow.

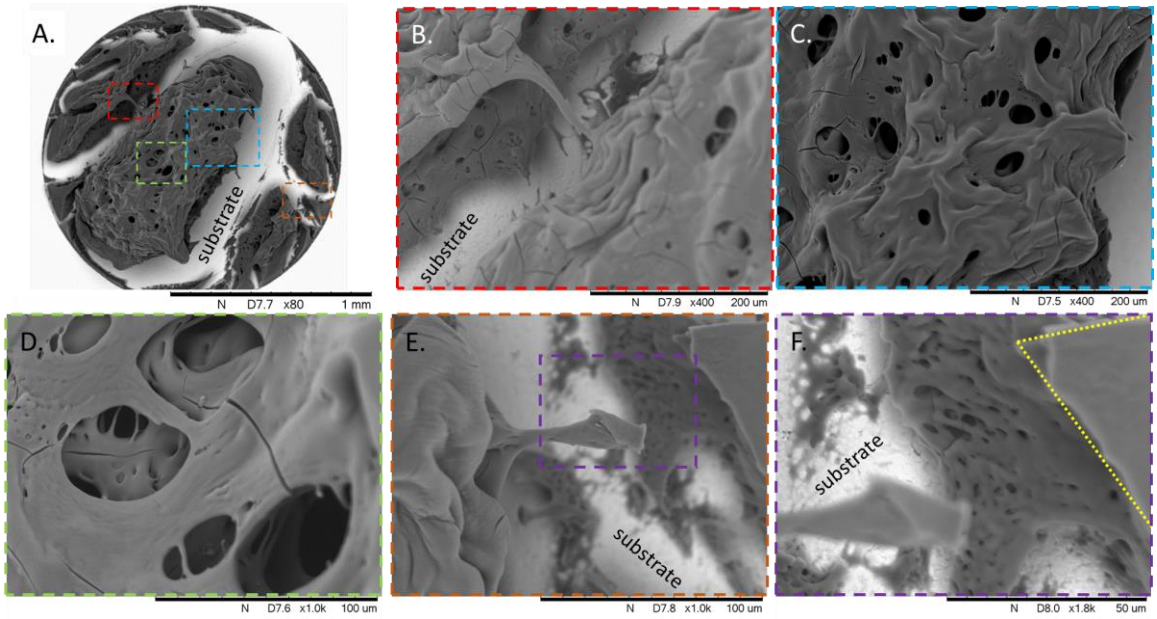

Figure 44. SEM image of a freeze-dried hemolymph droplet. Extraction method: pericardial space needle; incubation time: 6 minutes. The substrate is labeled with black text. (A) The overview of the entire droplet against the substrate. The solid material is porous with no preferential direction to the pores. (B - F) Zoomed-in images of the porous surface structure of the sample.

The formation of pores by directional freezing (known as freeze-casting) is a well-known method for formation of porous materials (49, 50). The porous structure is controlled primarily by the morphology of the solvent crystals and by the ability of the solutes to pack between the crystals (50). While no rigorous models exist yet to predict the structure of the freeze casted material, some empirical data is available. The solvent in all samples of hemolymph is water, which produces hexagonal crystals and typically results in lamellar structure of the dry material (50). Since the solvent is the same in all samples, the difference in structure is controlled by the mobility of the solutes. Typically, higher mobility leads to larger pores. For instance, that an increased concentration of polystyrene in an aqueous hydroxyapatite ceramic slurries results in smaller pore sizes

(51). Small additions of gelatin have also been shown to change the morphology and make the pores more cylindrical (52), while addition of poly(vinyl alcohol) makes pores more branchy. Perhaps the most relevant study was performed on the morphology of freeze-casted dispersion of cellulose nanocrystals (CNC), which can form a fibrous material, and hydrazone cross-linked poly(oligoethylene glycol methacrylate) (POEGMA) (53). By changing relative concentrations of CNC with POEGMA and total concentrations, the authors were able to produce fibrillary, cylindrical, and lamellar structures. The transition between the cylindrical to lamellar structures – similar to those we observed in hemolymph dripped from the wound and incubated for short and long time periods, respectively – was achieved by increasing the amount of cross-linked material. This is consistent with our hypothesis that the soft clot cross links as it matures and the incubation time increases above 20 minutes.

Some samples broke off from the metal substrate during freezing/drying, which allowed us to look closely at the material that remained adhered to the substrate (Figure 42). Imaging of this material revealed fibers throughout the samples that were incubated for longer than 20 minutes. These fibers are similar to those described by Geng *et al (37, 38).* Unlike in Geng's study, however, where the fibers were isolated and washed out, our samples preserved the original spacing of the fibers, which seems to be uniform throughout the samples. These fibers were not observed in samples incubated for less than 20 minutes or in the pericardial hemolymph.

6.2.5.2 Density mapping with x-ray microCT

One freeze-dried sample of hemolymph was imaged with X-ray microCT (Skyscan 1176) to determine the density distribution of the solutes after freeze-drying. The methodology can be summarized as follows. An X-ray source in tandem with a detector are rotated around the sample and take projection images of the sample. The resultant images are digitally reconstructed into a three-dimensional structure. The cross-sections of the three-dimensional structure can then be visualized. The resolution of the instrument is 9 μm per pixel, which is not enough to observe the internal structure of the freeze-dried clots but is enough to determine the internal distribution of relative material density.

A sample of hemolymph was rapidly frozen on the metal block in liquid nitrogen, freeze-dried under vacuum, detached from the metal block, mounted on a low-density Styrofoam block, and imaged with this technique (Figure 45). The images were reconstructed and are presented as a series of cross-sections of the sample from the side and top views in Figure 45 A and B. On the images, the yellow color represents higher density, purple represents lower density, and black represents absence of material. It can be seen that in all cross-sections, the material around the interface is of higher density. This implies that surface active material adheres to the interfaces, which is consistent with the DAH hypothesis.

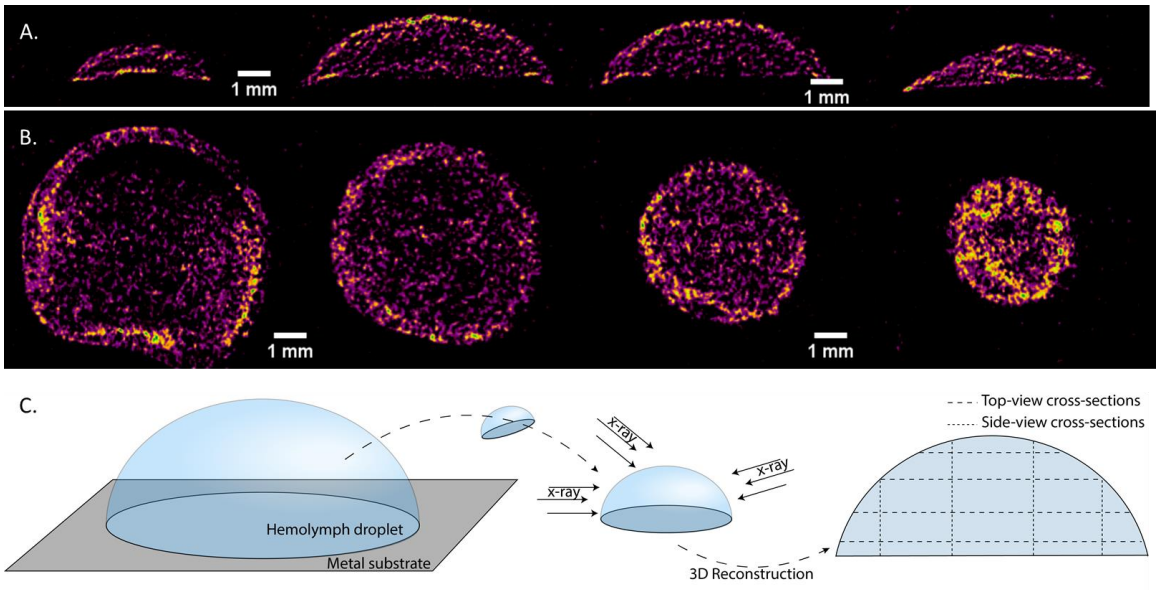

Figure 45. Cross-sections of a microCT scan of a freeze-dried hemolymph sample. The yellow color represents higher density, purple represents lower density and black represents absence of material. (A) A series of side view cross-sections of the freeze-dried droplet. (B) A series of top view cross-sections of the freeze-dried droplet. Left image corresponds to the bottom of the droplet, and the right image corresponds to the top of the droplet. On both images, the outer layer appears to have a larger density of the material. (C) A diagram depicting the sample preparation and the locations of the presented side and top-view cross-sections. The sample of hemolymph was rapidly frozen on the metal block in liquid nitrogen, freeze-dried under vacuum, detached from the metal block, mounted on a low-density Styrofoam block, and imaged with x-ray microCT. The image was then digitally reconstructed and the cross-sections were studied.

6.3 DISCUSSION AND CONCLUSIONS

Steinberg's differential adhesion hypothesis predicts aggregation and consolidation of adhesive hemocytes and proteins into close-packed structure. Our findings are consistent with the DAH hypothesis. We find that during the soft clot formation in the initial 10-20 minutes since wound creation, the aggregation of hemocytes occurs simultaneously with glycosylation of proteins and integration of the latter into the

hemocyte aggregates. Some hemocytes connect with others via pseudopodia to draw them closer, while others appear inert. Over time, these aggregates become more closely packed and more round in shape. Staining revealed that glycosylated proteins appear inside the cellular aggregates, possibly acting as an adhesive for hemocytes. This structure is highly adherent and readily sticks to foreign surfaces. When stirred with a needle, the proteins stretch into fibers and together with hemocytes form a large aggregate – constituting the soft clot – around the needle. These structures were not observed in hemolymph that was never in contact with the wound, indicating that the soft clot only forms in response to hemolymph contact with the wound.

These fibers appear to be of a different nature from the fibers discovered by Geng *et al*. SEM imaging of rapidly frozen freeze-dried incubated hemolymph samples indicate no presence of these fibers at incubation times lower than 20 minutes – during the soft clot formation. The fibers only become first visible in samples with incubation times higher than 20 minutes and become abundant at incubation times of 30 minutes or more. The formation of these fibers also corresponds in time with a change of morphology of the pores of the frozen sample near the substrate, which indicates a change in the way ice crystals grew through the sample and thus a change in the rheology and structure of the clot, most likely associated with the clot maturity. Neither fibers nor the structure were observed in hemolymph that was never in contact with the wound. This leads to the question of how the rheology of the clot changes with time. We will discuss this in chapters 8-10.

At the same time, we found that the density of freeze-dried sample of hemolymph frozen seconds after extraction is higher at the interface, suggesting that highly surface active material is present. This surface activity will be explored further in chapter 7.

6.4 MATERIALS AND METHODS

6.4.1 Caterpillars upkeep

M. sexta larvae were obtained from Carolina Biological Supply (https://www.carolina.com) or reared in house. In house larvae were mostly reared on food from Great Lakes Hornworms (https://www.greatlakeshornworm.com/) with a few feeding *ad libitum* on hornworm food from Carolina Biological Supply. Deposited eggs were from adults that emerged in a net enclosure (humidity ca. 65% and temperature ca. 27°C). Rearing containers were wide-mouth quart-size (liter) glass canning jars with strips (ca. 3x15 cm) of plastic gutter guard (Frost King Model VX620) inside as a climbing substrate and food support. Larvae were kept at controlled room temperature (about 25°C) and 24h. artificial light. To provide gas exchange the jar lids were replaced with aluminum window screen cut to fit the jar bands. Food (ca. 10ml) was added in the first three instars as needed. In later instars larvae were removed from jars and placed in clean jars with more food as food was consumed. The amount of larvae per jar was decreased as they grew, with 10 or fewer last instars per jar. Larvae that were moving to prepupation stage were not used for hemolymph as its composition changes rapidly during this stage. Prepupation larvae had a more yellowish thorax, stopped eating, and went into wandering behavior.

6.4.2 Hemolymph extraction

Manduca sexta larvae, 1-2 days before pre-pupation and weighting above 8.5 g, were washed free of contaminants with DI water and dried with a paper towel. To prevent movement of the caterpillars, they were placed into specially designed containers, which tightly grip the caterpillar along the whole length of the body while leaving the second and third proleg exposed. Once the caterpillar was secured, an incision was made with a razor blade on the third proleg. Hemolymph exiting the wound freely was either collected on a glass slide or probed directly on the body.

Hemolymph was extracted only once from a single specimen. All experiments were conducted at temperatures between 20 and 22°C.

6.4.2.1 Pericardial-puncture method

The pericardial puncture method is adapted from (38). A siliconized needle stock (Exel), obtained from a 30-gauge hypodermic needle by removing the plastic connector was inserted into the pericardial space of the larvae. The hemolymph was allowed to flow freely from the wound onto a glass slide. This method extracts a considerably smaller amount of hemolymph, and only several microliters of hemolymph could be extracted from each caterpillar with this method.

6.4.3 Peanut agglutinin (PNA) labeled fluorescent imaging

Rhodamine-labeled peanut agglutinin (PNA) was chosen for this study and the protocol was adapted form (39). The dye was shown to efficiently label the clots of *Drosophila* (39, 41, 42) and *Galleria* (46) by binding to the clotting proteins, which are known to be highly glycosylated in many species (40).

Fluorescence imaging was performed using an inverted microscope (Nikon Eclipse Ti) with 20x and 60x objectives and a DAPI cube. Phase enhanced microscopy was performed using the same set-up without the DAPI cube. Images were recorded with a black and white camera (Photometrics CoolSnap HQ2). For all images, the exposure was set to auto and the contrast look-up tables was adjusted manually for the best visibility.

To determine the amount of dye to be added to the sample for optimal contrast of stained images, the procedure in (39) for *Drosophila* was modified in the following manner. Hemolymph was extracted via the proleg wound method directly into a 8 well incubation optical cell. 4-5 droplets (80-100 ul) of hemolymph were placed into each of the four wells used. 5, 10 and 15 ul of 50 μg/ml of rhodamine-PNA solution in PBS buffer was added into three of the wells. One well was left without any dye as a control.

The fluorescent and the phase-enhanced images of the cells and structures adhered to the substrate from all four chambers are presented below. It was determined that the optimal amount of dye is between 5 and 10 ul of 50 μg/ml rhodamine-PNA solution per 100ul of hemolymph (Figure 46).

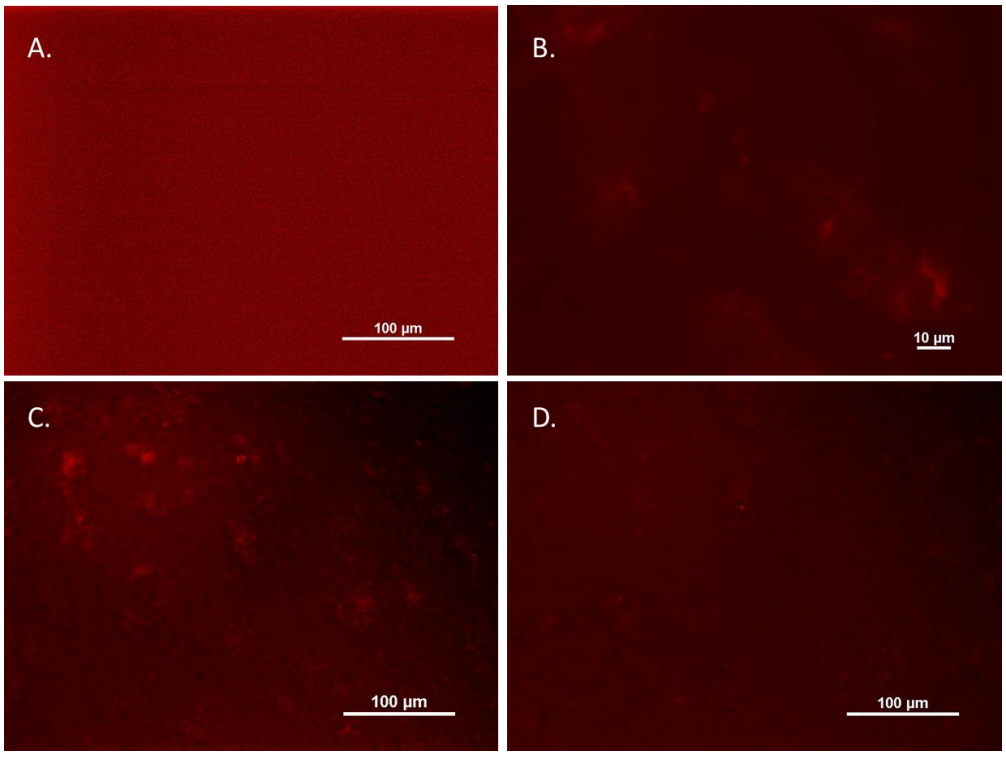

Figure 46. Hemolymph incubated with (A) 0 µl, (B) 5 µl, (C) 10 µl, and (D) 15 µl of 50 µg/ml rhodamine-PNA solution per 100ul of hemolymph. The best contrast between the labeled features and the background is obtained at 5 and 10 µl. Thus, the best amount of dye is between these two values.

6.4.3.1 Imaging of filamentous structure in incubated hemolymph – swirling and pullout.

To visualize fibrous structure in *M. sexta* larval hemolymph, the following procedure was used.

Four to five droplets (80-100 µl) of hemolymph were dripped from the wound on a caterpillar proleg directly onto a glass cover slip. 5 µl of 50 µg/ml rhodamine-PNA solution was added to the droplet. The mixture was lightly stirred using the micropipette tip. The mixture was then incubated and imaged at 8^{th} and 15^{th} minutes from the moment of extraction. At the 16^{th} minute since extraction, the mixture was repeatedly stirred. The

material that adhered to the stirrer – presumably the coagula – was then placed on a glass cover slip and imaged.

As a control, hemolymph obtained from the pericardial puncture method was used. Since only several microliters of hemolymph could be obtained from this method, the amount of dye was also lowered by diluting the solution to 0.5 μg/ml and adding 10 μl of it to the sample. The rest of the procedure was the same.

6.4.4 Rapidly frozen freeze-dried hemolymph

As hemolymph undergoes clotting, the material properties change as a function of time. By rapidly freezing the sample and slowly sublimating the water away, we are able to arrest the changes and preserve the sample for further analysis. This methodology is called freeze-drying.

The procedure to freeze-dry the samples is as follows. First, a 2cm x 10 cm x 20 cm steel block was suspended in liquid nitrogen, such that the top face of the block is exposed to air. The block was thus maintained at -190°C and aqueous droplets placed on its surface froze in under a second. Hemolymph was extracted from the caterpillar onto methanol-treated razor blades. After extraction, if incubation is necessary, the samples were incubated in a closed chamber with a water bath to maintain humidity. Once the appropriate incubation time had passed, the razor blades along with the samples were placed on the cold metal block. The samples froze within 1-2 seconds. After all samples were frozen, they were transferred to a freeze-drier, where the temperature is kept at -60°C and the low pressure is controlled, and are left overnight. Before the samples are exposed to the atmosphere, it is important to heat them up to at least 50°C to prevent

atmospheric vapor from depositing on the samples (47). To heat up the samples, they were irradiated with a standard desk lamp for 15 minutes.

After preparation, the samples were kept under 100% dry nitrogen at room temperature and transported in a desecrator.

6.4.4.1 Scanning electron microscopy of rapidly frozen freeze-dried hemolymph

The freeze-dried samples were sputter-coated with platinum for two minutes prior to imaging. During sample preparation and mounting, some cracks appeared along the sample. The SEM imaging was performed with a (Hitachi TM3000) microscope.

6.4.4.2 MicroCT

The freeze-dried sample was imaged with microCT (Skyscan 1176) to determine the density distribution of the solutes after freeze-drying. The methodology can be summarized as follows. An X-ray source in tandem with a detector are rotated around the sample. The resultant images are digitally reconstructed into a three-dimensional structure. The resolution of the instrument is 9 μm per pixel, which is not enough to observe the internal structure but is enough to determine the internal distribution of material density.

6.5 REFERENCES

1. Wyatt GR. The Biochemistry of Insect Hemolymph. Annual Review of Entomology. 1961;6:75-102.10.1146/annurev.en.06.010161.000451
2. Mullins DE. Chemistry and Physiology of the Hemolymph, in "Integument, Respiration and Circulation". In: Kerkut GA, editor.: Elsevier Science; 2013. p. 356-92,
3. Horohov DW, Dunn PE. Changes in the circulating hemocyte population of *Manduca sexta* larvae following injection of bacteria. J Invertebr Pathol. 1982;40:327-39.10.1016/0022-2011(82)90171-9
4. Wigglesworth VB. The Principles of Insect Physiology. 1982:1-7.10.1007/978-94-009-5973-6

5. Arnold JW. The hemocytes of insects. In: Rockstein M, editor. The physiology of insecta. 5. 2nd ed. New York: Academic Press; 1974. p. 201-54
6. Lavine MD, Strand MR. Insect hemocytes and their role in immunity. Insect Biochemistry and Molecular Biology. 2002;32:1295-309.10.1016/B978-012373976-6.50004-5
7. Strand MR. The insect cellular immune response. Insect Science. 2008;15(1):1-14.10.1111/j.1744-7917.2008.00183.x
8. Gregoire C. Hemolymph coagulation. In: Rockstein M, editor. The Physiology of Insecta. 5. New York: Academic Press; 1974. p. 309-60,
9. Ribeiro C, Brehélin M. Insect haemocytes: What type of cell is that? Journal of Insect Physiology. 2006;52:417-29.10.1016/j.jinsphys.2006.01.005
10. Salt GW. The cellular defence reactions of insects. Cambridge: Cambroidge University Press; 1970.
11. Gregoire CH. Blood coagulation in arthropods. V. Studies on hemolymph coagulation in 420 species of insects. Arch Biol. 1955;66((1)):103-48.
12. Rowley AF, Ratcliffe NA. The granular cells of Galleria mellonella during clotting and phagocytic reactions in vitro. Tissue and Cell. 1976;8:437-46.10.1016/0040-8166(76)90004-5
13. Gillespie JP, Kanost MR, Trenczek T. Biological mediators of insect immunity. Annual Review of Entomology. 1997;42:611-43.10.1146/annurev.ento.42.1.611
14. Pech LL, Strand MR. Granular cells are required for encapsulation of foreign targets by insect haemocytes. J Cell Sci. 1996;109:2053-60.
15. Pech LL, Strand MR. Plasmatocytes from the moth Pseudoplusia includens induce apoptosis of granular cells. Journal of Insect Physiology. 2000;46(12):1565-73.10.1016/s0022-1910(00)00083-4
16. Wigglesworth VB. Wound healing in an insect (Rhodnius prolixus hemiptera). Journal of Experimental Biology. 1937;14(3):364-81.
17. Steinberg MS. Reconstruction of tissues by dissociated cells. Science. 1963;141(357):401-8.10.1126/science.141.3579.401
18. Steinberg MS. Adhesion in development: An historical overview. Developmental Biology. 1996;180(2):377-88.10.1006/dbio.1996.0312
19. Steinberg MS. Differential adhesion in morphogenesis: a modern view. Current Opinion in Genetics & Development. 2007;17(4):281-6.10.1016/j.gde.2007.05.002
20. Holtfreter J. Significance of the cell membrane in embrionic processes. Annals of the New York Academy of Sciences. 1948;49(5):709-60.10.1111/j.1749-6632.1948.tb30962.x
21. Holtfreter J. Tissue affinity, an agent of embryonal shape formation. Archiv Fur Experimentelle Zellforschung. 1939;23(2):169-209.
22. Holtfreter J. Properties and functions of the surface coat in amphibian embryos. Journal of Experimental Zoology. 1943;93(2):251-323.10.1002/jez.1400930205
23. Holtfreter J. Observations on the migration, aggregation and phagocytosis of embrionic cells. Journal of Morphology. 1947;80(1):25-55.10.1002/jmor.1050800103
24. Holtfreter J. Chenges of structure and the kinetics of differentiation embrionic cells. Journal of Morphology. 1947;80(1):57-91.10.1002/jmor.1050800104

25. Holtfreter J. A study of the mechanics of gastrulation. Part I. Journal of Experimental Zoology. 1943;94(3):261-318.10.1002/jez.1400940302
26. Foty RA, Steinberg MS. Cadherin-mediated cell-cell adhesion and tissue segregation in relation to malignancy. Int J Dev Biol. 2004;48(5-6):397-409.
27. Foty RA, Steinberg MS. The differential adhesion hypothesis: a direct evaluation. Developmental Biology. 2005;278(1):255-63.10.1016/j.ydbio.2004.11.012
28. Duguay D, Foty RA, Steinberg MS. Cadherin-mediated cell adhesion and tissue segregation: qualitative and quantitative determinants. Developmental Biology. 2003;253(2):309-23.
29. Gonzalez-Rodriguez D, Guevorkian K, Douezan S, Brochard-Wyart F. Soft Matter Models of Developing Tissues and Tumors. Science. 2012;338(6109):910-7.10.1126/science.1226418
30. Brodland GW. The differential interfacial tension hypothesis (DITH): a comprehensive theory for the self-rearrangement of embryonic cells and tissues. Journal of Biomechanical Engineering-Transactions of the Asme. 2002;124(2):188-97.10.1115/1.1449491
31. Mattix B, Olsen TR, Gu Y, Casco M, Herbst A, Simionescu DT, Visconti RP, Kornev KG, Alexis F. Biological magnetic cellular spheroids as building blocks for tissue engineering. Acta Biomaterialia. 2014;10(2):623-9.10.1016/j.actbio.2013.10.021
32. Bulgakova NA, Klapholz B, Brown NH. Cell adhesion in Drosophila: versatility of cadherin and integrin complexes during development. Current Opinion in Cell Biology. 2012;24(5):702-12.10.1016/j.ceb.2012.07.006
33. Carthew RW. Adhesion proteins and the control of cell shape. Current Opinion in Genetics & Development. 2005;15(4):358-63.10.1016/j.gde.2005.06.002
34. Godt D, Tepass U. Drosophila oocyte localization is mediated by differential cadherin-based adhesion. Nature. 1998;395(6700):387-91.10.1038/26493
35. Hayashi T, Carthew RW. Surface mechanics mediate pattern formation in the developing retina. Nature. 2004;431(7009):647-52.10.1038/nature02952
36. Foty RA, Steinberg MS. Differential adhesion in model systems. Wires Dev Biol. 2013;2(5):631-45.
37. Geng CX, Dunn PE. Hemostasis in Larvae of *Manduca sexta*: Formation of a fibrous Coagulum by Hemolymph Proteins. Biochem Biophys Res Commun. 1988;155(2):1060-5.10.1016/s0006-291x(88)80604-1
38. Geng C. Studies of hemolymph coagulation in *Manduca sexta*. 1990,
39. Scherfer C, Karlsson C, Loseva O, Bidla G, Goto A, Havemann J, Dushay MS, Theopold U. Isolation and characterization of hemolymph clotting factors in Drosophila melanogaster by a pullout method. Current Biology. 2004;14(7):625-9.10.1016/j.cub.2004.03.030
40. Theopold U, Li D, Fabbri M, Scherfer C, Schmidt O. The coagulation of insect hemolymph. Cellular and Molecular Life Sciences. 2002;59:363-72.10.1007/s00018-002-8428-4
41. Lesch C, Theopold U. Methods to study hemolymph clotting in insects. Insect Immunology. 2008:1-12,

42. Bidla G, Lindgren M, Theopold U, Dushay MS. Hemolymph coagulation and phenoloxidase in Drosophila larvae. Developmental and Comparative Immunology. 2005;29:669-79.10.1016/j.dci.2004.11.007
43. Minnick MF, Rupp RA, Spence KD. A bacterial induced lectin which triggers hemocyte coagulation in *Manduca sexta*. . Biochem Biophys Res Commun. 1986;137(2):729-35.10.1016/0006-291x(86)91139-3
44. Hughes JA, Hurlbert RE, Rupp RA, Spence KD. Bacteria-induced haemolymph proteins of *Manduca sexta* pupae and larvae. Journal of Insect Physiology. 1983;29:625-32.10.1016/0022-1910(83)90014-8
45. Grace TDC. Establishment of 4 Strains of Cells from Insect Tissues Grown in Vitro. Nature. 1962;195(4843):788.DOI 10.1038/195788a0
46. Korayem AM, Hauling T, Lesch C, Fabbri M, Lindgren M, Loseva O, Schmidt O, Dushay MS, Theopold U. Evidence for an immune function of Lepidopteran silk proteins. Biochem Biophys Res Commun. 2007;352(2):317-22.10.1016/j.bbrc.2006.11.022
47. Williams RC. A Freeze-Drying Technique for Electron Microscopy. Journal of Applied Physics. 1953;24(1):115.
48. Zhang HF, Hussain I, Brust M, Butler MF, Rannard SP, Cooper AI. Aligned two- and three-dimensional structures by directional freezing of polymers and nanoparticles. Nat Mater. 2005;4(10):787-93.10.1038/nmat1487
49. Wegst UGK, Bai H, Saiz E, Tomsia AP, Ritchie RO. Bioinspired structural materials. Nat Mater. 2014;14:23-36.10.1038/nmat4089
50. Deville S. Freeze-Casting of Porous Biomaterials: Structure, Properties and Opportunities. Materials. 2010;3:1913-27.10.3390/ma3031913
51. Yook SW, Kim HE, Yoon BH, Soon YM, Koh YH. Improvement of compressive strength of porous hydroxyapatite scaffolds by adding polystyrene to camphene-based slurries. Mater Lett. 2009;63(11):955-8.10.1016/j.matlet.2009.01.080
52. Zhang Y, Zuo K, Zeng YP. Effects of gelatin addition on the microstructure of freeze-cast porous hydroxyapatite cerarmics. Ceram Int. 2009;35(6):2151-4.10.1016/j.ceramint.2008.11.022
53. Chau M, De France KJ, Kopera B, Machado VR, Rosenfeldt S, Reyes L, Chan KJW, Forster S, Cranston ED, Hoare T, Kumacheva E. Composite Hydrogels with Tunable Anisotropic Morphologies and Mechanical Properties. Chem Mater. 2016;28(10):3406-15.10.1021/acs.chemmater.6b00792

CHAPTER VII

EXTENSIONAL RHEOLOGY OF HEMOLYMPH OF CATERPILLARS

7.1 INTRODUCTION

In the previous two chapters, we have discussed the structure of the soft clot of *M. sexta* caterpillars and its rigidification kinetics. We have observed that after wounding, the hemocytes aggregate into large aggregates taking advantage of their adhesive properties and using pseudopodia to connect and hold the cells together. These aggregates adhere to foreign surfaces and quickly rigidify. We have also established that the walls of the hemocytes in the aggregates are lined with glycosylated proteins. When we stirred the clotting hemolymph with a stirrer, the aggregates broke apart, and the hemocytes in large numbers adhered to the stirrer, while the proteins stretched into long fiber-like structures. During the process of pulling out the stirrer from the hemolymph droplet, we could observe a liquid bridge formed between the stirrer and the droplet. This liquid bridge did not quickly disappear, as one would expect with water or other liquids of low viscosity. Instead, the liquid bridge remained for tens of seconds, slowly thinning out into a thin filament. The bottom end of the filament formed a liquid meniscus with the mother droplet. By moving the stirrer, the filament attached to it remained intact. During a lateral movement, the meniscus slid across the surface of the hemolymph droplet preventing additional filament stretching and breakup. By moving the stirrer up and down, the filament could be stretched into a longer one. When a clean stirrer was

dipped in the same drop after the first filament had disappeared, no new long-lived filaments formed upon pulling out the stirrer like before.

Similar behavior was observed previously by Theopold *et al* in the hemolymph of larvae of fruit flies (*Drosophila melanogaster*) (1, 2). When the authors stirred the incubated hemolymph and the stirrer pulled out, a filament formed. The study measured the draw-out length of the filament in samples with abundant phenoloxydase protein (PO), which is thought to participate in the cross-linking and hardening of the soft clot, and inhibited PO. In samples with abundant PO, the filaments could only be drawn out to 0.5 cm, while in the samples with inhibited PO, the filaments could be stretched to up to 2 cm. The kinetics of the filament thinning and disappearance were not studied by the authors. These kinetics, however, require special attention, since they are controlled by the rheology of the soft clot and the surface tension of hemolymph.

In this chapter, we provide a classification of observed filaments and relate the thinning behavior with the hemolymph structure.

7.1.1 Physics of filament disappearance

Break-up of a liquid bridge (also referred to as a liquid filament (3, 4) or a fluid thread (5-7)) is a process by which a single continuous liquid body breaks up into multiple liquid bodies. The most common example of this process is water flowing out of a tap: the flowing water forms a cylinder near the tap, but by the time it reaches the sink, the cylinder breaks up into droplets. A similar behavior is observed when a droplet of liquid is placed between two flat surfaces and the surfaces are quickly brought apart. The liquid first stretches into a liquid column which then breaks apart. Such a liquid column is

unstable. The argument is based on the Young-Laplace Law of capillarity, which states that the pressure differential, ΔP , is the difference between the pressure in the liquid filament and atmospheric pressure:

$$\Delta P = \sigma\left(\frac{1}{R_1} + \frac{1}{R_1}\right) \tag{1.1}$$

where σ is the surface tension of the liquid and R_1 and R_2 are the radii of the principal curvatures of the surface (8). Consider a straight cylindrical liquid column and draw two mutually perpendicular grid lines with the straight lines parallel to the cylinder axis as the parallels and the circles lying perpendicularly to the parallels as the meridians. The radius of curvature of parallels goes to infinity; hence the associated curvature in equation (1.1) does not contribute to the pressure differential; the radius of curvature of meridians is finite resulting in a finite contribution to equation (1.1) The pressure differential is positive hence the pressure in the cylinder is higher than the atmospheric pressure. The liquid thus tends to move out of the cylinder toward the base droplets. When some liquid escapes from the cylinder and the cylinder radius further decreases, the pressure increases. Eventually, the liquid bridge thins down and breaks up. In other words, the surface tension squeezes out the liquid from the liquid bridge. The molecules in the bulk of the liquid, meanwhile, tend to resist this motion. If the liquid is viscous, the resistance comes from the dissipative interactions between the molecules. If the liquid is elastic, additional resistance comes from deformation of the elastic components in the liquid.

The details of the liquid filament breakup via such capillary thinning depend on the following parameters of the system: the Reynolds number (Re), the capillary number (Ca), the Weber number (We), and the Deborah number (De).

The Reynolds number is a dimensionless parameter, estimating the role of the inertial forces relative to the viscous forces:

$$\mathrm{Re} = \frac{DuL}{\eta} \tag{1.2}$$

where D is the fluid density, u is the fluid velocity, L is the characteristic length, and η is the fluid viscosity.

The capillary number is a dimensionless parameter, estimating the effect of viscous forces relative to the surface tension force:

$$Ca = \frac{\eta u}{\sigma} \tag{1.3}$$

where σ is the surface tension of the liquid.

The Weber number is a dimensionless parameter, estimating the effect of inertial forces relative to the surface tension forces:

$$We = \frac{Du^2 L}{\sigma} \tag{1.4}$$

The Deborah number is a dimensionless parameter, estimating the effect of elastic forces in viscoelastic fluids relative to viscous forces:

$$De = \frac{\tau_r}{\tau_p} \tag{1.5}$$

where τ_r is the relaxation time, which characterizes the time needed for the material to adjust to the applied deformation and τ_p is the characteristic time of the flow process.

For Newtonian viscous fluids, when Re << 1, Ca ~ 1, We << 1, the radius of the thinnest part of the liquid bridge called the neck decreases linearly with time and the life-time of the bridge is proportional to the viscosity of the liquid (9-11). The radius of the thinnest part – the neck – of such a liquid bridge depends on surface tension and viscosity as (9-11)

$$R = R_0 - \frac{\sigma}{3\eta} t \tag{1.6}$$

where R_0 is the initial radius of filament and t is the time.

For viscoelastic Maxwell fluids, when Re << 1, Ca ~ 1, We << 1, and De ~1, the fluid elasticity stabilizes cylindrical filament over the time period comparable with the relaxation time τ_r. The radius decreases exponentially with time, and the decay constant is proportional to the relaxation time of the liquid (10-13):

$$R = R_0 \exp\left(\frac{-t}{3\tau_r}\right) \tag{1.7}$$

where $\tau_r = \frac{G}{\eta}$ is the relaxation time and G is the elastic modulus of the fluid.

We estimate the Reynolds number, the capillary number, and the Weber number for liquid bridges created from three substances: water, viscoelastic hemolymph with a water-like viscosity assuming a millisecond relaxation time, and soft clot with viscosity as measured in Chapter 3 and a relaxation time of 1s. The details of the calculations are presented in Table 8. In the case of water, the characteristic numbers sit outside of the acceptable parameters of equations (1.6) and (1.7) and the material thus cannot be studied

with the currently established theory. In experiment, we would see extensive oscillatory motion of the material during the entire decay of the liquid bridge. In the two supposed hemolymph cases, the characteristic numbers sit within the acceptable bounds and thus, equations (1.6) and (1.7) can be used to analyze such liquid bridges.

Table 8. Estimations of the Reynolds, capillary, and Weber numbers for the hemolymph extension experiments

Description	Parameters	Reynolds number, $\mathrm{Re} = \frac{D\left(2R_0/\tau_p\right)d}{\eta}$	Capillary number, $Ca = \frac{\eta\left(2R_0/\tau_p\right)}{\sigma}$	Weber number, *We* $We = \frac{D\left(2R_0^{\,2}/\tau_p^{\,2}\right)2R_0}{\sigma}$
Water	$\eta = 10^{-3}$ Pa·s $D = 10^{3}$ kg/m^3 $\sigma = 70\cdot10^{-3}$ N/m $2R_0 = 10^{-4}$ m $\tau_p = 10^{-3}$ s	10	10^{-1}	10^{-2}
Hemolymph of water-like viscosity, some elasticity	$\eta = 10^{-3}$ Pa·s $D = 10^{3}$ kg/m^3 $\sigma = 70\cdot10^{-3}$ N/m $2R_0 = 10^{-4}$ m $\tau_p = 10^{-1}$ s $\tau_r = 10^{-1}$ s $De \sim 1$	10^{-1}	10^{-3}	10^{-6}
Soft clot, as measured in Chapter 3	$\eta = 20$ Pa·s $D = 10^{3}$ kg/m^3 $\sigma = 70\cdot10^{-3}$ N/m $2R_0 = 10^{-4}$ m $\tau_p = 1$ s $\tau_r = 1$ s $De \sim 1$	10^{-6}	10^{-1}	10^{-8}

7.1.2 Review of kinetics of filament breakup

The kinetics of liquid column disappearance have been studied in liquids of different rheological properties. (9, 10, 14-30). Main applications of this research are inkjet printing (31), liquid faucets and dispensers (13, 31, 32), and rheological characterization of liquids available in small quantities (10, 14, 22). The latter application is of particular interest to us, since we are interested in rheological characterization of hemolymph.

A simple and attractive method of studying rheology of a liquid in response to extension was developed by Entov, Bazilevskii and Rozhkov later adopted by other groups. (14-20). The method is based on creating a liquid column between two surfaces and tracking the decrease of the diameter of its neck as a function of time. The methodology has been used to study low viscosity liquids(21-23), high viscosity liquids(9, 15, 23), viscoelastic liquids (21-25), suspensions (11, 23, 26, 33), liquid crystals(27), as well as various biological fluids (10) and has been thoroughly reviewed (26, 28-30). The decay kinetics of the liquid bridges with different rheological properties exhibit distinguishing characteristic features. For instance, Newtonian liquids demonstrate a linear decay of the thinnest part of the liquid bridge. A Maxwell viscoelastic liquid develops a uniform liquid filament with an exponential time decay of its radius. A high molecular weight polymer, meanwhile, might develop droplets on the surface of the liquid filament. To understand extensional rheological properties of hemolymph, in this chapter, we study the decay kinetics of the hemolymph liquid bridges. In the next chapter, we study the internal structure of these liquid bridges.

7.2 RESULTS

7.2.1 Methodology

The experiments were configured such that the studied hemolymph was observable with a high frame rate camera. The caterpillar was placed in a tubular holder with an opening for the wound and positioned between a camera and a light source. The light source was positioned to function as a backlight with a diffusor. The camera was positioned such that the caterpillar wound was at the edge of the screen and the studied hemolymph traveled across the screen. Depending on the experiment, either a high frame rate – low resolution camera (IDT Technologies MotionProX3, 200-900 fps, 512-640 pixels) or a low frame rate – high resolution camera (Grasshopper, Point Grey, 100 - 140 fps, 1920-1200pixels) were used.

Three types of experiments were performed. First, the caterpillar was positioned with the wound pointing up and a metal ball, attached to a long cantilever, was placed on the wound. The experiment consisted of quickly lifting the metal ball via the cantilever and observing the liquid bridge between the ball and the hemolymph at the wound cite. Second, the caterpillar was suspended in air in such a way, that the hemolymph exiting the wound would form a droplet and drip under gravity, similar to how water would drip from the tap. The experiment consisted of the observation of the liquid bridge between the falling droplet and the hemolymph remaining at the wound cite. Third, the hemolymph was drained form the wound onto a methanol-cleaned glass slide and a metal ball probe was dipped in the sample. The experiment again consisted of quickly lifting the metal ball and observing the liquid bridge between the ball and the hemolymph on the

slide. The details of the experimental protocol are described in the Materials and Methods section.

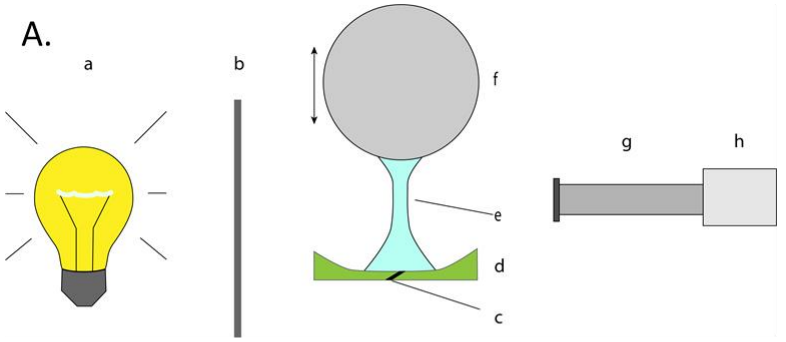

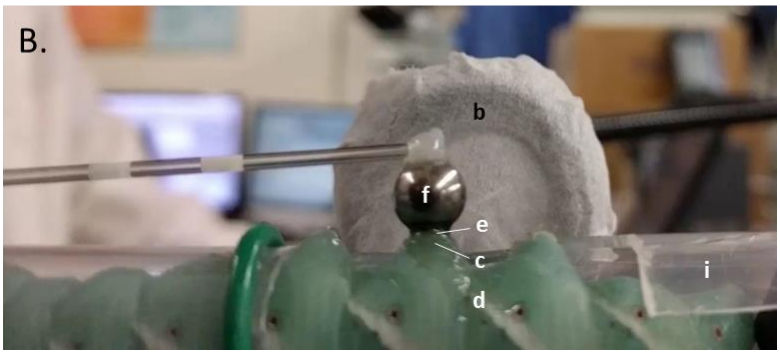

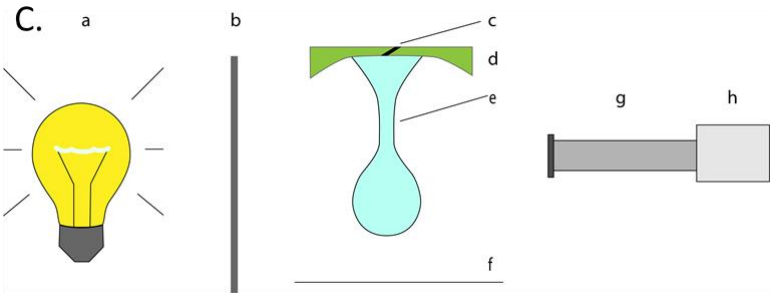

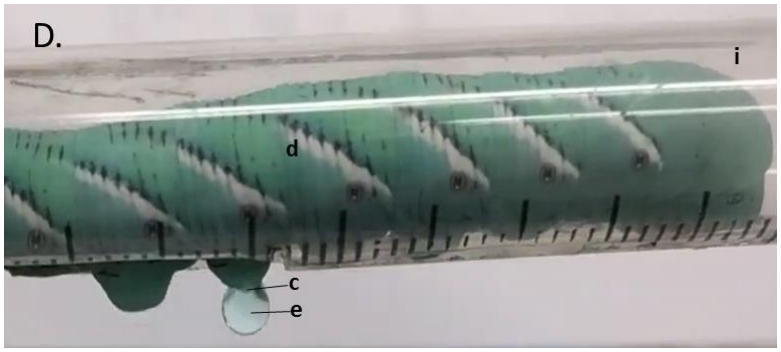

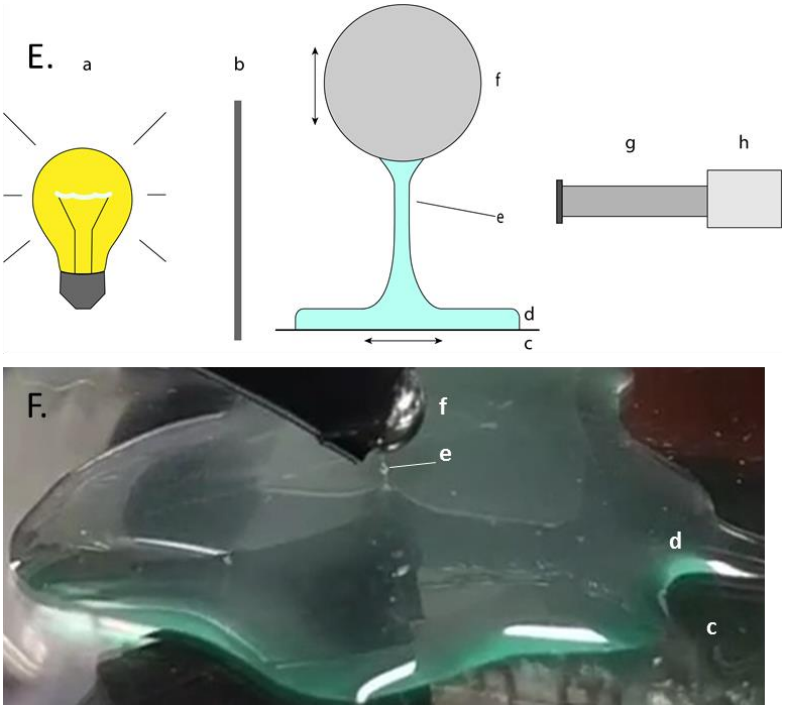

Figure 47. (A, C, E) schematics and (B, D, F) photographs of the extensional experiments.

(A, B) The *M. sexta* caterpillar (d) was placed in the holder (i) with the prolegs facing up and an incision (c) was made on the third proleg. The hemolymph exited the caterpillar and collected around the wound. The probe (f), attached to a long cantilever, was placed on the wound in the hemolymph. The probe was lowered down into the sample quickly lifted up during the experiment. The liquid bridge (e) was formed between the probe and the wound. The light source (a) and a diffusor (b) provided the backlighting for the camera (h) with the lens (g) to enhance contrast between the liquid and the background.

(C, D) The caterpillar (d) was placed in the holder (i) with the prolegs facing down and an incision (c) was made on the third proleg. The hemolymph exited the wound and formed pendant droplets and drip directly from the wound. As the hemolymph dripped, it formed liquid bridges (e) between the droplets ad the wound. The light source (a) and a diffusor (b) provided the backlighting for the camera (h) with the lens (g) to enhance contrast between the liquid and the background.

(E, F) The hemolymph (d) was dripped to form a large droplet on a clean glass slide (c). The probe (f) was lowered down into the hemolymph droplet and quickly lifted up during the experiment. The liquid bridge (e) was formed between the probe and the droplet. To probe an untested incubated material, the sample was moved laterally relative to the probe. The light source (a) and a diffusor (b) provided the backlighting for the camera (h) with the lens (g) to enhance contrast between the liquid and the background.

7.2.2 The first method – probing hemolymph directly from the wound with a stainless-steel ball

In the first method, the probe was placed directly on the wound. After performing a cut on the third proleg of the caterpillar, and placing the probe on the wound and lifting the probe, the first liquid bridge assumed a shape of a filament and took a long time (1-40 seconds) to thin down and break up (Figure 48). We call these liquid bridges 'long-lived filaments' (LLF) indicating that their life-time is greater than 1 second. These LLFs would sometimes develop a single or multiple droplets on them, which either remained on the filament until break-up or moved to one side and reabsorbed into the wound or droplet attached to the steel ball.

In the second attempt to form a filament, when the probe was lowered back on the wound, the second liquid bridge could behave in two ways. Sometimes, another LLF would form; much more often, however, liquid bridges would assume the shape of a filament and break up in less than 1 second (Figure 49). We called these liquid bridges 'short-lived filaments' (SLF).

In the other cases, when the wound was touched by the probe and the probe was raised, the formed liquid bridge was so thin that upon stretching by moving the probe upward, the liquid bridge broke up even before the probe had reached its equilibrium position (Figure 50). In those cases no filament was formed between the wound and the final equilibrium position of the probe and we call those cases 'no filament' (NF).

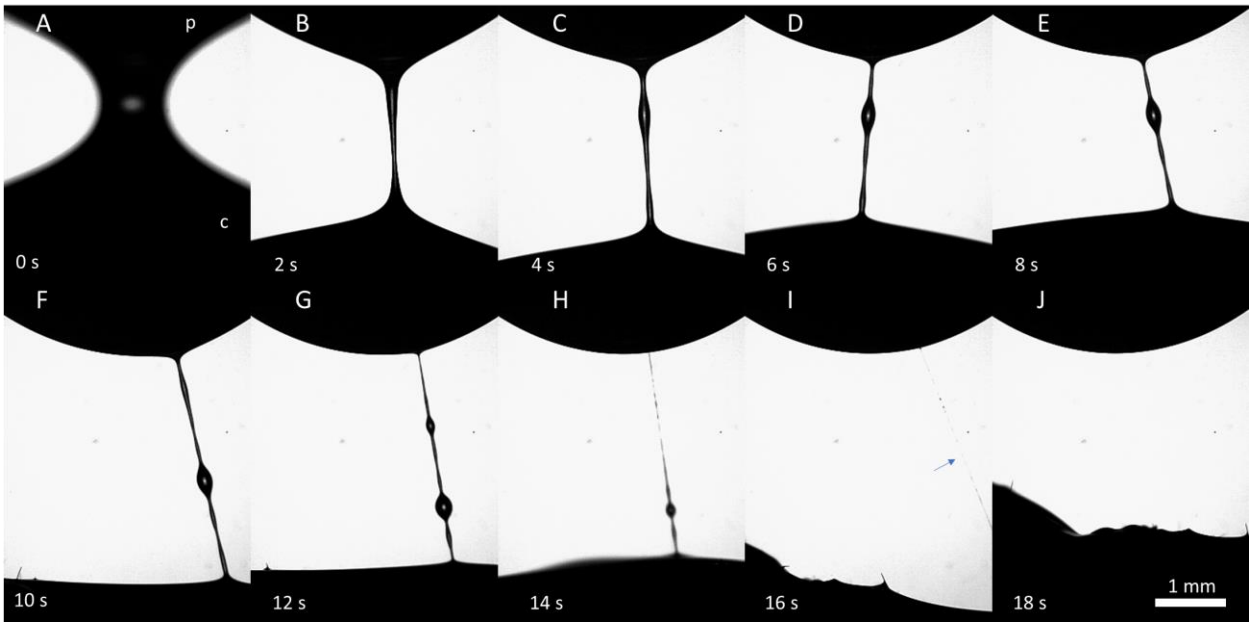

Figure 48. A series of frames illustrating the features of the formation and breakup of the long lived filament (LLF). The filament has been formed between a stainless steel probe (p) and a wound of the caterpillar (c). The probe is on the top, the caterpillar is on the bottom of this series of frames. The wound is not visible in the video. The caterpillar is constantly moving causing the filament to move with it.

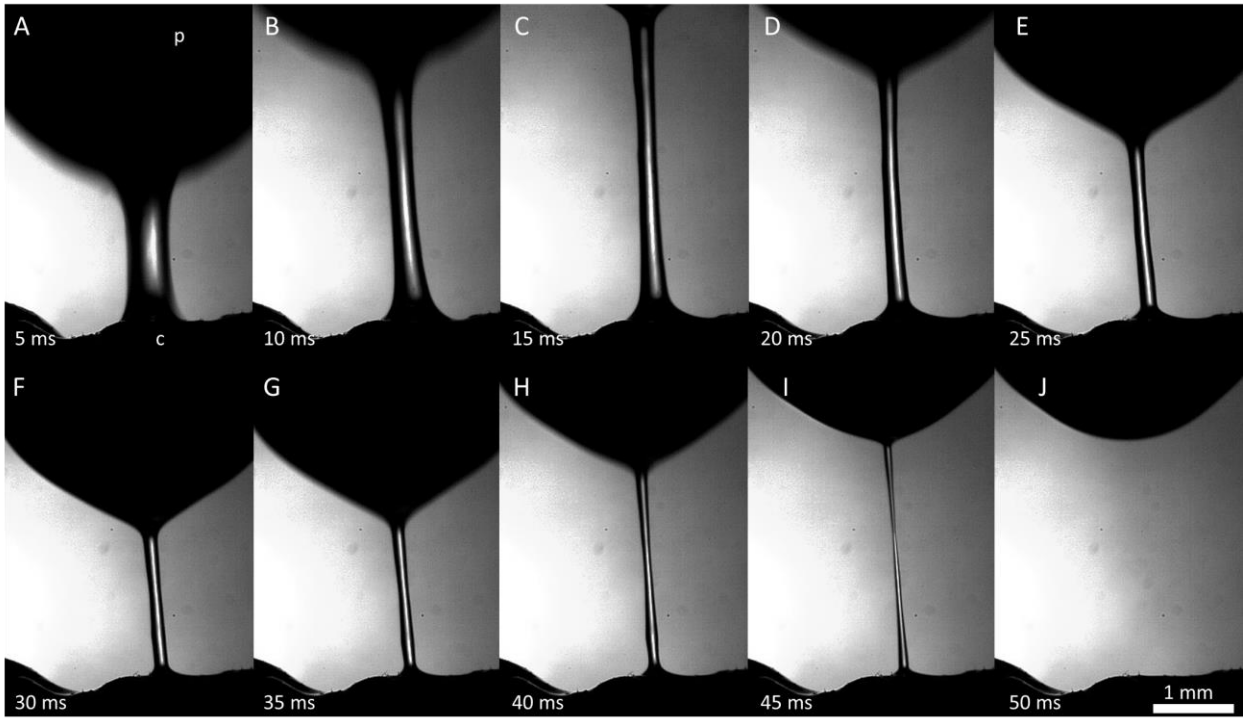

Figure 49. A series of frames illustrating the features of the formation and breakup of the short lived filament (SLF). The filament has been formed between a stainless-steel probe (p) and a wound of the caterpillar (c). The probe is on the top, the caterpillar is on the bottom of this series of frames. The wound is not visible in the video.

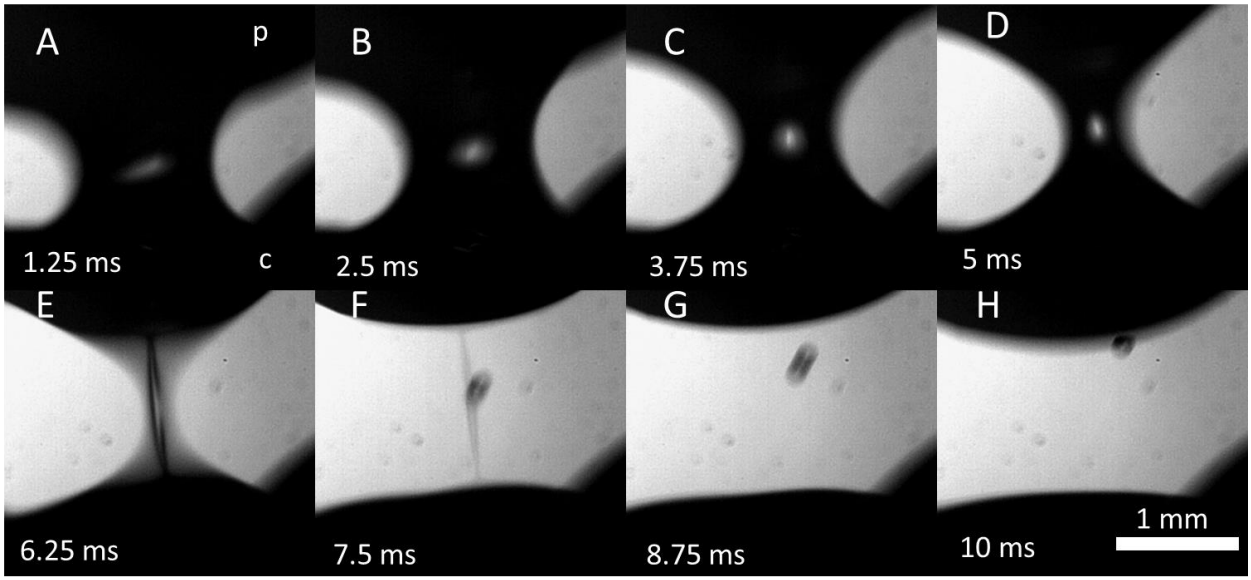

Figure 50. The no filament (NF) case when the liquid bridge between the stainless-steel probe (p) and the caterpillar (c) broke before the probe reached its equilibrium position (H).

At total of 18 caterpillars were probed with this method and 117 liquid bridges were made between the wound cite and the probe. Of those, 53 liquid bridges were made in the timespan of 1 to 3 minutes after the cut was made and 64 were made in the timespan of 8 to 48 minutes after the cut was made. Of the ones made in the first 3 minutes, 13 were LLF, 18 were SLF, and 22 were NF. Of the 64 liquid bridges that were formed after 8 minutes, only a single LLF, 11 SLF, and 52 NF were formed.

A natural question arose regarding the reason for this drastic change in the liquid bridge behavior. This method, however, provided too little control over the studied system to answer this question. The biggest limitation was that we could not control the volume of the material under the probe. First, we had no control over how much the insect bled. Second, the hemolymph that exited the wound quickly, left the wound cite due to gravity. Third, sometimes the caterpillar would simply move too much and shift

the position of the wound relative to the probe without our knowledge, leaving us to measure the extension of a thin hemolymph film over healthy skin. We thus believe that some of the NF and SLF measurements were erroneous and were a result of too little hemolymph under the probe.

To test the hypothesis that those NF and SLF were erroneous, we performed extensional experiments on viscosity standards (Cannon instrument company, S600) and well-characterized viscoelastic liquids (aqueous CPCl-NaSAL: 0.1 wt%, 0.5 wt%, 1 wt% and 2 wt% (34-37)) at low volumes in an environmental chamber to prevent evaporation. We found that at low viscosity and relaxation times and at sample volumes lower than 15 μl, the kinetics of liquid bridge disappearance significantly change as a full filament cannot form between the probe and the substrate during extension. Thus, when the volume of the liquid is too small, it produces an NF measurement not due to the rheology of the liquid, but due to the low volume.

Thus, to characterize the material more carefully, we had to adjust the methodology.

7.2.3 The second method – Probing hemolymph dripping from the wound

In the second method, the wound was pointed down and the hemolymph was free to drip from the wound. This method allowed us to start probing the hemolymph several seconds after the wound was made as it did not require any probes to form the liquid bridge. Due to the activity of the live insects shortly after the incision, however, it was difficult to focus on the liquid droplet, so success rate of the experiment was roughly 5%. Using this method, we observed the following. During the first several seconds after the

cut was made, the liquid bridges typically did not form filaments of uniform radius and, instead, exhibited a thin neck and produced satellites Figure 51. This behavior is typically observed with non-elastic liquids of low viscosity (38-40), suggesting that mostly water-like plasma was dripping from the wound.

After 10-15 seconds, the uniform radius filaments begin forming, indicating that hemolymph has either thickened or became elastic. The lifetimes of these early filaments are ~ 20-30 microseconds, similar to the SLF we discussed in the first experiment (Figure 52). As time goes on, the lifetime of these filaments increases. For instance, a droplet produced 75 seconds after the incision has a lifetime of 240 microseconds.

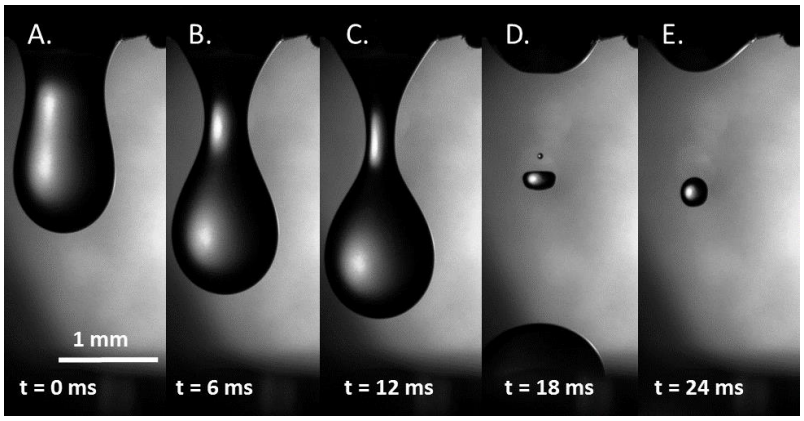

Figure 51. Hemolymph dripping from the wound of a caterpillar several seconds after the wound was made. No filament can be observed, which indicates that the hemolymph at this time scale is not highly viscous or elastic.

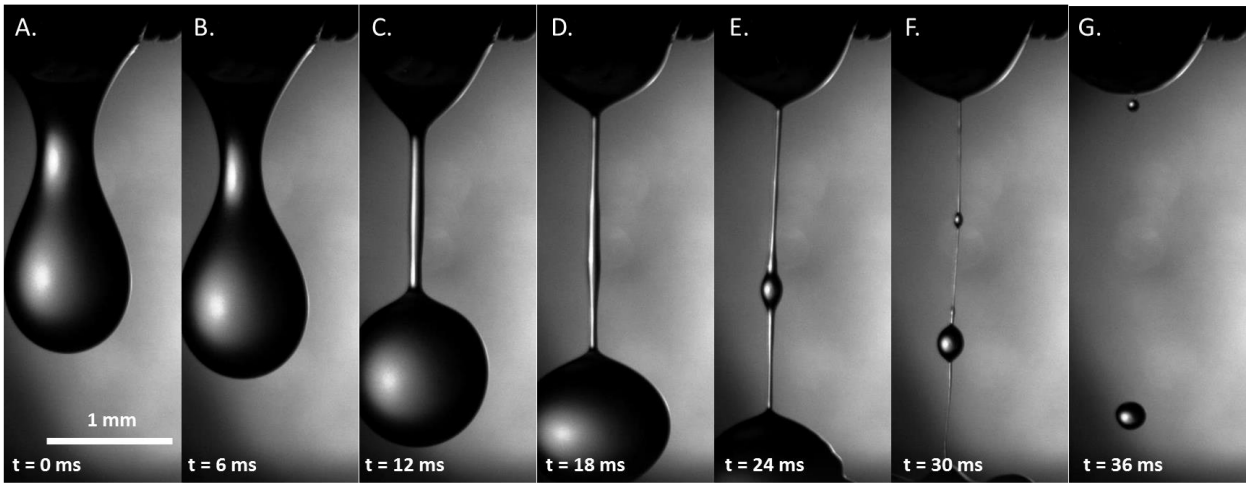

Figure 52. Hemolymph dripping from the wound of a caterpillar. This set of frames was taken in the time span of 10-15 seconds after the wound was made. A clear filament can be seen, indicating that the hemolymph has changed its rheological properties.

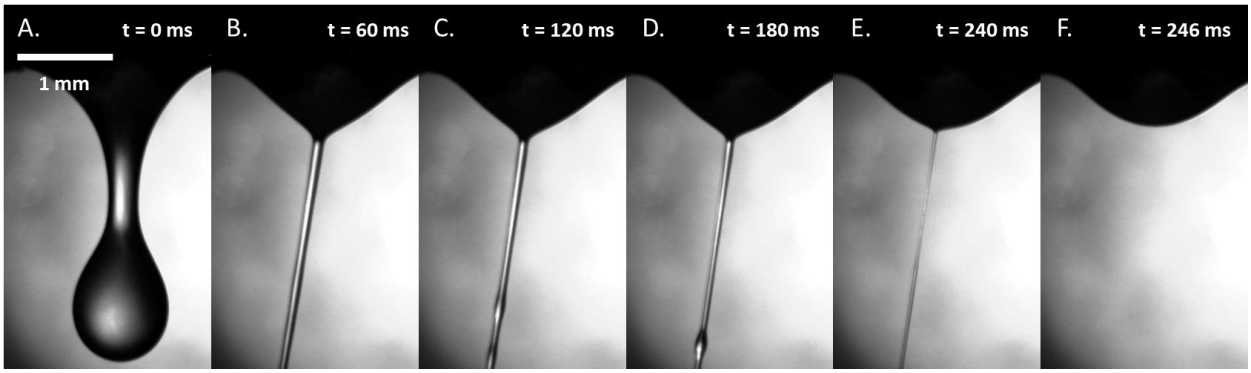

Figure 53. Hemolymph dripping from the wound of a caterpillar. This set of frames was taken in the time span of 75 seconds after the wound was made. A clear filament can be seen and its lifetime is at least 10 times longer than that of the filaments formed at earlier incubation time, indicating further change of the hemolymph rheology.

Typically, the bleeding stops and hemolymph stops dripping from the wound after 60-90 seconds. In roughly 5% of the cases, the last droplet falling off the wound produces a LLF. Due to the rareness of the LLF formation in such a way, we were not able to record this event on the video.

In the other cases, the flow of hemolymph stops before the LLF-forming droplet could be detached and thus no LLFs can be formed. If that last hanging droplet, however, is collected with a glass rod or a pipette tip, a LLF forms between the wound and the collected droplet. These results indicate that the properties of hemolymph quickly change: hemolymph starts seeping as water-like almost inviscid fluid, then it quickly changes its rheological properties. Since this method relies on the natural flow of hemolymph from the wound, it does not allow for control of when to perform the measurement. Since the rheology of hemolymph quickly changes, such control is strongly desirable.

7.2.4 The third method – probing hemolymph collected on a glass slide with a stainless-steel ball

In the third method, the hemolymph was pooled on a glass slide and a stainless-steel ball attached at the tip of a cantilever was used as a probe. This method offers a controlled stretching of the liquid bridge. By noting the time passed between the extraction of the hemolymph from the wound and the hemolymph extension experiment, we were able to track a correlation between the changes of rheological properties of hemolymph and its incubation time, τ_i. Another advantage of this method was that it did not require imaging of moving insects, so the experiments were much more controlled. Finally, this methodology also allowed us to test the same material multiple times by dipping the probe back into the tested material and repeating the measurement. Alternatively, by making a wide pool of hemolymph on the substrate, we could test one part of it, while leaving the other parts undisturbed for further incubation and testing. All

of the time-dependent data were produced using this method. Thus, from now on, we will only talk about the results obtained with this experimental setup.

Typically, it took roughly 1-1.5 minutes to collect hemolymph from the bleeding caterpillar on the slide, to set-up the probe, and begin the measurement. Thus, we were not able to study the behavior of liquid bridges observed with the second method in the first minute since the hemolymph extraction. Instead, we focused on the behavior of the LLF probed from the droplets after incubation time of τ_i = 1-1.5 minutes and longer. We conducted experiments on nine caterpillars, in which we tracked the time since the hemolymph extraction. In these, we did not strictly control the location on the surface of hemolymph puddle where the filament was taken from: the puddle was probed at various locations until a LLF was observed.

We noticed that during the first 8-10 minutes, the LLF was typically produced only once at the first time a particular surface area of hemolymph puddle was probed. The consequent times that the same surface area was probed, only SLFs were produced. These results were the same regardless of whether the probe was cleaned or not.

To investigate this pattern more rigorously, a series of experiments was performed, where the location of the probe was noted and a distinction was made between the first time that the hemolymph puddle was probed and consequent times it was probed. The 'location probed' was considered to be as a 5x5 mm area of the hemolymph puddle centered at the probe. Hemolymph from 10 caterpillars was tested using this method and 119 liquid bridges were made between the substrate and the probe. In the experiments, where the hemolymph was incubated for less than 10 minutes, the

first liquid bridge formed at a particular location in the sample was typically LLF and more rarely SLF. The consequent liquid bridges at the same location in the sample were typically SLF (Table 9). This drastic change of liquid properties indicates that the material that is present in the stretched sample during the first run is not present in the second run.

Table 9. The statistics on the filament creation on the first and the consecutive times the same location was probed in a pooled sample during the first 10 minutes of incubation and during the following three minutes of incubation. 26 of liquid bridges created for the first time in the sample were LLF, 17 were SLF, and 8 were NF. Of the runs that yielded LLF on the first run, the consequent runs at the same location produced 6 LLF, 20 SLF, and 0 NF. Of the runs that yielded SLF on the first run, the consequent runs at the same location produced 0 LLF, 12 SLF, and 0 NF. If the first run produced NF, the consequent runs at the same location only produced NF and were not recorded.

	Created for the first time			After an initial LLF			After initial SLF		
Incubation time, τ_i	LLF	SLF	NF	LLF	SLF	NF	LLF	SLF	NF
1- 10 min [N]	26	17	8	6	20	0	0	17	0
1- 10 min [%]	51	33	16	23	77	0	0	100	0
10-13 min [N]	1	11	0	0	1	0	0	12	0
10-13 min [%]	8	92	0	0	100	0	0	100	0

After the initial 10-13 minutes of incubation, LLFs became less frequent and SLFs were produced almost exclusively (Table 9). The SLFs exhibited similar breakup kinetics. The LLFs, however, exhibited distinct types of instabilities, which we will discuss in larger detail in the next section.

As a control for interaction of hemolymph with the epidermal level, we probed the hemolymph extracted via a needle from the pericardial space. Due to the low volume of hemolymph that could be extracted with this method (50-100 μl), to prevent evaporation, we performed the measurements in an environmental chamber. The 8 samples from 3 caterpillars were tested in this manner at different incubation times. All tested samples demonstrated the SLF behavior.

7.2.5 Types of filaments observed with the ball-puddle method

As discussed above, the hemolymph incubated for more than a minute formed either SLF of LLF. This dichotomy indicates that two different materials are being probed. To understand the nature of these materials, we will look closely into the kinetics of disappearance of both types of filaments. We will first look at the LLF.

7.2.5.1 Types of LLF instabilities

All filaments may have two common features: all of them have cylindrical core or 'backbone' and 'droplets' formed on this backbone. In different filaments the backbone may either be of a constant radius along its length (Figure 54, D-F), or have one side thicker and the other side thinner Figure 54, A-C). During the filament thinning, some filaments develop non-uniformities in the radius (Figure 54, G-I). Some of these non-uniformities develop into distinct droplets (Figure 54, I) characterized by a symmetrical shape and a finite length, while others have more complex shape (Figure 54, H). In those LLF that exhibit a non-uniform backbone, one can see the flow of the material inside the filament following the movement of the backbone non-uniformities (Figure 55).

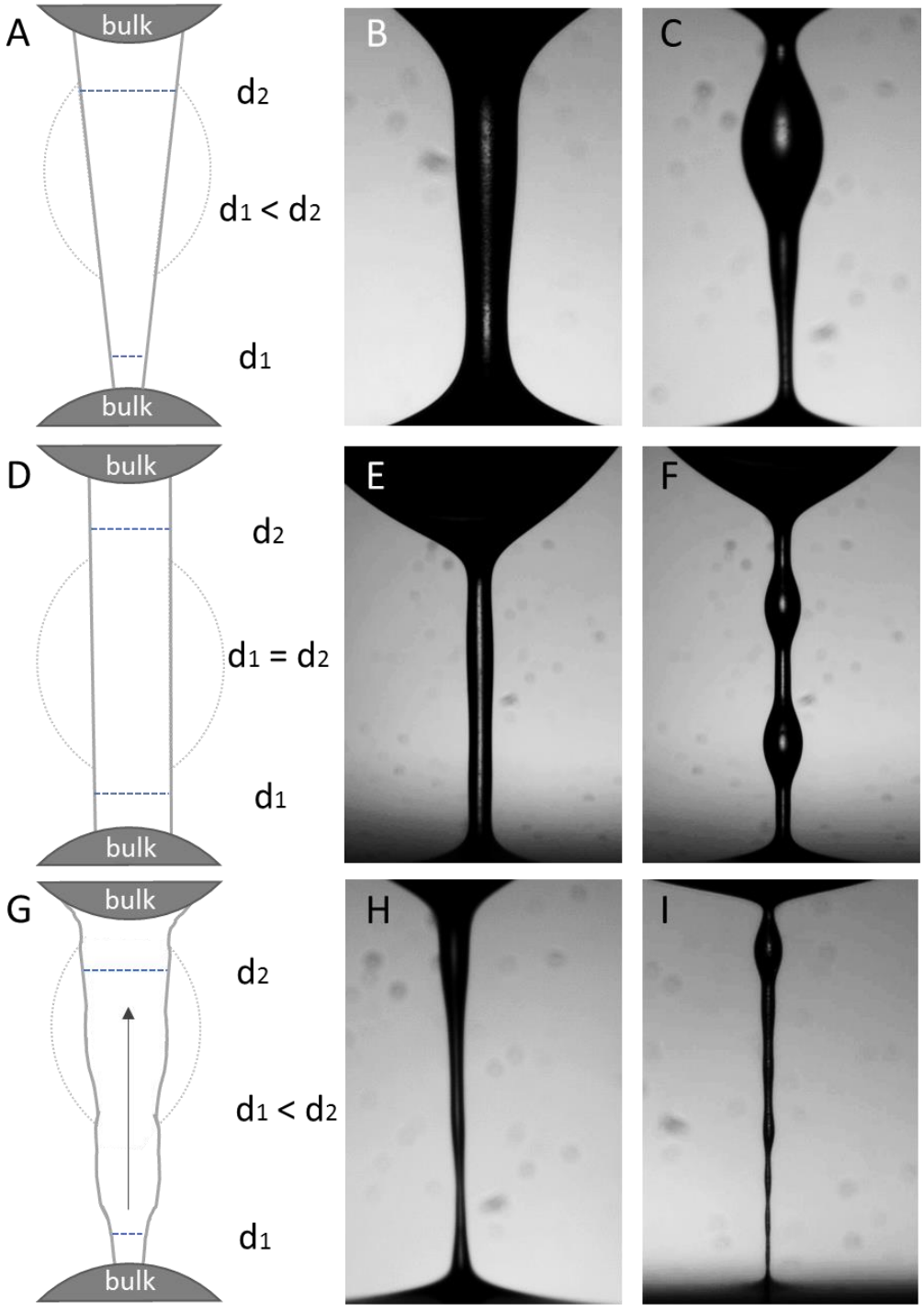

Figure 54. Sketches and images of the filament thinning examples. (A, D, G) The sketches depict the shape of the backbone (solid line) as well as droplets that may or may not appear on the backbone (dotted line). The sketches depict a single droplet for illustration purposes, but actual filaments may host a single or multiple droplets. The

backbone was either of a uniform diameter, $d_1 = d_2$, or wider on one side $d_1 \neq d_2$. (B, E, H) The examples of filaments without a droplet. These examples correlate to the sketches on their left (C, F, I) The examples of filaments with one or multiple droplets. The examples correlate to the sketches on their left.

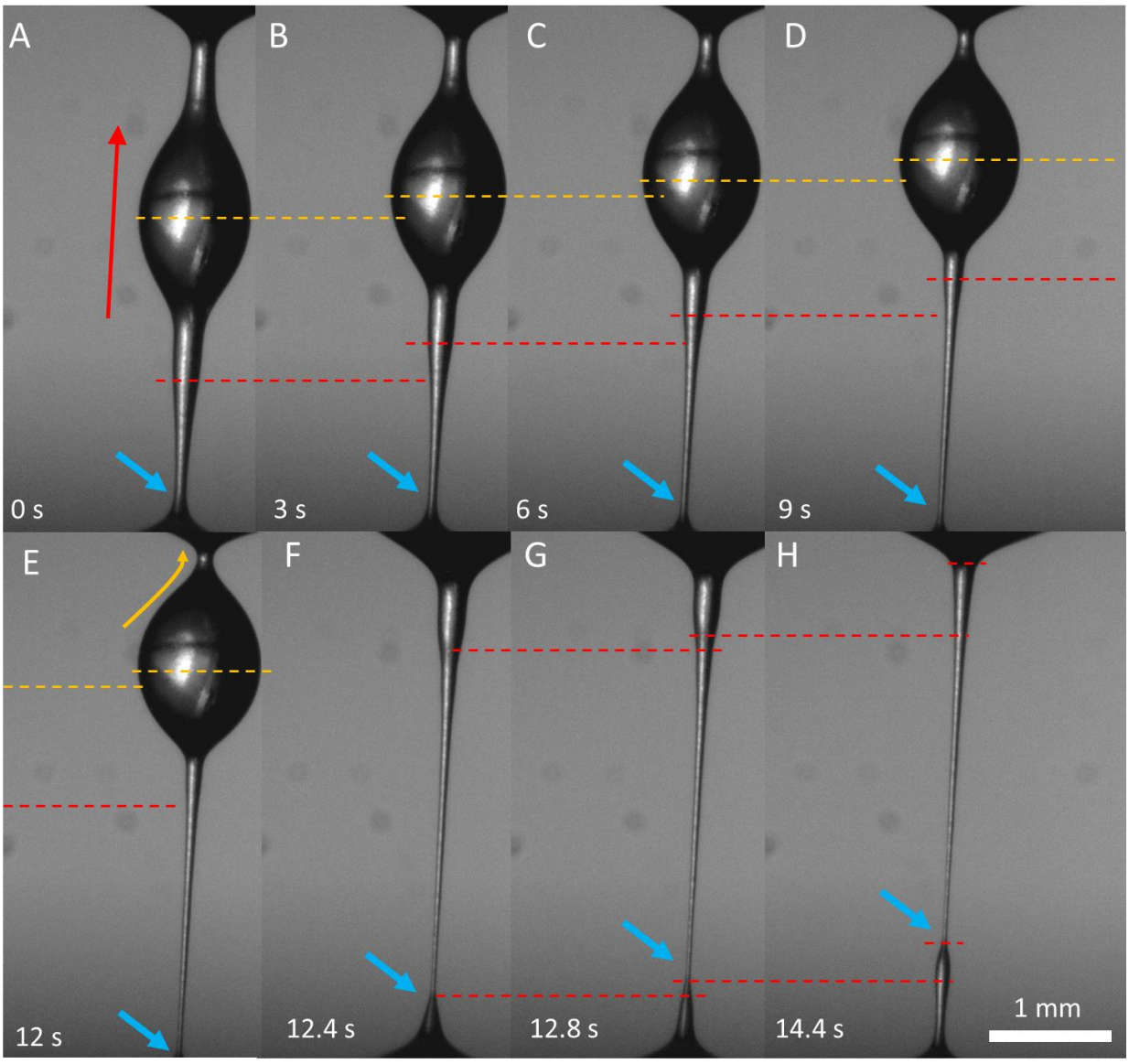

Figure 55. Movement of a droplet and non-uniformities during filament thinning. The red arrow points in the direction of movement of the uniformities labeler with red dashed lines. The blue arrow points to the part of the filament with the smallest radius.

Two distinct mechanisms of the filament breakup have been revealed on all observed LLFs.

In the first breakup scenario, (Figure 56) the filaments undergo a capillary Plateau-Rayleigh instability with formation of either a single or multiple droplets. The capillary Laplace pressure spontaneously set as soon as a cylindrical filament has been formed. This pressure forces the liquid to move from the filament toward the droplets sitting at the filament ends where the pressure is much lower.

According to the Plateau criterion of stability of straight liquid cylinders (41, 42), a long cylindrical filament is always unstable and tends to form a system of capillary waves. In Newtonian fluids, fluid density and viscosity significantly affects the wave pattern; however, for the low Reynolds numbers, viscosity is the main limiting factor affecting the wave development (42, 43). In non-Newtonian viscoelastic fluids such as polymer solutions, polymer elasticity affects the wave development

As illustrated in Figure 56, some waves with infinitesimally small amplitudes spontaneously form on the initially uniform cylindrical surface (Figure 56, B). With time, the waves develop into distinct droplets (Figure 56, C-E).

The probe was fixed at its equilibrium position and the thickness of hemolymph puddle was not significantly changed. However, the droplets can be seen slightly moving (Figure 56, C-E); the droplets marked with the red and yellow dashed lines move slightly upward, while the droplet marked with the blue dashed line moves slightly downward. This indicates that the fluid in the filament moves in the opposite directions with respect to the filament center. Thus, there is a net flow of the liquid in this Plateau-Rayleigh

scenario. Accordingly, the filament length does change in these experiments but not appreciably.

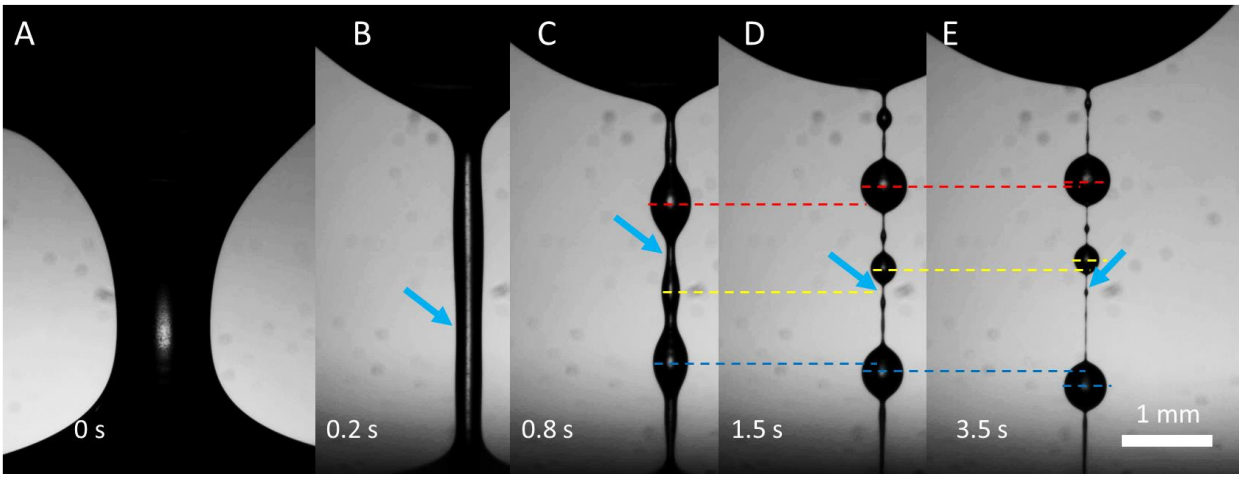

Figure 56. A set of frames illustrating a LLF developing the Plateau-Rayleigh instability. The liquid is being squeezed out of the filament and moves in both directions towards the base droplets. The blue arrow points to the part of the filament with the smallest radius.

In the second breakup scenario, (Figure 56) the filaments undergo a convective capillary Plateau-Rayleigh instability when the liquid is pumped from one end to the other during the filament thinning and breakup. This behavior, when either some parts of the filament (Figure 55, A-E) or the entire filament emerging from one end droplet (Figure 57) being absorbed by the other end droplet, was observed with only some LLFs after a certain point in their thinning. In the LLFs where the entire backbone moved from one base droplet to the other, the droplets moved along with the backbone. Thus, the waves are transferred together with the entire filament simultaneously growing into droplets. Therefore, the term convective capillary Plateau-Rayleigh instability reflects this effect of the movement of wave packet.

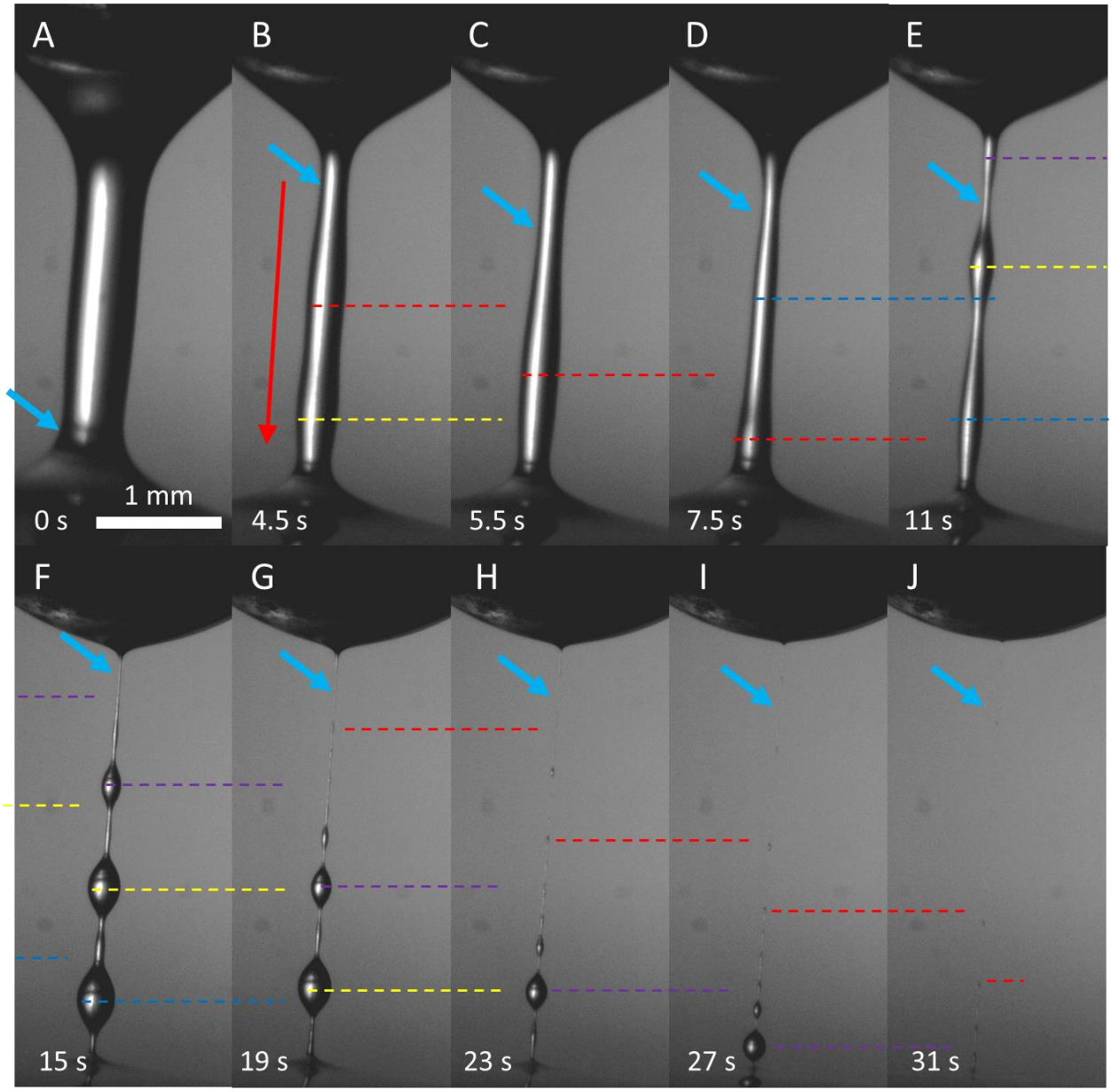

Figure 57. A set of frames illustrating a LLF developing the convective Plateau-Rayleigh instability. The liquid is being squeezed out of the filament and moves in one direction towards the base lower droplet. The local non-uniformities and droplets are labeled with the dashed lines of different colors. On neighboring panels, the same color pertains to the same non-uniformities. The direction of the movement of the features is indicated with the red arrow. The blue arrow points to the part of the filament with the smallest radius.

7.2.6 Tracking of the change of the neck thickness of the filaments

We define the neck of the filament as its part with the thinnest diameter. This part of the filament is thus easy to find algorithmically and is well defined. Due to its definition, the location of the neck may sometimes jump during the filament evolution, especially in the convective Plateau-Rayleigh filaments. In Figure 55, Figure 56, and Figure 57, the neck is marked with a blue arrow. The details of the algorithm that determines the diameter of the thinnest segment of the filament are presented in the Materials and Methods section.

The time changes of the thinnest diameter of the LLFs undergoing convective and non-convective Plateau-Rayleigh instabilities are distinguishable. During the first 0.5 seconds of the process, the change of the filament radius r follows an exponential time dependence, $R = R_0 \exp\left(-t/3\tau_r\right)$ Afterwards, the filament radius follows a linear time dependence $R = R_0 - mt$, where $m = \sigma/3\eta$. The slope m of the decay in the linear regime was measured for 6 filaments to be $m = 2.9 \pm 0.5 * 10^{-5}$ m/s (Figure 58).

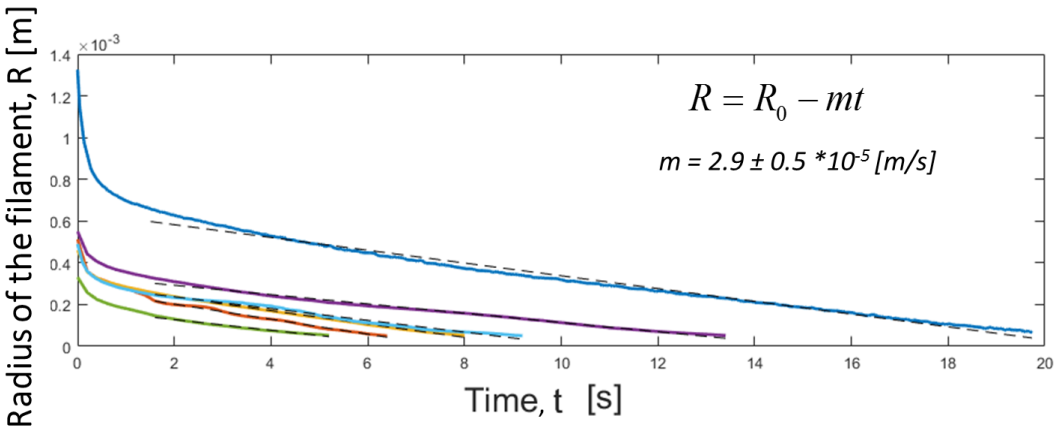

Figure 58. The radius of the filament as a function of time for six LLFs decaying via capillary thinning.

One way to interpret the linear kinetics of the radius decrease due to capillary thinning is by using equation (1.6) for a Newtonian liquid, where the slope is inversely proportional to the viscosity, $m = \sigma/3\eta$. Thus, to relate the slope to the viscosity, we measured the surface tension of the *M. sexta* caterpillar hemolymph using the pendant droplet method to be σ = 62 ± 3 mN/m. The measurements as well as their time-dependence will be discussed in Chapter 9. Here, we estimate the viscosity of the material composing the LLF decaying due to capillary thinning to be η = 600 ± 100 Pa*s. This estimate suggests that the hemolymph material is highly viscous, about six orders of magnitude greater than that of water!

The LLFs undergoing convective Plateau-Rayleigh instability also demonstrate an almost linear decay of the filament radius with a decay rate similar to that of the filaments

decaying via capillary thinning. To see this, we analyzed seven such filaments, and the slope of the linear region was similar, $m = 2.8 \pm 1 * 10^{-5}$ m/s (Figure 59).

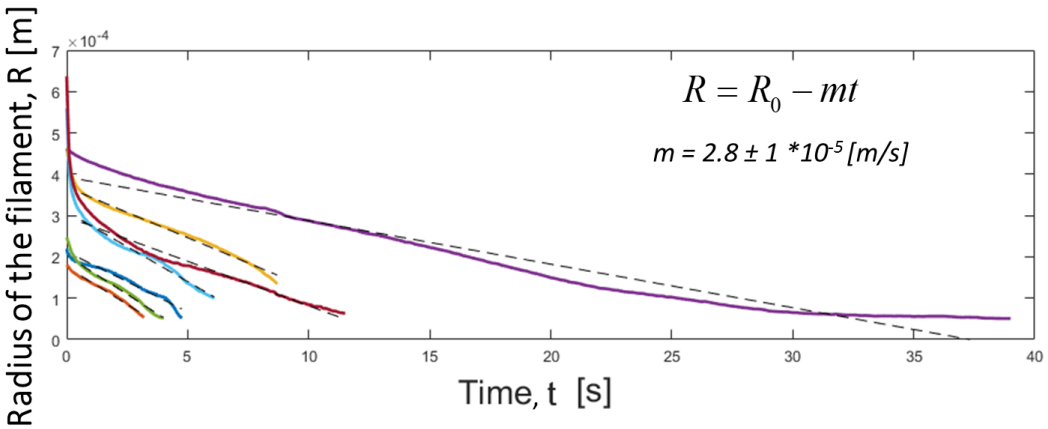

Figure 59. The kinetics of the bridge breakup in the case of development of a convective instability on LLFs. Seven filaments were analyzed, and the slope of the linear region was m = 2.8 ± 1 *10^{-5} m/s.

It is also instructive to classify only the first filament produced at a particular location in an incubating hemolymph puddle, when the structure of the soft clot inside it is not previously perturbed. We performed 30 experiments on the hemolymph puddles collected from 7 caterpillars and the filaments were classified as either following the convective or non-convective Plateau-Rayleigh instability. We found that out of these 30 LLF, seven filaments followed non-convective Plateau-Rayleigh instability and 23 filaments demonstrated the material pumping and developed convective Plateau-Rayleigh instability. All but one of those filaments that developed non-convective Plateau-Rayleigh instability typically did not break and dried out leaving behind a string with several droplets on it; one of those filaments broke. Those filaments that developed

convective Plateau-Rayleigh instability, however, broke in 18 out of the 23 cases and remained intact in 5 cases.

For the LLF following convective Plateau-Rayleigh instability, the incubation time of the hemolymph puddle was $\tau_i = 4 \pm 3$ minutes. The LLF following non-convective convective Plateau-Rayleigh instability were obtained from the hemolymph puddles incubated for the longer time, $\tau_i = 12 \pm 5$ minutes. In other words, the younger liquid bridges seem to carry some mobile soft clots which were suspended in the hemolymph puddle; the older liquid bridges seem to be formed by a homogeneous highly viscous clot.

7.2.6.1 Kinetics of disappearance of SLF

The filaments with a lifetime smaller than 1 second (classified as SLF) exhibited a reproducible pattern with little variation in the development of the filaments. Shortly after a filament of a uniform radius was formed, its radius quickly decreased to zero, at which point the filament broke, Figure 60. No droplets or other features were formed on the filament during this time, i.e. the filaments were straight cylindrical. The radius of the cylindrical filaments decreased exponentially with time for all filaments. To fit the experimental data, we modeled these filament materials as Maxwell fluids, see equation (1.7). The relaxation times were calculated for 65 samples and the results are presented in a histogram in Figure 62. The relaxation time τ_r varied drastically across the samples. The distribution of the relaxation times ranges between $\tau_r = 10^{-3}$ and $\tau_r = 0.5$ seconds.

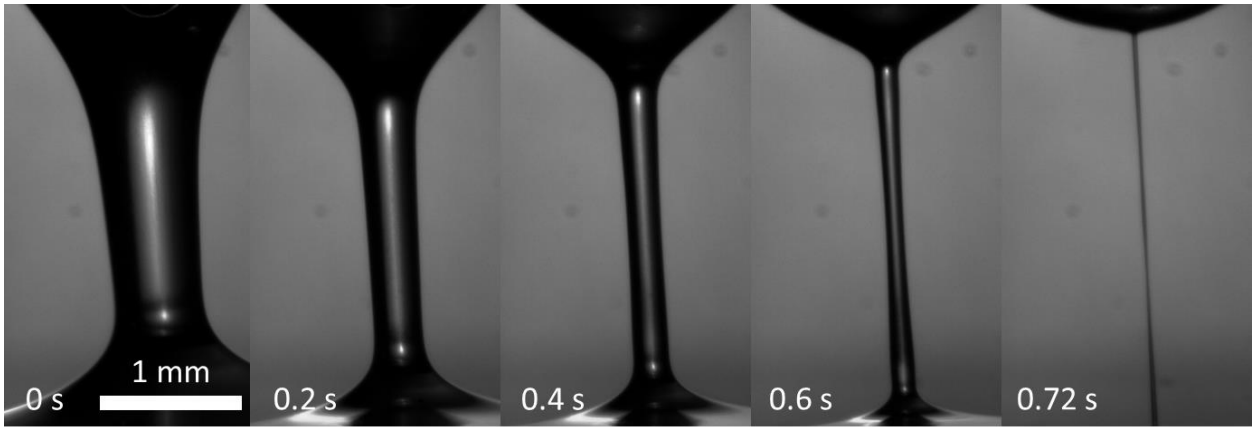

Figure 60. An example of an SLF decaying via a capillary thinning.

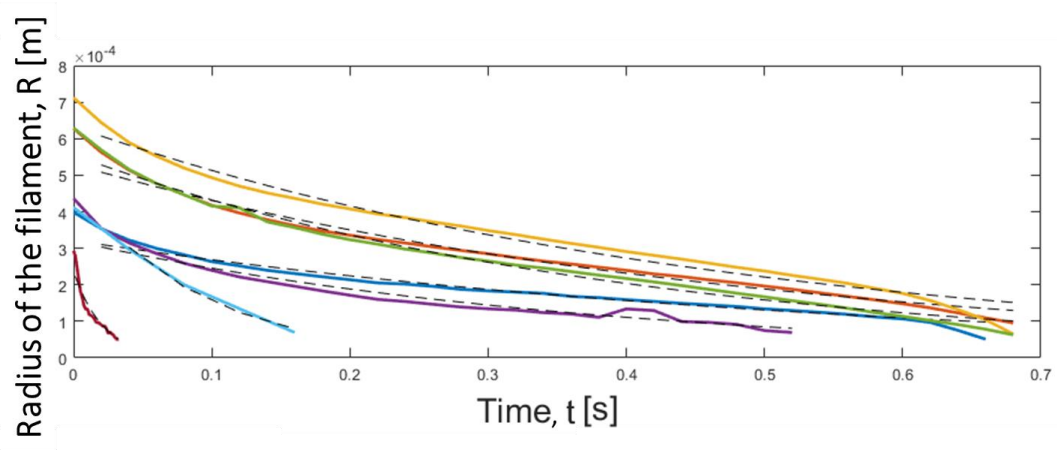

Figure 61. Examples of exponential decays of the radii of SLF.

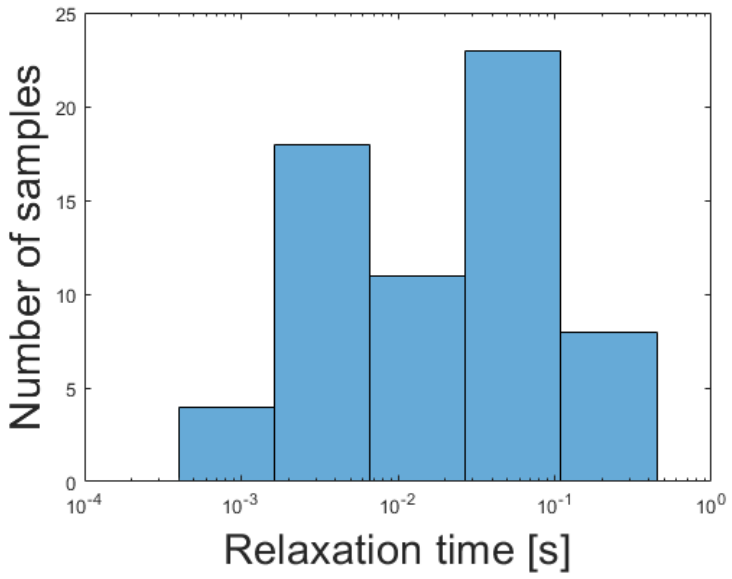

Figure 62. Histogram of relaxation times of SLF.

7.3 DISCUSSION

The analysis of the breakup kinetics of the liquid bridges that hemolymph forms upon extension led to several important findings. First, it was found that in the first 90 seconds after wounding, hemolymph rigidifies and the primary clot forms to stop the bleeding. This was also evident from the gradual elimination of capillary instability and drops-on-string patterns as the hemolymph was dripping from the wound and formation of the straight cylindrical filaments indicative to either high viscosity or inherent elasticity in the stretched fluid. After 90 seconds, hemolymph at the wound exhibits a dichotomy of properties – the dripping fluid forms either LLFs or SLFs, indicating that two types of materials are present.

The material that produces SLFs can be an elastic Maxwell fluid with a range of relaxation times.

The material that produces LLF behaves differently, depending on how long it has been incubated. If hemolymph was incubated for less than 7 minutes, the resulting LLF follows convective Plateau-Rayleigh instability. That is, the liquid is continuously moved along the filament in one direction and, simultaneously, a system of capillary waves develops. If incubated for longer than 7 minutes, the filament undergoes non-convective Plateau–Rayleigh instability forming a periodic system of droplets. Typically, these filaments do not completely break and dry out leaving behind a thin string with droplets suspended on it.

The formation of the droplets on the LLFs deserves separate attention. The scenario of liquid bead formation on a solid string was explored in a classical work by Boys (44). In it, he demonstrates that the driving mechanism of this phenomenon is capillary thinning of a liquid film. Subsequent experiments and simulations have shown the capillary instability of the liquid film leads to the breakup of the liquid layer into droplets (45-47). The process is slowed down by the viscous interaction between the substrate and the thinning liquid layer. The process leads to an interactive instability that results in droplets that form on the solid fiber. In our case, however, there is no solid backbone to form fibers on, so a different physical phenomenon must be present.

The scenario of bead formation on the surface of a liquid filament with no solid string backbone has been experimentally studied by Oliveira *et. al. (48)* and numerically studied by Bhat *et. al.* (49)in the context of Deborah and Reynolds numbers. According to their analysis, at high Reynolds numbers, a single bead can form on a filament if the De ~ 0.1 and multiple beads can only form if the De ~ 0.01. At low Reynolds numbers,

such as in our experiment, only a single bead can form De ~ 0.01 and multiple beads cannot form at all!

We hypothesize that the resolution to the paradox is that the LLF consists of two parts: a relatively rigid or gel-like backbone and a liquid plasma that forms droplets, similarly to how water forms droplets on a string in the work by Boys (44) and obtains the shape originally described by Plateau (50) (Figure 63). This hypothesis is consistent with the observations of the convective Plateau-Rayleigh instability, where the backbone seems to move in the same direction along the LLF, rather than away from the center of the filament. This motion can thus be explained by the fact that the material is too strong to be broken apart and is moved to one side or the other by the forces of surface tension or differential adhesion of the backbone to the substrates. This is consistent with the nanorheological experiments from the previous chapters, which showed that the clot is a strong adherent material with an exponentially increasing viscosity with time.

Also, as shown in the previous chapters, as incubation time increases and the clot matures, it becomes less adhesive. When the stainless-steel probe is lowered into this mature hemolymph, less of the clot material adheres to it. Since it is less adherent, the backbone no longer travels in one direction and remains stationary stretched between the probe and the substrate. Instead, it serves as a strong backbone for the droplets to develop over and for plasma to travel along to leave the filament due to the capillary thinning.

This would also explain the dichotomy of the SLF and the LLF formations at the same location in the hemolymph puddle one after the other: if the probe destroys or

adheres to the soft clot material that forms the LLF during the first run of the experiment, the soft clot material does not get stretched during the second experiment and the SLF forms only from the plasma. To verify the hypothesis of the complex structure in the filaments, we capture the filaments and study their structure with microscopy in the next chapter.

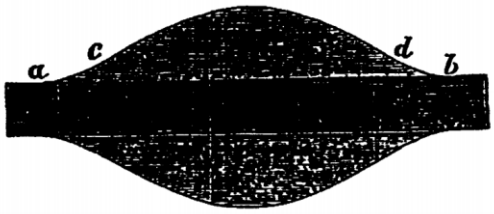

Figure 63. The shape of a droplet of liquid on a solid substrate. (a) and (b) mark the edges of the droplet. (Copied form original work by Plateau(50))

7.4 MATERIALS AND METHODS

7.4.1 Video analysis

To analyze the behavior of the liquid bridges as a function of time, their profiles need to be extracted. We created a custom software using LabVIEW Vision Development Module to extract and analyze the profile of the liquid bridges at each frame.

The profile image extraction algorithm is as follows. Each step of the algorithm with user interaction is illustrated in Figure 64.

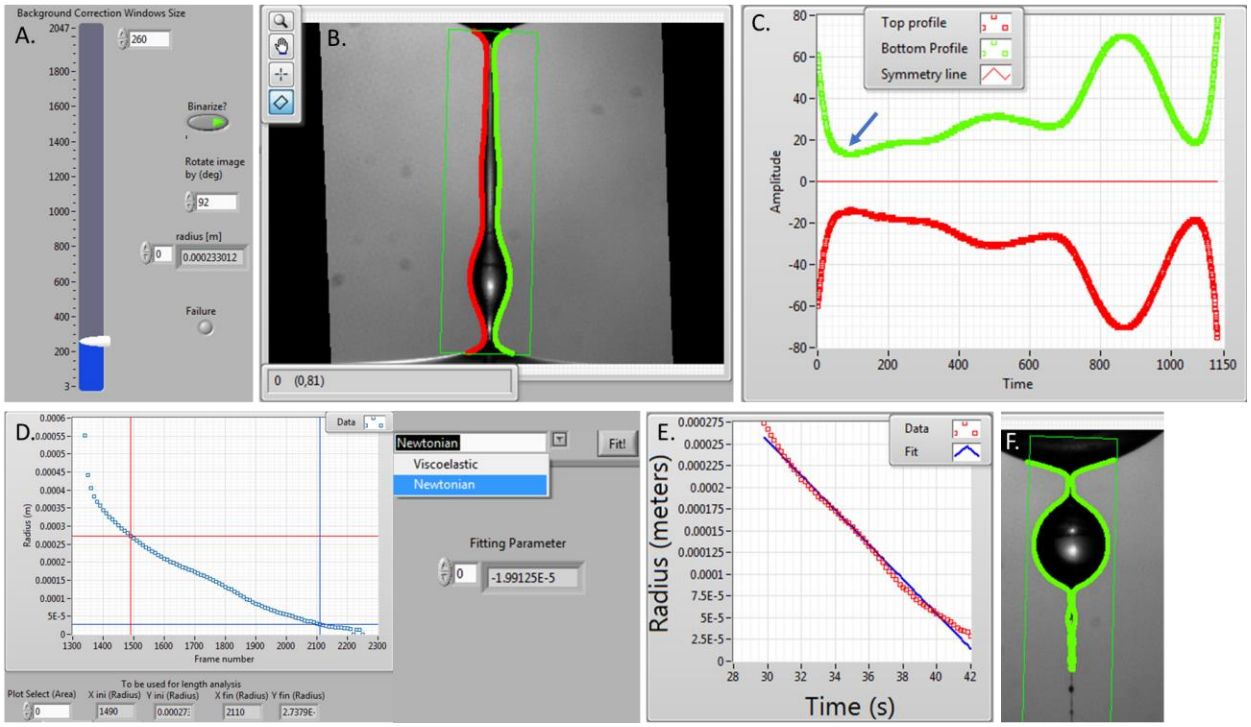

Figure 64. Key steps of the image analysis algorithm. (A) The parameters of the image analysis. The user manually selects the acceptable parameters.(B)The extracted contour of the filaments superimposed with the image. (C) The extracted contour data, rotated around the symmetry line. The minimum diameter is labeled with a blue arrow. (D) A plot of the radius minima of the filament for all frames in the video. The user moves the cursers on the plot to encapsulate the data of interest. (E) The selected data is fitted with the desired model. (F) An example of a failed contour extraction, where the thickness of the filament is too small for the program to detect.

First, the user rotates the image using the controls in Figure 64, A, so that the filament is vertical. The user then specifies the region of interest where the software should find the liquid bridge; all information outside of this region is disregarded (Green box in Figure 64, B).

Depending on the quality of the image, it may be more efficient to either binarize the image (make it black-white) or use the grayscale gradient to detect the edge of the liquid bridge. If the image needs to be binarized, it is done using either constant threshold

values or background correction via IMAQ Local Threshold algorithm. Binarization of the image sometimes causes artificial holes to appear in objects; these holes are automatically filled in using IMAQ FillHole algorithm to insure correct further analysis. Another prominent issue occurs when the diameter of the neck is too small for the program to resolve. The algorithm then fails to correctly separate the left edge from the right edge of the droplet and cannot analyze it further (Figure 64, F). If the binarization is successful and produces an artifact-free image, the contour is extracted using the IMAQ Extract Contour algorithm. The user looks at the extracted contour superimposed on the image (Figure 64, B) and makes a judgement call on the quality of the extraction. If the extraction is poor, the user has an option to change the properties of the extraction (Figure 64, A).

If the background is non-uniform or the liquid bridge has a low contrast, it is better to use the IMAQ Extract Contour algorithm without prior binarization of the image; in this case, the algorithm finds and extracts the contour of an object with a highest grayscale gradient in the region of interest.

Once the liquid bridge profile is extracted, it needs to be analyzed to extract the width of the neck. To perform this or any other analysis, the contour needs to be rotated, such that it is oriented along a common axis – in this case, the x-axis (Figure 64, C). To do that, the centerline of the liquid bridge needs to be found. The process is as follows. First, the contours for the left and right edges are separated. The data points in the left and right profiles are then interpolated, such that each data point in one profile has a sister data point in the other profile. This ensures that two profiles are symmetric. The

data is then fitted with a line; due to the fact that both curves are symmetric, the best fit line is the centerline of the two profiles. The angle of the best fit line is then extracted and the profiles are rotated by the angle of the best fit line. The data is thus oriented along the x-axis (Figure 64, C).

The radius of the neck of the liquid bridge is then easily found as the minimum of one of the profiles (Figure 64, C, blue arrow). This is done for each frame of interest in the video. To select the region of interest in the data for further analysis, the user moves the markers on a plot (Figure 64, D). The user then fits the selected data with the selected model, and is presented with the fitted results (Figure 64, E).

The data is stored for any future analysis as a spreadsheet, in which the profile of the liquid bridge at each frame is stored.

7.5 REFERENCES

1. Bidla G, Lindgren M, Theopold U, Dushay MS. Hemolymph coagulation and phenoloxidase in Drosophila larvae. Developmental and Comparative Immunology. 2005;29:669-79.10.1016/j.dci.2004.11.007
2. Lesch C, Theopold U. Methods to study hemolymph clotting in insects. Insect Immunology. 2008:1-12,
3. Castrejon-Pita AA, Castrejon-Pita JR, Hutchings IM. Breakup of liquid filaments. Physical review letters. 2012;108(7):074506,
4. Ledesma-Aguilar R, Nistal R, Hernández-Machado A, Pagonabarraga I. Controlled drop emission by wetting properties in driven liquid filaments. Nat Mater. 2011;10(5):367,
5. Kawano S. Molecular dynamics of rupture phenomena in a liquid thread. Physical review E. 1998;58(4):4468,
6. Kwak S, Pozrikidis C. Effect of surfactants on the instability of a liquid thread or annular layer: Part I: Quiescent fluids. Int J Multiphas Flow. 2001;27(1):1-37,
7. Thompson J. Stability of a liquid thread and stability and nonlinear evolution of multi-layer fluid flow: University of East Anglia; 2016.
8. De Gennes P-G, Brochard-Wyart F, Quéré D. Capillarity and Gravity. Capillarity and Wetting Phenomena: Springer; 2004. p. 33-67,

9. McKinley GH, Tripathi A. How to extract the Newtonian viscosity from capillary breakup measurements in a filament rheometer. Journal of Rheology. 2000;44(3):653-70.Doi 10.1122/1.551105
10. Bazilevsky AV, Entov VM, Rozhkov AN. Breakup of a liquid bridge as a method of rheological testing of biological fluids. Fluid Dynamics. 2011;46(4):613-22.10.1134/S0015462811040119
11. Alexandrou AN, Bazilevskii AV, Entov VM, Rozhkov AN, Sharaf A. Breakup of a Capillary Bridge of Suspensions. Fluid Dynamics. 2010;45(6):952-64.10.1134/S001546281006013x
12. Clasen C, Plog JP, Kulicke WM, Owens M, Macosko C, Scriven LE, Verani M, McKinley GH. How dilute are dilute solutions in extensional flows? Journal of Rheology. 2006;50(6):849-81.10.1122/1.2357595
13. Tuladhar TR, Mackley MR. Filament stretching rheometry and break-up behaviour of low viscosity polymer solutions and inkjet fluids. Journal of Non-Newtonian Fluid Mechanics. 2008;148(1-3):97-108.10.1016/j.jnnfm.2007.04.015
14. Bazilevsky AV, Entov VM, Rozhkov AN, editors. Liquid filament microrheometer and some of its applications. The Golden Jubilee Meeting of the British Society of Rheology and Third European Rheology Conference; 1990; Edinburgh, UK.
15. McKinley GH, Sridhar T. Filament-stretching rheometry of complex fluids. Annu Rev Fluid Mech. 2002;34:375-415.10.1146/annurev.fluid.34.083001.125207
16. Marshall KA, Liedtke AM, Todt AH, Walker TW. Extensional rheometry with a handheld mobile device. Exp Fluids. 2017;58(6). 10.1007/s00348-017-2351-9

17. Anna SL, Rogers C, McKinley GH. On controlling the kinematics of a filament stretching rheometer using a real-time active control mechanism. Journal of Non-Newtonian Fluid Mechanics. 1999;87(2-3):307-35.Doi 10.1016/S0377-0257(99)00072-5
18. Campo-Deano L, Clasen C. The slow retraction method (SRM) for the determination of ultra-short relaxation times in capillary breakup extensional rheometry experiments. Journal of Non-Newtonian Fluid Mechanics. 2010;165(23-24):1688-99.10.1016/j.jnnfm.2010.09.007
19. Niedzwiedz K, Buggisch H, Willenbacher N. Extensional rheology of concentrated emulsions as probed by capillary breakup elongational rheometry (CaBER). Rheol Acta. 2010;49(11-12):1103-16.10.1007/s00397-010-0477-2
20. Roche M, Kellay H, Stone HA. Heterogeneity and the Role of Normal Stresses during the Extensional Thinning of Non-Brownian Shear-Thickening Fluids. Physical Review Letters. 2011;107(13). 10.1103/PhysRevLett.107.134503

21. Dinic J, Zhang YR, Jimenez LN, Sharma V. Extensional Relaxation Times of Dilute, Aqueous Polymer Solutions. Acs Macro Letters. 2015;4(7):804-8.10.1021/acsmacrolett.5b00393
22. Galindo-Rosales FJ, Alves MA, Oliveira MSN. Microdevices for extensional rheometry of low viscosity elastic liquids: a review. Microfluidics and Nanofluidics. 2013;14(1-2):1-19.10.1007/s10404-012-1028-1
23. Mackley MR, Butler SA, Huxley S, Reis NM, Barbosa AI, Tembely M. The observation and evaluation of extensional filament deformation and breakup profiles for

Non Newtonian fluids using a high strain rate double piston apparatus. Journal of Non-Newtonian Fluid Mechanics. 2017;239:13-27.10.1016/j.jnnfm.2016.11.009
24. Bazilevskii AV, Rozhkov AN. Dynamics of capillary breakup of elastic jets. Fluid Dynamics. 2014;49(6):827-43.10.1134/s0015462814060143
25. Bazilevskii AV. Dynamics of horizontal viscoelastic fluid filaments. Fluid Dynamics. 2013;48(1):97-108.10.1134/s0015462813010110
26. Hubbe MA, Tayeb P, Joyce M, Tyagi P, Kehoe M, Dimic-Misic K, Pal L. Rheology of Nanocellulose-rich Aqueous Suspensions: A Review. Bioresources. 2017;12(4):9556-661.
27. Godinho MH, Pieranski P, Sotta P. Hygroscopic study of hydroxypropylcellulose Structure and strain-induced birefringence of capillary bridges. European Physical Journal E. 2016;39(9).10.1140/epje/i2016-16089-2
28. Haward SJ. Microfluidic extensional rheometry using stagnation point flow. Biomicrofluidics. 2016;10(4).10.1063/1.4945604
29. Petrie CJS. One hundred years of extensional flow. Journal of Non-Newtonian Fluid Mechanics. 2006;137(1-3):1-14.10.1016/j.jnnfm.2006.01.010
30. Hou YY, Kassim HO. Instrument techniques for rheometry. Review of Scientific Instruments. 2005;76(10).10.1063/1.2085048
31. Basaran OA, Gao HJ, Bhat PP. Nonstandard Inkjets. In: Davis SH, Moin P, editors. Annual Review of Fluid Mechanics, Vol 45. Annual Review of Fluid Mechanics. 452013. p. 85-113.10.1146/annurev-fluid-120710-101148
32. Hoath S, Martin G, Tuladhar T, Mackley M, Hutchings I. Links between fluid rheology and drop-on-demand jetting and printability. Nip24/Digital Fabrication 2008: 24th International Conference on Digital Printing Technologies, Technical Program and Proceedings. 2008:130.
33. Mathues W, McIlroy C, Harlen OG, Clasen C. Capillary breakup of suspensions near pinch-off. Phys Fluids. 2015;27(9). 10.1063/1.4930011

34. Berret JF, Roux DC, Porte G. Isotropic-to-Nematic Transition in Wormlike Micelles under Shear. J Phys Ii. 1994;4(8):1261-79.
35. Walker LM, Moldenaers P, Berret JF. Macroscopic response of wormlike micelles to elongational flow. Langmuir. 1996;12(26):6309-14.DOI 10.1021/la960662v
36. Chevry L, Sampathkumar NK, Cebers A, Berret JF. Magnetic wire-based sensors for the microrheology of complex fluids. Physical Review E. 2013;88(6).10.1103/PhysRevE.88.062306
37. Loosli F, Najm M, Berret JF. Viscoelasticity of model surfactant solutions, determined by magnetic rotation spectroscopy. Colloids and Surfaces a-Physicochemical and Engineering Aspects. 2016;510:143-9.10.1016/j.colsurfa.2016.06.019
38. Castrejón-Pita JR, Castrejón-Pita AA, Thete SS, Sambath K, Hutchings IM, Hinch J, Lister JR, Basaran OA. Plethora of transitions during breakup of liquid filaments. Proceedings of the National Academy of Sciences of the United States of America. 2015;112:4582-7.10.1073/pnas.1418541112
39. Day RF, Hinch EJ, Lister JR. Self-similar capillary pinchoff of an inviscid fluid. Physical Review Letters. 1998;80(4):704-7.DOI 10.1103/PhysRevLett.80.704

40. Collins RT, Harris MT, Basaran OA. Breakup of electrified jets. J Fluid Mech. 2007;588:75-129.10.1017/S0022112007007409
41. Plateau JAF. Statique expérimentale et théorique des liquides soumis aux seules forces moléculaires: Gauthier-Villars; 1873.
42. Michael DH. Meniscus Stability. Annu Rev Fluid Mech. 1981;13:189-215.DOI 10.1146/annurev.fl.13.010181.001201
43. Rayleigh L. XVI. On the instability of a cylinder of viscous liquid under capillary force. The London, Edinburgh, and Dublin Philosophical Magazine and Journal of Science. 1892;34(207):145-54,
44. Boys CV. Soap bubbles and the forces which mould them. 1st American ed. Garden City, N.Y.,: Doubleday Anchor Books; 1959. 156 p,
45. Goren SL. The Instability of an Annular Thread of Fluid. J Fluid Mech. 1962;12(2):309-19.Doi 10.1017/S002211206200021x
46. Goren SL. Shape of Thread of Liquid Undergoing Break-Up. J Coll Sci Imp U Tok. 1964;19(1):81-&.Doi 10.1016/0095-8522(64)90009-1
47. Kalliadasis S, Chang HC. Drop Formation during Coating of Vertical Fibers. J Fluid Mech. 1994;261:135-68.Doi 10.1017/S0022112094000297
48. Oliveira MSN, Yeh R, McKinley GH. Iterated stretching, extensional rheology and formation of beads-on-a-string structures in polymer solutions. Journal of Non-Newtonian Fluid Mechanics. 2006;137(1-3):137-48.10.1016/j.jnnfm.2006.01.014
49. Bhat PP, Appathurai S, Harris MT, Pasquali M, McKinley GH, Basaran OA. Formation of beads-on-a-string structures during break-up of viscoelastic filaments. Nat Phys. 2010;6(8):625-31.10.1038/Nphys1682
50. Plateau FlAJ. Experimental and Theoretical Statics of Liquids Subject Only to Molecular Forces. Paris: Gauthier-Villars; 1873.

CHAPTER VIII

STRUCTURE OF LONG-LIVED AND SHORT-LIVED FILAMENTS

8.1 INTRODUCTION

8.1.1 Complex structure, consisting of proteins and hemocyte aggregates in untouched hemolymph and pulled out clots

As discussed previously, hemolymph of *M. sexta* is a complex liquid, which consists of adhesive and non-adhesive cells suspended in plasma. After exiting the body via a wound, the cells aggregate by using pseudopodia and differential adhesion to form clusters. These clusters presumably form the soft clot on the wound. These structures rigidify with time on the scale of minutes. The structures are partly held together with glycosylated proteins, which could be observed after staining, lining the walls of the cells inside the cellular aggregates. After swirling the sample with a stirrer and 'pulling out' the clot, the glycosylated proteins stretched into long fibers, which were surrounded with large cellular aggregates.

When probed with extensional methods, the hemolymph exhibited a dichotomy of properties – the same droplet of hemolymph, when probed twice back-to-back could produce a liquid filament that decayed in tens of seconds (long-lived filament, LLF) followed by a filament that decayed in less than a second (short-lived filament, SLF). This suggests that the two consecutive experiments may actually probe different materials.

8.1.2 Hypothesis

Based on the fact that the soft clot is highly adherent and was shown to be able to be ‘pulled out’ with a glass stirrer, we hypothesize that the material that constitutes the LLF at least in part consists of the soft clot. If this hypothesis is correct, the observations can be explained as follows. When the probe is lowered into the sample, the soft clot, due to its adhesive nature, adheres to the probe. Then the probe is raised, the soft clot is partly pulled out of the droplet along with the liquid around it. The liquid then wants to leave the liquid column as it is squeezed out by its surface tension. This leaves the soft clot behind, which does not break up, but rather pulls itself to one side (either to the probe or the droplet) in a large patch. If it moves towards the metal probe, it likely adheres to it and does not get detached next time the probe is lowered. Hence during the second measurement, we only probe the liquid hemolymph and not the soft clot and observe the SLF.

In this chapter, we collect the LLF and SLF during their lifetime on glass and plastic substrates to image any internal structure that they exhibit and relate it to the rheological measurements.

8.1.3 Methodology

To image the structure in the filaments with microscopy, the material has to be collected during the lifetime of the filament. The LLF were collected using two methods. The first method allowed us to collect the LLF exactly as they were during the experiment. It relied on first creating the LLF between a glass substrate and the metal ball probe and then sliding a glass slide between the two surfaces to collect the material on the slide. The material would remain adhered to the slide and could be covered with a cover

slip for microscopy. The second method allowed us to first dye the glycosylated proteins with a fluorescent rhodamine-PNA dye prior to making the LLF. It consisted of mixing the extracted hemolymph with the dye with minimal interaction on a glass slide, incubating the sample, producing the LLF with a metal probe, and then touching the metal ball to the glass slide. The LLF material would thus adhere to the glass slide and remain in place for further imaging.

Collection of the SLF was a challenge due to their short lifetime which prevented any manual manipulation of the collectors or the filaments. Instead, we used electrostatic attraction to collect the material. We were only able to make this technique work with the hemolymph that was dripping from the wound of the caterpillar. The method relied on placing a charged plastic microscopy slide next to future trajectory of the droplet. When the droplet fell and the SLF was formed, the liquid became attracted to the slide and the SLF flew towards it. By aligning the plastic coverslip just right and removing it immediately after a successful collection, we were able to obtain only the relevant material from the SLF and not the droplet itself.

8.2 RESULTS

8.2.1 Long fibrous protein structure in LLF

Hemolymph collected from the LLF with and without staining demonstrates similar structure: long thin oriented fibers along with hemocytes propagate along the length of the filament. Figure 65 shows such structure from a filament collected without staining with roughly 1.5 minutes of incubation after wounding. Panel (A) shows the entire length of the collected filament is over 3 mm. The fibrous structure is in the center

of the image and the light grey plasma surrounds it. This fibrous structure is what forms the backbone of the LLF. Panel (B) is zoomed in on the center region of the fibrous backbone. Cellular aggregates are located along the backbone and the concentration of cells outside of the backbone is low. Panels (C) and (D) are even further zoomed in on two regions of the filament. A structure, which consists of multiple thin long fibers with embedded cellular aggregates and individual cells is evident. These observations are consistent with our hypothesis of a backbone structure in the LLF.

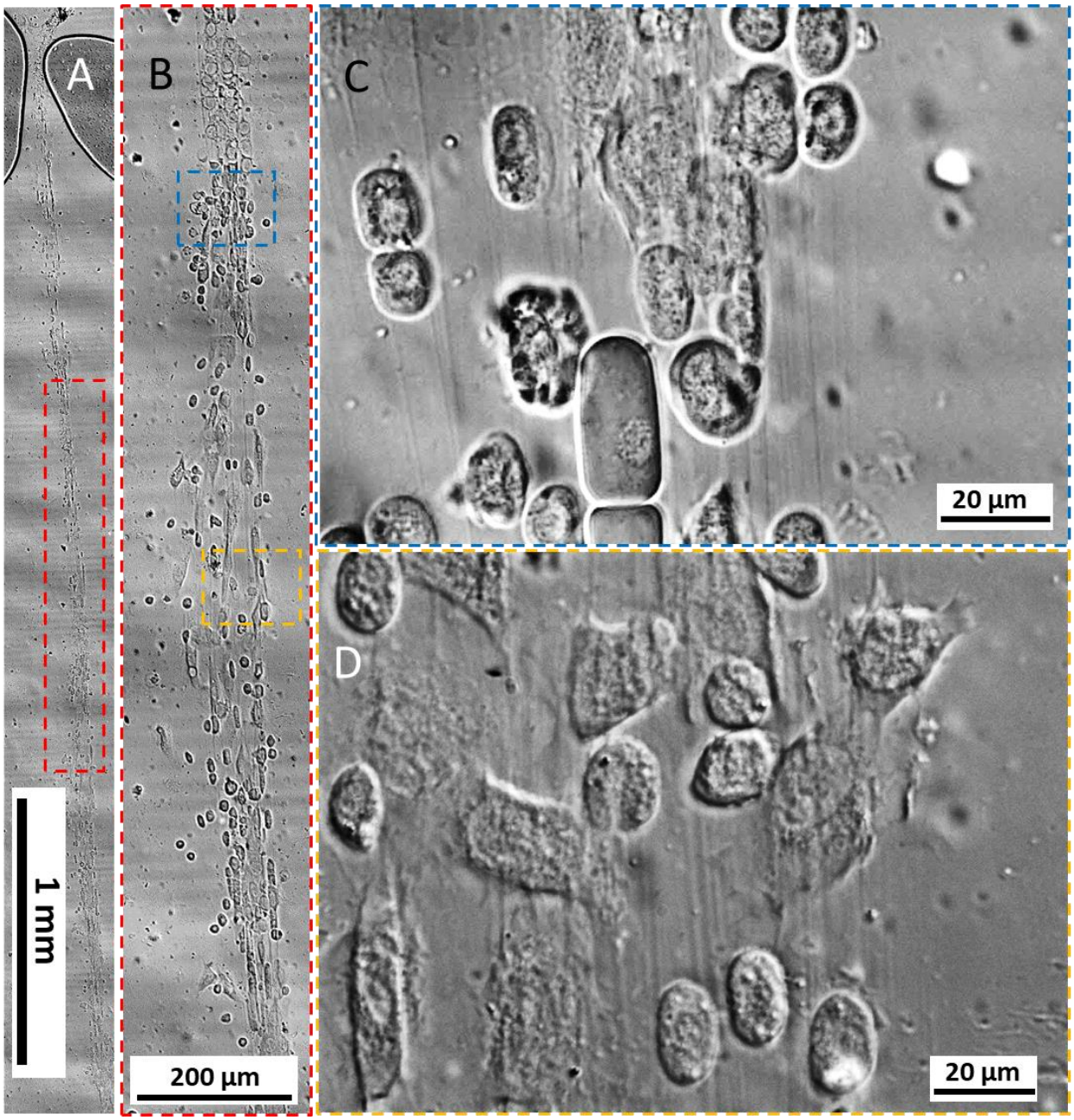

Figure 65. A phase-enhanced image of an LLF captured on a glass slide created from hemolymph incubated for approximately 1.5 minutes after wounding. (A) The entire length of the collected filament is over 3 mm. The fibrous structure is in the center of the image and the light grey plasma surrounds it. (B) A closer look at the same filament. Cellular aggregates are located along the backbone and the concentration of cells outside of the backbone is low. (C) and (D) are even further zoomed in on two regions of the filament. Hemocyte aggregates and single hemocytes are seen adhered to a bundle of fibers

To gain insight into the material composing the fibers, we perform staining of the glycosylated proteins with a florescent rhodamine-PNA dye prior to formation of an LLF with a metal probe. This labeling was challenging, since the labeling procedure (outlined in chapter 5) called for stirring of the sample to mix the dye in and incubation for 10 minutes to let the dye adhere to the protein. In our experiment (and as reported in the previous chapter), however, the LLF change their behavior and typically stop appearing altogether after 10-12 minutes of incubation. The incubation time prior to the LLF formation was thus lowered to 5 minutes to remain in the time window during which liquid filament can be formed. We also saw that stirring led to the adhesion of the soft clot to the stirrer and consequential removal of the soft clot from the sample. We thus had to eliminate the destructive stirring step from the protocol. Because of this, the quality of the staining suffered, but the fibrous material is nevertheless visible.

Images of the stained hemolymph after the LLF was formed are presented in Figure 66. The bulk of the sample was similar to the bulk images presented in Chapter 5. In the vicinity of the liquid filament, however, a clear fibrous structure composing of glycosylated proteins (Figure 66 B and D) surrounded with aggregated hemocytes (Figure 66 A and C) is visible. There are two parallel fibrous structures visible in panels (A and B). This suggests that during the LLF evolution, multiple strands of the stretched soft clot can come together under the effects of the surface tension and adhere together to form the backbone of the LLF. These results strongly support the hypothesis that the fibers are comprised of the same glycosylated proteins observed in the soft clot.

After incubation of more than 40 minutes, fibers became darker and more visible under phase-enhanced microscopy (Figure 66 E and F). These fibers propagated through the liquid filament. The fact that the orientation of these darker fibers is the same as that of the glycosylated proteins and cellular aggregates suggests a connection between the two structures.

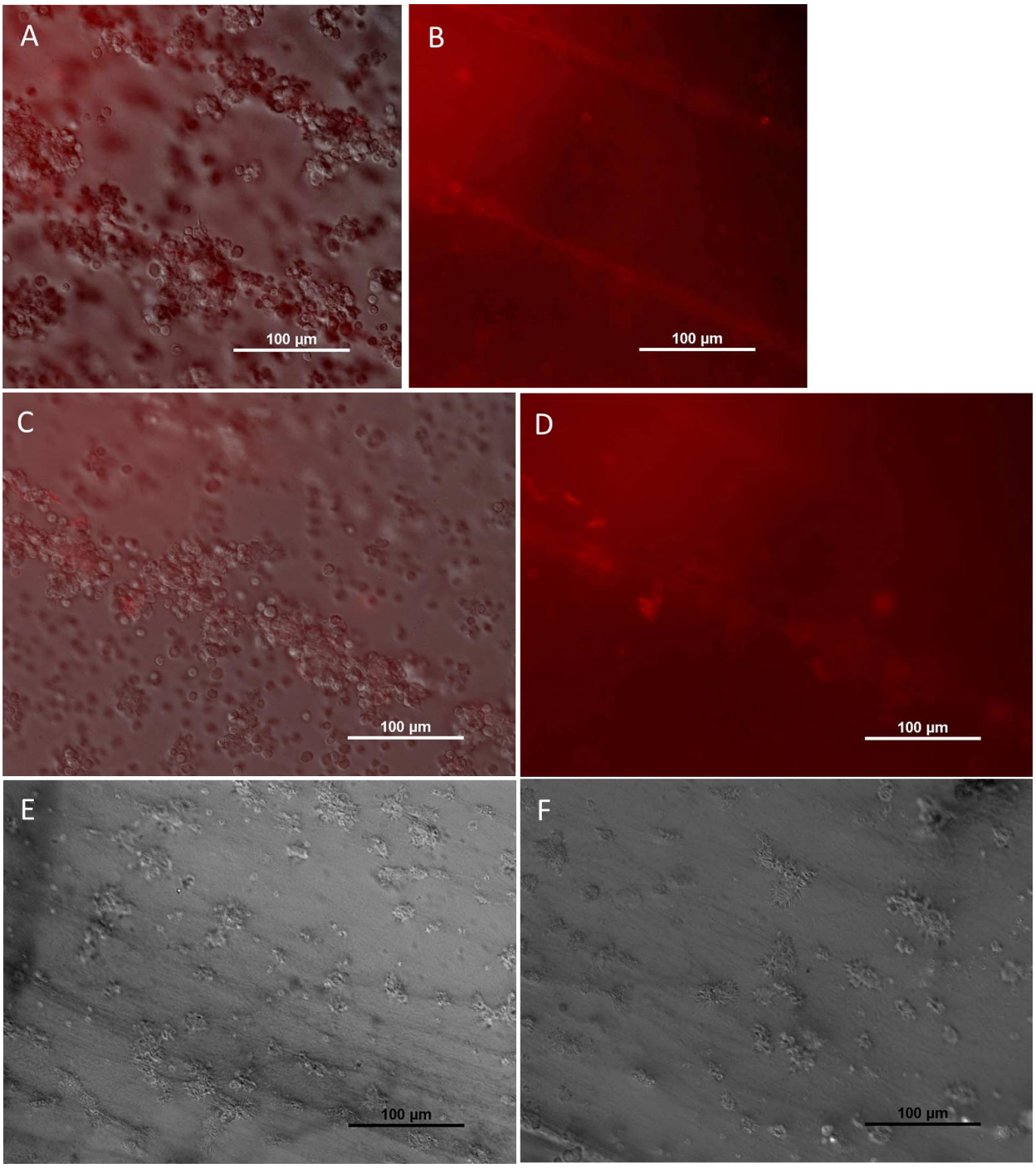

Figure 66. Fluorescent and phase-enhanced micrographs of a liquid filament made from hemolymph mixed with PNA dye and incubated for 5 minutes; liquid filament was collected during its initial second of lifetime. (A, C) phase enhanced overlayed with (B, D) fluorescent images of the fibrous structure in the sample near the liquid filament. The structure composed of cells and glycolated proteins is apparent. (E, F) Phase enhanced

images of the liquid filament, demontrating oriented fibrous structure. The amount of dye in this region was too high to produce a fluorescent image

8.2.2 No observable microstructure in SLF

The collected SLF exhibited none of the structure found in the SLF. First, it did not contain any fibers – aligned along the direction of stretching or otherwise. Second, there were no hemocyte aggregates – there were few hemocytes at all (around 10 per filament). Typically, the collected SLF looked like a homogeneous liquid sample with no distinguishing features under phase-enhanced microscopy. For that reason, no images of it are presented.

8.3 DISCUSSION

Long-lived and short-lived liquid filaments produced from hemolymph of larval *M. sexta* were collected and imaged under phase-enhanced and fluorescent microscopy. The LLF contain multiple bundles of fibrous glycosylated proteins with adhered aggregates of hemocytes oriented in the direction of stretching. The SLF, however, do not contain any visible microstructure or hemocytes. This is consistent with our hypothesis and means that the LLF consist of the soft-clot material at the core with plasma surrounding it. The SLF, meanwhile consist of just the plasma and while the liquid at the onset of the SLF may contain individual or aggregates of hemocytes, they are all squeezed out of the filament during the later stages of thinning.

8.4 MATERIALS AND METHODS

8.4.1 Collection of an LLF on glass slide with no dying

For imaging of material inside of LLF without dying, the collected liquid filaments were extended with a probe from a large hemolymph droplet on a substrate as described in section 7.2.4. Since the LLF can exist for seconds, one can carefully swipe a small piece of glass coverslip over the filament to collect it. Because of a small working distance of several mm between the probe and the droplet, however, there is a high chance of contamination of the sample with the material from the bulk. Another challenge arises that if the filament breaks during the collection, the material will all collect at the edge of the cover slip and would be impossible to image. Figure 67 illustrates this issue. In it, the leading edge of the collector slide attached to the LLF, the large liquid bead was collected on the slide, and the material that was between the edge and the bead was collected. The filament that was between the liquid bead and the metal ball, however, broke and flew to the probe or the bead. Due to these two challenges, only four LLF were successfully collected and imaged.

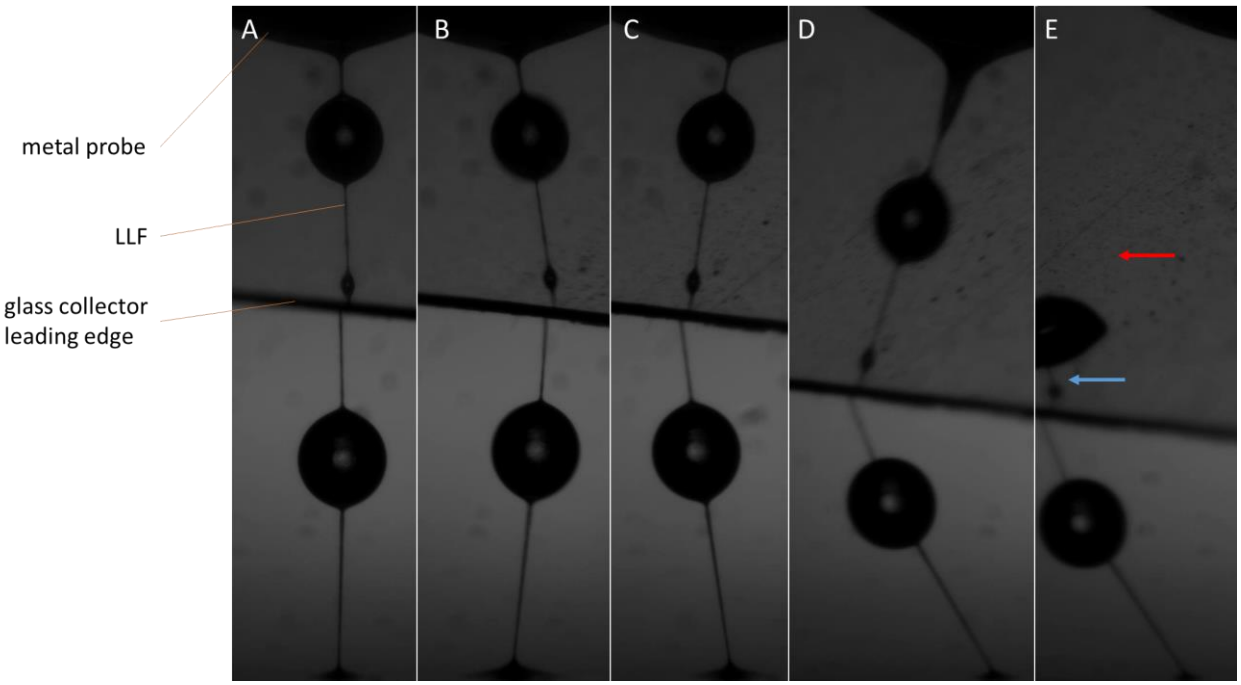

Figure 67. A gallery of frames illustrating a partially successful collection of LLF, depicting the metal probe, the LLF with a liquid bead, and the glass collector. (A - C) The leading edge of the collector slide is brought in contact with the LLF. A part of the LLF adheres to the leading edge and can be moved. (D) The LLF is stretched during the collection. (E) The LLF is broken near the metal probe. The liquid bead adheres to the collector and the segment of the LLF between the bead and the leading edge of the collector adheres with it. The part of the LLF between the bead and the probe gets either absorbed into the bead or adhered to the probe. In either case, its structure is not observable under the microscope. The blue arrow points to the segment that was captured. The red arrow points to the absence of a captured filament between the liquid bead and the probe, because it broke during collection.

The procedure for the collection with this method was as follows. Prior to collection, glass cover slips were cut into 5 mm wide strips and cleaned with methanol. The caterpillar was mounted in its tubular holder and an incision was made on the third proleg. The hemolymph was allowed to drain onto a glass slide and incubated for 2 minutes. A metal probe was then lowered into the sample and raised to a height of 5-10 mm. In an LLF formed, the pre-cut cover slip strip was then swiped across the LLF to

collect it. Immediately after the attempt, the sample was covered with another cover slip to prevent evaporation and imaged under a phase-enhanced microscope.

8.4.2 Collection of a dyed LLF

For florescent imaging of glycosylated proteins inside the LLF, the procedure was as follows. A caterpillar was placed in the tubular container and an incision was made on the third proleg. Four to five droplets (80 – 100 ul) of hemolymph was dripped directly onto a glass cover slip. 5 ul of 50 μg/ml rhodamine-PNA solution was added to the droplet. The mixture was not stirred to prevent the destruction of the structure and was incubated for 5 minutes. A metal ball was then dipped in the droplet and lifted out, thus forming a liquid filament between the ball and the droplet. While the liquid filament was still present, the bottom of the ball was touched to the glass slide roughly 5 mm away from the edge of the droplet. The liquid filament was thus adhered to the slide. The sample was then imaged under a fluorescent microscope with an environmental chamber (name) under 100% humidity.

8.4.3 Collection of SLF on a plastic slide

For imaging of the material inside of the SLF, the collected liquid filaments were created using the dripping method, described in section 7.2.3. As discussed earlier, this method produces SLF with a lifetime of under 1 second. Such a short lifetime makes the filament collection challenging. Moreover, additional care had to be taken to collect the

liquid just from the filament itself and not the droplet or the wound. This was important, as the structure in the bulk was possibly different than the structure in the filament. Since the rate with which the droplets fell from the wound was fast (initially after wounding: several droplets per second, and after a minute of incubation: a droplet e 10 seconds) and could not be controlled, the collection technique had to be swift. We used the force of electrostatic attraction to pull the liquid filament towards the substrate and collect it.

A plastic microscopy slide was used as a charged collector for the filament. The slide was mounted vertically in a specially designed holder (schematic in Figure 68 F-J). The holder consisted of a thin slit for the plastic slide and a well for the droplet to fall into. The depth of the well was approximately 1 cm and served to make sure that the droplet never touched the plastic slide, thus preventing the contamination of the sample with bulk material (hemolymph from the drop). To improve the efficiency of the collection method three such slit-wells were used in each experiment. Thus, each time a caterpillar was cut, three attempts at filament collection could be made. In order to make sure that the collected sample was indeed an SLF, the collection process had to be monitored by a high-speed camera. The process is illustrated from the side view in Figure 68 and the front view in Figure 69.

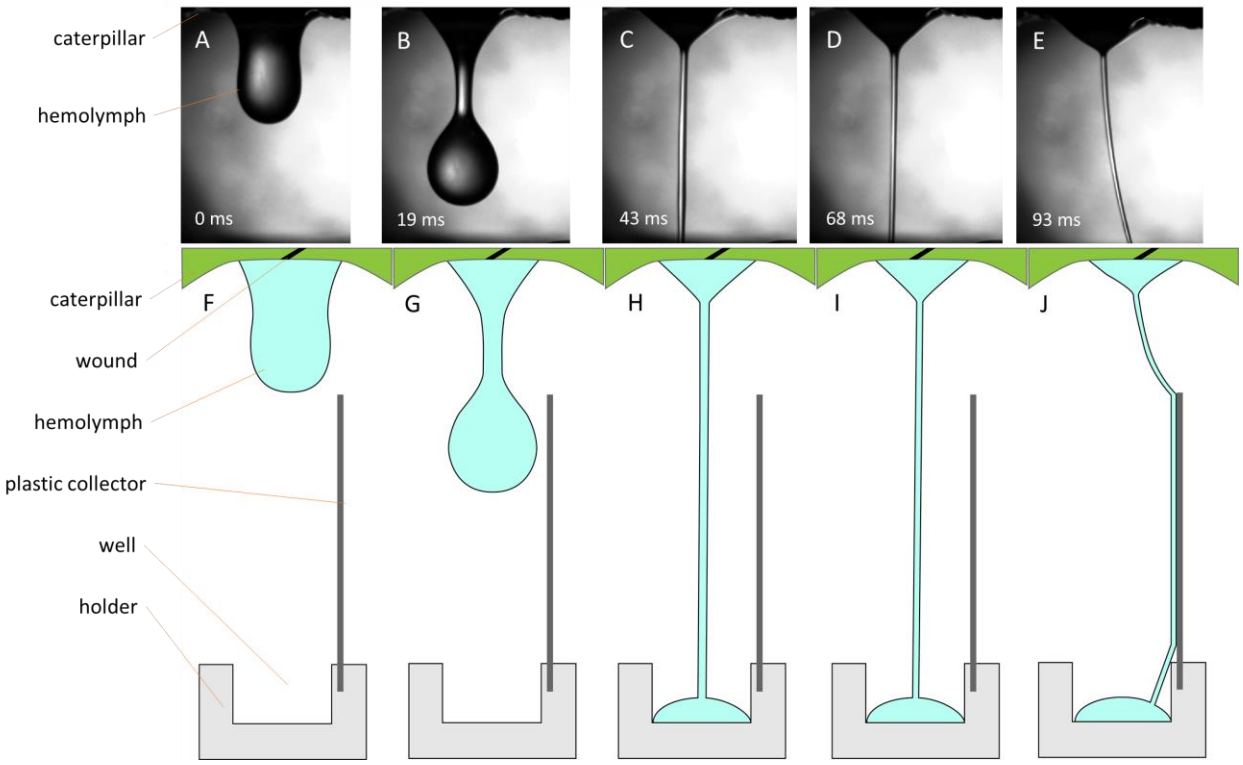

Figure 68. (A-E) A gallery of frames depicting the caterpillar and the top of the SLF as wells as (F-K) schematics depicting the caterpillar, the wound, the hemolymph, and the plastic collector in the holder with a well during the process of SLF collection from the side view. (A, F) The droplet is hanging from the wound. (B, G) The droplet begins falling, stretching the liquid bridge into a filament. (C, H) The droplet flies by the collector and falls into the well. (D, I) The filament is left behind, attracted to the plastic collector. (E, I) The filament snaps to the plastic collector due to the electrostatic attraction force. The droplet does not touch and contaminate the sample.

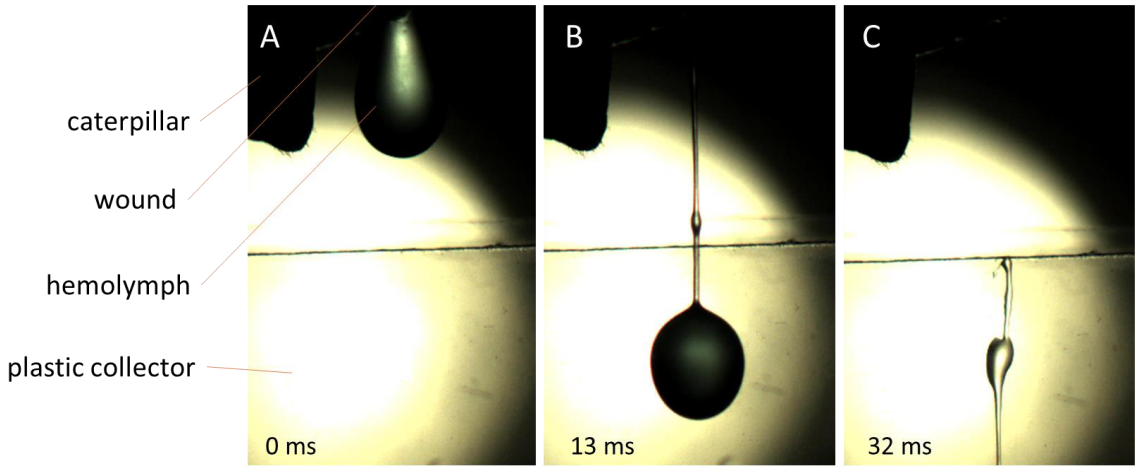

Figure 69. A gallery of frames of the SLF collection from the front view. (A) The droplet hemolymph is hanging from the wound of the caterpillar. (B) The droplet is falling and the liquid bridge is stretching into a filament. (C) The droplet fell and the filament attached to the plastic slide collector.

The procedure for the collection was as follows. First, the caterpillar was placed in a plastic tubular container to restrict its motion, as described in the previous chapter. The container had an opening for a proleg, where the incision would be made. A plastic collector slide was then mounted into each of the three slits in the holder. The first plastic slide was aligned such that it was directly underneath the opening of the caterpillar container. The high-speed camera (Point Grey, Grasshopper) was then focused on the plastic slide to monitor the collection of the sample. Since immediately after the incision, hemolymph comes out under pressure, the container with the caterpillar was temporarily brought away from the collection set-up to make the incision. After 5-10 seconds after the incision, the caterpillar was brought back to its original position over the collector slide. To collect the produced SLF, the slide had to be close enough to the trajectory of the droplet to attract the filament. On the other hand, if the trajectory of the droplet was

too close to the collector slide, the edge of the droplet would contaminate the sample. Thus, after each falling droplet of hemolymph, the position of the collector slide was adjusted – if no filament was collected, the slide was moved closer to the wound; if the droplet touched the collector, it would be discarded and the next collector was moved under the wound to attempt to collect the next sample. After a successful collection, the plastic slide is removed from the holder, and covered with a glass cover slip for observation under the microscope. Five SLF were collected and studied in this manner.

CHAPTER IX

SURFACE PROPERTIES OF HEMOLYMPH OF ADULTS AND CATERPILLARS

9.1 INTRODUCTION

In Chapter 3, we discussed microrheology of hemolymph of adult butterflies and moths and found that the viscosity of *M. sexta* moth is significantly higher than that of *V. cardui* and *D. plexippus* butterflies. We hypothesized that it was due to *M. sexta* needing more energy as it spends more time flying and hovering during feeding and thus requires more fuel. The fuel is transported from the fat body to the muscles with the carrier particles. These particles are amphiphilic and are surface active. We showed that a reasonable surface charge of the particles could explain the viscosity increase. Since some of the energy carriers were shown to be surface active (1) and since we have observed this surface activity during the crust formation of a hemolymph sample between two cover slips, a study of the surface tension isotherms of hemolymph would be an important step in the validation of this hypothesis. In this chapter, we study the surface tension isotherms of hemolymph of adult *M. sexta, V. cardui*, and *D. plexippus*, as well as caterpillar *M. sexta* by diluting the extracted hemolymph in buffer at different dilution ratios, measuring the surface tension of the solution, and thermodynamically analyzing the data.

Furthermore, as discussed in Chapter 7, the phenomenon of the droplet formation on a filament formed from hemolymph could be facilitated by changing surface properties of incubating hemolymph. We investigate these properties to shed light on that

phenomenon. In particular, we study how the surface tension and surface viscosity of caterpillar hemolymph change with time during the aging of surface.

When the surface-active solutes adhere to the surface, their local concentration increases and the surface tension is expected to decrease. With that, we expect the local viscosity to increase. The surface rheology is difficult to measure using conventional methods as it requires precise measurement of delicate interactions between the surface and a probe. We propose to probe it by placing a magnetic microwire (50 um in diameter and several mm in length) on the surface of the sample and rotating it with a magnetic field. It is impossible to measure the surface rheology independently from the bulk rheology, as it would require complete isolation of the probe from the bulk, which is impossible to accomplish experimentally. Because of that, to adequately probe the surface rheology, the interaction of the probe with the bulk needs to be characterized. That interaction is dependent on how much of the probe is submerged under the surface, which is in turn dependent on the contact angle of the liquid with the probe. This contact angle may be dependent on the amount of the solute adsorbed to the surface and thus needs to be carefully characterized. This is challenging to do, due to the small size of the meniscus on the thin cylindrical probe and has not been accomplished yet. Here, we limit the analysis to extracting the apparent viscosity of the surface-probe system and use it to qualitatively describe the surface process.

9.2 THEORETICAL BACKGROUND

9.2.1 Surfactants

(For a full overview of surfactants, see the following books: (2) and (3))

Surfactants (short for surface active agents) are soluble in the fluid carrier and are strongly adsorbed to surfaces. In the aqueous environment such as hemolymph, surfactants have both hydrophilic and lyophilic parts and are thus called amphiphilic. The adsorption is driven by the amphiphilic properties of surfactants. For instance, at the water-air interface, a surfactant molecule aligns such that its hydrophilic part is immersed in water, while its hydrophobic part is surrounded by air. When the concentration of surfactants at the interface is sufficient to cover the surface, surfactants form a 2D continuum, a monolayer called the Gibbs monolayer.

9.2.1.1 Effect of surfactants on surface tension

When surfactants are added to water, they adhere to the surface, forcing the surface tension to decrease.

Due to adhesion, the concentration of surfactants at the interface, C_σ, is different from that in the bulk, C_α. Here, by the 'surface', we mean a mathematical surface of zero thickness at the boundary of the bulk material. For a two-phase system (α and β) such as a liquid and surrounding gas coexisting in equilibrium and separated by a flat interface (marked by σ) between them, the measure of the difference of solute concentration in the bulk and a surface layer is the surface excess of surfactant or adsorption, defined as $\Gamma^\sigma = \frac{C^{total} - C^a - C^\beta}{A}$, where A is the area of the surface, C^a is the surfactant concentration in the phase a , C^β is the surfactant concentration in the phase b and C^{total} is the total surfactant concentration.

At lower concentrations, the surface tension γ decreases almost linearly. With increase of concentration, the surface tension decreases logarithmically; in this region, the adsorption Γ^{σ} is almost constant. At a certain surfactant concentration, the surface tension stops changing. This is due to the fact that the surface becomes saturated with the surfactant and no new surfactants can adsorb to the surface any longer. Instead, surfactants begin forming structures in the solutions called micelles. For this reason, the surfactant concentration at which the surface tension stops changing is called the critical micelle concentration.

9.2.1.2 Gibbs surface tension isotherm and adsorption

Before considering the adsorption of surfactants to a surface, we need to introduce the concept of the Gibbs surface tension isotherm originally derived by Gibbs [The collected works of J.W. Gibbs, 191. P219]. It relates the surface tension, adsorption, and temperature. In the differential form, this relation is written as

$$d\gamma = -\frac{1}{RT}\sum \frac{\Gamma_i^{\sigma}}{C_i} dC_i \Big|_T \tag{9.8}$$

where R is the gas constant, T is the temperature, and the index i corresponds to the surface active component i in a multicomponent solution. In solutions with a predominant population of one surface active component, say a b component, at a constant temperature, $C_b \gg C_i, i \neq b$this equation is simplified to

$$d\gamma = -\frac{1}{RT}\frac{\Gamma_b^{\sigma}}{C_b} dC_b \ . \tag{9.9}$$

The adsorption of a surfactant to the surface is characterized by its surface excess, which is a function of how fast the surface tension changes with concentration and is calculated by the rearranged equation (9.9):

$$\Gamma_b^\sigma = -\frac{C_b}{RT}\frac{d\gamma}{dC_b} \ , \tag{9.10}$$

or

$$\Gamma_b^\sigma = -\frac{1}{RT}\frac{d\gamma}{d\ln C_b} \ . \tag{9.11}$$

9.2.1.3 Kinetics of adsorption

When a new surface forms, the solute concentration in the subsurface region is initially the same as that in the bulk. This concentration drops to near-zone, however, due to its adsorption to the surface. The concertation drop causes diffusion of the particles from the bulk towards the subsurface region, where they immediately adhere to the surface. During this time, the adsorption of the solute to the surface is controlled by this diffusion as:

$$\frac{d\Gamma_b^\sigma}{dt_s} = \left(\frac{D_i}{\pi}\right)^{1/2} C_b t_s^{\ -1/2} \tag{9.12}$$

so that

$$\Gamma_b^\sigma = 2C_b\left(D_i t_s / \pi\right)^{1/2} \tag{9.13}$$

where D is the diffusion coefficient of the solute and t_s is the age of the surface, i.e. the time the solute takes to get to the surface. During the early stages of maturation of the surface, when the surface tension can be related to the diffusion by combining equations (9.11) with (9.13) and integrating to obtain

$$\gamma(t) = \gamma_0 - 2RTC_b\left(\frac{D_i t_s}{\pi}\right)^{1/2} \tag{9.14}$$

With time, as the adsorbed amount of material increases and more solute remains in the subsurface layer, the back diffusion of the solute from the subsurface to the bulk becomes significant. At this time, the simple diffusion begins to overestimate the rate of adsorption and a more complex model has to be used (4). Eventually, the surface and the bulk reach an equilibrium, no new solute gets adsorbed to the surface, and the surface tension ceases to change.

9.2.2 Thermodynamics of a Gibbs monolayer

This section follows the logic of (2).

The behavior of monolayers is best described in an analogy to the osmotic pressure. The concept of osmotic pressure is best visualized by placing a membrane that is permeable to the solvent and impermeable to the solute between a container of the solution and a pure solute. The surplus of the solvent molecules on the side of pure solvent will create a net flux of solvent into the solution, increasing its hydrostatic pressure until an equilibrium is reached. The osmotic pressure is then defined as $P_{osm} = D_l gh$, where D_l is the density of the liquid, *h* is the difference between the height of the levels of solution and water, and *g* is the acceleration due to gravity. The osmotic pressure can be measured directly if the semipermeable membrane in the experiment is replaced with an impermeable membrane and the pressure across it is measured.

A parallel can be drawn between osmotic pressure (3D) and the surface pressure (2D) in a surface-active solution. The surface pressure can be measured if the two liquids are separated with an impermeable membrane, but the pressure drop is measured across a thin float, separating two surfaces. The first device to measure the film pressure in such a way is called the Pockels-Langmuir-Adam-Wilson-McBain trough or a PLAWM trough (2). This device confirmed the relationship between the surface pressure in the film, π_s, and the surface tensions of the two liquids, $\sigma_{solvent}$ and $\sigma_{solution}$, as $\pi_s = \sigma_{solvent} - \sigma_{solution}$. This relationship allows the surface pressure to be measured indirectly, by measuring the surface tensions of both liquids using the Wilhelmy plate method. Moreover, by physically controlling the total area that the film occupies, it is possible to measure the surface pressure as a function of the exclusion area of the surface-active molecules. Such a device is called the Langmuir – Blodgett (LB) trough (2).

Consider a dilute monolayer of a surface-active material. In this case, the solute-solute interactions are not important and the variation of surface tension with the concentration is linear with slope *m*,

$$\sigma = \sigma_{solvent} - mC_b \tag{9.15}$$

Thus,

$$\frac{d\sigma}{dC_b} = -m \tag{9.16}$$

The slope *m* can be measured in experiments. Combining equation (9.16) with Gibbs equation (9.10) and solving for Γ_b^σ provided that concentration C_b is known, we get

$$\Gamma_b^\sigma = mC_b / (RT) \tag{9.17}$$

On the other hand, due to definition of the surface pressure, we have

$$\pi_s = mC_b = \Gamma_b^\sigma RT \tag{9.18}$$

Adsorption Γ_b^σ has the units of moles / surface area. Areas that a mole of material and an individual molecule occupy at the surface could be defined from adsorption as $A = 1/\Gamma_b^\sigma$ and $A_m = 1/N_A\Gamma_b^\sigma$, respectively, where N_A is Avogadro's number.

At low concentrations of the surfactant, $\pi_s A/RT \approx 1$. As surfactant concentration increases, the ratio $\pi_s A/RT$ deviates from 1. The Amagat-type Law known for gasses at high pressure (2) is typically used for this range of concentrations (1, 2, 5)

$$\pi_s = \frac{qRT}{A - A_0} \tag{9.19}$$

where A_0 has the aspect of an excluded area per mole and q is a constant reflecting effect of measuring intermolecular interactions. Taking q=1, one reduces this equation to the Volmer-Mahnert equation(6):

$$\pi_s (A - A_0) = RT \tag{9.20}$$

9.2.2.1 Surface thermodynamics of a monolayer of Apolypophorin-III

One constituent in the lipid transfer cascade is apolypophorin-III (ApoL-III). The surface adsorption of ApoL-III – was previously studied in Ref. (1). Figure 70 shows the data for ApoL-III from source (7). At low surface pressures, the behavior follows a linear pattern, but deviates away from it at higher surface pressures. This indicates a phase transition in the surfactant behavior.

ApoL-III is a long chain with hydrophobic and hydrophilic regions. In its free configuration, it is folded over on itself such that the hydrophobic parts are not exposed to water. It is relatively unstable in this configuration, when compared to other globular proteins(8). When it binds to a lipid or a water surface, it unfolds, exposing its hydrophobic parts (9). In the lipid bound form, it was found to be significantly more stable than in the free form (10). That suggests that it is energetically preferable for it to adsorb to a lipid or a free surface than to remain in the free coiled from.

To determine the molecular area of ApoL-III in the bound regime, ApoL-III, was isolated from adult *M. sexta* using a protocol described in (11) and studied using a Langmuir-Blodgett trough. A powder of isolated ApoL-III was found to be poorly soluble in water and formed a stable film on water surface. This allowed the ApoL-III film to be dispersed on a LB trough and form a monolayer. The monolayer was stable for at least 30 minutes. The area of the monolayer surface was constricted and the resultant surface pressure was measured (Figure 3). The shape of the curve was repeatable for several constriction/unconstriction cycles.

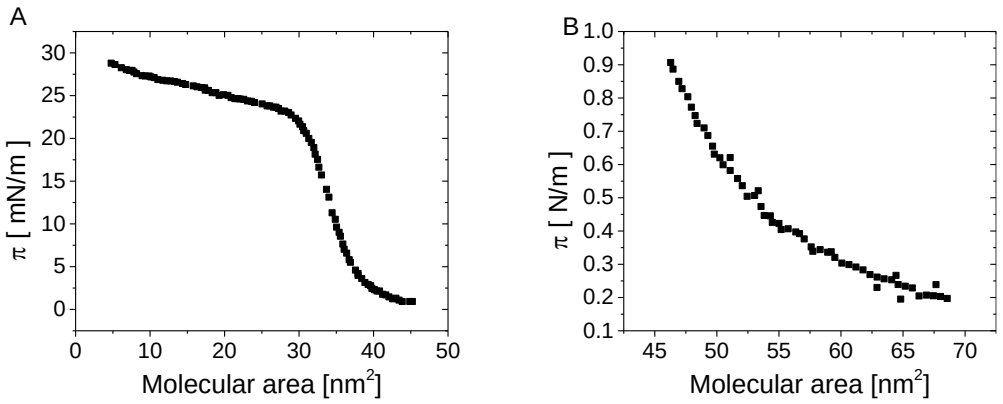

Figure 70. Surface pressure versus molecular area for ApoL-III. (adapted from (7)) A. The full surface pressure curve B. Surface pressure curve in the region under 1 N/m. The behavior in this region follows that of equation (9.20).

In their thermodynamic treatment of experimental data, Kawooya *et al.* analyzed the semi-dilute regime of the monolayer formation in Figure 70.B with equation (9.20) to determine the limiting molecular area $A_0 = 38$ nm^2. The interpretation of this data is questionable, however, since the instrument used in the study (Lauda Filmwaage, Type FW1) was not able to control concentration of surfactant in the bulk and adsorption of the material on the other – 'clean' – side of the trough. (12)

9.2.3 Shape of a droplet on a thread – Unduloid equation

In Chapter 7, we briefly discussed droplets that formed on the long-lived filaments. These droplets could form on both types of filaments that decayed via the capillary thinning and via the pullout instability. Assuming that the droplets are coexisting with the liquid bridges in equilibrium and slow flow of hemolymph does not affect their shape, we can apply the theory of equilibrium liquid bodies to describe their shapes (2, 3). The equilibrium shape of such droplets, called an *unduloid*, is dictated by a constant pressure throughout the droplet and a contact angle between the droplet and the liquid bridge on

which the droplet forms (13). The contact angle is a measure of the interaction between the materials comprising the droplet and the filament and if the contact angle is zero, both materials are presumably made of the same chemical compound.

The derivation of the Unduloid equation is as follows. A small droplet of liquid in equilibrium and absence of significant gravitational contribution has a shape defined by the Laplace law.

$$\Delta P = \sigma\left(\frac{1}{R_1}+\frac{1}{R_2}\right) = const. \tag{9.21}$$

where ΔP is the pressure inside the drop measured relative to the atmospheric pressure, γ is the surface tension of the droplet, and R_1 and R_2 are the two principal radii of curvature of the droplet. For an axisymmetric droplet, the Laplace law can be written in a differential form as:

$$\begin{aligned}\frac{du}{dy} &= \frac{1}{u}\left(\frac{1+u^2}{y}-\frac{\Delta P}{\sigma}\left(1+u^2\right)^{3/2}\right)\\ \frac{dx}{dy} &= \frac{1}{u}\end{aligned} \tag{9.22}$$

Where x is the coordinate along the liquid cylinder modeling the liquid bridge and y is the radius of the drop at the given point x. For a droplet on a fiber of radius, R_f, with a maximum radius, R_d, relative to the central axis, and a contact angle θ_c, a force balance can be set-up as

$$\begin{aligned}&\sigma\left(2\pi R_d\right)-\Delta P\left(\pi {R_d}^2-\pi {R_f}^2\right)+\sigma_{sl}\left(2\pi R_f\right)-\sigma_{sg}\left(2\pi R_f\right)=0\\ &\sigma_{sg}=\sigma_{sl}+\sigma\cos\theta_c\end{aligned} \tag{9.23}$$

where σ_{sg} and σ_{sl} are surface tension of the liquid bridge/air interface and liquid bridge/droplet interface, respectively. Combining equations (9.22) and (9.23), we get an expression for the droplet shape that depends only on geometrical parameters R_d, R_f and θ_c:

$$\begin{aligned} \frac{du}{dy} &= \frac{1}{u}\left(\frac{1+u^2}{y} - \frac{2\left(R_d - R_f \cos\theta_c\right)}{{R_d}^2 - {R_f}^2}\left(1+u^2\right)^{3/2} \right) \\ \frac{dx}{dy} &= \frac{1}{u} \end{aligned} \tag{9.24}$$

The equation can be written in its integral form (14):

$$\begin{aligned} x(y) &= b \cdot R_f \cdot F(k,a) + R_d \cdot E(k,a) \\ b &= \frac{\left(R_d \cdot \cos(\theta_c) - R_f\right)}{\left(R_d - R_f \cdot \cos(\theta_c)\right)} \\ k &= 1 - \left(\frac{b^2 {R_f}^2}{{R_d}^2} \right) \\ a &= \sin\sqrt{\frac{\left(1 - \frac{y^2}{{R_d}^2}\right)}{k}} \end{aligned} \tag{9.25}$$

where $F(k,a)$ and $E(k,a)$ are first and second kind elliptic integrals. The equation can be solved numerically.

9.3 RESULTS

9.3.1 Surface tension as a function of concentration

The surface pressure of hemolymph of insects of three species, *M. sexta* (adults and caterpillar stage), *V. cardui* (adults), and *D. plexippus* (adults), were measured at different solute mass fractions. The solute mass fractions were varied by diluting extracted

hemolymph with 7.2 pH phosphate buffer solution (PBS). The solute mass fraction in the undiluted hemolymph, $w_{s0,}$ of adults was measured in chapter 3; it was measured in the same way for the *M. sexta* caterpillars to be $w_{s0} = 0.075 \pm 0.003$.

Expectedly, the surface pressure π changes linearly with solute mass fraction w_s at low mass fractions and, unexpectedly, it changes exponentially at higher mass fractions. This suggests that only one component of surface-active particles contributes most in the surface adsorption.

To determine the parameters of this behavior, we split the data into two regions and fitted one dataset with a linear function (Figure 71. A) and the other with an exponential function (Figure 71. B). As Barnes and Gentle suggest, the change of behavior should be expected at the surface pressures of about $\pi \approx 5$ mN/m, so that we split the data at that value. Since the surface pressure of pure solvent is 0, the linear regression was performed with the y-intercept pinned at 0 and the best fit slopes were 46±7, 15±3, 1.4±0.2, and 1.3±0.2 [N/m] for adult *M. sexta*, adult *V. cardui*, adult *D. plexippus*, and caterpillar *M. sexta*, respectively. These values are presented in in Table 10 and are discussed in the discussion section.

The data with $\pi > 5$ mN/m was fitted with an exponential function. The exponential coefficients π_s were equal to a = 3.2±0.3, 3.2±0.6, 3.5±1.5, and 2.1±0.4 [mN/m] and the y-intercepts were equal to b = 35±3, 31±3, and 26±9, and 16±1 [mN/m] for adult *M. sexta*, adult *V. cardui*, adult *D. plexippus*, and caterpillar *M. sexta*, respectively. These values are also presented in in Table 10 and are discussed in the discussion section.

Table 10. Summary of the experimental parameters of the surface tension isotherms for hemolymph of adult *M. sexta*, adult *V. cardui*, adult *D. plexippus*, and caterpillar *M. sexta*.

Species	Life stage	Slope in linear regime, m [N/m]	Exponential coefficient, *a* [mN/m]	Exponential y-intercepts, *b* [mN/m]
M. sexta	Adult	46±7	3.2±0.3	35±3
V. cardui	Adult	15±3	3.2±0.6	31±3
D. plexippus	Adult	1.4±0.2	3.5±1.5	26±
M. sexta	Caterpillar	1.3±0.2	2.1±0.4	16±1

The uncertainties represent the 95% confidence interval. The results of the regressions for each species are also presented in their respective figures. No samples had a surface pressure above 20 mN/m. One adult *M. sexta* hemolymph sample with the highest solute mass fraction can be seen significantly to the right of the best fit curve, possibly indicating a critical micelle concentration. That region, however, is difficult to probe, since it requires low dilutions of the sample and thus a large volume of extracted hemolymph.

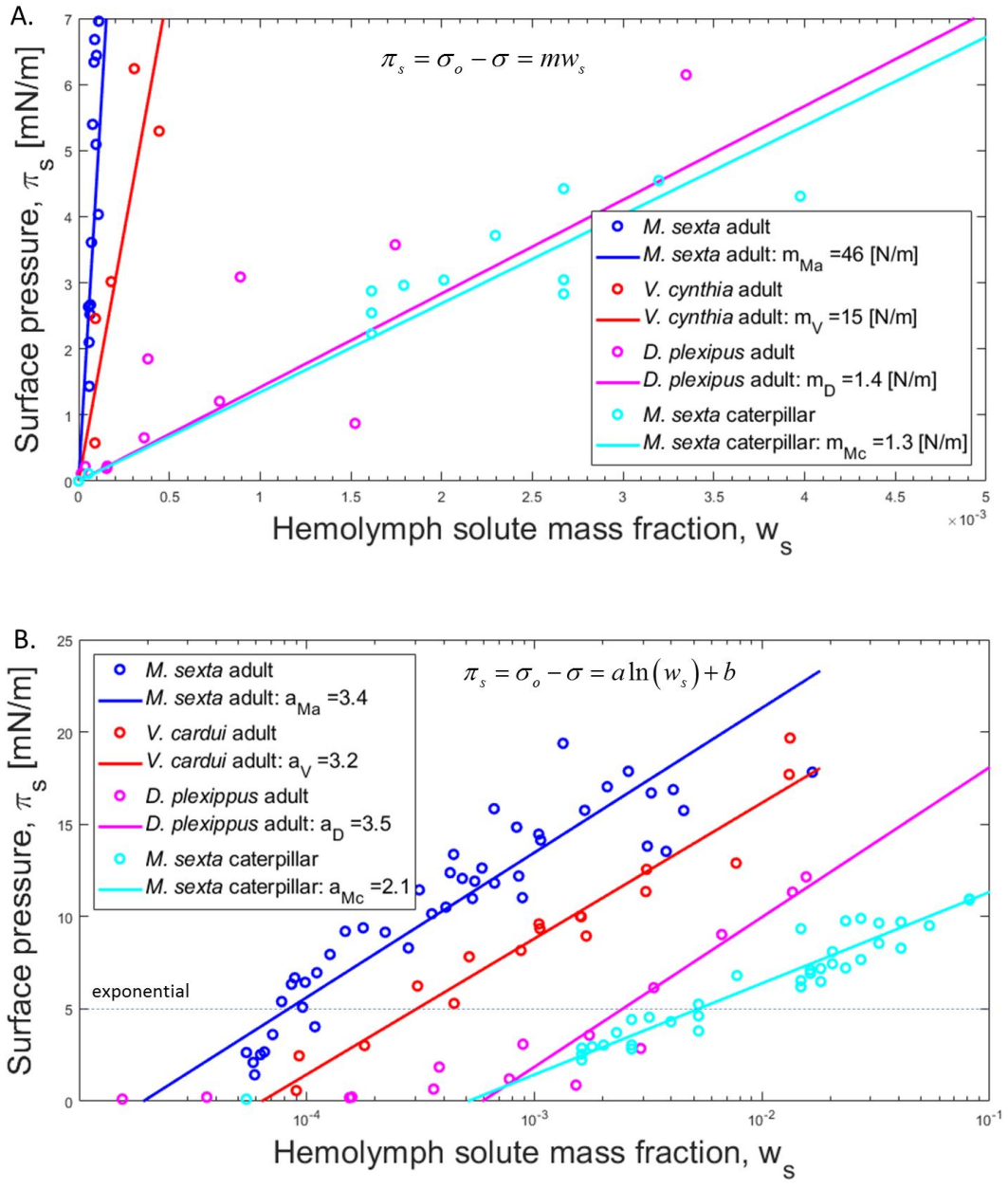

Figure 71. A plot of surface pressure vs. total solute concentration of hemolymph for the three species of Lepidoptera – 3 adults and one caterpillar. (A) As expected, the surface pressure π_s at surface pressures π_s < 5 mN/m follows a linear trend and was fitted with a line. The slopes m of the best fit lines are presented in the legend. (B) The x-axis is logarithmic in scale. At surface pressures π_s > 5 mN/m, the surface pressures increase exponentially with the mass fraction w_s. That data was fitted with an exponent and the best fit parameters are presented in the legend.

9.3.2 Caterpillars: surface tension as a function of time

Surface tension of a pendant droplet formed from incubated hemolymph of *M. sexta* caterpillars was measured as a function of surface age of the droplet, t_s, at incubation times t_i ranging from 2 to 40 minutes since the extraction of hemolymph. Each measurement consisted of extracting the hemolymph from the caterpillar onto a glass slide, collecting the hemolymph into a clean glass syringe, incubating the hemolymph in the syringe for a set amount of time t_i (up to 40 minutes), producing a pendant drop, and tracking the surface tension of that drop via image analysis as a function of the surface age of the drop, t_s. For each droplet, the surface tension decreased over several minutes of the surface age. Since equation (9.14) only describes the early kinetics in the absence of back diffusion, we use the data from the initial 60 seconds of the surface development and fit it with equation (9.14) with the initial surface tension γ_0 and a coefficient $c = \frac{2RTC_b D_i^{1/2}}{\pi}$ as adjustable parameters. We studied 10 droplets from 3 specimens and found no dependency of c or γ_0 on the incubation time of hemolymph and on average, c = 0.8 ± 0.4 $mNm^{-1}s^{-1/2}$ and γ_0 = 62 ± 3 mN/m.

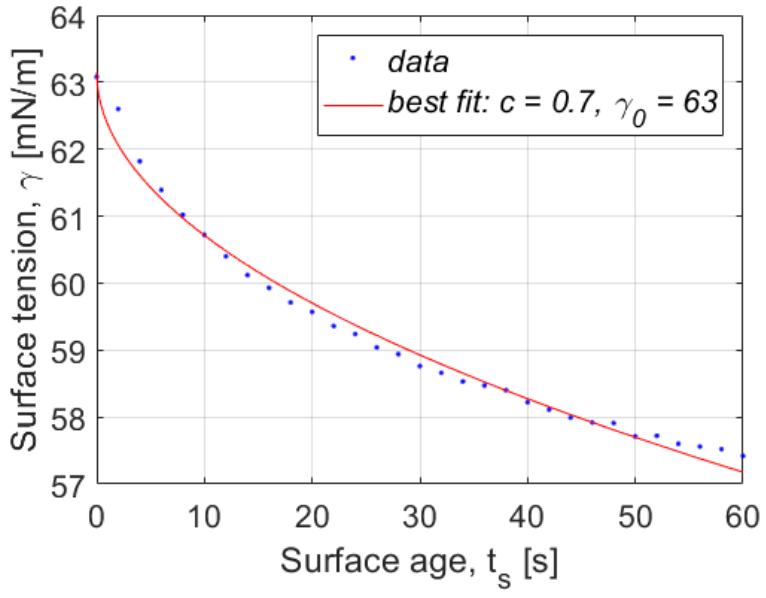

Figure 72. An example of the surface tension vs surface age curve. Only the first 60 seconds of life of the drop were fitted with equation (9.14) *due to the effect of back-diffusion at later incubation times.*

9.3.3 Surface rheology of hemolymph of caterpillars.

A magnetic microwire was placed on the surface of incubating hemolymph and rotated with a magnetic field. There are three major results from these experiments. First, the surface behavior of an incubating sample of hemolymph changes as a function of time. Initially, it behaves as a surface with Newtonian viscosity. As time goes on, viscosity increases and the surface becomes elastic. This was evident from the motion of the probes – initially, their motion had both oscillatory components as well as a rotating mean orientation. With time, the average orientation became constant, indicating that the material behaves like a gel. With further incubation, the amplitude of the oscillation decreased, indicating a more viscous and a more elastic material. Such behavior was not observed with a model surfactant solution of aqueous sodium-dodecyl-sulfite of any

concentration. This suggests that gelation occurs not only at the surface but propagates deeper in the bulk of the liquid.

Second, by placing two probes in the same sample that was incubated for several minutes – one pinned to the surface and one in the bulk – we see a drastic change of the properties between the two locations. The probe on the surface was oscillating with a small amplitude around a non-changing average orientation – the behavior we would expect from a probe in a gel. The probe suspended deeper in the bulk, however, was rotating freely, oscillating around an increasing average orientation – a behavior impossible for a probe in a gel. An image of the probes in the sample along with their extracted trajectories are presented in Figure 73. This unique dichotomy of material behavior indicates significant surface activity and interaction of the solutes in hemolymph of *M. sexta* caterpillars.

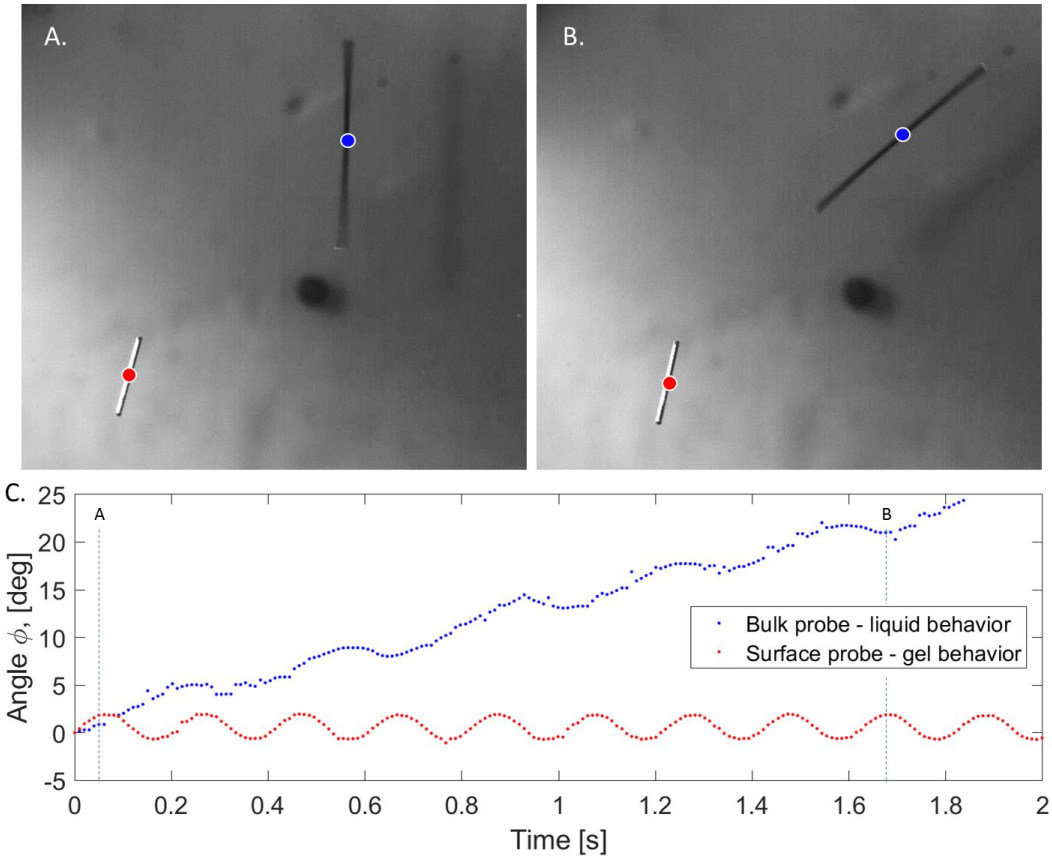

Figure 73. Behavior of a probe on the surface and in the bulk of the same incubating hemolymph sample. (A and B) The bulk probe (labeled with a blue dot) can be seen freely rotating in the liquid. The surface probe (marked with a red dot) is almost motionless. (C) An extracted profile of the orientation angle φ for both the surface and the bulk probes. The surface probe's trajectory is oscillating around a constant average indicative of a gel, while the bulk's probe rotation oscillates around an increasing average orientation, indicative of a liquid.

Third, by tracking the motion of the probes over a long period of time, we find that the surface viscosity changes linearly with time. The experiment consisted of rotating the field for 10 revolutions, relaxing the material for 1 second, then rotating the field for 10 more revolutions, *et cetera*. The motion of the probe after each relaxation begins by oscillating around an increasing average orientation, but then changes to oscillating around a constant average (Figure 74, A). This motion is indicative of a rod rotating in a

gel above the critical frequency. For simplicity of the analysis, we can analyze the first several oscillations assuming Newtonian model to probe the apparent viscosity of the surface. Such analysis of two probes in two samples from two different caterpillars is presented in Figure 74. The two samples demonstrate a linearly increasing viscosity, although at different rates and with a different y-intercept. As mentioned above, to correctly characterize the properties, the probe-liquid interaction needs to be well-characterized and controlled. Furthermore, in the performed experiment, the depth of the sample was not controlled, which could affect the interaction of the clot structures, which propagate from the substrate through the bulk, with the surface and the probe. We do, however, demonstrate that in both samples the viscosity increases linearly and not exponentially as in the case of the clot structures, indicating a different physical process.

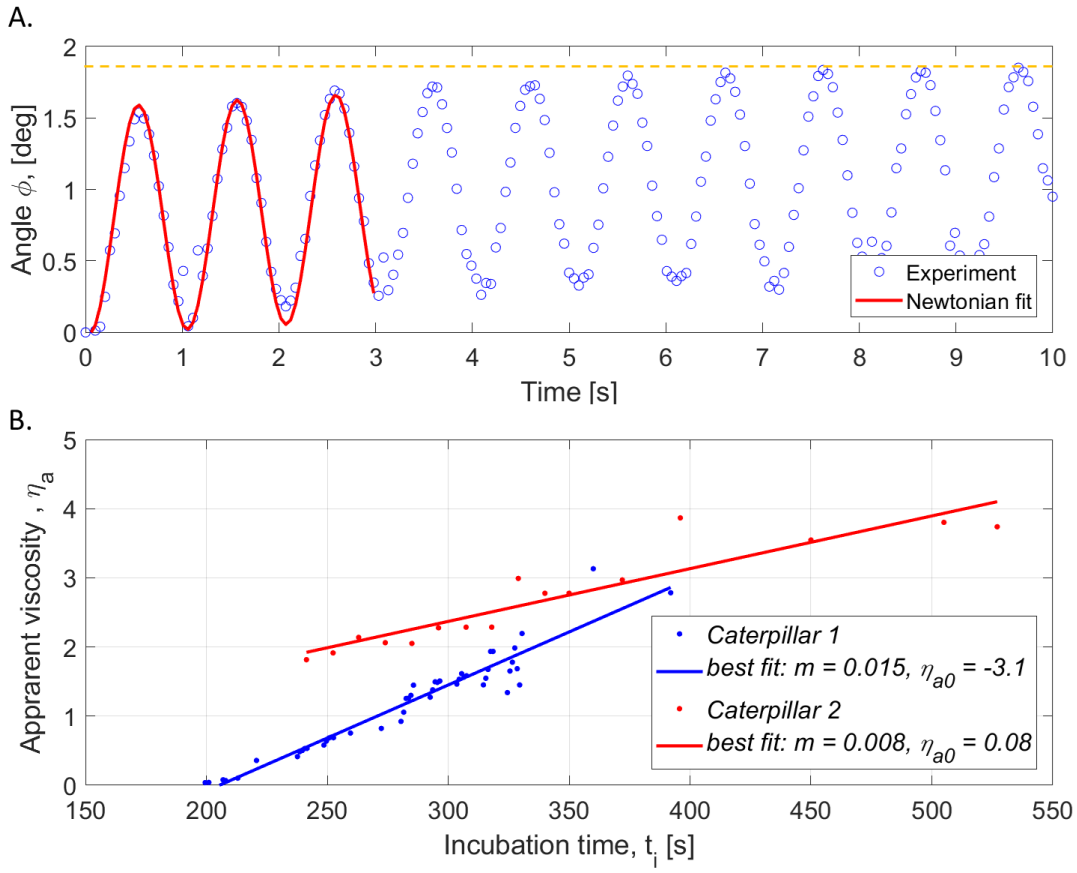

Figure 74. (A) A profile of a trajectory of a probe in response to 10 rotations of a magnetic field after 1 second of material relaxation. The rod can be initially seen oscillating around an increasing average orientation and then reaching a saturation angle – labeled with a dashed orange line – after which it oscillates around a constant average orientation. The first 3 oscillations can be analyzed with Newtonian model of rotation to get apparent viscosity. (B) The dependency of the measured apparent viscosity of the surface of hemolymph on incubation time. Since the surface was created at the same time as the cut was made, the incubating time is the same as the surface age, $t_i = t_s$.

9.3.4 Contact angle of a droplet on long-lived filaments of stretched hemolymph

Droplets that appeared on the surface of long-lived filaments studied in Chapter 7 were analyzed. The surface profile was extracted and fitted with the unduloid equation. Two types of droplets were analyzed: ones that appeared on the long-lived filaments that decayed via the pullout instability (Figure 75, A and B) and ones that appeared on the

surface of long lived filaments that decayed via capillary thinning (Figure 75, C and D). To ensure that the analyzed droplets have achieved their relaxed configurations, the droplets of the largest possible surface age were considered. Thus, for the pullout instability case, the last frame before the filament collapse was studied, which yielded surface age of $t_s = 55$ s. Similarly, for the capillary thinning case, the frame was used after all motion of the liquid in the filament had ceased, yielding the surface age of $t_s = 8$ s. The best fit contact angle in both cases was $\theta = 0$, which means that the material in the filament and in the droplet is the same.

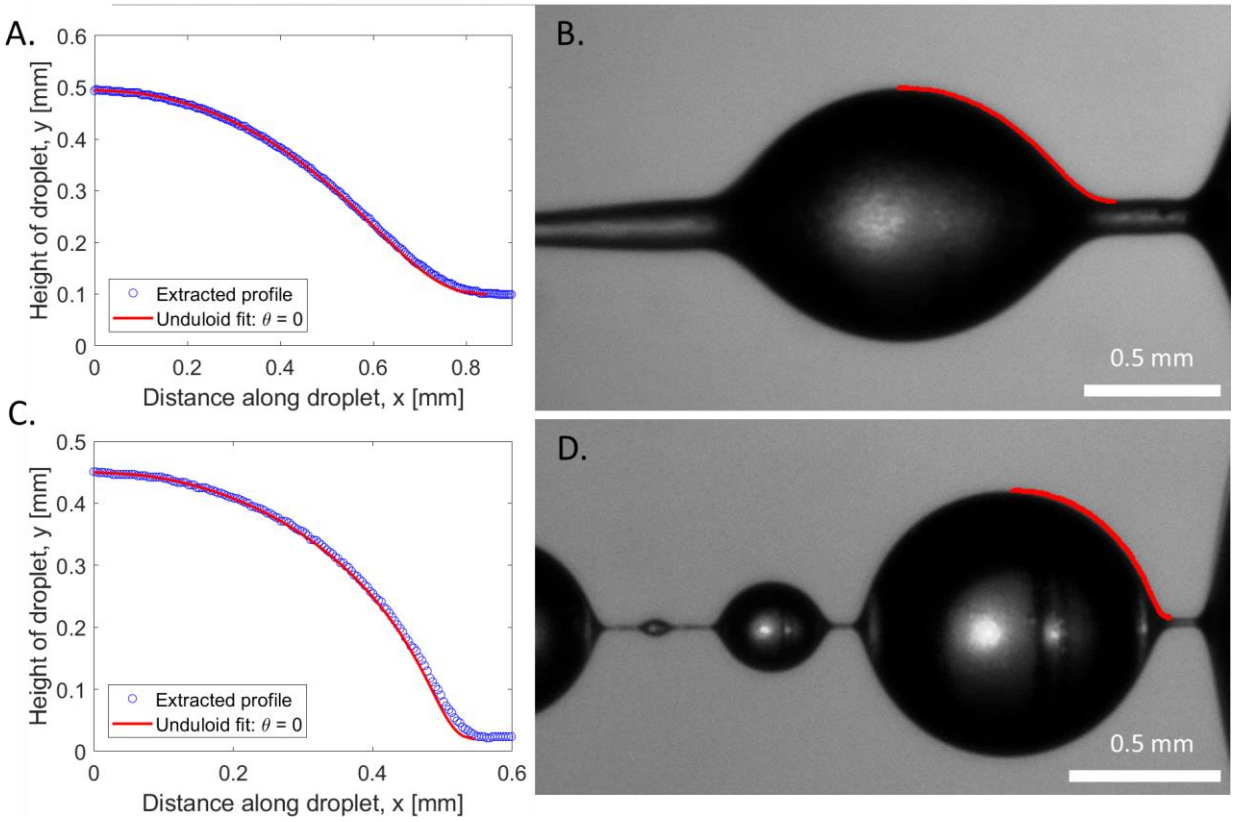

Figure 75. The surface profiles of droplets appearing on long-lived filaments decaying via the (A, B) pullout instability right before the filament collapse, and (C, D) capillary thinning after the filament stabilized and no longer moved. (A) The extracted droplet profile fitted with unduloid equation yielding best fit contact angle $\theta = 0$. (B) The bet-fit unduloid is superimposed on an image of the droplet on a pullout filament. (C) The

extracted droplet profile fitted with unduloid equation yielding best fit contact angle θ = 0. (D) The best-fit unduloid is superimposed on an image of the droplet on a capillary thinning filament.

9.4 DISCUSSION

The logarithmic portion of the surface tension isotherms of hemolymph of adult *M. sexta*, adult *V. cardui*, adult *D. plexippus*, and caterpillar *M. sexta* in conjunction with equation (9.11) can be used to describe the surface excess in the constant absorption region. The three species of adults had nearly identical exponential constants of a = 3.3 mN/m, which suggests that the adsorbing molecules are the same in all three species, which is consistent with our hypothesis. For these insects, the surface excess is calculated as $\Gamma^{\sigma}_{adults} = \frac{a}{RT} = 1.4 \cdot 10^{-6}\,\text{mol m}^{-2}$. The molecular area can be calculated from this surface excess as: $A_m = 1 \big/ \Gamma^{\sigma}_{b} A_N = 1.2\ \text{nm}^2/\text{molecule}$. This result cannot be directly compared to Kawooya's *et al*'s result of limiting molecular area of the apoL-III A_0 = 37 nm^2/molecule, because the limiting molecular area is an empirical parameter that has no direct interpretation. One point, in which the data can be compared, however, is that in apoL-III, a phase transition was observed at $\pi_s \approx 20$ mN/m. In our experiments, no sample was measured to have surface pressure larger than 20 mN/m, possibly indicating a critical micelle concentration at around that surface pressure. For the caterpillars, the parameter a = 2.1 mN/m is smaller than that in adults and corresponds to $\Gamma^{\sigma}_{caterpillars} = \frac{a}{RT} = 8.6^{-7}\,\text{mol m}^{-2}$ and $A_m = 1 \big/ \Gamma^{\sigma}_{b} A_N = 1.9\ \text{nm}^2/\text{molecule}$, a larger area per adsorbed particle. This means that the surface-active molecules are different in the studied species caterpillar from their adult

counterparts. This is not surprising, since the lipoproteins have been found to undergo structural changes during metamorphosis of *M. sexta*. (15)

The linear portion of the surface tension isotherm describes the behavior of the surface in the dilute regime. In this region, the surface pressure is a linear function of the concentration of the surface-active material. The above analysis yielded that the surface-active particles in hemolymph of adults of the three studied species occupy the same area per particle. If from this we assume that the surface-active particles in all three species are the same, then the ratios of the slopes of the linear portions of the surface tension isotherms would give the relative concentrations of these particles in the hemolymph of the respective species. We take the concentration of surface active particles in *M. sexta* as a reference. The relative concentration of the surface-active material in painted lady is $m_V / m_{Ma} = 15/46 \approx 0.33$. Similarly, the relative concentration of the surface-active material in monarch $m_D / m_{Ma} = 1.4/46 \approx 0.03$. This is consistent with the hypothesis that the amount of surface active material in these insects is correlated with the energy demands of flight – the heavier the insect is, the more energy it needs to fly, the more surface -active energy carriers it has. Caterpillars, which seem to have different surface-active agents cannot be compared to adults in this manner.

In hemolymph of caterpillars, when the surface-active material adsorbs to the surface, it changes the surface rheology of the liquid – the surface becomes gel-like with a linearly increasing apparent viscosity with time. At the same time, the rheology of the bulk probed deeply under the surface remains liquid-like. This unique dichotomy of

material behavior indicates significant surface activity and interaction of the solutes in hemolymph of *M. sexta* caterpillars. During surface maturation, the surface tension slowly decreases following square root of time kinetics due to the slow diffusion of surface agents to the surface.

The droplets that form on the surface of the long-lived filaments formed in response to stretching of hemolymph clots also experience adsorption of surface agents and, as a result, change their surface tension. The development of the filaments takes 10-20 seconds and in this time, the surface tension decreases by roughly 1-2 mN/m, which is not significant to the kinetics of the droplet and filament development. More importantly, the droplet formed on both the pullout and the capillary thinning filaments towards their end of their lifetimes have perfectly unduloid shapes with contact angles of $\theta = 0$, which means that the material comprising the droplet and the filament is the same.

9.5 MATERIALS AND METHODS

9.5.1 Surface tension measurement to determine presence of surface active lipids

To determine the presence of surface active lipids and their critical micelle concentration (CMC) surface tension isotherm measurements were performed. The surface tension was found for multiple concentrations of hemolymph solute by diluting extracted untreated hemolymph in phosphate buffer solution.

9.5.1.1 Methodology

To thermodynamically characterize the surface behavior of hemolymph, the surface tension isotherms for the three species of Lepidoptera were measured. Hemolymph was collected according to the protocol described in Chapter 5 and diluted. When mixed with DI water, some proteins denaturized and precipitated out. Hemolymph was found to be stable, however, when diluted in 7.2 pH phosphate buffer solution (PBS) (Ricca, 5800-32).

Thus, the surface tension isotherms were measured as a function of dilution ratio with PBS. For each sample, the first 2 droplets were discarded to prevent contamination, the measurement was performed on 3-4 droplets and the average value was recorded. The surface tension was measured at each dilution, the surface pressure and the mass fraction were calculated, and their relation was analyzed at low solute concentrations.

At each dilution, there are two parameters of interest: the mass fraction of water, w_w, and the mass fraction of hemolymph solute, w_s. In the undiluted hemolymph, the sum of the two equals unity, $w_w^h + w_s^h = 1$, where the superscript *h* specifies the undiluted hemolymph values. As hemolymph is diluted with the buffer, the mass fraction of solute approaches 0, $w_s \to 0$ and the mass fraction of water approaches the mass fraction of the buffer, $w_w \to w_w^b$, where the superscript *b* specifies the buffer.

At each dilution, the mass fraction was calculated as follows. The average mass fraction of water in undiluted hemolymph, $w_w^h = \dfrac{m_w^h}{m_w^h + m_s^h}$ was previously measured for each species, where *m* denotes the mass, the subscripts *w* and *s* refer to water and solute

respectively. The water mass fraction of solute in PBS is provided by the supplier as $w_w^b = \frac{m_w^b}{m_w^b + m_s^b} = 0.9524$, where the superscript *b* refers to the contents of the buffer. At each dilution, the mass fraction of water is calculated as $w_w = \frac{w_w^h}{1+D_r} + \frac{w_w^b}{\frac{1}{D_r}+1}$, where $D_r = \frac{m_w + m_b}{m_w^h + m_s^h}$. Similarly, the mass fraction of hemolymph solute at each dilution was calculated as $w_s = \frac{w_s^h}{1+D_r}$.

The surface pressure was calculated as $\pi_s = \gamma_{solvent} - \gamma_{solution}$.

9.5.1.2 Sample preparation

To perform surface tension measurement, hemolymph was first collected into a capillary tube. The volume collected was analyzed by performing image analysis of the length of the liquid. The collected hemolymph was added to PBS to create an initial dilution to simplify further work with the sample. Small volumes of the initial dilution sample were separated using calibrated micropipettes into clean containers to dilute further with PBS.

Prior to the surface tension measurement, a glass syringe and a 1.5 mm needle were cleaned with acetone and water and dried under nitrogen gas. The needle diameter was measured using calipers.

The first measurements of surface tension were made with pure PBS to have a standard for the room's particular temperature and humidity and consequent measurements were made with the diluted hemolymph samples; 200-300 μL of the

sample was taken into the syringe and placed in the Krüss DSA Apparatus. The camera was focused on the needle, and the magnification factor was calculated based on the diameter of the needle in the droplet analysis software. Using the manual micro dispenser on the apparatus two sample drops were discarded. During the measurement, the largest drop possible was made and the image was captured. The software was used to extract and fit the profile of the drop to find its surface tension. This was repeated for multiple drops and for each solution.

9.5.2 Time-dependent surface tension

Hemolymph was drained from the caterpillar onto a glass slide via an incision in the third proleg with a razor blade. During the hemolymph extraction, the caterpillar was securely held in a tubular holder; 200-300 μl of hemolymph was extracted from each caterpillar in this manner. After the extraction, hemolymph was collected into a clean glass syringe (Cadence Science, W034276) fitted with a d = 1.65 mm needle (Nordson Precision Tips. 4002051140). The syringe was placed in the surface tension analyzer (Kruss DSA 10), which was set to record the shape of the droplet at 1 frame per second. Three hemolymph droplets were made and discarded. The fourth drop was created with a maximum possible size and observed as a function of the surface age, t_s. The incubation time, t_i of each drop was recorded as the time that passed between the incision and the creation of the droplet. Each droplet was observed for roughly 10 minutes. After that time period, another droplet was made and the new t_i was recorded. The maximum incubation time was 40 minutes. At the end of each experiment, the syringe and the needle were

cleaned multiple times with soap and water until visibly clean and rinsed with methanol 3 times.

If during the lifetime of the droplet any liquid evaporated, more hemolymph was manually added to the droplet. A constant droplet length was maintained to the best ability of the operator by noting the length of the initial droplet on the screen and adding liquid into the droplet to maintain that length during the experiment.

The surface tension of the pendant droplet was obtained from the shape of the droplet from the image analysis using the Kruss DSA software. Thus, only 1 data point could be collected per sample; 3-4 samples per insect were studied.

9.5.3 Surface rheology of hemolymph of caterpillar

The surface rheology was measured by placing a magnetic stainless steel (SUS 304) microrod onto the surface of a large droplet of hemolymph and rotating the nanorod, using the magnetic rotator presented in Chapter 3. Once placed on the surface, the probe remained pinned to the surface and did not sink. If manually pushed below the surface, it would sink to the bottom of the sample. When the probe was on the surface, however, any curvature of the surface led to the probe sliding to the lowest point due to gravity. Thus, when placed and rotated on the surface of a sessile drop, the probe was unstable and fell to the edge of the drop in a matter seconds. Making a larger droplet with a relatively flat top surface did not adequately resolve the issue, as the probe would travel around an imperfectly flat surface until it got close to the edge and fell as well. To adequately resolve the issue, a surface with an upward-facing curvature was created by placing hemolymph into a small container and sucking some liquid out, taking advantage

of the contact hysteresis phenomenon. The container of choice was the center of a white sintering vial cap. The radius of the container was small enough to create enough of a curvature to keep the rod in the center and the white background provided good contrast for observation of the probe.

The procedure was as follows. First, the probe was prepared by magnetizing a stainless-steel wire (SUS 304, d = 50 μm) with a strong permanent magnet, cleaning it with methanol, and cutting a 2-3 mm long rod from the wire with precision scissors. The magnetization of the magnetized probe was measured using an alternating gradient field magnetometer (AGM 2900 Princeton Measurement, Inc). The caterpillar was secured in a tubular holder and an incision was made on the third proleg. Hemolymph was bled directly into the center chamber of the scintillator vial cap. Once the container was full, the caterpillar was set aside and the excess hemolymph was removed with a pipette to create a slight upward curvature of the surface of the sample. The prepared probe was then placed onto the surface of the liquid. The cap was then placed in the magnetic rotator and a rotating field was induced.

The induced field had the amplitude of A=400 μT and the frequency of 1 Hz. The field was rotated for 10 revolutions and then aligned along the y-axis of the instrument for 1 second, allowing the rod to align with the field and any high relaxation time processes to relax. The field was then again rotated for 10 oscillations and then again aligned for 1 second. This process was repeated until stopped by the user.

9.5.4 Fitting of the droplet on the long-lived filaments with the Unduloid equation.

The long-lived filaments were created, imaged, and had their contours extracted as described in Chapter 8. The frames for analysis were chosen from the end of evolution of those filaments that did not break at the end of their life but remained intact with their profiles non-changing. All analysis is performed in LabVIEW.

To fit the profile with an unduloid equation, two approaches can be taken. The first relies on solving the differential equation (9.24) and the second relies on solving the integral form of the equation (9.25). We show below that both methods produce identical results at various contact angles, θ (Figure 76), and fiber to droplet radii ratios, $n = R_f / R_d$ (Figure 77). We also find that the determination of the numerical solution for the differential equation is time consuming at low contact angles θ and is impossible at θ = 0. The determination of the numerical solution to the integral equation, meanwhile, encounters no such shortcomings. Both methods are outlined below.

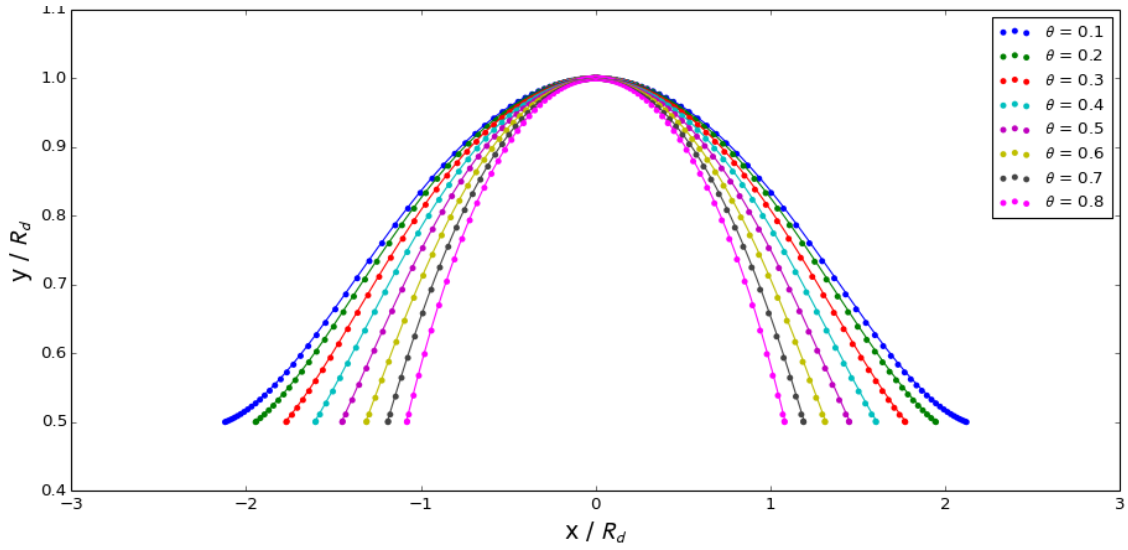

Figure 76. Numerically obtained normalized profiles of droplets of a filament at $n=R_f/R_d=0.5$ and θ ranging from 0.1 to 0.9. The dots represent the results obtained with a differential equation method and the lines are solutions obtained with the elliptic integral method. The two methods produce results indistinguishable from one another.

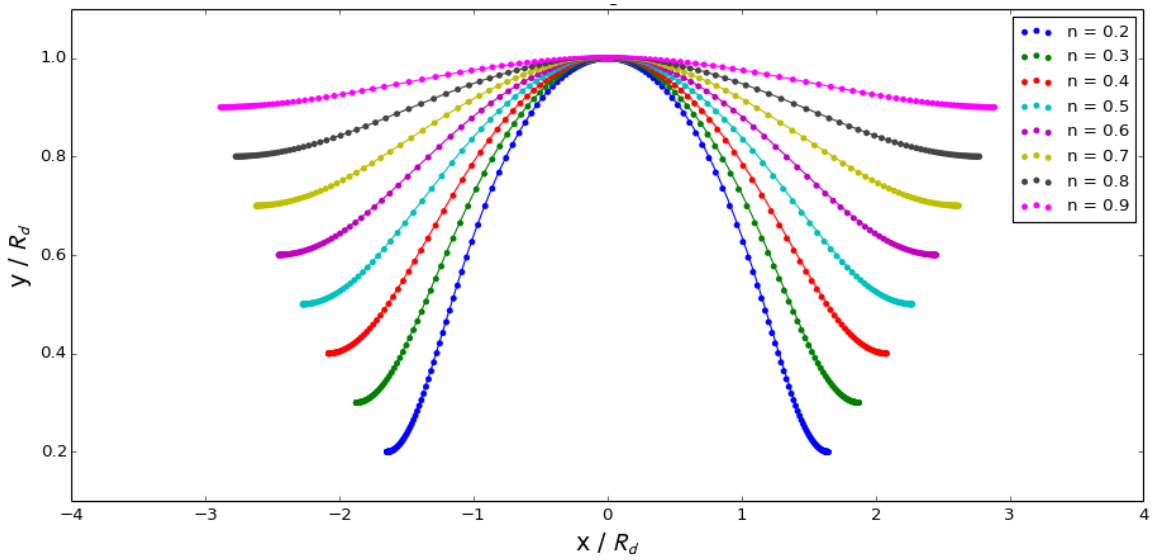

Figure 77. Numerically obtained normalized profiles of droplets of a filament at θ = 0.005 (arbitrarily close to θ = 0) and $n = R_f/R_d$ ranging from 0.2 to 0.9. The dots represent the results obtained with a differential equation method and the lines are solutions obtained with the elliptic integral method. The two methods produce results indistinguishable from one another.

9.5.4.1 Determination of a numerical solution of the differential equation

Equation (9.24) is a second order differential equation, so we will need two boundary conditions to solve it. Before we set up the boundary conditions, we need to normalize both x and y by the maximum radius of the droplet, $Y = \frac{y}{R_d}$, $X = \frac{x}{R_d}$. The equation thus becomes

$$\begin{aligned} \frac{dU}{dY} &= \frac{1}{U}\left(\frac{1+U^2}{Y} - \left(\frac{2}{1-n^2} - \frac{2\cos\theta}{\frac{1}{n}-n}\right)\left(1+U^2\right)^{3/2}\right) \\ \frac{dX}{dY} &= \frac{1}{U} \\ n &= \frac{R_f}{R_d} \end{aligned} \tag{9.26}$$

The center of coordinates is chosen such that Y = 0 at the center of the filament and X = 0 at the maximum height of the droplet. The problem is axisymmetric, which means that we only need to solve for $X \geq 0$. Both R_f and R_d are obtainable from experiment. R_d is the maximum point on the profile of the droplet and R_f is the point at which the profile of the droplet stops changing (protocol is described below). Thus, n is known from experiment and θ becomes an adjustable parameter.

If we originate our solution at $X_0 = 0$, the boundary conditions are as follows:

$$\begin{aligned} X(1) &= 0 \\ X'(1) &= 0 \end{aligned} \tag{9.27}$$

These boundary conditions are not unique for unique θ, which makes the problem difficult to solve. One method that allows to find the solution is the shooting method, which relies on guessing a θ, solving for a solution, finding the intersection point at Y =

n, calculating the angle at that point, and comparing that angle to θ. This method is time-consuming and difficult to implement.

Instead, we solve the problem from right to left and originate at a point of contact of the droplet with the filament. To do that, we temporarily shift the X-position, such that X = 0 at the contact line, find the solution, find the maximum Y of that solution, find the X of that maximum, and then shift the solution by -X. The obtained result is thus in the initially defined coordinate system. The boundary condition for this method are:

$$\begin{aligned} X(n) &= X_0 \\ X'(n) &= \tan\theta \end{aligned} \tag{9.28}$$

where $X_0 = -X\left(\max\left(Y\right)\right)$ is found after the solution is obtained.

9.5.4.2 Determination of a numerical solution of the integral equation

To find the numerical solution of equation (9.25), the equation first needs to be rewritten in terms of non-dimensional parameters $Y = \frac{y}{R_d}$, $X = \frac{x}{R_d}$

$$\begin{aligned} X\left(y\right) &= b \cdot n \cdot F\left(k,a\right) + E\left(k,a\right) \\ b &= \frac{\cos\left(\theta\right)}{1 - n \cdot \cos\left(\theta\right)} - \frac{1}{\frac{1}{n} - \cos\left(\theta\right)} \\ k &= 1 - \left(b^2 n^2\right) \\ a &= \sin\sqrt{\frac{\left(1 - Y^2\right)}{k}} \end{aligned} \tag{9.29}$$

which can be solved directly. The only challenge is computing the elliptical integrals, but any commercial software can compute them numerically quickly.

9.5.4.3 Extraction of relevant data from a filament profile.

The profile of the droplet on a filament is obtained from an image as described above and is plotted. Using cursors on the plot, the user selects the approximate bounds of the droplet (Figure 78, left). The user then selects the side of the droplet to fit to the right of the maximum or to the left of the maximum and the model with which to fit the droplet – integral or differential (Figure 78, right).

The program then performs the following steps.

1. Records the x and the y positions of both cursors.
2. Symmetrizes the droplet by averaging the top and the bottom profiles. To do that, the coordinates of the profiles are interpolated at equal x- coordinates and the absolute values of the y-coordinates are averaged.
3. Extracts the coordinates of the maximum radius of the droplet – which is specified by the two cursors - with a PeakDetector algorithm, which finds the maximum at a subpixel level by fitting localized data with a parabola.
4. All the data that is not between the selected cursor and the maximum of the droplet is discarded.

In a liquid filament, the contact line is difficult to resolve experimentally, so R_f is difficult to precisely determine. Steps 5 and 6 resolve this problem by introducing R_f as a bound adjustable parameter, which can be varied by 5%, and adding a preferential weight to the well-resolved data point far away from the filament.

5. The minimum y coordinate is obtained from the data and set as the initial guess for R_f in the fitting algorithm. From this value, a bound interval is determined as (R_f - 0.05*R_f, R_f + 0.05*R_f) During the fitting, R_f will be adjusted within this interval to determine the best fit.
6. The weighing function is applied to give the well-resolved data more weight during the fitting $w = (y - R_f)^2$. Several functions were empirically tested for the weight function, and the above produced the best fitting results.
7. The data is then fitted with a constrained Liebenberg-Marquardt algorithm and plotted for the user. During the fit, the data points that have x-coordinates, $x > x(R_f)$ are discarded.

The results of a sample fit with an integral equation are presented in Figure 79.

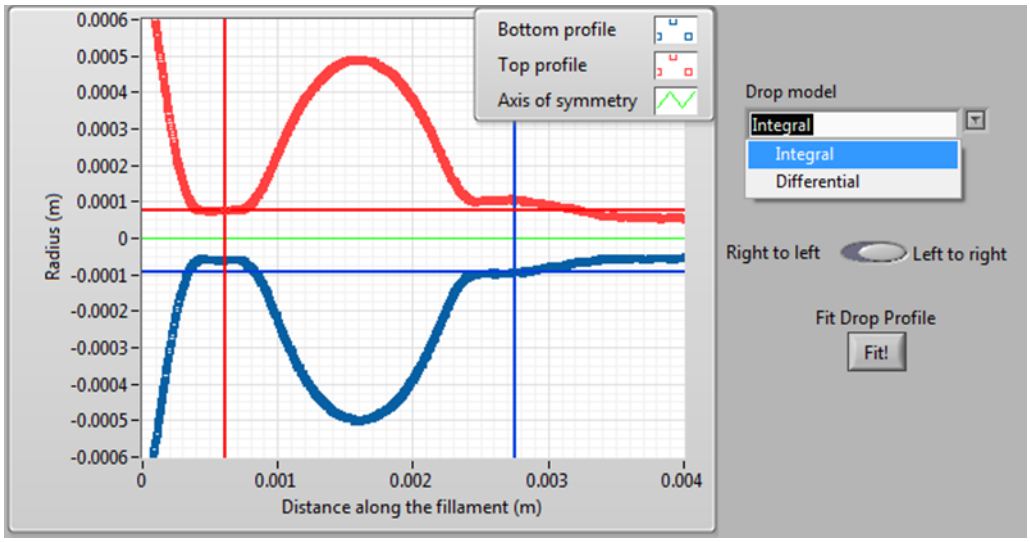

Figure 78. A screenshot of the data and fitting parameter selection as seen by the user during analisys.

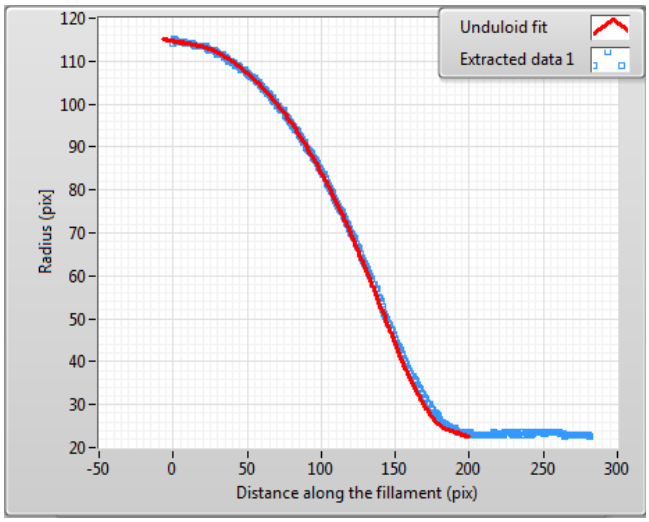

Figure 79. A screenshot of an example fit of a droplet using integral equation method, as seen by the user during the data analysis.

9.6 REFERENCES

1. Kawooya JK, Meredith SC, Wells MA, Kézdy FJ, Law JH. Physical and surface properties of insect apolipophorin III. The Journal of biological chemistry. 1986;261:13588-91,
2. Adamson AW, Gast AP. Physical chemistry of surfaces. 6th ed. New York: Wiley; 1997. xxi, 784 p. p,
3. Barnes G, Gentle I. Interfacial science : an introduction. 2nd ed. Oxford ; New York: Oxford University Press; 2011. xxii, 325 p. p,
4. Ward AFH, Tordai L. Time-Dependence of Boundary Tensions of Solutions .1. The Role of Diffusion in Time-Effects. J Chem Phys. 1946;14(7):453-61.Doi 10.1063/1.1724167
5. Vold MJ. The packing ofn-alkyl chains in Gibbs monolayers. J Colloid Interf Sci. 1984;100(1):224-32,
6. Volmer M, Mahnert P. Solution of solid substances in liquid surfaces and the characteristics of layers. Z phys Chem. 1925,
7. Kawooya JK, Meredith SC, Wells MA, Kezdy FJ, Law JH. Physical and surface properties of insect apolipophorin III. Journal of Biological Chemistry. 1986;261(29):3588-91.
8. Ryan R, Oikawa K, Kay C. Conformational, thermodynamic, and stability properties of *Manduca sexta* apolipophorin III. Journal of Biological Chemistry. 1993,
9. Weers PMM, Ryan RO. Apolipophorin III: Role model apolipoprotein. Insect Biochemistry and Molecular Biology. 2006;36:231-40.10.1016/j.ibmb.2006.01.001
10. Wientzek M, Kay C, Oikawa K, Ryan R. Binding of insect apolipophorin III to dimyristoylphosphatidylcholine vesicles. Evidence for a conformational change. Journal of Biological Chemistry. 1994,
11. Kawooya JK, Keim PS, Ryan R, Shapiro, P J, Samaraweera P, Lawn JH. Insect Apolipophorin III: purification and properteis. The Journal of biological chemistry. 1984;259:10733-7,
12. Phone conversation with Lauda sales team. Phone conversation with Lauda sales team ed2017,
13. Delaunay C. Sur la surface de révolution dont la courbure moyenne est constante. Journal de Mathématiques Pures et Appliquées 1841:309-14,
14. Carroll BJ. Accurate Measurement of Contact-Angle, Phase Contact Areas, Drop Volume, and Laplace Excess Pressure in Drop-on-Fiber Systems. J Colloid Interf Sci. 1976;57(3):488-95.Doi 10.1016/0021-9797(76)90227-7
15. Prasad SV, Ryan RO, Law JH, Wells MA. Changes in Lipoprotein Composition during Larval-Pupal Metamorphosis of an Insect, Manduca-sexta. Journal of Biological Chemistry. 1986;261(2):558-62.